

Electronic DC Transformer with High Power Density

Electronic DC Transformer with High Power Density

PROEFSCHRIFT

ter verkrijging van de graad van doctor
aan de Technische Universiteit Delft,
op gezag van de Rector Magnificus prof. dr. ir. J. T. Fokkema,
voorzitter van het College voor Promoties,
in het openbaar te verdedigen op maandag 11 september 2006 om 15:00 uur
door

Martin PAVLOVSKÝ

Inžinier, Technická Univerzita Košice
geboren te Prešov, Slovakije

Dit proefschrift is goedgekeurd door de promotor: Prof. dr. J.A. Ferreira

Toegevoegd promotor: Ir. S.W.H. de Haan

Samenstelling promotiecommissie:

Rector magnificus, voorzitter

Prof. dr. J.A. Ferreira, Technische Universiteit Delft, promotor

Ir. S.W.H. de Haan, Technische Universiteit Delft, toegevoegd promotor

Prof. dr. ir. R.W. de Doncker, Aachen University of Technology, Germany

Doc. ing. J. Dudrik PhD, Technical University of Kosice, Slovakia

Prof. ir. M. Antal, Technische Universiteit Eindhoven (emiritus)

Prof. dr. C.I.M. Beenakker, Technische Universiteit Delft

Prof. ir. J.J. Smit, Technische Universiteit Delft

This research was funded by IOP (Innovatiegerichte Onderzoeksprogramma's) of the Dutch government.

ISBN 80-7165-558-9

Printed by

Vydavateľstvo Michala Vaška

Námestie Kráľovnej pokoja 3

Prešov

Slovakia

Copyright © 2006 by Martin Pavlovský

All rights reserved. No part of the material protected by this copyright notice may be reproduced or utilised in any form or by any means, electronic or mechanical, including photocopying, recording or by any information storage and retrieval system without written permission of the copyright owner.

For the people with smile on their faces,
for making our days more beautiful.

Table of Contents

TABLE OF CONTENTS	VII
LIST OF SYMBOLS	XI
CHAPTER 1 INTRODUCTION	1
1.1 VOLTAGE SCALING.....	1
1.1.1 <i>History of Voltage Scaling</i>	1
1.1.2 <i>Evolution of Low-Power Dc-Dc Conversion</i>	2
1.1.3 <i>Evolution of High-Power Dc-Dc Conversion</i>	5
1.1.4 <i>Applications for High-Power Dc-Dc Converters with Galvanic Isolation</i>	5
1.2 PROBLEM DEFINITION; THREE CORNERSTONES OF CONVERTER DESIGN.....	7
1.2.1 <i>Reducing the Size of Passives</i>	8
1.2.2 <i>Topologies & Losses</i>	8
1.2.3 <i>Thermal Management</i>	9
1.2.4 <i>Integration of the Three Cornerstones; Integral Design Process</i>	9
1.3 STATE-OF-THE-ART – TECHNOLOGICAL DEVELOPMENT	11
1.3.1 <i>Passive Components</i>	11
1.3.2 <i>Semiconductor Devices</i>	12
1.3.3 <i>Converter Topologies</i>	12
1.3.4 <i>Thermal Management</i>	13
1.4 THESIS LAYOUT.....	15
CHAPTER 2 DC-DC CONVERTER TOPOLOGIES	17
2.1 INTRODUCTION	17
2.2 “OPTIMAL CURRENT WAVEFORM”	17
2.3 TOPOLOGIES USING “OPTIMAL CURRENT WAVEFORM”	19
2.4 ANALYSIS OF OPERATION OF OUTPUT FILTER RESONANT ZVS QUASI-ZCS CONVERTER TOPOLOGY	21
2.4.1 <i>OFRC Converter Model</i>	22
2.4.2 <i>Operating Modes of OFRC Converter</i>	22
2.4.3 <i>Calculated Waveforms</i>	28
2.4.4 <i>Bi-Directional OFRC topology</i>	30
2.5 LOSS ANALYSES	31
2.5.1 <i>Power Loss of Switches and Resonant Circuit Parameters</i>	31
2.5.2 <i>Turn-off Instant and Dead Time Setting</i>	32
2.5.3 <i>Reverse Recovery Loss in Rectifier</i>	34
2.5.4 <i>Power Loss in Resonant Capacitors</i>	36
2.6 VOLTAGE CONTROL IN OFRC TOPOLOGY	36

2.7	CONVERTER DEMONSTRATORS.....	39
2.7.1	<i>Applications and Specifications of Converter Prototypes</i>	40
2.7.2	<i>IGBT Modules Under ZVS, Quasi-ZCS</i>	41
2.7.3	<i>Converter Circuits</i>	43
2.7.4	<i>Measurements on Converter Prototypes</i>	45
2.8	CONCLUSIONS.....	48
CHAPTER 3	HIGH POWER DENSITY IN POWER MAGNETICS.....	51
3.1	INTRODUCTION.....	51
3.2	MAGNETIC MATERIALS.....	51
3.3	WINDING TECHNOLOGIES.....	52
3.4	HIGH-FREQUENCY HIGH-POWER TRANSFORMER.....	53
3.4.1	<i>Volumetric Optimisation of the Transformer Structure</i>	53
3.4.2	<i>Foil Winding Technology for Transformer Windings</i>	55
3.4.3	<i>Losses in Transformer Foil Windings</i>	57
3.4.4	<i>Leakage Inductance</i>	60
3.5	FILTER INDUCTORS.....	66
3.5.1	<i>Filter Inductor Design – Power Loss Calculation</i>	68
3.6	RESULTS OF PRACTICAL EXPERIMENTS.....	70
3.6.1	<i>Practical Implementation and Measurements on Transformer Prototypes</i>	70
3.6.2	<i>Measurements on Filter Inductors</i>	77
3.7	CONCLUSIONS.....	79
CHAPTER 4	THERMAL MANAGEMENT.....	81
4.1	INTRODUCTION.....	81
4.2	THERMAL MANAGEMENT ON COMPONENT LEVEL.....	82
4.2.1	<i>Thermal Management of Active Components</i>	82
4.2.2	<i>Thermal Management of Magnetic Components</i>	83
4.2.3	<i>Thermal Management of Capacitors</i>	90
4.3	THERMAL MANAGEMENT ON CONVERTER LEVEL AND SYSTEM LEVEL.....	91
4.4	PROPOSED CONVERTER THERMAL MANAGEMENT CONCEPT.....	93
4.5	DESIGN PROCESS OF THERMAL MANAGEMENT.....	94
4.5.1	<i>Conceivable Thermal Management Solutions</i>	97
4.6	THERMAL MANAGEMENT OF PROPOSED SOLUTION.....	101
4.6.1	<i>Practical Implementation of Proposed Solution</i>	101
4.6.2	<i>FEM Thermal Analysis of Proposed Structure</i>	102
4.7	PRACTICAL EVALUATION OF THERMAL MANAGEMENT.....	103
4.8	CONCLUSIONS.....	106
CHAPTER 5	INTEGRATION OF THE THREE CORNERSTONES.....	107
5.1	INTRODUCTION.....	107
5.2	SPATIAL INTEGRATION OF COMPONENTS.....	107
5.2.1	<i>Restrictions of Spatial Integration of Components</i>	107
5.2.2	<i>Integrated Converter Structure</i>	108
5.3	SCALING-UP.....	112
5.3.1	<i>Component Performance and Scaling up; Single Unit approach</i>	112
5.3.2	<i>Power Density and Scaling up; Single Unit Approach</i>	118
5.4	CONCLUSIONS.....	119
CHAPTER 6	CONCLUSIONS AND RECOMMENDATIONS.....	121

6.1	SUMMARY.....	121
6.2	CONCLUSIONS; THREE CORNERSTONES OF THE CONVERTER DESIGN.....	122
6.2.1	<i>Reduction of Size</i>	122
6.2.2	<i>Reduction of Losses</i>	123
6.2.3	<i>Thermal Management</i>	123
6.2.4	<i>Conclusions</i>	124
6.3	RECOMMENDATIONS FOR FUTURE RESEARCH.....	124
REFERENCES	127
APPENDIX A.	AC RESISTANCE OF PARTIALLY INTERLEAVED WINDINGS.....	133
APPENDIX B.	OVERVIEW OF HEAT REMOVAL METHODS.....	137
APPENDIX C.	FEM THERMAL ANALYSIS OF PROPOSED CONVERTER STRUCTURE	143
SUMMARY	151
SAMENVATTING	153
ACKNOWLEDGEMENTS		155
CURRICULUM VITAE		159

List of Symbols

Latin Letters

A	Area	[m ²]
A_c	Core area	[m ²]
A_m	Core magnetic material area	[m ²]
A_w	Winding window area	[m ²]
B	Magnetic flux density	[T]
B_m	Peak flux density	[T]
B_s	Saturation flux density	[T]
c_p	Specific heat	[J/kgK]
C	Capacitance	[F]
C_r	Resonant capacitance	[F]
C_r'	Resonant capacitance recalculated to transformer primary side	[F]
C_{snb}	Snubber capacitance	[F]
d_c	magnetic core depth	[m]
d_{c_e}	magnetic core depth with equality of thermal resistances in compared thermal concepts	[m]
dV_{Cr}	Peak to peak voltage swing across the resonant capacitor	[V]
D_h	Hydraulic diameter	[m]
E_{Ls_off}	Energy store in leakage inductance in instant of turn-off	[J]
E_{leak_w}	Energy of the leakage inductance related to foils and isolation	[J]
E_{leak_layer}	Energy of the leakage inductance related to leakage layer	[J]
E_{SW}	Switching energy loss	[J]
f_0	Filter cut-off frequency	[Hz]
f_s	Switching frequency	[Hz]
$F_{1,2}$	Shape factor in heat transfer by radiation	
g	Air-gap length	[m]
h_c	Convection coefficient	[W/m ² K]
h_f	Foil thickness	[m]
h_i	Isolation thickness	[m]
h_{leak}	Leakage layer thickness	[m]
h_p	Thickness of the p-th winding layer	[m]
h_w	Winding height	[m]
H	Magnetic field intensity	[A/m]
H_{ct}	Total magnetic core height	[m]
H_g	Air-gap field intensity	[A/m]
H_{leak}	Leakage layer field intensity	[A/m]
H_{re}	Magnetic field intensity real component	[A/m]
$i(t)$	Current as a function of time	[A]
i_n	Partial current through n-th winding layer	[A]

i_f	Interleaving factor	
i_s	Loop current	[A]
I_{av}	Average current	[A]
I_d	Diode current	[A]
I_{dc}	Dc current component	[A]
I_{X_endY}	Current in component X at the end of interval Y	[A]
I_i	Input current	[A]
I_{iBR}	Input current of the bridge section	[A]
I_{X_in}	Initial current in component X	[A]
I_{max}	Peak current	[A]
I_{off}	Turn-off current	[A]
I_{off_min}	Minimal turn-off current	[A]
I_{rms}	Rms current	[A]
I_o	Output current	[A]
I_o'	Current through the output filter inductor	[A]
I_o	Current through the output filter inductor recalculated to transformer primary side	[A]
I_{oBR}	Output current through the bridge section	[A]
I_p	Primary current	[A]
I_{p_rms}	Primary rms current	[A]
I_{r_fs}	Resonant circuit current ripple	[A]
I_{r_io}	Current ripple penetrating through resonant inductor	[A]
I_{rr}	Reverse recovery current	[A]
I_X	Current in a component X	[A]
I_{sw}	Switch current	[A]
J	Colburn factor	
J	Current density	[A/m ²]
J_h	Current density at top surface of conductors	[A/m ²]
J_{re}	Current density real component	[A/m ²]
J_{rms}	Rms current density	[A/m ²]
k	Core loss coefficient	
k	Thermal conductivity	[W/mK]
k_c	Core factor $k_c=A_m/A_c$	
k_{c_a}	Core thermal conductivity along the core laminations	[W/mK]
k_f	Thermal conductivity of copper foil	[W/mK]
k_{fill}	Winding fill factor	
k_I	Filter ratio	
k_i	Thermal conductivity of isolation	[W/mK]
k_{leak}	Ratio between air-gap length and leakage layer width, $k_{leak}=2g/w_{leak}$	
k_{w_a}	Thermal conductivity along the winding layers	[W/mK]
k_{w_p}	Thermal conductivity perpendicular to the winding layers	[W/mK]
K	Scaling factor	
K_w	Waveform factor	
l	Length	[m]
l_{leak}	Leakage layer length	[m]
l_t	Mean turn length	[m]
L	Inductance	[H]
L_f	Filter inductance	[H]
L_i	Input filter inductance	[H]
L_{leak}	Leakage inductance	[H]
L_{leak_sp}	Leakage inductance per meter length	[H/m]

L_{σ}	Leakage inductance	[H]
L_{leak_w}	Leakage inductance related to foils and isolation	[H]
$L_{leak_{layer}}$	Leakage inductance related to leakage layer	[H]
L_o	Output filter inductance	[H]
L_p	Parallel inductance of transformer model	[H]
L_s	Series inductance of transformer model	[H]
n	Transformer turn ratio	
m	Number of layers in non-interleaved winding section	
m_p	Number of primary interleaved layers	
m_s	Number of secondary interleaved layers	
N	Number of turns	
N_1	Number of primary transformer turns	
N_2	Number of secondary transformer turns	
$N_{interleaved}$	Number of interleaved turns in partially interleaved windings	
N_r	Reynolds number	
p	Number of a winding layer	
P	Power loss	[W]
P	Peltier factor	[V]
P_{con}	Conduction losses of semiconductor switches	[W]
$P_{c_{sp}}$	Specific core loss	[W/m ³]
P_d	Dielectric losses of capacitor	[W]
P_{HP}	Losses in heat pipes due to eddy currents	[W]
P_o	Output power	[W]
P_{rec}	Reverse recovery losses	[W]
P_{sw}	Switching losses of semiconductor switches	[W]
P_t	Thermal losses in capacitor	[W]
P_T	Total power loss of a switch	[W]
P_{Tr}	Overall transformer power loss	[W]
P_w	Winding losses	[W]
$P_{w_{Lf}}$	Losses in winding of filter inductor	[W]
q, Q	Removed heat	[W]
Q_{rr}	Reverse recovery charge	[C]
R_{ac}	Ac resistance	[Ω]
R_{C_s}	Series resistance of a capacitor	[Ω]
R_{dc}	Dc resistance	[Ω]
$R_{p_{ac}}$	Ac resistance of primary interleaved winding section	[Ω]
$R_{s_{ac}}$	Ac resistance of secondary interleaved winding section	[Ω]
R_{th}	Thermal resistance	[K/W]
$R_{th_{ch}}$	Horizontal thermal resistance of the core structure	[K/W]
$R_{th_{cv}}$	Vertical thermal resistance of the core structure	[K/W]
$R_{th_{diode}}$	Diode thermal resistance junction to heatsink	[K/W]
$R_{th_{igbt}}$	IGBT thermal resistance junction to heatsink	[K/W]
R_{th_t}	Total heatsink thermal resistance	[K/W]
R_{th_w}	Winding thermal resistance	[K/W]
R_{w0}	Dc winding resistance	[Ω]
$R_{w_{ac}}$	Ac resistance of non-interleaved winding section	[Ω]
s	Diode snap factor	
S	Apparent power	[VA]

$\left(\frac{S}{V}\right)_c$	Core surface to volume ratio	[m ⁻¹]
$\left(\frac{S}{V}\right)_w$	Winding surface to volume ratio	[m ⁻¹]
t	Time	[s]
t_{off}	Turn-off instant	[s]
t_{on}	Switch <i>on</i> time	[s]
t_{rr}	reverse recovery time	[s]
$\tan \delta_0$	Dielectric loss factor	
T	Switching period	[s]
T	Temperature	[°C]
T_{max}	Maximal temperature	[°C]
$T_{w,max}$	Maximal winding temperature	[°C]
v	Velocity	[m/s]
v_f	Fluid velocity	[m/s]
$v(t)$	Voltage as a function of time	[V]
$v_i(t)$	Voltage before scaling	[V]
$v_o(t)$	Voltage after scaling	[V]
V	Volume	[m ³]
V_{Cri}	Voltage of the input resonant capacitor	[V]
V_{Cro}	Voltage of the output resonant capacitor	[V]
V_{Csnb_on}	Snubber capacitor voltage of a capacitor in parallel to the switch that was <i>on</i>	[V]
V_{Csnb_off}	Snubber capacitor voltage of a capacitor in parallel to the switch that was <i>off</i>	[V]
V_d	Voltage across a diode	[V]
V_i	Input voltage	[V]
V_{ip}	Voltage induced in p-th layer	[V]
V_{leak}	Volume of leakage layer	[m ³]
V_{ON}	On-state voltage	[V]
V_o	Output voltage	[V]
V_{o1}, V_{o2}	Voltage of the fixed outputs	[V]
V_{o3}	Voltage of the controllable output	[V]
V_{o3-1}, V_{o3-2}	Output voltage of auxiliary secondary	[V]
V_{oBR}	Output voltage bridge section	[V]
V_{pp}	Peak to peak voltage across a capacitor	[V]
V_{rp}	Resistive voltage drop in p-th layer	[V]
V_{sw}	Voltage across a switch	[V]
V_{Tr}	Transformer volume	[m ³]
V_w	Winding volume	[m ³]
V_{X_endY}	Voltage of component X at the end of interval Y	[V]
V_{X_in}	Initial voltage of component X	[V]
w_c	Central core leg width	[m]
w_{leak}	Leakage layer width	[m]
w_w	Winding width	[m]
W_{ct}	Total magnetic core width	[m]
Z	Impedance	[Ω]
Z_C	Impedance of capacitor	[Ω]
Z_L	Impedance of inductor	[Ω]
Z_r	Resonant impedance	[Ω]

Z_w	Winding impedance	[Ω]
x	Position with respect to reference	[m]
x	Distance between hot-spot and heat-exchange point	[m]

Greek Letters

α	Core material constant, frequency exponent	
α	Phase shift between converter sub-modules	
β	Core material constant	
δ	Skin depth	[m]
ε	Emissivity	
Δ	Variation of a parameter	
ΔT	Temperature rise	[$^{\circ}\text{C}$]
ϕ	Magnetic flux	[Wb]
μ	Dynamic viscosity	[kg/ms]
μ	Permeability	[Wb/Am]
μ_0	Permeability of vacuum, $4\pi 10^{-7}$	[Wb/Am]
μ_r	Relative permeability	
ρ	Resistivity	[Ωm]
ρ_f	Fluid density	[kg/m ³]
σ	Stefan-Boltzmann constant, 1.38×10^{-23}	[J/K]
ω_r	Resonant frequency	[rad ⁻¹]

Acronyms

ac	Alternating current
dc	Direct current
EMC	Electromagnetic compatibility
EMI	Electromagnetic interference
FEM	Finite element modelling
FRC	Full resonant converter
FS	Field stop
GTO	Gate turn-off thyristor
HF	High frequency
IGBT	Insulated gate bipolar transistor
JFET	Junction gate field-effect transistor
MOSFET	Metal oxide field effect transistor
NPT	Non punch through
OFRC	Output filter resonant converter
PCB	Printed circuit board
PC	Personal computer
PSRC	Partial series resonant converter
SMD	Surface-mount devices
TNM	Thermal network modelling
ZCS	Zero current switching
ZVS	Zero voltage switching
XGA	Extended graphics array

Chapter 1 *Introduction*

1.1 Voltage Scaling

Often, the available electric power is not compatible with the electric power as required by a load. There may be differences in voltage level, frequency, type of waveform, type of current and so on. Examples of incompatibilities are: a computer supplied from a public 230 V ac grid whose chips require 3.3 V dc to run, a modern TV set supplied from 230 V ac while the majority of its circuits require a supply voltage below 12 V dc, and an ac traction locomotive which is typically supplied from a 25 kV ac catenary but the traction motors require voltages in range of 1 kV ac. To accommodate these incompatibilities, one or more functions like voltage scaling, frequency conversion and galvanic isolation are required.

In the last century, many techniques were developed to realise these functions. The function that is often needed is voltage scaling with galvanic isolation, where voltage scaling is defined as:

$$v_o(t) = K \cdot v_i(t), \quad (1-1)$$

where v_o and v_i are voltages after and before scaling and K is the scaling factor, both for dc and ac. For ac, the frequency remains unchanged by the voltage scaling operation. Galvanic isolation is often required to separate the load from the supply for safety and other reasons. The following paragraphs will focus on voltage scaling with galvanic isolation, the associated technology, its history, the state-of-the-art, and its application. The main focus will be on power density as one of the main requirements of the converter design process.

1.1.1 History of Voltage Scaling

In the past, voltage scaling was feasible only with ac. A conventional 50 Hz transformer performed this function by using electromagnetic induction to transfer the energy via a magnetic coupling. Galvanic isolation is a natural property of ac transformers. The performance of ac transformers has been improved since these transformers were first introduced in 1885, even though their principle and main construction features have remained unchanged (Figure 1-1). Nowadays, they offer a high efficiency and reliability almost unbeatable by any of the other voltage scaling concept.

Conventional ac transformers cannot be used for dc voltage scaling; for this purpose power electronics is needed. Electronic dc-dc conversion was first used in the late 1920s/1930s, when vibrating contacts were employed in combination with a transformer and a vacuum tube rectifier to scale dc (Figure 1-2 [1]). Vibrating contacts created ac, which could be transferred through the transformer. At the output, dc was recreated by the tube rectifier.

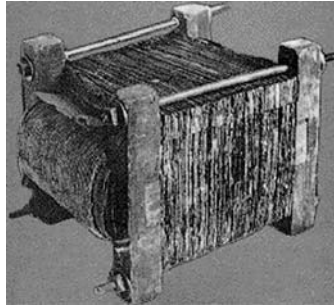


Figure 1-1: First practical transformer built by William Stanley Jr. in 1885

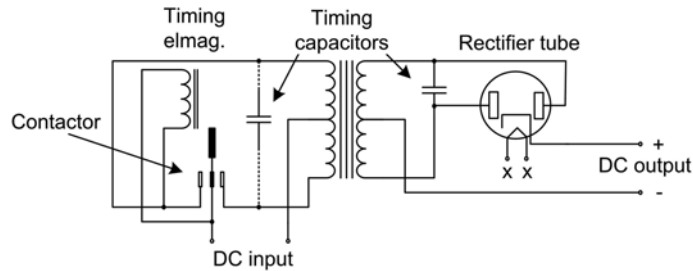


Figure 1-2: One of the first electronic dc-dc converters; a combination of vibrating contacts, transformer and vacuum tube rectifier [2]

Modern power electronics dates back to 1948, when the bipolar transistor was invented by Bell Laboratories. Later, in 1956, the same laboratory invented the thyristor. This started possibly the greatest revolution in the history of electrical power conversion and allowed for efficient voltage scaling in dc without mechanical parts. The development led to various circuit topologies with and without galvanic isolation [3], [4], [5]. Voltage could be scaled up or scaled down and it could be controlled to a specified value by controlling the duty ratio of the switches. Nowadays, modern semiconductor devices are used as switches.

In general, dc-dc converters can be divided into two groups: with and without the use of a transformer. Converters without a transformer consist of a relatively small number of inductors, capacitors and semiconductor switches. By proper connection of these components, the required function is realised such as: buck, boost, two-quadrant, four-quadrant operation [6]. The main advantage of converters without a transformer is that they are relatively simple. Their main disadvantage is the absence of the galvanic isolation and a limited scaling factor K because of ineffective use of semiconductors. If a larger scaling factor K or a galvanic isolation is required, a transformer must be combined with inductors, capacitors and switches. In such a case, the transformer can be used only for power transfer (forward converter and others) [6] or it can also function as an inductor (fly-back converter) [6].

1.1.2 Evolution of Low-Power Dc-Dc Conversion

One of the targets pursued in power electronics is high power density. Figure 1-3 shows the power density evolution of power electronic conversion systems. As can be seen, the power density of electronic converters increased linearly on a logarithmic scale in the last 30 years. The power density of a state-of-the-art converter is presently 1 to 3 W/cm³ (1 to 3 kW/l). The evolution curve indicates that power converters with power densities around 10 W/cm³ (10 kW/l) are expected to be available in 2010. Advanced low power converters have such power densities even today as will be shown later. Measures that were needed to realise such high power densities are discussed below.

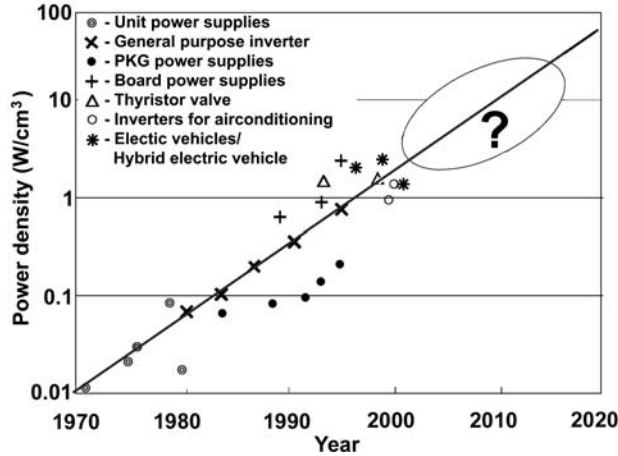


Figure 1-3: Evolution of power density of power electronic converters [7]

The conventional 50 Hz solutions as shown for example in Figure 1-4a are bulky and therefore they are being replaced by more advanced power electronic converters as for example shown in Figure 1-4b. The advanced power converters are used even though they are more complex, mostly less reliable and often with lower efficiency than conventional transformer-based solutions. They are preferred because they are lighter and more compact, which is a must for many applications. The power density of a state-of-the-art power supply is presently almost thirty times higher than that of the conventional solution with a 50 Hz transformer. Increase of the operating frequency is the main contributor to the increased power density because it reduces the size of passive components (capacitors, inductors and transformers) (see Section 1.2.1) and hence allows a better integration of passive and active components.

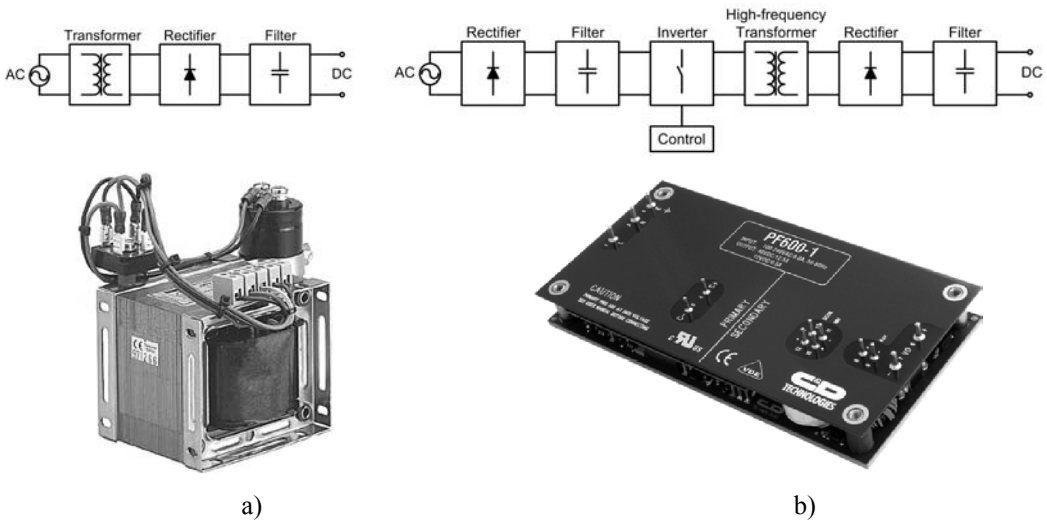


Figure 1-4: Comparison of a) conventional 50 Hz power supply (0.03 W/cm³, 40W/kg) and b) state-of-the-art high-frequency power supply technology (CD Technologies, >5 W/cm³ converter only, >0.75 W/cm³ including filters and heatsink)

The trend indicated above is clearly noticeable in applications such as PC power supplies, supplies for consumer electronics and supplies for portable devices. Figure 1-5 shows the evolution of PC power supplies. The main contributors to increased power density in this application are the aforementioned increase in operating frequency, reduction of power loss, improvement of the cooling and the more effective use of the space inside the housing. The technology to attain these improvements is mainly based on the use of conventional low-cost components and PCB technology because the design of these applications is highly cost-driven. As Figure 1-5 shows, the power available from a package of the same size has been doubled. A similar development can be observed in consumer electronics and power supplies for portables as shown in Figure 1-6. The figure shows examples of consumer power supplies, namely a 400 W XGA (eXtended Graphics Array) screen power supply and a 20 W mobile phone charger. As can be seen here too, conventional component technologies are used in combination with high-frequency designs.

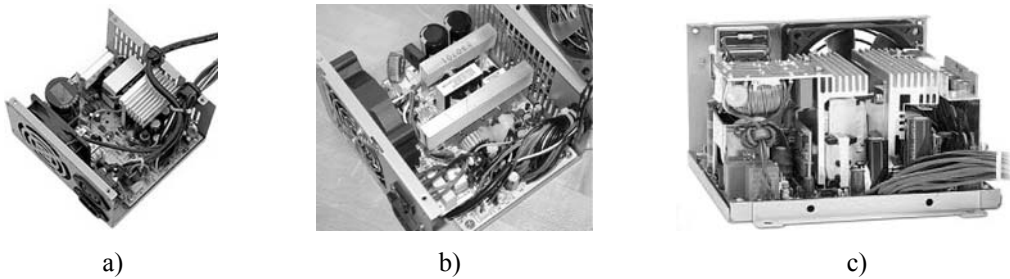


Figure 1-5: Evolution of power density in ATX PC power supplies (anno 2005); a) 280W (0.15 W/cm^3), b) 430W (0.24 W/cm^3), c) 500W (0.28 W/cm^3); all shown power supplies have the same size

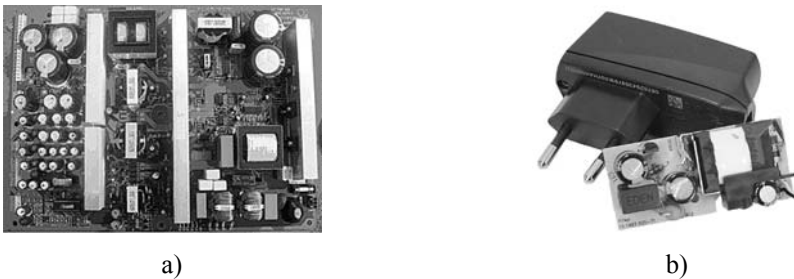


Figure 1-6: Consumer electronics and portable power supplies based on conventional components and PCB technology (anno 2005); a) 400W XGA screen supply (0.12 W/cm^3), b) 20 W mobile phone charger (0.5 W/cm^3)

The power density can be further increased by implementing new technologies such as planar and embedded magnetics, advanced PCB technologies and power SMD components. These technologies are applied in power supplies for communications where the limited space requires implementation of new technologies. Unlike the previously mentioned applications, these designs are primarily size-driven. Every five to seven years, the package size halves, while the new package delivers 65-75% of the power of the previous package [8]. Figure 1-7 shows the evolution of technologies in communication power supplies. It shows a power supply based on conventional components and advanced power supplies based on a planar technology and on a common heatsink concept. The advanced designs attain high power densities by applying technologies with high efficiency (Figure 1-7b, efficiency up to 97%), efficient heat removal (Figure 1-7c, efficiency of 90%) and a high degree of integration between active and passive components (both Figure 1-7 b and c).

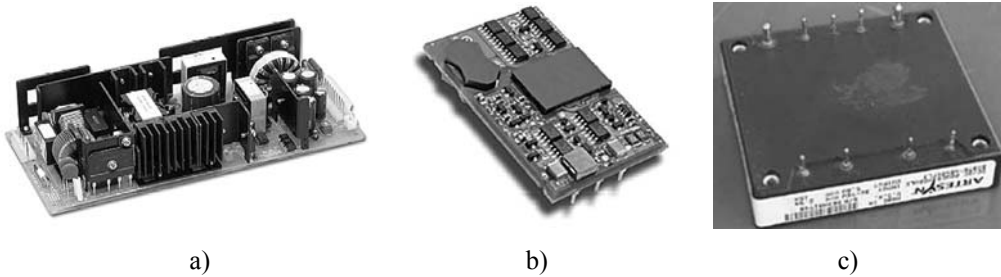


Figure 1-7: Communication power supplies (anno 2005); a) 225 W conventional technology (0.24 W/cm^3 including rectifier), b) 240 W planar technology (11.2 W/cm^3 , no heatsink needed), c) 350 W common heatsink concept (10 W/cm^3 calculated without a heatsink, heatsink needed)

1.1.3 Evolution of High-Power Dc-Dc Conversion

At high power, the technology for high power density is different from low power. In the field of power converters for ac drives, a technology shift concerning power density can be observed. Conventional power modules are being replaced by so-called “intelligent power modules” – also called “smart power modules”. These modules integrate power devices, drivers and some control circuits in one package. However, the passive components are still not integrated in the same package.

Non-isolated dc-dc converters are broadly used in dc drives and dc traction. They are still based on relatively simple buck and boost topologies employing IGBT switches operating at medium frequencies (several kHz). In the multi-MW power range, GTO thyristors are in use.

In practice, isolated dc-dc converters for high power are hardly applied although there is a need for them. They are needed for applications which require galvanic isolation for safety or functional reasons and for applications which require a large input to output ratio. Examples of such applications are auxiliary converters for traction, which require galvanic isolation for safety reasons, converters to supply ships moored in harbours, which require galvanic isolation to prevent corrosion, and main traction converters for 25 kV ac traction, which require a large input to output ratio (25 kV ac to approximately 1 kV variable frequency ac). Currently, a combination of conventional low-frequency transformers and high-frequency converters is applied to realise the required function.

1.1.4 Applications for High-Power Dc-Dc Converters with Galvanic Isolation

The main group of applications that would benefit from advanced high-power dc-dc converters is traction. Any mobile application requires a small size and light weight. Typical power levels of these applications are in the range from kW up to MWs.

In a railway system with ac catenary, the voltage level is usually in the 10 to 25 kV range and needs scaling down to several kVs to be fed to traction machines. Conventional transformers are used for this purpose (Figure 1-8). In Germany, a frequency of $16 \frac{2}{3} \text{ Hz}$ is used at the catenary, which leads to large on-board transformers with excessive weight. Savings in size and weight would be the main benefits of using high-frequency transformers, as discussed in [9] and [10]. High-frequency transformers are already used at lower power (up to 50 kW) in some auxiliary converter designs, as shown in Figure 1-9. The displayed system provides two outputs, one to supply three-phase low-voltage loads and the other to charge on-board batteries. Dc-dc converters (3 and 6) are used for voltage scaling. An inverter (4) is used to convert dc into three-phase ac. The other blocks (1, 2, 5 and 7) provide filtering and control.

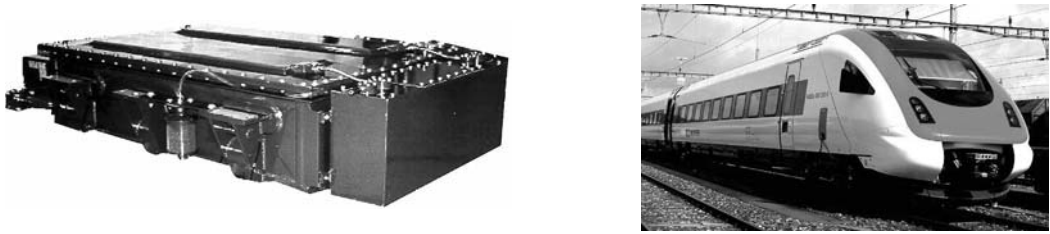


Figure 1-8: Traction transformer and the rail vehicle in which it is installed; the transformer usually has the width of the rail vehicle (ABB 2 MVA 16 $\frac{2}{3}$ Hz)

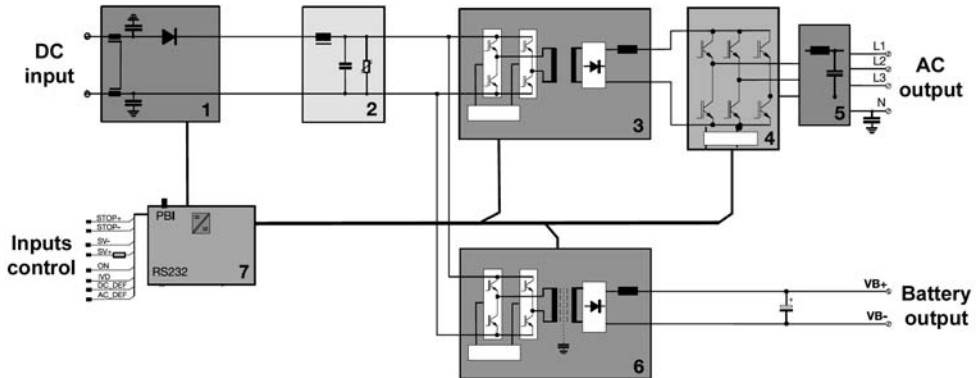


Figure 1-9: State-of-the-art auxiliary traction converter; voltage scaling realised by dc-dc converters with galvanic isolation (ABB)

Another application field that could benefit from high-frequency dc-dc converters is ship power supplies. The distribution grid aboard a ship has specific voltage and frequency (e.g. 230 V, 50 Hz), but the power available in harbours around the world may be different. Therefore, power converters are placed aboard to supply the specified power while the ship is moored in a harbour. Galvanic isolation is required, inter alia, for safety and to prevent corrosion. A typical configuration of the state-of-the-art shore converter is shown in Figure 1-10. This converter separates two independent ac grids (shore grid and on-board grid) using galvanic isolation and intermediate dc. The voltage is scaled by two conventional 50 Hz transformers. One of them provides the mentioned galvanic isolation and the other is designed as an autotransformer. The power converter is compact but the low-frequency passives, especially the two transformers, are bulky. A dc-dc converter with galvanic isolation is a much smaller and lighter device that could realise the same scaling function and galvanic isolation as the two transformers.

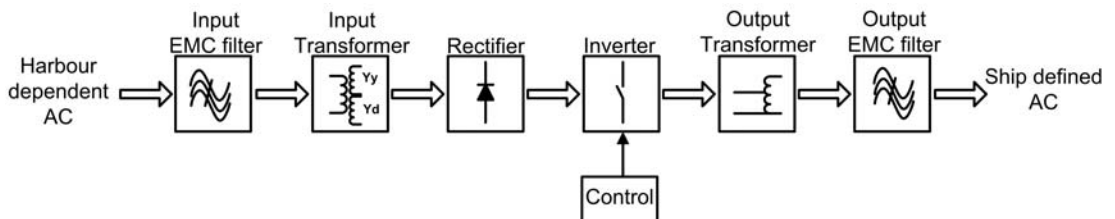


Figure 1-10: Block diagram of ship shore power supply

1.2 Problem Definition; Three Cornerstones of Converter Design

The discussion above shows that there is a technology gap between the isolated low-power and high-power high-frequency dc-dc converters. The discussion also shows that knowledge on realising high power densities is available in the low-power field. Applying this knowledge and combining it with new technologies could bring real benefits to high-power applications. The main objective of this thesis is to implement the available knowledge, to identify suitable technologies and to develop a methodology for designing isolated high-power high-frequency dc-dc converters. The main design targets are high power density, high efficiency and a simple thermal management.

The main design targets are translated into three cornerstones of converter design as:

- Reduction of converter size
- Reduction of losses
- Advanced thermal management

The three cornerstones are depicted in Figure 1-11 and discussed in the following paragraphs.

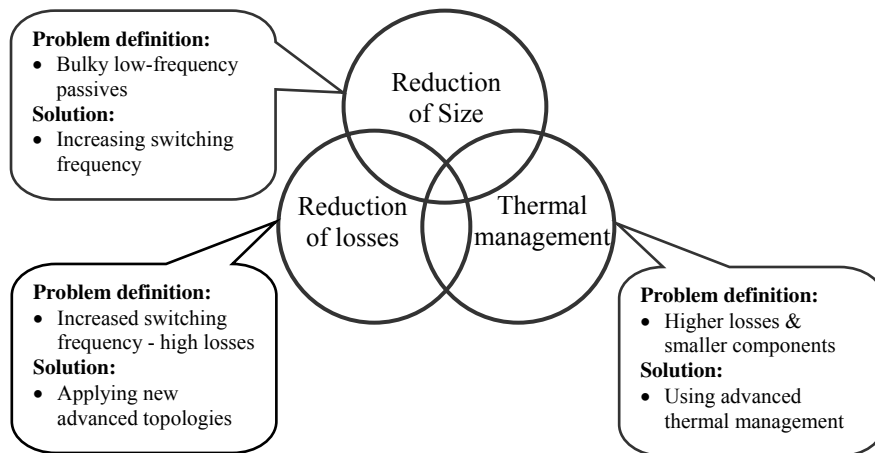


Figure 1-11: Three cornerstones of the converter design

Reduction of the converter size is directly related to attaining a high power density. The preview of applications suggests that, to obtain smaller converters at high power, the size of their passives must be reduced. Passives are in general the bulkiest components of any converter, but this is even more pronounced in high-power converters. At high power, usually low-frequency passives are used and they can have massive sizes, as shown in Figure 1-8. Increasing the operating frequency reduces the size of passives substantially (paragraph 1.2.1) and hence increases the power density.

On the other hand, high operating frequencies also result in increased losses in passive but primarily in active components (paragraph 1.2.2). High losses mean low efficiency, which is in contradiction with the requirement of an efficient energy conversion, one of the main design targets. A complex and bulky thermal management system is usually another consequence of high losses. The bulky thermal management may greatly counterbalance the gained improvement of power density. In order to reach the design targets, the power loss must be kept as low as possible and therefore new topologies which reduce the power loss by improving the shape of the switching waveforms must be investigated.

Decreased component size and increased operating frequency lead to higher power loss generation in smaller volumes. Therefore, high-power converters with high power densities require advanced thermal management to remove the generated heat from the component bodies. Thermal management is also included in the overall converter power density and hence it must be as small as possible. Simplicity and low maintenance are other important requirements for the thermal management.

One of the conclusions of the preceding discussion is that the three cornerstones are closely interconnected. This is illustrated in Figure 1-11 by the three intersecting circles. In spite of the close interconnection, we shall approach each of the cornerstones separately at first by introducing each of them in sections 1.2.1, 1.2.2 and 1.2.3. The interdependencies between the cornerstones are discussed in section 1.2.4. Later, the state-of-the-art and technological development of each of the cornerstones will be discussed in section 1.3 and the layout of the thesis will be introduced in section 1.4.

1.2.1 Reducing the Size of Passives

Passive components are usually the bulkiest components of any converter design. This is more pronounced in high-power than in low-power converters because of the lower operating frequencies at high power. The size of passives is directly related to the operating frequency and therefore operation at high frequencies is one of the keys to reaching high power density. The relation between the size of passives and the operating frequency is briefly discussed here.

In general, three main types of passive components are used in power converters; inductors, capacitors and transformers. Considered as filters, inductors and capacitors “separate” the internal high-frequency switching-waveforms from low-frequency or dc waveforms at the converter terminals. The capacitor’s ability to “short-circuit” high frequencies and the inductor’s ability to “resist” high frequencies originate from the behaviour of their impedances calculated as: $Z_C=1/(2\pi f_s C)$ and $Z_L=2\pi f_s L$. From the impedance equations it follows that filtering a higher frequency requires smaller component values in order to preserve the same filtering effect. Smaller values of L and C yield smaller components. A similar relation between the operating frequency and size could be shown for the inductors and capacitors used as energy storage elements.

Concerning a transformer, the following equation describes a relation between the core size and its apparent power [6]:

$$S = K_w f_s B_m J_{rms} k_{fill} A_w A_m , \quad (1-2)$$

where S is the apparent power transported through the transformer, K_w is the waveform factor, f_s is the switching frequency, B_m is the peak flux density, J_{rms} is the rms current density, k_{fill} is the winding fill factor, A_w is the cross-section of the winding and A_m is the effective cross-sectional area of the core. As can be seen in this equation, the processed power S is linked to the transformer size-related parameters A_w and A_m and design parameters B_m , J_{rms} and f_s . Equation 1-2 shows that if the power S and design parameters B_m and J_{rms} are fixed, then increasing the switching frequency f_s results in a smaller value of A_w and A_m , which means a smaller transformer.

This discussion shows that the size of passive components is directly coupled to the operating frequency. Magnetic components and their size are addressed in Chapter 3 in more detail.

1.2.2 Topologies & Losses

A high switching frequency is required to decrease the size of passives and hence increase the power density. A high switching frequency results in an increase of switching losses, eddy current losses and hysteresis losses in converter components. The higher power losses yield reduced converter efficiency and require larger heatsinks, which consequently reduce the effect of the higher operating frequency on the overall power density.

The power losses in active components usually cover the largest part (typically around 80%) of the overall converter power loss [11], [12]. Therefore, special measures must be taken to reduce the power loss of active components and hence to keep the converter efficiency and overall power density high.

Both hard and soft switching are applied in the state-of-the-art topologies. In hard switching, converter waveforms and the power loss are defined only by properties of semiconductor switches and by parasitics of converter circuits. Soft switching is often used to reduce the switching losses. The

achieved loss reduction is substantial [11] but in some applications it might not be enough to enable the operation at required high frequencies. Therefore, a new type of switching waveform and a new converter topology are proposed and analysed in Chapter 2.

1.2.3 Thermal Management

One of the by-products of electrical power conversion is heat. The heat is generated inside converter components and must be removed to prevent them from overheating. The term “Thermal management” is used here to cover all aspects of managing the heat in electronic equipment starting from the heat generation inside components and ending with the heat exchange with the environment.

Thermal management is based on three essential methods of heat transfer: convection, conduction and radiation (for details see [13]). Each of them offers different characteristics and, depending on the application, one of them is usually prevailing. These basic methods are often combined in advanced, high heat-flux methods as discussed in [14]. The advanced methods are usually more complex. A final thermal design is often a combination of several basic and advanced heat-removal methods.

The main objective of this thesis is to attain an effective, small in volume and simple thermal management system. The proposed thermal management concept is discussed in Chapter 4.

1.2.4 Integration of the Three Cornerstones; Integral Design Process

The three cornerstones of the high-power, high power density converter design are closely interconnected. For this reason, all three cornerstones should be approached in parallel. This can be accomplished in so-called integral design process.

The integral design process can be described as a “sequence” of design steps that must be made to reach the final solution. The block diagram of the process implemented in this thesis is shown in a simplified form in Figure 1-12. The simplification relies on presenting only the direct paths between the tasks. The position of the tasks on the horizontal axis represents their temporal organisation. The real process might also contain loops repeating a certain sequence of tasks. The main design aspects are marked by a thicker outline. The interdependencies are indicated by overlaying related blocks.

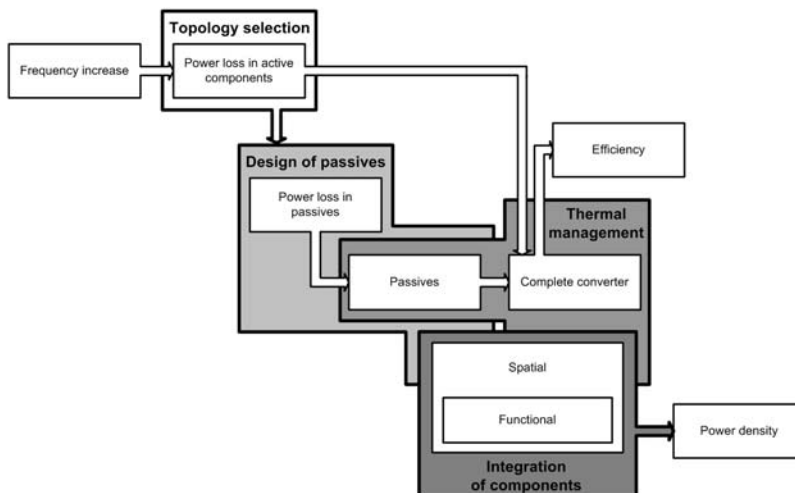


Figure 1-12: Diagram of integral design process; temporal organisation of tasks on horizontal axis

The first design aspect addressed in the integral design process is the topology selection. It covers topology selection, converter circuit design and selection of active components. Values of passive component required by the circuit design must be checked for their viability. Therefore, the topology

selection task is overlaid with the design of passives on the horizontal axis. The output of the topology selection is the converter circuit as well as the power losses in active components. The power losses in passive components can be also roughly estimated in this step in conjunction with the design of passives. The topology considered in this thesis is analysed in Chapter 2.

The design of passives, as the second aspect of the integral design, is addressed in Chapter 3 with special attention to magnetics. The interdependencies of this aspect are rather complex because the design of passives directly influences and is also influenced by the topology selection, thermal management and spatial placement of components. The thermal management of passives is represented in the design phase by selecting materials, technologies and concepts which assure good thermal performance. The spatial aspect of the design must consider component shapes and dimensions in order to obtain easy spatial integration with other converter components.

The thermal management interacts directly with design of passives and with spatial integration of components, as indicated in Figure 1-12. On the other hand, off-the-shelf active components are often used, which enforces a specific method of heat removal. Therefore, the relation between the thermal management and topology selection is not indicated by overlapping the related blocks. The interaction between the topology selection and the thermal management is via the power loss in active components. Another loss input is the power loss in passives. These inputs effectively define the size of the thermal management. It is also indicated that the efficiency of the converter design can be determined directly after validating the viability of the heat removal from the passive and active components. This can be done because detailed thermal management design and spatial organisation of components have little effect on the converter efficiency.

The spatial integration of the converter components is usually the last step of the converter design. If high power density is the main requirement then the component integration must be a part of all other converter design aspects. This is due to the fact that unsuccessful component integration has a direct influence on the converter power density. In some cases, slightly larger components but with dimensions and shapes which are easy to integrate might result in a higher power density. The spatial organisation of components must be performed in a way that component and converter functions are not affected. Therefore, the functional aspect is included in the spatial component integration.

Other important aspects of the converter design are EMI and EMC. These must be considered essentially in every design step. Because of the complexity and uniqueness of the related problems, EMI and EMC are not addressed in this thesis and therefore they are not represented in Figure 1-12.

The presented integral design process is very complex with overlaying tasks. In principle, it can be simplified by assuming the following:

- active components generate the largest power loss (many times over 80%) and high heat fluxes (up to 500 W/cm²) must be realised to remove the generated heat
- passive components are the bulkiest components in power converter designs

These two facts translate into the following assumptions:

- active components limit the maximal operating frequency and efficiency
- passive components limit the power density

These two assumptions allow splitting the design process into two parts. In the first part, the frequency limit is determined by considering converter topologies, semiconductors and thermal management of active components. Maximal operating temperature and minimal acceptable efficiency are used as the design constraints. In the second part, the size of passives is reduced by implementation of high-frequency design and advanced thermal management. Maximal operating temperature is used as a design constraint, whereas high power density is the main design target.

The simplified process can be used for initial converter designs where its simplicity is a great advantage. The essence of this process relies on the possibility of splitting the main design tasks and performing them independently. This is also used in this thesis. The chapters on topology selection and electromagnetic integration are considered as independent parts which are unified in the chapters on thermal management and integration of the three cornerstones and scaling up.

1.3 State-of-the-Art – Technological Development

1.3.1 Passive Components

An effort to increase the power density of power converters targets directly passive components because they are usually the bulkiest. The three main approaches to reducing the size of passive components are:

- increasing the operating frequency
- using improved thermal management
- integration of passives

All three approaches can be found in state-of-the-art solutions. The application of these approaches at low to medium power levels is more developed than at high power levels.

As mentioned above, the size and weight of passives can be reduced by increasing their operating frequency. Higher operating frequency means also higher losses caused by high-frequency effects such as hysteresis and eddy currents. Low-loss, high-frequency materials and advanced heat removal are needed to allow for increased operating frequency. The increase of power density in power transformers is illustrated in Figure 1-13. Using ferrite and a high-frequency winding technology allowed for a substantial increase of the operating frequency to tenths or even hundreds of kHz. The size and weight are rapidly reduced as shown in Figure 1-13b.

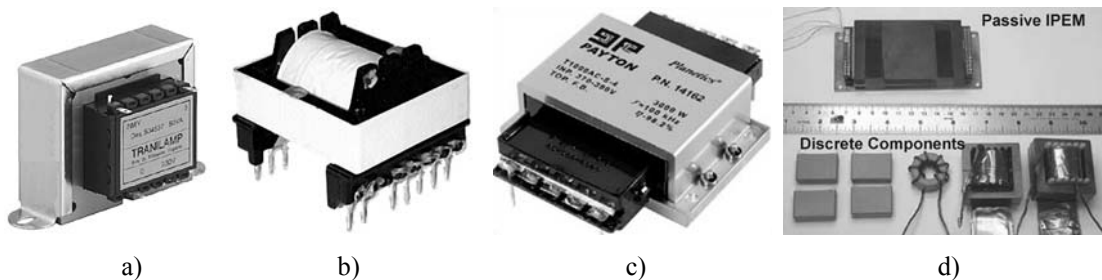


Figure 1-13: Evolution of power magnetics (passive) technology demonstrated on power transformer (figures not in scale); a) conventional 50 Hz technology (Tranilamp, 750 W approximately 0.35 W/cm^3), b) high-frequency technology (800 W approximately 15 W/cm^3), c) planar technology with advanced thermal management (Payton, 20 kW approximately 12 W/cm^3), d) integrated passives (power density four times higher in comparison with a discrete solution) [15]

High-power passives usually suffer from a low surface to volume ratio in comparison with low-power passives because of their larger size. The low surface to volume ratio causes difficulties with cooling of high-power components. Improved thermal management is needed to realise high power densities at high power levels. Figure 1-13c shows a transformer which uses planar windings and a core encapsulated in a heatsink. Power densities comparable to low-power designs were reached by using this concept.

The integration of functions of several passive components is another approach which can be used to increase the power density. This was done in [15] (Figure 1-13d) where several capacitors, inductors and a transformer were integrated into a single component. The integration resulted in power density four times higher than the discrete solution. Integrated passives are still a novelty and are currently the subject of research. A simpler form of the integration approach, integration of resonant inductors inside of power transformers, is already widely accepted in the industry [16], [17].

1.3.2 Semiconductor Devices

Semiconductors have evolved tremendously since 1948, when the first transistor was invented by Bell laboratories. Modern power semiconductors cover the range of voltages up to 12 kV per device and the range of currents up to 6 kA per device. Different semiconductor types have different properties and therefore each of them is suitable for a specific range of applications.

Power MOSFETs and IGBTs are the most used fully controllable semiconductor devices at power levels of our interest (kW to hundreds of kW). Both devices are voltage-controlled, which simplifies driver circuits and both can be used without additional snubbers which results in simpler converter designs.

Power MOSFETs offer the best properties when high-frequency switching is required. Switching frequencies reach tenths up to hundreds of kHz depending on the processed power. The drawback of these devices with respect to the considered applications is higher conduction power loss and a limited power range. CoolMOS™ devices introduced in recent years reduce the conduction power loss and also extend the voltage range up to 800 V. Performance of conventional MOSFET and CoolMOS™ devices are compared in [18], [19]. A clear advantage of the CoolMOS™ technology is noticeable in lower losses and hence increased efficiency of compared set-ups.

In the high power range, IGBT devices exhibit superior conduction losses in comparison to MOSFETs. They are also available for voltages up to 6.5 kV and for currents up to 3.6 kA per device. Their slower switching speed and the presence of the current tail limit their use to maximum of several tenths of kHz. The comparison of 1200 V and 1700 V IGBTs shows that for hard-switching, the switching frequency is limited to approximately 5 kHz if 250 W power loss is assumed per IGBT module [20]. The frequency can be increased to about 15 kHz when double power loss is acceptable. However, the increased power loss might be too high for standard IGBT packages. As can be seen, the attainable switching frequencies are low and are even lower for high-voltage IGBTs. Soft-switching is often applied to reduce the switching losses and to increase the switching frequency.

1.3.3 Converter Topologies

A power converter designer can choose from many converter topologies. For a specific application, several topologies are suited.

An overview and comparison of several basic dc-dc converter topologies is discussed in [21]. The comparison will be briefly discussed in the following lines. Table 1-1 lists the compared topologies and their main characteristics. Simplified circuit diagrams are shown in Figure 1-14. The bridge converter with series connection of the output and input was included in the comparison because it does not have galvanic isolation, which makes the comparison with boost topology fairer. The compared topologies are not interchangeable in all aspects and therefore step-up and step-down topologies were compared separately. The parameters used in the comparison were assumed to reflect the size and costs of the components. The considered parameters are:

- utilisation ratio for semiconductors [6]
- energy content and rms current for capacitors
- area product for magnetic components [6]

Table 1-1: Basic dc-dc converter topologies and their main functional properties

	Step down operation	Step up operation	Galvanic isolation
Boost converter	—	■	—
Buck converter	■	—	—
Bridge converter	■	■	■
Bridge converter with series connection of output and input	—	■	—

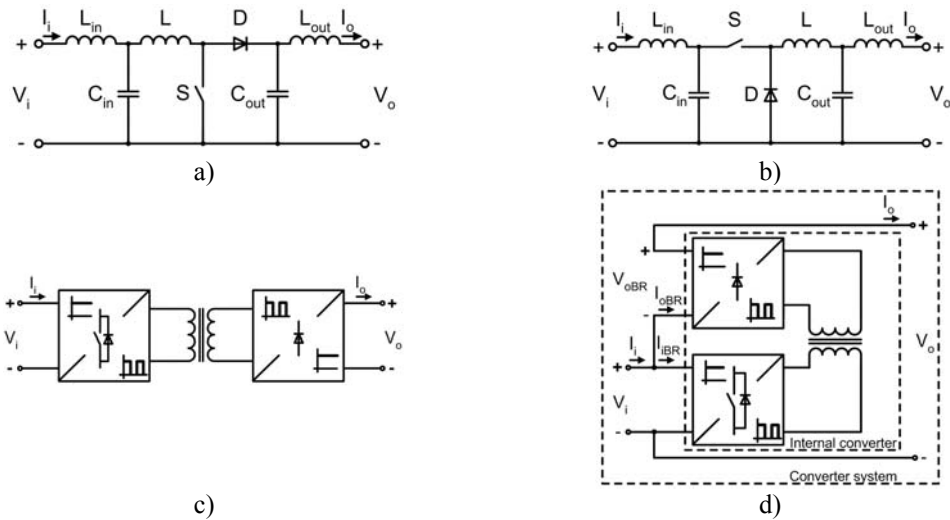


Figure 1-14: Basic dc-dc converter topologies; a) boost converter, b) buck converter, c) bridge converter, d) bridge converter with series connection of output and input

The comparison showed that the compared parameters are heavily dependent on the input to output ratio. Boost and buck topologies are more suited to a ratio close to one. The bridge topologies have better results for high input to output ratios (> 5 for step up and < 0.5 for step down).

The main requirements of the applications considered in this thesis are:

- galvanic isolation
- high input to output voltage ratio
- high power density
- high efficiency

The full-bridge converter is the only topology in the comparison that complies with these requirements. For this reason, the full-bridge converter with galvanic isolation is the topology of choice for further investigations.

1.3.4 Thermal Management

Thermal management has become an indispensable part of any power electronic converter. The need for increased power density puts stringent requirements on the thermal management subsystem. Nowadays, thermal management must be able to realise large heat fluxes, remove large amounts of heat, occupy a small volume and be reliable. The three basic heat-removal concepts – convection, conduction and radiation – are combined in various ways to meet the needs of each application.

There has been large improvement of the heat removal from low-power power electronics. Advanced solutions in the low-power field primarily use conduction to remove the heat from the heat-generating bodies together with convection at outer surfaces. Heat conduction is relatively simple and offers high cooling capacity if used for relatively short distances. The use of conduction at low power is demonstrated in Figure 1-15.

The examples showed in Figure 1-15 illustrate also the utilisation of thermal management for other than heat removal functions. The figure shows examples of advanced low-power power converters based on lead-frame, thermal bus-bar, and heatsink-encapsulated-component technologies. The lead-frame-based converter uses a copper lead frame for both the electrical connections and for the removal of heat from the semiconductors. In a similar way, the thermal bus-bar-based concept (Figure 1-15b) uses a copper bus-bar that combines functions such as: an inductor winding, an electrically conducting

element, a heat removal path and a mechanical support element. The heatsink encapsulated component technology as shown in Figure 1-15c uses an aluminium structure to encapsulate the power components. The encapsulation provides a large surface area for the heat removal and it also allows placing components in a 3D space, which yields more effective utilisation of the converter volume. These thermal management technologies contribute to the realisation of high power densities.

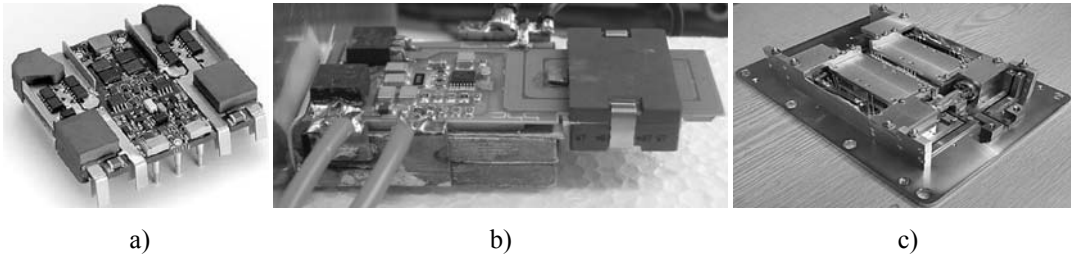


Figure 1-15: Low-power power-converters which use primarily conduction for heat removal; a) lead frame based thermal management [22], b) thermal bus-bar based converter for automotive [23], c) heatsink encapsulated power converter for high temperature automotive [24]

Unlike in low power, state-of-the-art high-power solutions use a simple thermal management system where heat is primarily removed by natural or forced air convection. A 3D model of a conventional high-power converter is shown in Figure 1-16 as an example. In such systems, conduction (black arrows in HF converters) is used to remove the heat from devices with high power dissipation like semiconductors, for example. Devices with low power dissipation use conduction to remove the heat via connecting leads. Apart from this locally used conduction, convection is the primary heat-removal method as indicated in the figure (light grey arrows). Convection is applied to individual components, which means that empty spaces must be present between the components and inside of some components to allow air to flow. This increases the converter volume and lowers the power density.

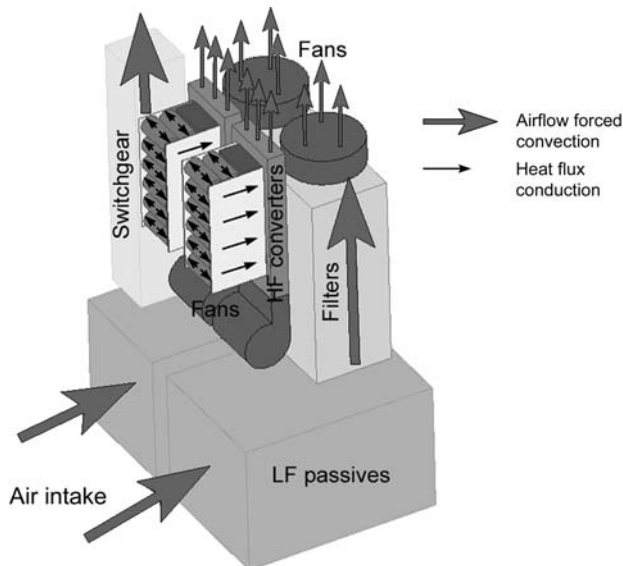


Figure 1-16: Model of conventional high-power converter system with indication of heat removal

The required increase of power density means that the power loss is generated in a smaller volume, which demands advanced thermal management. In Chapter 4, the thermal management is considered in detail. The main attention is paid to acquiring thermal management which allows for effective heat removal but is still technically simple. Several heat-removal concepts are introduced and at the end one of them is selected, optimised and implemented.

1.4 Thesis Layout

The layout of the thesis follows the three cornerstones: reduction of losses, reduction of size, and thermal management.

First, dc-dc converter topologies are discussed in Chapter 2. An optimal current waveform for high frequency switching is proposed. With this waveform, minimising both the conduction and at the same time the switching losses is attempted. A new ZVS Quasi-ZCS topology, which implements the principles of the optimal current waveform, is introduced and analysed in detail. The chapter is concluded by a presentation of the results of measurements on a converter prototype.

Chapter 3 covers the reduction of size of passives as the second cornerstone. The discussion is focused on the size reduction of magnetic components and especially of the transformer because these are the bulkiest components of power converters. Transformer shape is studied with main attention to power density. Several winding structures are evaluated and new so-called “partial interleaving” is introduced for foil windings. Furthermore, so-called “leakage layer” is introduced as an enhancement of the transformers leakage inductance. The results are demonstrated on transformer prototypes.

The third cornerstone, thermal management, is discussed in Chapter 4. It covers thermal management on component, converter and system level. Heat generation and transportation inside of the component packages is analysed at the lowest component level. The converter level concerns the heat removal from the components. For this level, the power density and its relation to the thermal management are discussed. The universality of the thermal management system is considered on the system level. Various possibilities for heat removal from the components are deliberated yielding the final thermal management concept. The proposed concept is further analysed in detail with respect to heat-removal possibilities, hot-spots in components and temperature distribution in the converter. The proposed thermal management is evaluated by using experimental results obtained from the converter prototypes.

Chapter 5 covers the integration of the three cornerstones presented in the preceding chapters. Spatial integration of components is discussed as the converter design aspect which influences and is also influenced by all three cornerstones. The integrated converter structure is used to demonstrate the implemented spatial solution and the reached power density. Application of the developed concepts at higher power (scaling up) is also considered. The main attention concerning scaling up is paid to qualitative performance of various components and also to the relation between the converter power level and power density.

The last chapter, Chapter 6, concludes the thesis and gives an indication of the possible direction, content and scope of future research.

Chapter 2 *Dc-Dc Converter Topologies*

2.1 Introduction

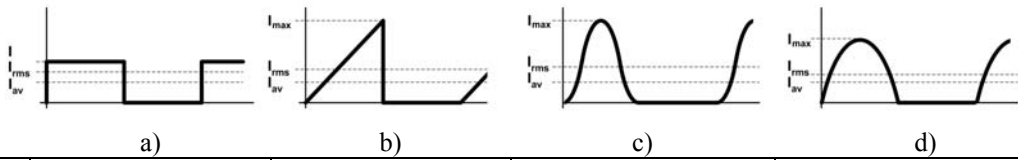
A low loss is essential for high power density in high-power converters (paragraph 1.2). To reduce the overall converter losses, the power loss of each active and passive component must be reduced. As mentioned in paragraph 1.2.2, the active components typically generate the largest portion of the converter power loss. Therefore, the discussion in this chapter primarily concerns the loss generation in active components.

Firstly, an optimal current waveform for high-frequency switching is proposed to minimise the combined conduction and switching loss in active components. Topologies that utilise a waveform similar to the optimal waveform are briefly discussed and one of them is selected for further application. The selected topology is then analysed in detail with respect to operational waveforms and losses. The suitability of different types of IGBTs for application in the selected topology is investigated. The possibility of realising bi-directional operation and voltage control is addressed next. The chapter is concluded with results of measurements on the converter prototype.

2.2 “Optimal Current Waveform”

The power loss of converter switches can be divided into three parts: turn-on loss, conduction loss and turn-off loss. Each of the parts is highly dependent on the shape of the current flowing through the switches in a particular time interval. The values that characterise any switched current waveform can be identified as: the maximal (peak) current I_{max} , the average current I_{av} and the turn-off current I_{off} . It is assumed that the average current I_{av} is related to the average power supplied to the load. The peak current I_{max} is associated with the conduction loss because a high peak current results in high rms current I_{rms} and hence in high conduction loss. The turn-off current I_{off} is one of the factors which determines the turn-off loss. In order to minimise the overall converter loss, the current ratios I_{max}/I_{av} (represents conduction loss) and I_{off}/I_{av} (represents turn-off loss) should be kept as low as possible.

Several common current shapes and their characteristic values I_{av} , I_{max} , I_{rms} and I_{off} are shown in Figure 2-1. The shown waveforms represent: a) hard-switching topology, b) ZVS topology with triangular current waveform, c) and d) resonant soft-switching topologies. The hard-switching topologies are characterised by a good current waveform from the conduction loss point of view (typically flat waveform) but they exhibit high switching losses. On the other hand, soft-switching topologies (ZVS, ZCS) attain reduced switching losses but their current waveforms (Figure 2-1b, c, d) are worse from the conduction loss point of view because of their high rms currents. Typically, a resonance is used to obtain soft-switching, which results in a waveform with a current peak (rms current is higher than average current) and hence in increased conduction loss. In soft-switching topologies, there are also extra component stresses and power loss introduced due to a circulating reactive power [25].



I_{\max}	I	$2I$	$2I$	$\frac{\pi}{2}I$
I_{av}	$\frac{I}{2}$	$\frac{I}{2}$	$\frac{I}{2}$	$\frac{I}{2}$
I_{rms}	$\frac{I}{\sqrt{2}}$	$\sqrt{\frac{2}{3}}I$	$\frac{\sqrt{3}}{2}I$	$\frac{\pi}{4}I$
I_{off}	I	$I_{\max} = 2I$	0	0

Figure 2-1: Most common shapes of current waveforms in simplified forms; a) hard switching, b) ZVS turn-on, c)-d) resonant soft switching

To reduce the power loss more than in conventional soft-switching converters, the shape of the current waveform must be modified. In an “ideal” case, the waveform would exhibit:

- ZVS turn-on
- ZCS turn-off
- flat top waveform with rms current equal to average current

In practice, it is not possible to attain all three features at the same time. In Figure 2-2a, an optimal switching current waveform is proposed that approaches the ideal waveform. The proposed waveform has influence on turn-on, turn-off and conduction loss, and can be optimised to minimise the total loss. Resonant principles are typically used to generate the optimal waveform. The description below is based on the switching cell with switch, antiparallel diode and snubber capacitor connected in parallel, as shown in Figure 2-2b.

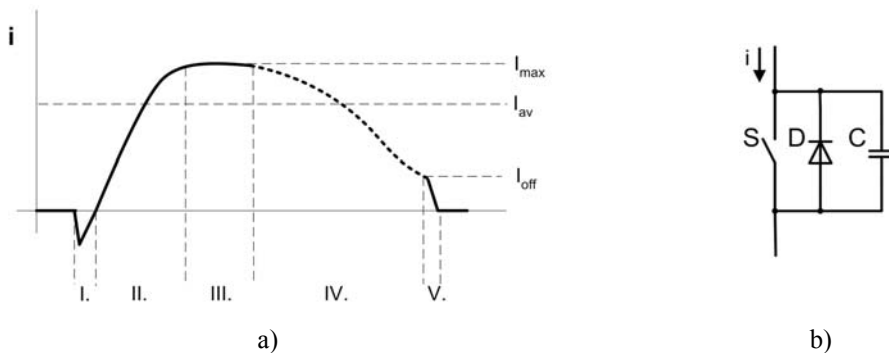


Figure 2-2: a) Proposed optimal current waveform for high frequency switching, b) switching cell

Low turn-on loss is realised in Interval I by employing zero-voltage-switching (ZVS). The switch S is turned on while its antiparallel diode D conducts. After the diode stops conducting, the switch takes the current over and Interval II starts. Intervals II, III and IV are resonant intervals where the current is firstly increased to its maximum (Interval II), then it is held “constant” (Interval III) and finally it is reduced to its turn-off value (Interval IV). The shape of the current waveform in these intervals (Intervals II, III, and IV) is defined by a resonant circuit used in a particular topology. For low conduction losses, Intervals II and IV should be short in comparison to Interval III (in the ideal waveform, duration of intervals II and IV would approach zero). After Interval IV, the switch turns off

in Interval V and the current commutates to the snubber capacitor C . The capacitor limits the voltage rise across the switch, which, together with relatively low current value being turned off (Quasi-ZCS), results in a low turn-off loss.

2.3 Topologies Using “Optimal Current Waveform”

There are several topologies that utilise a current waveform similar to the optimal waveform. The current waveforms of each of these topologies are slightly different in shape and therefore in main parameters describing the waveforms (I_{max} , I_{av} , I_{off}) and in generated power loss. To choose the most suitable topology, three topologies that belong to different topology groups are briefly compared. The compared topologies are:

- Series resonant topology – represents full resonant converters
- Partial resonant topology – represents partially resonant converters
- Output filter resonant topology – new converter topology

The presented topologies use resonance to create current waveforms similar to the optimal waveform. Because they use resonance, some waveforms are similar in shape to the conventional waveforms as presented in Figure 2-1c and d. The topologies employ simultaneously ZVS and so-called Quasi-ZCS as proposed by the optimal current waveform. The three topologies are shortly discussed in the following paragraphs and the current waveforms obtained by simulation are briefly compared.

Full Resonant Converter (FRC)

The series resonant converter is an example of full resonant converters [26]. Operation of the full resonant topologies in the region above the resonant frequency yields a current waveform (Figure 2-3b) similar to the optimal waveform. The standard series resonant circuit is equipped with the snubber capacitors C_1 , C_2 connected in parallel to the switches (see Figure 2-3a). This reduces the turn-off loss of the switch by reducing the voltage rise during the turn-off interval. The resonance is defined by the transformer leakage inductance L_s and the resonant capacitor C_r . The capacitors C_3 and C_4 are dc-link capacitors which serve as a voltage divider for the half-bridge inverter.

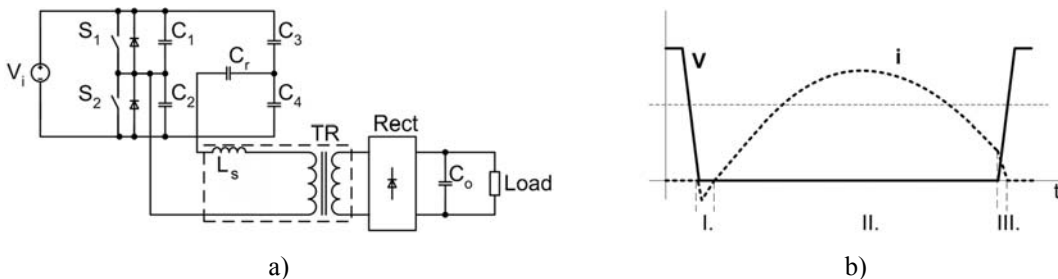


Figure 2-3: Full resonant converter; a) converter circuit, b) basic waveforms

The current waveform of FRC consists of three main intervals. During Interval I, zero-voltage-switching conditions are maintained for the turn-on of the switches by antiparallel diodes conducting. Interval II includes current rise and also current reduction. The current shape is the result of the resonance. Interval III is the turn-off interval where the switches are turned off with reduced current (Quasi-ZCS) and a voltage that is reduced by the snubber capacitors C_1 , C_2 .

Partial Series Resonant Converter (PSRC)

Partial Series Resonant Converter topology is based on the series resonant converter described above. The modifications are: using the dc-link capacitors C_{r1} , C_{r2} as the resonant capacitors, the addition of the clamping diodes D_1 , D_2 in parallel to each of the resonant capacitors C_{r1} , C_{r2} and the addition of the inductance L_p in parallel to the primary of the transformer. The circuit of the converter and its waveforms are shown in Figure 2-4.

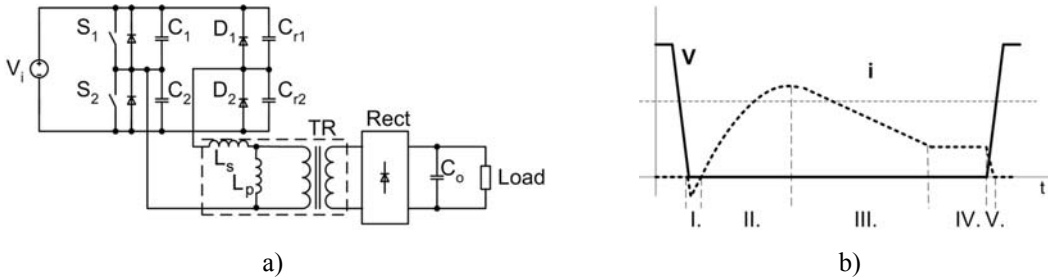


Figure 2-4: Partial series resonant converter; a) converter circuit, b) basic waveforms

The current waveform consists of five main intervals. Interval I involves ZVS turn-on of the switches while antiparallel diodes conduct. Interval II, the current rise interval, is characterised by high frequency resonance between the series inductance L_s , the parallel inductance L_p and the resonant capacitors C_{r1} , C_{r2} . Interval III is the interval where the current decreases. Two types of the current decrease may occur. With the first type, the current decreases by a low frequency resonance between the inductor L_p and the capacitors C_{r1} , C_{r2} . With the second type, the current of the inductor L_s simply decreases in a linear manner. The occurrence of type I or II depends on which of the two values, the resonant capacitor voltage or the series inductance current, reaches zero as first. Details are described in [27] Interval IV is a freewheeling interval when the current of the inductor L_p flows through one of the switches and one of the diodes D_1 , D_2 . The switch can be turned off (Interval V) with low power loss as the current flowing through it is low. Details about the topology can be found in [27].

Output Filter Resonant Converter (OFRC)

A New, ZVS, Quasi-ZCS topology that is a modification of the series resonant converter is proposed. The circuit diagram is shown in Figure 2-5. The topology is a conventional half-bridge dc-dc converter with a relatively small resonant capacitor C_r connected to the rectifier output. The capacitor C_r forms a resonant circuit together with the transformer leakage inductance L_s and the magnetising inductance L_p . The resonant current waveform implemented in the converter is shown in Figure 2-5b. The capacitor C_r is part of the resonant circuit and therefore an additional filter is needed to smooth the output voltage. This filter is formed by the components L_o and C_o .

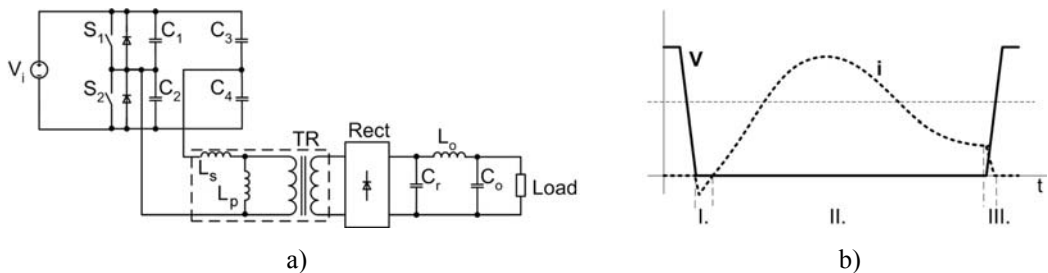


Figure 2-5: ZVS, Quasi-ZCS converter; a) converter circuit, b) basic waveforms

The current waveform consists of three main intervals: zero-voltage-switching turn-on interval (Interval I), current resonance interval (Interval II) and quasi-zero-current-switching turn-off interval (Interval III). The resonant current interval includes the current rise interval and the current decrease interval. The resonant current waveform is the result of a resonance primarily between the resonant capacitor C_r and the leakage inductance of the transformer L_s .

Comparison of Current Waveforms

The current waveforms of the presented topologies and their characteristic values I_{av} , I_{max} , I_{rms} and I_{off} were compared by simulation [28]. The component values were selected such that the simulated topologies had the same nominal power rating at the desired operating mode. Simulations were performed for full power (800 W) and half power (400 W). For all simulations, the load remained constant and the power was controlled by adapting the switching frequency. In the case of FRC and OFRC topologies, the switching frequency was increased and in the case of PSRC topology, the switching frequency was decreased to reduce the power. Details of the simulations and the comparison are published in [28].

The comparison of the waveforms at full power showed that the three compared topologies are similar regarding the shape of the current waveforms. The situation is different at half power where FRC and OFRC lose their Quasi-ZCS at turn-off. For the applications considered in this thesis (Chapter 1), power flow control by the dc-dc converter is not required. The control was included in the comparison only to assess the behaviour of the three topologies in this mode of operation. Because the control is not required, the power loss increase at half power in the case of FRC and OFRC topologies is not relevant for the topology selection.

Assuming operation at high power levels, PSRC topology is in an unfavourable position because it exists only as a half-bridge topology. This implies double current rating for the semiconductor switches in comparison with the full-bridge configuration which is available for FRC and OFRC topologies. An advantage of OFRC is that the filter capacitors are not required to carry high current ripples as the capacitive current is smoothed by the presence of the inductive filters. The inductive filters can be used also in case of the FRC topology if high output quality is required. This improves the filtering but it does not reduce the current through the capacitors as these are still connected directly to the rectifier output.

2.4 Analysis of Operation of Output Filter Resonant ZVS Quasi-ZCS Converter Topology

The ability to perform low loss switching, low current ripple content in the filtering capacitors, the possibility of bi-directional operation and the relatively low component count make the OFRC full-bridge converter topology one of the favourites for dc-dc voltage scaling applications. Therefore, the OFRC topology will be considered in more detail in the following paragraph.

The topology behaviour is analysed by using a simplified model. First, the operating modes are identified and equivalent linear models are constructed for each of the modes. For every model, a set of differential equations is derived which are subsequently solved in the laplace form. The time domain representation of loop currents is found by the inverse laplace transformation. The analytical model of the converter is obtained by coupling together the time domain equations. Finally, the analytical model is used to generate the converter waveforms and to analyse the converter operation.

Correct initial conditions are required to obtain cyclic-stable converter waveforms. For each of the operating modes, the initial values of the current of the series inductor L_s (I_{L_s}), the current of the parallel inductor L_p (I_{L_p}) and the voltage of the resonant capacitor C'_r ($V_{C'_r}$) must be defined. In the model these values are always calculated as the end values of the previous interval. There is not previous interval to Interval I in the model. Therefore, the proper initial conditions for this interval are calculated by using an iteration process. In this process, the end conditions after one cycle are

compared with the initial conditions of the cycle. If the compared values match with a specified accuracy, the steady state is reached and the initial conditions are assumed correct. The steady state is typically reached in several iterations.

In this thesis, the model is used only for the steady-state analysis. In principle, the same approach could be used to simulate the dynamic response of the converter. Starting the model with zero initial conditions and recording the calculated waveforms all the way to the steady state would simulate the converter start-up. In a similar way, a response to a load step change could be calculated. The short-circuit condition at the converter output could be simulated by changing the load impedance to near zero value and recording the response of the model. In spite of the model's ability to simulate the dynamic response, the dynamics are not considered here because they exceed the scope of this thesis.

2.4.1 OFRC Converter Model

The simplified model of the OFRC converter is shown in Figure 2-6. The simplifications made for deriving the model are:

- the transformer is modelled as an ideal transformer where the leakage inductance and magnetising inductance are modelled by separate inductors L_s and L_p
- the load part of the converter is replaced by a current source which represents the current through the output inductor L_o
- switches and primary diodes are modelled in a simplified form – constant voltage drop for on-state and linear transitions for turning on and off
- secondary diodes are assumed to be ideal
- all other components and connections are assumed to be ideal

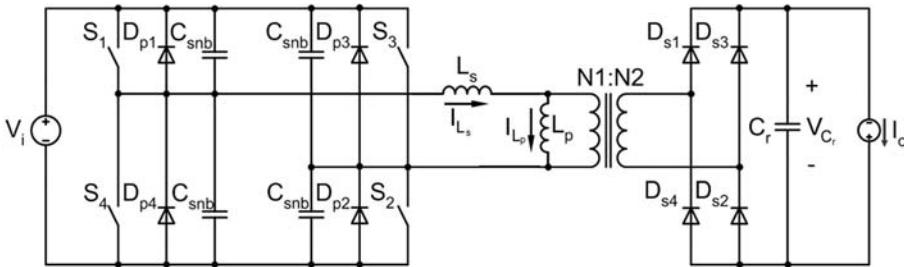


Figure 2-6: Simplified circuit diagram of the OFRC converter used for the analyses

2.4.2 Operating Modes of OFRC Converter

Eight intervals of operation can be identified. For the purpose of the analyses, the secondary circuit is transferred to the primary side of the transformer and the associated voltages and currents are denoted with a prime. The capacitance C_r is recalculated to the primary by equation 2-1 and the current source I_o by equation 2-2. The voltage $v_{C'r}$, the followed currents $i_{L's}$, $i_{L'p}$, $i_{C'r}$ as shown in Figure 2-6 and all identified intervals are depicted in Figure 2-7.

$$C'_r = \left(\frac{N_2}{N_1} \right)^2 C_r \quad (2-1)$$

$$I'_o = \frac{N_2}{N_1} I_o \quad (2-2)$$

Several characteristic resonant frequencies are defined as:

$$\omega_{r_c} = \sqrt{\frac{C'_r + C_{snb}}{L_s C_{snb} C'_r}}, \tag{2-3}$$

$$\omega_{r_s} = \sqrt{\frac{1}{L_s C'_r}}, \tag{2-4}$$

$$\omega_{r_p} = \sqrt{\frac{1}{L_p C'_r}}, \tag{2-5}$$

$$\omega_{r_sp} = \sqrt{\frac{L_p + L_s}{C'_r L_p L_s}}. \tag{2-6}$$

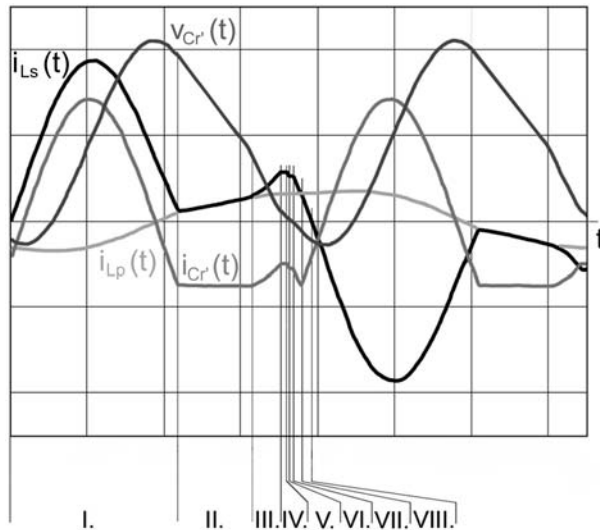


Figure 2-7: Generic waveform of the OFRC converter with marking of relevant time intervals

It is assumed that the first interval (Interval I) starts immediately after the current commutates from the diodes D_{p1} and D_{p2} to the switches S_1 and S_2 . Depending on the mode of operation and values of the resonant components, some intervals might be missing in the sequence (typically Interval II and Interval III). After Interval VIII is finished and the current i_{Ls} crosses zero, the cycle continues in the second half period with an interval similar to Interval I where all currents have reversed directions. This implies that in the second half period, the switches S_3 and S_4 conduct the main current.

Interval I. – Resonant Interval

Interval I starts at the moment when the current of the series inductor L_s crosses zero and starts to flow through the switches S_1 and S_2 , which have been previously turned on. The active part of the circuit and its linear model are shown in Figure 2-8a and b respectively. During this interval, the main current (through L_s) is shaped by the resonance between the inductor L_s , the capacitor C'_r and partially also by the inductor L_p . The derived loop currents are described by equations 2-7 and 2-8.

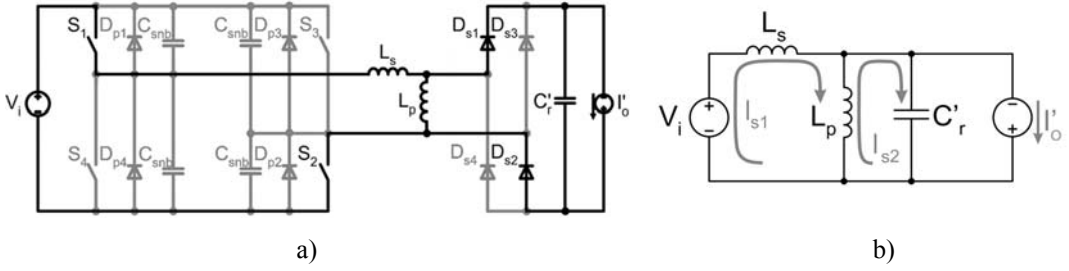


Figure 2-8: Interval I, a) active part of converter circuit, b) equivalent circuit model

$$i_{s1}(t) = \frac{\omega_{r_s}^2}{\omega_{r_sp}^2} \left[\begin{aligned} & \left(I_{Lp_in} + I'_o \right) + \frac{\omega_{r_p}^2}{\omega_{r_s}^2} I_{Ls_in} + C'_r \omega_{r_p}^2 t V_i - \\ & - \left(I_{Lp_in} - I_{Ls_in} + I'_o \right) \cos(\omega_{r_sp} t) + \\ & + C'_r \omega_{r_sp} \sin(\omega_{r_sp} t) \left(\frac{\omega_{r_s}^2}{\omega_{r_sp}^2} V_i - V_{C'r_in} \right) \end{aligned} \right], \quad (2-7)$$

$$i_{s2}(t) = -I'_o + \left(I_{Lp_in} - I_{Ls_in} + I'_o \right) \cos(\omega_{r_sp} t) - C'_r \omega_{r_sp} \sin(\omega_{r_sp} t) \left(\frac{\omega_{r_s}^2}{\omega_{r_sp}^2} V_i - V_{C'r_in} \right), \quad (2-8)$$

where I_{Lp_in} is the initial current of the inductor L_p , I_{Ls_in} is the initial current of the inductor L_s and $V_{C'r_in}$ is the initial voltage of the capacitor C'_r .

Interval II. – Rectifier Diodes off, $I_{Ls}=I_{Lp}$

Interval II starts at the moment when the voltage across the inductor L_p exceeds the voltage of the capacitor C'_r . At that moment, the rectifier diodes turn off and disconnect the output part of the converter from the input part. The current I_{Ls} flows through the inductor L_p . The model of this operating mode is shown in Figure 2-9b. This interval occurs only at a certain combination of initial conditions and values of the resonant circuit components. Most of the time, it is not present in the sequence of intervals. Equation 2-9 describes the current in the input part of the model, whereas the Current I'_o flows in the output part of the model.

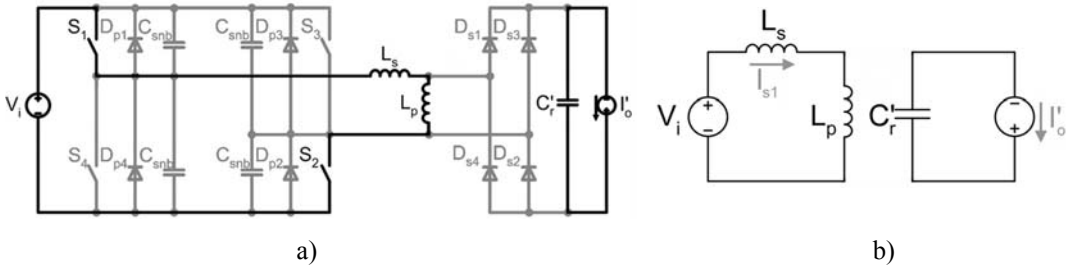


Figure 2-9: Interval II, a) active part of converter circuit, b) equivalent circuit model

$$i_{s1}(t) = \frac{V_i t + L_s I_{Ls_end1} + L_p I_{Lp_end1}}{L_s + L_p}, \quad (2-9)$$

where the currents $I_{L_s_end1}$ and $I_{L_p_end1}$ are the currents of inductors L_s and L_p at the end of Interval I.

Interval III. – Resonant Interval

Interval III is identical in behaviour to Interval I and therefore modelled in the same way. The interval occurs when the rectifier diodes turn on again after being off during Interval II. The resonance of Interval I continues with initial conditions taken as the end values of Interval II.

Interval IV. – Commutation Switch-Snubber Capacitor

The converter enters Interval IV at the moment when the conducting switches S_1 and S_2 are turned off in the current minimum in so-called Quasi-ZCS. The voltage rise across the switches is limited by the snubber capacitors C_{snb} . The time duration of this interval equals the turn-off time of the used switches. The only currents assumed to vary are the currents of the switches and the currents of the snubber capacitors. The current commutation from the switches S_1 and S_2 to the snubber capacitors is assumed to be caused by a linear decrease of the switch current during its turn-off. The varying currents are described by equations 2-10 and 2-11. All other currents are assumed to be constant.

$$i_{s1}(t) = I_{L_s_end3} - \frac{I_{L_s_end3}}{t_{fs}} t, \tag{2-10}$$

$$i_{C_{snb}}(t) = \frac{I_{L_s_end3} - i_{s1}(t)}{2}, \tag{2-11}$$

where the current $I_{L_s_end3}$ is the current of the inductor L_s at the end of Interval III.

Interval V. – Charging / Discharging of Snubber Capacitors

Interval V starts after the switches have turned off and the current has commutated to the snubber capacitors C_{snb} . The current continues to flow through the inductors L_s and L_p during this interval. The energy stored in the inductor L_s is used to charge respectively discharge the snubber capacitors. This interval lasts until the voltages of the snubber capacitors in parallel to the switches S_1, S_2 reach the value of the input voltage V_i or the current of the inductor L_s has become zero. The loop currents are described by equations 2-12 and 2-13.

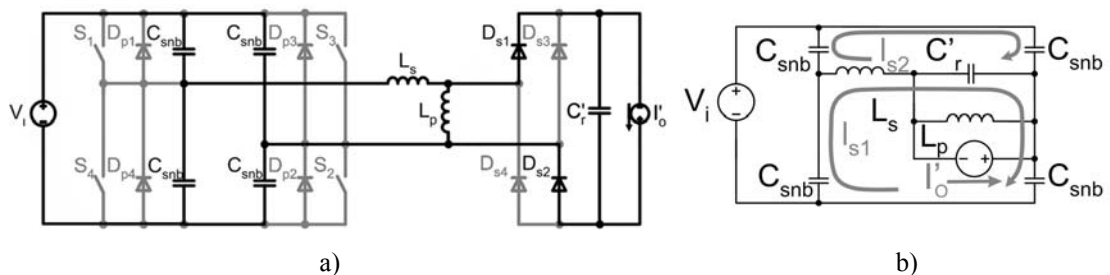


Figure 2-10: Interval V, a) active part of converter circuit, b) equivalent circuit model

$$i_{s1}(t) = \frac{1}{2} \frac{\omega_{r_s}^2}{\omega_{r_c}^2} \left[\left(I_{L_p_end4} + I'_o \right) + \left(\frac{\omega_{r_c}^2}{\omega_{r_s}^2} I_{L_s_end4} - I_{L_p_end4} - I'_o \right) \cos(\omega_{r_c} t) - \right. \\ \left. - C'_r \omega_{r_c} \sin(\omega_{r_c} t) \left(V_{C'_r_end4} + V_{C_{snb_on_end4}} - V_{C_{snb_off_end4}} \right) \right], \tag{2-12}$$

$$i_{s2}(t) = -i_{s1}(t), \tag{2-13}$$

where the currents $I_{L_s_end4}$ and $I_{L_p_end4}$ are the currents of the inductors L_s and L_p at the end of Interval IV, the voltage $V_{C_r_end4}$ is the voltage of the capacitor C_r at the end of Interval IV, and the voltages $V_{C_{snb_on_end4}}$ and $V_{C_{snb_off_end4}}$ are the voltages of the snubber capacitors in parallel to the switches that were previously *on* respectively *off*.

For efficient converter operation, it is important that at the beginning of Interval V there is enough energy stored in the series inductance L_s to fully charge respectively discharge the snubber capacitors. Should the inductance L_s fail to do so, the capacitors are only partially charged at the end of this interval which results in current spikes in the switches at their next turn-on. These current spikes reduce the converter efficiency and might even destroy the switches in some cases. The calculation of the current spikes is not included in the model. The presence of the spikes can be deduced visually from the voltage waveforms of the snubber capacitors.

Interval VI. – Commutation Snubber Capacitor – Antiparallel Diode

Interval VI represents a simple linear current commutation from the snubber capacitors to the antiparallel diodes. The current commutates to the antiparallel diodes of the switches that were previously *off*, which means that in the discussed case it commutates to the antiparallel diodes D_{p3} , D_{p4} . The time duration of the commutation equals the turn-on time of the diode. All currents, apart from the currents of the appropriate diodes and the currents of the snubber capacitors, are assumed to be constant. The voltage of the resonant capacitor C_r behaves as described by equation 2-14.

$$v_{C_r}(t) = \frac{1}{C_r} \int i_{C_r}(t) dt + V_{C_r_end5}, \tag{2-14}$$

where the voltage $V_{C_r_end5}$ is the voltage of the capacitor C_r at the end of Interval V.

Interval VII. – Freewheeling Interval $I_{L_s} > I_{L_p}$

During the freewheeling interval, Interval VII, the current of the series inductor L_s freewheels through the antiparallel diodes D_{p3} , D_{p4} on the primary side of the converter and through the diodes D_{s1} , D_{s2} on the secondary side as shown in Figure 2-11a. During this interval, the switches S_3 , S_4 can be turned on with ZVS because the voltages across them are fixed to zero by the conducting diodes. The model shown in Figure 2-11b is used to derive the analytical equations for this interval. Equations 2-15 and 2-16 describe the loop currents i_{s1} and i_{s2} .

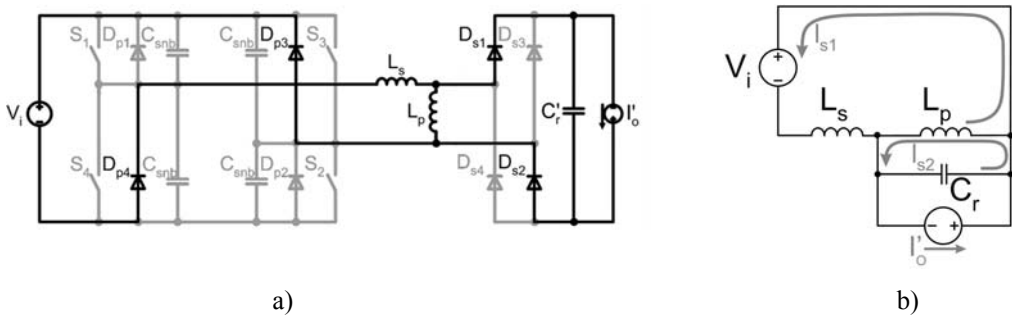


Figure 2-11: Interval VII, a) active part of converter circuit, b) equivalent circuit model

$$i_{s1}(t) = \frac{\omega_{r-s}^2}{\omega_{r-sp}^2} \left[\begin{aligned} & \frac{\omega_{r-p}^2}{\omega_{r-s}^2} I_{Ls_end6} + I_{Lp_end6} + I'_o - C'_r \omega_{r-p}^2 t V_i + \\ & + (I_{Ls_end6} - I_{Lp_end6} - I'_o) \cos(\omega_{r-sp} t) - \\ & - C'_r \omega_{r-sp} \sin(\omega_{r-sp} t) \left(V_{C'r_end6} + \frac{\omega_{r-s}^2}{\omega_{r-sp}^2} V_i \right) \end{aligned} \right], \quad (2-15)$$

$$i_{s2}(t) = \left[\begin{aligned} & I'_o + (I_{Ls_end6} - I_{Lp_end6} - I'_o) \cos(\omega_{r-sp} t) - \\ & - C'_r \omega_{r-sp} \sin(\omega_{r-sp} t) \left(V_{C'r_end6} + \frac{\omega_{r-s}^2}{\omega_{r-sp}^2} V_i \right) \end{aligned} \right], \quad (2-16)$$

where the currents I_{Ls_end6} and I_{Lp_end6} are the currents of the inductors L_s respectively L_p at the end of Interval VI, and the voltage $V_{C'r_end6}$ is the voltage of the capacitor C'_r at the end of Interval VI.

Interval VIII. – Freewheeling Interval, $I_{Ls} < I_{Lp}$

The current of the inductor L_s decreases during Interval VIII and the energy stored in the magnetic field of the inductor is transferred to the input and output. At the moment when the current of the inductor L_s becomes smaller than the current of the parallel inductor L_p , the output rectifier reverses its polarity (diodes D_{s1} , D_{s2} turn off and diodes D_{s3} , D_{s4} turn on; this transition is assumed to be instantaneous) and the difference between the currents of the inductors L_s and L_p ($I_{Lp} > I_{Ls}$) is supplied from the output part of the converter. The converter circuit and model are shown in Figure 2-12. The interval ends at the moment when the current I_{Ls} reaches zero and reverses its direction. The reversed current starts flowing in the switches S_3 , S_4 and another half period starts.

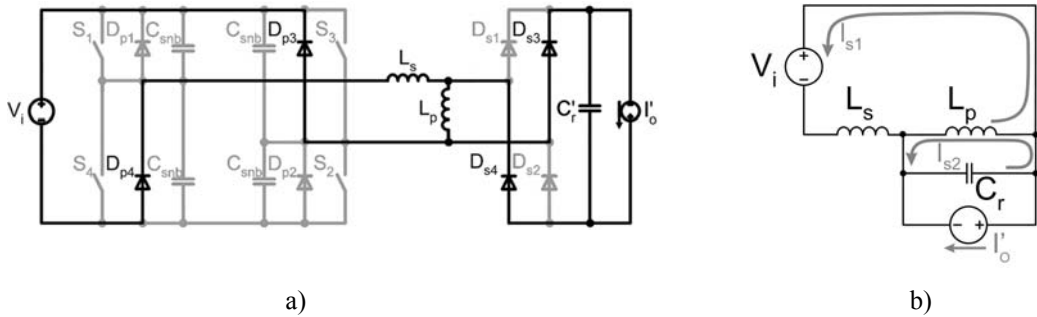


Figure 2-12: Interval VIII, a) active part of converter circuit, b) equivalent circuit model

$$i_{s1}(t) = \frac{\omega_{r-s}^2}{\omega_{r-sp}^2} \left[\begin{aligned} & I'_o - I_{Lp_end7} - \frac{\omega_{r-p}^2}{\omega_{r-s}^2} I_{Ls_end7} + C'_r \omega_{r-p}^2 t V_i - \\ & - (I_{Ls_end7} + I'_o - I_{Lp_end7}) \cos(\omega_{r-sp} t) - \\ & - C'_r \omega_{r-sp} \sin(\omega_{r-sp} t) \left(V_{C'r_end7} - \frac{\omega_{r-s}^2}{\omega_{r-sp}^2} V_i \right) \end{aligned} \right], \quad (2-17)$$

$$i_{s2}(t) = I'_o - (I_{Ls_end7} - I_{Lp_end7} + I'_o) \cos(\omega_{r_sp} t) - C'_r \omega_{sp} \sin(\omega_{r_sp} t) \left(V_{Cr_end7} - \frac{\omega_{r_s}^2}{\omega_{r_sp}^2} V_i \right), \quad (2-18)$$

where the currents I_{Ls_end7} and I_{Lp_end7} are the currents of the inductors L_s respectively L_p at the end of Interval VII, and V_{Cr_end7} is the voltage of the capacitor C'_r at the end of Interval VII.

2.4.3 Calculated Waveforms

The modelling process described in the previous paragraphs is implemented in a MathCAD model. The model is used to calculate converter waveforms and their properties such as maximal, rms and average values. The waveforms constantly followed by the model are the currents of the resonant circuit components (I_{Ls} , I_{Lp} , I_{Cr}), the input current I_i and the voltage of the resonant capacitor C'_r (V_{Cr}). These waveforms in their normalised form are depicted in Figure 2-13. The voltages are normalised by the input voltage V_i . The currents are normalised using $V_i Z_r$ as the unit where $Z_r = 1/\sqrt{L_s C'_r}$. The time normalisation unit is $\omega_{r_s} t_{on}$ where ω_{r_s} is the resonant frequency calculated by equation 2-4 and t_{on} is the on time of the switches (switches are conducting during t_{on}).

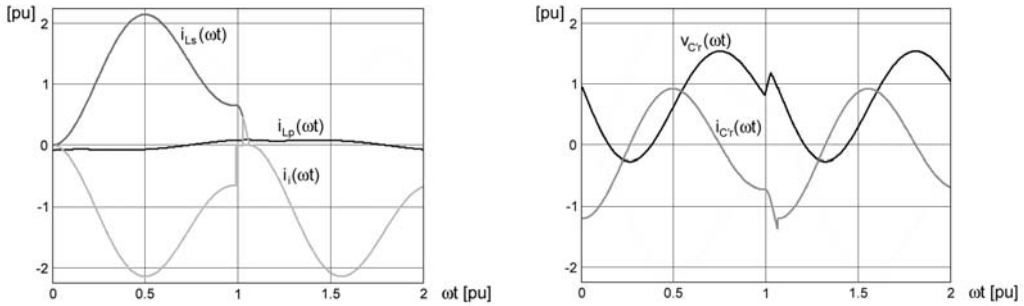


Figure 2-13: Examples of calculated waveforms in per unit representation

The relation between the output voltage and the output current for several operating frequencies is shown in Figure 2-14. For the calculations, all model parameters were kept constant apart from the switching frequency ω_s . As can be seen, from the output voltage point of view, the converter behaves as impedance where frequencies closer to the resonant frequency result in a lower voltage drop because of lower impedance. Note that operation at frequencies other than $0.5\omega_{r_s}$ would result in a tremendous increase of the switching losses. This will be discussed in loss analysis in section 2.5. The irregularities of the calculated points were caused by slight inaccuracies in the initial conditions of the model.

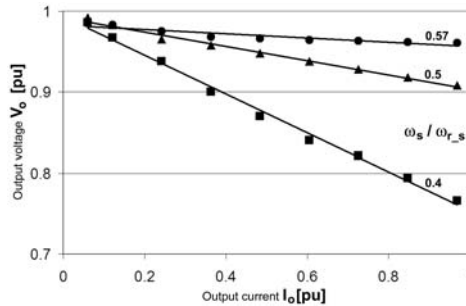


Figure 2-14: Output voltage versus output current for several operating frequencies ω_s

The shape of the converter waveforms is strongly related to the parameters of the resonant circuit. In paragraph 2.2, the maximal current I_{max} and the turn-off current I_{off} were identified as the values which characterise the optimal current waveform. For the converter design, the rms current of the capacitor C_r and the peak voltage across this capacitor are also important. In Figure 2-15, variations of waveform parameters are depicted in relation to the resonant circuit impedance Z_r . The depicted parameters are: the switch rms current $I_{rms,S}$ (relates also to the maximal current $I_{max,S}$), the switch turn-off current I_{off} , the energy E_{Ls_off} stored in the series inductance L_s at the moment of turn-off calculated as $1/2 L_s I_{off}^2$, the rms current of the resonant capacitor $I_{C'r_rms}$ and the voltage swing $dV_{C'r}$ across the resonant capacitor C'_r . It is assumed that the voltage swing $dV_{C'r}$ is related to the peak voltage of the components. The energy E_{Ls} is included in the figures because of the requirement of the minimal energy required to fully charge respectively discharge the snubber capacitors during Interval V. The presented curves were calculated by using the MathCAD model. In the model, the resonant parameters (L_s , C'_r) varied for each configuration, whereas the input voltage V_i , the input power P_i , the output current I_o and the switching frequency f_s were kept constant. The graphs in the figure represent variations of circuit waveforms with respect to a selected reference case ($L_s=40\mu H$ and $C'_r=270nF$).

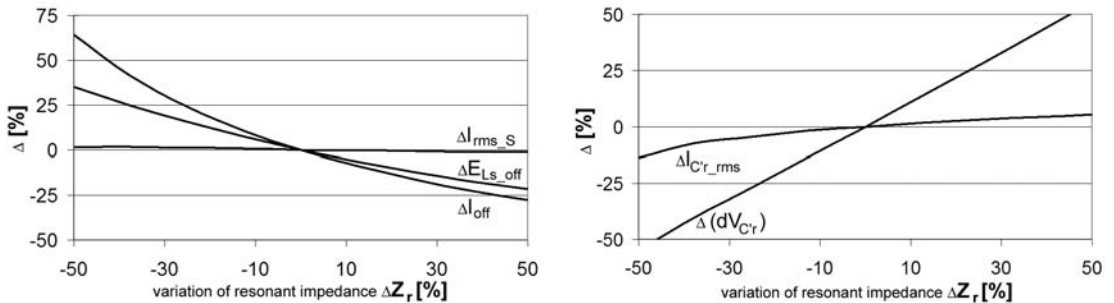


Figure 2-15: Variation of waveform parameters with respect to resonant circuit impedance Z_r ; $I_{rms,S}$ – switch rms current, I_{off} – switch turn-off current, $I_{C'r_rms}$ – rms current of resonant capacitor, $dV_{C'r}$ – resonant capacitor voltage ripple, E_{Ls_off} – energy stored in the resonant inductance L_s

As can be seen from Figure 2-15, the current $I_{rms,S}$ changes little in the considered impedance range. This means that the conduction losses remain “constant” for the varying impedance Z_r . On the other hand, there is a large variation observed in the turn-off current I_{off} . Its value decreases rapidly as the impedance Z_r increases (approximately 100% I_{off} decrease in the followed impedance range). The turn-off current decrease could result in the switching loss decrease. On the other hand, the voltage ripple of the resonant capacitor increases with the impedance Z_r increasing due to a reduction in capacitance C'_r . This means that the voltage stresses on the devices increase with the impedance rising which could counterbalance the turn-off current reduction. Another fact is that the stored energy E_{Ls_off} decreases with the impedance Z_r increasing, which could result in higher losses (higher turn-on losses) and potentially in damaging the semiconductor switches.

The resonant impedance Z_r must be optimised in order to achieve the lowest overall converter loss. The impedance is limited by the restriction of the maximal voltage across the converter components due to the voltage swing $dV_{C'r}$ increasing with the impedance rising. A balance between the turn-off current I_{off} , the voltage stress due to the voltage swing $dV_{C'r}$ and the energy E_{Ls_off} must be established for the optimal converter performance. The power loss of active components with respect to the current waveform variations will be investigated in the section on loss analyses.

2.4.4 Bi-Directional OFRC topology

All previous discussions in this chapter consider the ZVS Quasi-ZCS topology as a unidirectional topology. In principle, the unidirectional topology consists of an active bridge and a passive bridge. IGBT switches and diodes are used in the active bridge, whereas the passive bridge uses diodes only. Replacing the passive bridge by another active bridge results in a bi-directional topology, as shown in Figure 2-16. For both directions of operation, this topology acts as unidirectional where one bridge is active and the other is passive. The active respectively passive function of the bridges is related to the direction of the power flow, which is determined by the converter control circuit based on the ratio between the input and output voltage.

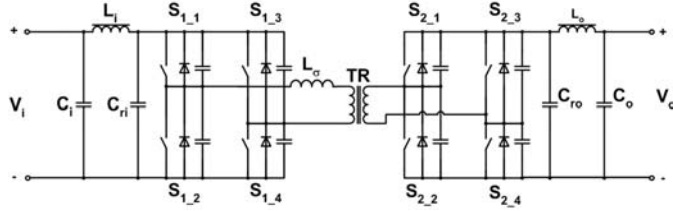


Figure 2-16: Bi-directional ZVS, Quasi-ZCS converter topology.

To realise the zero-voltage-switching quasi-zero-current-switching in both directions of operation, both bridges are equipped with snubber capacitors and resonant capacitors, and a C-L-C filter circuit was also added to the input. Figure 2-16 shows that the resulting circuit is completely symmetrical with respect to the input and output. The two resonant capacitors C_{ri} and C_{ro} are effectively connected in series from the resonance point of view. If the converter requires the same ripple conditions across the resonant capacitors at the input and the output ($dV_{C_{ri}}/V_i = dV_{C_{ro}}/V_o$) then the ratio between the two capacitors should be equal to the square of the transformer ratio. The two resonant capacitors are larger in value than a single capacitor used in the unidirectional topology because they are effectively connected in series. Therefore, the amplitude of the voltage ripple across them is smaller. As the consequence of the smaller ripple, the voltage stress on the converter components is reduced, and the filter inductors L_{is} and L_o can also have smaller values.

As shown in the simulated waveforms in Figure 2-17, placing the snubber capacitors in both bridges results in a change in the current waveforms. The presented current waveforms exhibit a “jump” (interval with higher di/dt than observed in the unidirectional waveforms) at the instance of the current reversal at the turn-on. This jump is caused by the reversal of the voltage on the secondary side of the transformer – hence at the input of the rectifier. The voltage reversal at the rectifier input cannot occur instantaneously due to the presence of the snubber capacitors. The capacitors effectively short-circuit the transformer output (equivalent circuit is shown in Figure 2-18) which results in the high di/dt (current jump). The di/dt in this interval follows from:

$$L_s \frac{di}{dt} = V_{C_{ri}}, \quad (2-19)$$

The di/dt in the operation without the snubber capacitors on the secondary side is defined as:

$$L_s \frac{di}{dt} = V_{C_{ri}} - V_{C_{ro}}, \quad (2-20)$$

As can be seen, a higher voltage across the inductance L_s causes a higher di/dt in the bi-directional operation. The high di/dt also modifies the initial conditions of the resonant circuit and therefore it results in current shapes that are slightly different from the unidirectional case. The described effect is clearly visible in Figure 2-17, which shows the switch current, the diode current and the current of the snubber capacitors in the passive bridge.

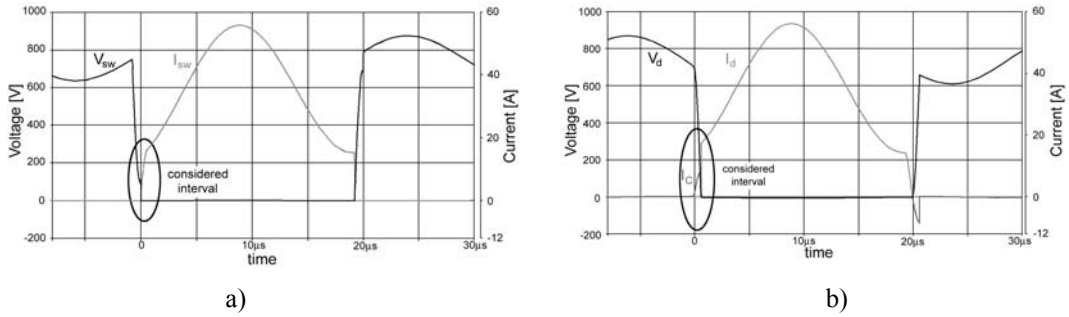


Figure 2-17: Simulated voltage and current waveforms for bi-directional OFRC topology, a) active bridge, b) passive bridge

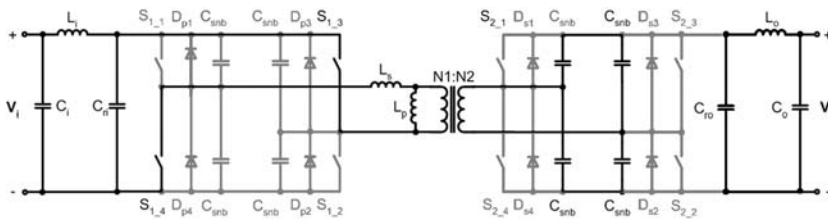


Figure 2-18: Equivalent circuit of the bi-directional OFRC converter at the moment of voltage reversal

2.5 Loss Analyses

Operation of any power converter is always accompanied by generation of power loss in its components. From the topology point of view, the main contributors to the converter power loss are active components (up to 80% [11]). The losses in active components can be divided as follows:

- switching loss of switches
- conduction loss of switches
- reverse recovery loss of rectifier diodes
- conduction loss of rectifier diodes

Influence of the current waveform on each part of the power loss is discussed below. The switches and the diodes exhibit similar behaviour with respect to the conduction loss. Therefore, the conduction loss is discussed only for the switches and the same conclusions are adopted for the diodes as well.

Passive components are other contributors to the overall converter losses. The influence of the current waveforms on the losses in passives is not considered in this section because the losses in passives are very design-specific. The losses in power magnetics are analysed in Chapter 3 with respect to the selected current waveform. At the end of section 2.5, only the equations for the power losses in resonant capacitors are given.

2.5.1 Power Loss of Switches and Resonant Circuit Parameters

The power losses in the switches were calculated by the MathCAD model of the converter. The switching losses were calculated by multiplying the device voltage with the current waveforms and integrating the results over the switching period. The conduction losses were calculated from the modelled current waveforms and IGBT characteristics published in datasheets. The calculations showed that the turn-on losses are negligible because the switches turn on with ZVS while the antiparallel diodes conduct. Therefore, the switching losses were assumed to be primarily due to turn-off. The average current through the switch (related to the transferred power) and the resonant frequency were kept constant throughout the analysis.

The power losses with respect to the resonant impedance Z_r are depicted in Figure 2-19. As can be seen, for increasing impedance Z_r the switching losses decrease substantially, whereas the conduction losses remain constant. The switching losses decrease in spite of the fact that the voltage at the moment of turn off increases. The conclusion is that the resonant impedance Z_r should be as high as possible to minimise the switching loss. The only limitation is the peak voltage across the switches, as mentioned in paragraph 2.4.3.

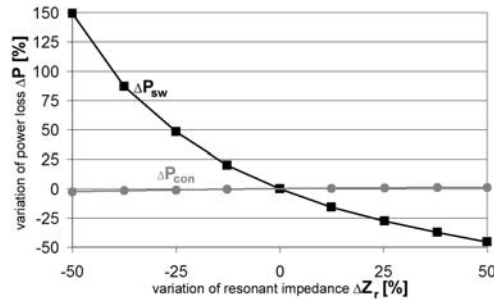


Figure 2-19: Power loss in switches with respect to resonant circuit impedance Z_r ; P_{sw} – switching loss, P_{con} – conduction loss

One of the key points of a converter design is the choice of the operating frequency. The frequency limit is defined by the maximal power loss that can be removed from the components. In conventional power converters, the switching loss is usually linearly proportional to the switching frequency, but the relation might be different for the OFRC topology because of the complex current shape. Therefore, the relation between the switching frequency and the power loss was investigated. For this analysis, the amplitude of the resonant voltage across the resonant capacitor was kept constant by adjusting the resonant circuit impedance. In this way, constant output power was maintained, and this made the results at different frequencies comparable. As shown in Figure 2-20, the conduction loss remains constant and the switching loss varies linearly with the resonant frequency ω_r ($\omega_r = \frac{1}{2}$ of the switching frequency). The slight spread between the calculated data points and the fitted curve can be explained by an inaccuracy in the initial conditions of the model. These were obtained from an iteration process as described in paragraph 2.4.

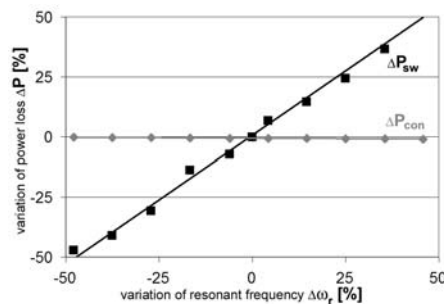


Figure 2-20: Power loss versus resonant frequency ω_r ; P_{sw} – switching loss, P_{con} – conduction loss

2.5.2 Turn-off Instant and Dead Time Setting

In Quasi-ZCS topologies, turning off the current at its minimum yields the lowest turn-off loss. Figure 2-21 shows the variation of the conduction and switching losses for non-optimal switching (not turning off at the current minimum). As can be seen, even a small variation of the turn-off instant results in a substantial increase of the switching loss, whereas the conduction loss remains constant.

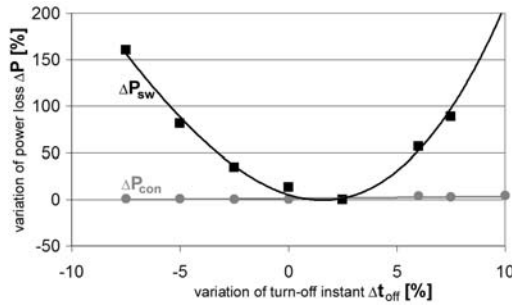


Figure 2-21: Power losses versus turn-off instant t_{off} ; P_{sw} – switching loss, P_{con} – conduction loss

The turn-off current may affect the ZVS at the following turn-on as well. In order to guarantee ZVS turn-on, the snubber capacitors must be fully charge / discharge prior to turn-on. The following requirements must be fulfilled to obtain this:

- the turn-off energy of the resonant inductance L_s must be large enough
- dead time between the switches' turn-off and -on must be long enough

If one of the two conditions is not fulfilled, the snubber capacitors are charged / discharged only partially and the residual energy is consequently dissipated in the switches at their next turn-on. This results in current spikes which increase the switching loss and generate EMI.

In order to prevent the loss of zero-voltage-switching, a minimal current must flow through the switch at the moment of turn-off. This current can be calculated from:

$$I_{off_min} = \sqrt{\frac{C_{snb} V_i^2}{L_s}} \tag{2-21}$$

where C_{snb} is the snubber capacitance, V_i is the input voltage and L_s is the resonant inductance. The resulting turn-off current might be higher than the minimum of the current waveform. In such a case, a compromise current value which minimises the overall converter losses should be used. The turn-off current can be increased by modifying the switching frequency (by moving the turn-off point on the current waveform).

For a proper converter operation, a so-called dead time is required between the turn-off of the conducting switch and the turn-on of the consequent switch. This dead time is required to charge respectively discharge the snubber capacitors. A proper dead time setting is illustrated in Figure 2-22. In this figure, the switch turns off the minimal current I_{off_min} required to charge / discharge the snubber capacitors. As can be seen, the dead time must be set to a value that the next switch turns on just at the moment when the voltage of the snubber capacitor reaches its maximum.

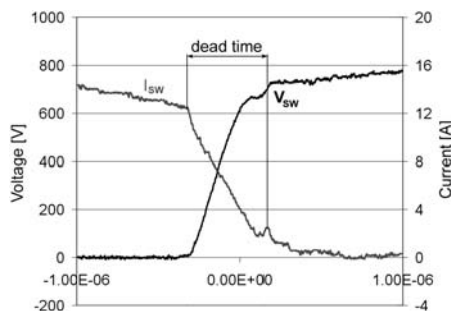


Figure 2-22: Dead time setting for switching with minimal possible turn-off current

2.5.3 Reverse Recovery Loss in Rectifier

The reverse recovery loss of the rectifier diodes is another factor which limits the converter's switching frequency. The recovery loss is affected by the intrinsic properties of the diode and by the circuit in which the diode is implemented. Therefore in this paragraph, the reverse recovery loss is discussed with respect to the resonant circuit impedance Z_r and resonant frequency ω_r .

The reverse recovery loss is modelled for the purpose of this investigation by simplified voltage and current waveforms as shown in Figure 2-23. The reverse recovery current I_{rr} and the reverse recovery time t_{rr} are calculated by equations published in [6].

$$t_{rr} = \sqrt{\frac{2Q_{rr}(1+s)}{di/dt}}, \quad (2-22)$$

$$I_{rr} = \sqrt{\frac{2Q_{rr}di/dt}{1+s}}, \quad (2-23)$$

where Q_{rr} is the reverse recovery charge, s is the so-called diode snap factor where $s=t_b/t_a$, and di/dt is the rate of the current decrease at the diode turn-off. For the recovery charge Q_{rr} and the snap factor s , typical values of power diodes implemented in converter prototypes were used for the analysis ($Q_{rr}=25\mu\text{C}$, $s=0.2$).

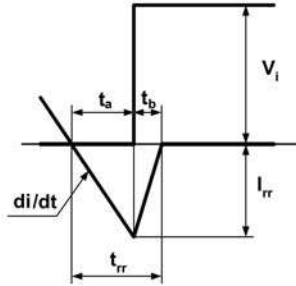


Figure 2-23: Simplified current and voltage waveform used to model reverse recovery losses

The model shown in Figure 2-24 was used to calculate the di/dt at the diode turn-off. The model represents a simplified converter circuit for Interval VII (Figure 2-11) in which the rectifier diodes turn off. The current decay, according to this model, follows from:

$$-L_s \frac{di}{dt} = V_i + V_{C_r}, \quad (2-24)$$

It is assumed that at the moment of the switch turn-off, the voltage across the resonant capacitor is approximately equal to the input voltage (true for practical waveforms), which means that the current decreases with the rate: $di/dt=2V_i/L_s$. Substituting the di/dt into (2-22) and (2-23) results in the following equations for the reverse recovery time and current:

$$t_{rr} = \sqrt{\frac{Q_{rr}(1+s)L_s}{V_i}}, \quad (2-25)$$

$$I_{rr} = \sqrt{\frac{4Q_{rr}V_i}{(1+s)L_s}}. \quad (2-26)$$

By using the calculated t_{rr} and I_{rr} and the model waveforms of Figure 2-23, the reverse recovery loss P_{rec} is estimated by multiplying voltage and current waveforms. The calculated t_{rr} , I_{rr} and P_{rec} are plotted in Figure 2-25 with respect to the resonant impedance Z_r and in Figure 2-26 with respect to the resonant frequency ω_r .

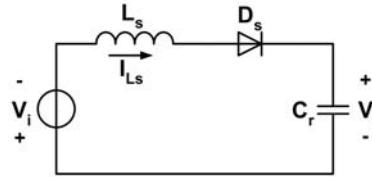


Figure 2-24: Simplified converter circuit model for Interval VII. used for modelling of reverse recovery

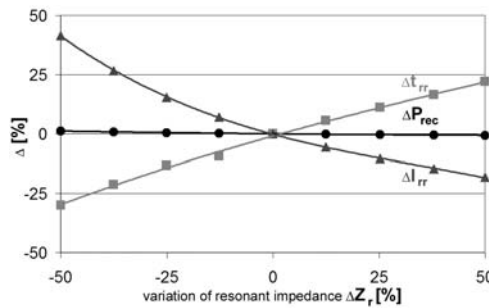


Figure 2-25: Reverse recovery versus impedance of the resonant circuit Z_r ; t_{rr} – reverse recovery time, I_{rr} - reverse recovery current, P_{rec} – reverse recovery losses

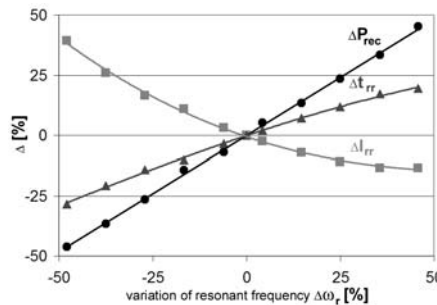


Figure 2-26: Reverse recovery versus resonant frequency ω_r ; t_{rr} – reverse recovery time, I_{rr} - recovery current, P_{rec} – reverse recovery losses

As can be seen from Figure 2-25, the reverse recovery loss P_{rec} is independent of the resonant circuit impedance. This is because the increase of I_{rr} is fully compensated for by the decrease of t_{rr} . In Figure 2-26, a linear relation between the recovery loss P_{rec} and the resonant frequency can be observed. In this case again, the non-linear variation of I_{rr} with respect to frequency is compensated for by the inverse non-linear variation of t_{rr} . The resulting relation between the recovery loss and the frequency is therefore linear. For a real converter circuit, the situation might be different than presented here because the recovery charge Q_{rr} might vary with different circuit conditions and therefore the recovery loss might behave differently.

2.5.4 Power Loss in Resonant Capacitors

In resonant converter topologies, resonant capacitors are subject to high power loss due to high currents and high voltage swings. In order to assess the power loss in the resonant capacitors, datasheet-based loss calculations were used.

The power loss in capacitors is in general caused by two phenomena:

- Dielectric losses – caused by charging and discharging of dielectrics
- Thermal losses – caused by currents flowing through electrodes

The dielectric losses as well as the thermal losses can be calculated from the parameters of the used capacitors. The dielectric losses are calculated as:

$$P_d = \frac{1}{2} CV_{pp}^2 f_s tg \delta_0, \quad (2-27)$$

where C is the capacitance of the used capacitor, V_{pp} is the peak-to-peak value of the ripple voltage across the capacitor, f_s is the operating frequency and $tg \delta_0$ is the dielectric loss factor. The thermal losses are then calculated as:

$$P_t = R_{C_s} I_{rms}^2, \quad (2-28)$$

where R_{C_s} is the series resistance of the used capacitor and I_{rms} is the rms current flowing through the capacitor.

To assess a total capacitor loss on a general base is difficult because only certain specific capacitance values are made. The value required by the topology is usually a result of a series-parallel combination of several capacitors. This makes the assessment of the losses in capacitors difficult because for each calculated point a new series-parallel combination must be found. For this reason, the general loss characteristics are not included here. The above written equations were used in the converter design to calculate losses in the capacitors for specific design points. The dielectric loss factor $tg \delta_0$ and the series resistance R_{C_s} from the datasheets were used for these calculations.

2.6 Voltage Control in OFRC topology

Zero-voltage-switching, quasi-zero-current-switching operation requires that the switches are turned-on and off at specific instants. This implies that the possibility to control the voltage and consequently also the power by adapting the duty cycle or frequency is sacrificed to the realisation of low switching losses. In principle, a ZVS Quasi-ZCS converter operates as a dc transformer where the current flowing through it depends only on the ratio between the input and output voltage. The converter can be represented by the circuit as shown in Figure 2-27. If the output is passive then the current flowing through the converter is related only to the impedance of the load and the impedance of the converter itself. The following paragraphs discuss the possibilities of voltage control in the OFRC topology. Problems with the duty cycle and frequency control are discussed first, and this is followed by an introduction of two new methods of voltage control.

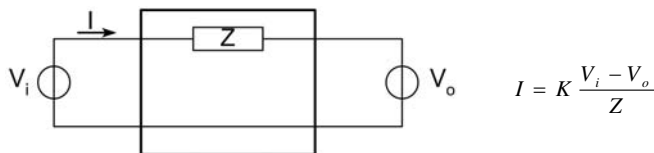


Figure 2-27: Converter represented as impedance; k is the scaling factor

Voltage Control by Frequency Modulation

One of the conventional methods of output voltage control in resonant converters is by a variation of the operating frequency. Increasing the operating frequency without changing the properties of the resonant circuit yields shorter current pulses and hence the amount of energy transferred to the output is reduced. The disadvantage of this method in the case of OFRC is that the topology loses quasi-zero-current-switching when the frequency is different from the optimal frequency. The loss of quasi-zero-current-switching together with a higher operating frequency results in increased switching losses. The increase of the turn-off loss with respect to the change of frequency can be demonstrated in Figure 2-21 where the change of operating frequency f_s is represented by the variation of the turn-off instant Δt_{off} . As is shown, the non-optimal switching yields a large power loss increase even for small switch on-time variations.

Voltage Control by Duty Cycle Modulation

Duty cycle control is another way to control the output voltage in conventional power converters. In principle, it can be applied also in ZVS Quasi-ZCS topologies but doing so results in several negative changes in the converter waveforms. Firstly, quasi-zero-current-switching is lost by moving away from the optimal switching point. This is demonstrated in Figure 2-28, where the current is turned off at its maximum ($t=5 \mu\text{s}$ approximately). The figure also shows that, during the interval when the switches are *off* (5 to 20 μs), a high-frequency resonance occurs between the resonant inductance and the snubber capacitors. This resonance may cause EMI problems. Further, the consequence of holding the switches *off* for the extended time period is that the voltage across the switches is not zero at the turn-on instant (Figure 2-28). This results in current spikes through the switches due to discharging of the snubber capacitors when the switches are turned on again. The current spikes together with the large turn-off current yield high total switching losses.

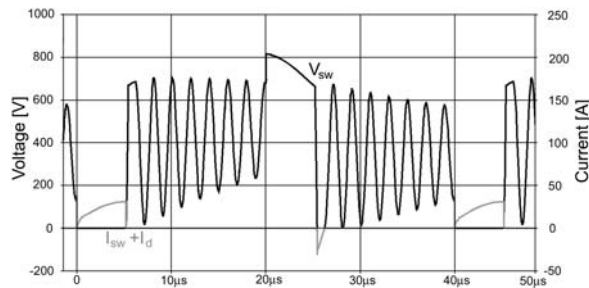


Figure 2-28: Simulated waveforms for duty cycle modulated ZVS Quasi-ZCS topology

A small modification of the OFRC topology allows the voltage control by duty cycle modulation. The modification is based on an auxiliary bi-directional switch added in series with the primary of the transformer as is shown in Figure 2-29. The auxiliary switch allows the main switches to operate with a constant duty cycle of 50% by disconnecting the transformer for the time interval when the power is not transferred to the output. By doing that, the main switches lose Quasi-ZCS and they operate as they would in a conventional ZVS converter but the additional loss due to discharging of the snubber capacitors through the switches is prevented. The output voltage is controlled by the duty cycle of the auxiliary switch and its timing in relation to the main switches. The auxiliary switch turns-on without the current flowing in the circuit and turns-off when the current is zero again. The basic principle is shown in the simulated waveforms of Figure 2-30. The advantage of this topology is the loss reduction in comparison with the conventional duty cycle voltage control and at the same time keeping ZVS Quasi-ZCS properties if voltage control is not required. The disadvantage is the presence of the bi-directional switch in the current path which increases the conduction losses in comparison with the conventional ZVS Quasi-ZCS topology.

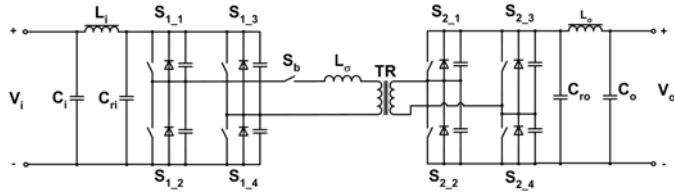


Figure 2-29: Modified ZVS Quasi-ZCS topology for duty cycle voltage control

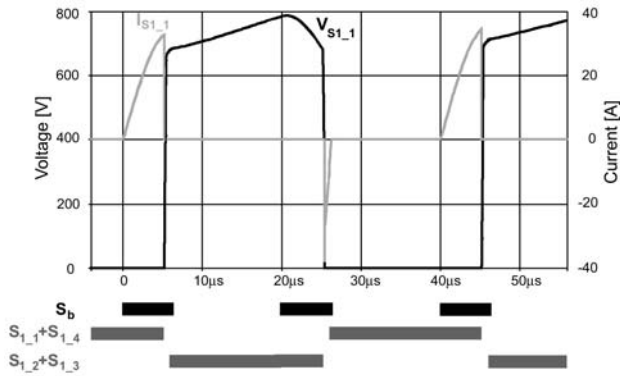


Figure 2-30: Simulation of duty cycle voltage control in modified ZVS Quasi-ZCS topology

Partial Voltage Control by Phase Shifting of Individual Converters

The control methods mentioned above suffer from increased losses in comparison with the standard ZVS Quasi-ZCS topology. By interleaving two converters connected in series as shown in Figure 2-31, the ZVS Quasi-ZCS operation is preserved and partial control of the output voltage is obtained.

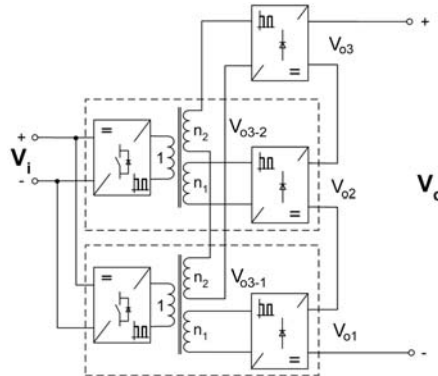


Figure 2-31: ZVS Quasi-ZCS topology with voltage control by phase shifting of individual converters

The system is based on transformers with two secondary and one primary winding. One of the secondaries (n_1 ratio in Figure 2-31) is considered as the main secondary winding and the ZVS Quasi-ZCS operation is established by the resonance between its leakage inductance and the resonant capacitor. The output voltage of this section is calculated as: $V_{o1}=V_{o2}=V_i n_1$. The auxiliary secondary windings (n_2 ratio in Figure 2-31) are used for the partial voltage control. They are of considerably lower power rating than the main secondary windings in order not to disrupt the resonance. In the presented configuration, the two auxiliary windings are connected in series and the voltage at the

rectifier input is controlled by the phase shift α between the two converter sub-modules. The voltage control is illustrated in Figure 2-32. The total voltage of the controlled voltage section follows from:

$$V_{o3} = \frac{2V_i n_2}{T} \left(\frac{T}{2} - \alpha \right), \quad (2-29)$$

where the time T is the switching period, the voltage V_i is the input voltage and the ratio n_2 is the auxiliary turn ratio. The disadvantage of this approach is that the total output voltage can be controlled only in a limited range; in the shown case: $V_o = V_{o1} + V_{o2} + V_{o3}$. For this reason, this control strategy is suitable only for applications that do not require voltage control in the full output voltage range but use this control only for voltage adjustment. A full analysis of the proposed solution is beyond the scope of this thesis and will therefore have to be a part of future research.

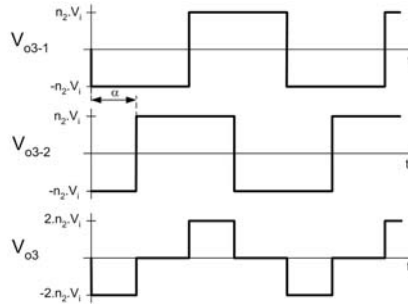


Figure 2-32: Illustrative voltage waveforms for voltage control by phase shifting individual converters

2.7 Converter Demonstrators

Several aspects were addressed during the converter design and model development. These are:

- Topology investigation and circuit analyses
- Electromagnetic design
- Thermal management
- Spatial placement of components

With respect to these design aspects, the main objectives of the converter demonstrators are:

- to evaluate the applied technologies
- to characterise converter performance
- to validate assumptions made during the model development and converter design
- to allow for the concept and design adaptation if necessary

It would be difficult and cumbersome to perform all required tests and measurements and to make necessary modifications on the final high-power-density prototype. Therefore, Converter Demonstrator I was built in a conventional way with easy access to all components. Its main purpose was to validate the circuit theory presented in Chapter 2, to test the functionality of the topology and to tune the converter's performance if required. Converter Demonstrator II used the knowledge gathered from Demonstrator I. Its main purpose was to demonstrate and to evaluate the functionality, high power density and thermal performance. The discussions concerning each of the two demonstrators and related design aspects are divided between the appropriate chapters and paragraphs as follows:

- Chapter 2 (2.7.1 to 2.7.3) – General description of the prototypes and applications
 - Description of converter circuits (Demonstrator I & II)
- Chapter 2 (2.7.4) – Evaluation of circuit operation of Demonstrator I
- Chapter 3 (3.5) – Evaluation of electromagnetic design of power magnetics (Demonstrator I & II)

- Chapter 4 (4.6.2) – Evaluation of thermal management (discussed results primarily of Demonstrator II)
- Chapter 5 – Spatial component organisation (Demonstrator II)

2.7.1 Applications and Specifications of Converter Prototypes

As discussed in Chapter 1, main and auxiliary traction converters, and ship converters are examples of applications where high-power, isolated, dc-dc converters are required. The properties and requirements of these applications were considered in the specifications of the converter demonstrators. A constraint was the suitability of the demonstrators to be built and tested in the laboratory environment. The resulting main specifications are listed in Table 2-1.

Table 2-1: Main specifications of converter demonstrators

Nominal output power	50 kW
Nominal input voltage	750 V
Nominal output voltage	600 V
Operating frequency	20 - 50 kHz
Operating heatsink temperature	70 °C
Maximal ambient temperature	40 °C

A power level of 50 kW was specified as the nominal power of the converter demonstrators. This value was chosen as a compromise between the ability to test the prototypes in the TU Delft / EPP laboratory and at the same time to represent the power level of the considered high-power applications. The converter design at 50 kW is essentially the same as at higher power levels and therefore high enough to observe and investigate all issues related to high-power converters. The power level of 50 kW also corresponds to the power range of auxiliary traction converters [29] and ship converters.

The selected voltage levels of 750 V and 600 V were identified as suitable for applications in light traction and in auxiliary converters. These voltage levels were also considered suitable for testing in EPP laboratory. The converter module with the voltage ratio 750 V - 600 V can be used directly in light traction vehicles like subways and trams. These operate from 750 V source and supply traction machines of typically 600 V. Furthermore, series parallel combinations of such modules, as shown in Figure 2-33, can be implemented in applications like suburban trains supplied from 1.5 kV (2 modules in series) or 3 kV (4 modules in series) catenary. An application of the developed principles to ship converters would result in a voltage reduction. These converters operate typically at voltage levels of rectified three-phase or single-phase grid which would allow implementation of low-voltage power-devices with better dynamic properties. Due to the better dynamics, these devices could be applied in the presented concepts without significant changes. As presented in Figure 1-9, auxiliary converters for traction provide also low voltage outputs for charging on-board batteries. The low voltages in this case would require the use of low-voltage and high-current technology. This would lead to fast switching transients at high current levels and hence increased attention to low-inductance circuit-design. The design concepts proposed in this thesis should be applicable also to these applications.

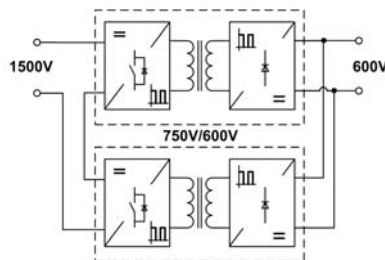


Figure 2-33: Series – parallel connection of converter modules for operation at higher voltage levels

In order to obtain small passives, the operating frequency was specified in the range 20 – 50 kHz. The final value of 25 kHz was a result of an optimisation process based on the models presented in this thesis and of initial measurements performed on Converter Demonstrator I. The models indicated that high power density and high efficiency were reachable at the frequency of 25 kHz.

The thermal concept proposed in this thesis (Chapter 4) utilises heat collection on dedicated thermal surfaces where further heat exchange with the environment is established. The type of heat exchange between the thermal surfaces and the environment can vary (forced air, water, etc.) depending on the application. The design constraints on the heat exchange system were set at a maximal thermal surface temperature of 70 °C and a maximal ambient temperature of 40 °C. The thermal surface temperature of 70 °C was chosen as a compromise between the safe operation of all used components and small heatsinks. Details on the thermal design are discussed in Chapter 4.

2.7.2 IGBT Modules Under ZVS, Quasi-ZCS

Many types of IGBT power modules are available on the present semiconductor market and each of them offers different properties [30]. In a converter design process, usually a designer must choose one of the available semiconductor technologies that suits the best to the specific application.

One of the main design criteria is overall converter efficiency. To reach the maximal efficiency, a balance between the conduction and switching losses must be established. This is especially important in the case of ZVS, Quasi-ZCS topologies with respect to their resonant current waveforms. In the following paragraphs, the performance of two planar and a trench IGBT structures under ZVS, Quasi-ZCS conditions is discussed. The goal of the investigation is to identify an IGBT technology which suits the best to ZVS, Quasi-ZCS applications [28].

Review of Compared IGBT Technologies

The following IGBT modules were chosen for the comparison:

- IGBT A – Eupec – BSM100GB120DLcK
- IGBT B – Semikron – SKM 100GB125DN
- IGBT C – Fuji – 2MBi150U4B120 (Trench-Field-Stop IGBT)

IGBT A power module is a non punch through (NPT) device based on the conventional planar technology. The device is optimised for low conduction losses which are traded for slower switching and longer tail current. These properties limit its use to applications with low switching frequencies where the low conduction losses are of increased importance. This device was included in the comparison because it was assumed that under ZVS Quasi-ZCS conditions, the device would exhibit low switching losses due to the current being turned-off close to zero.

On the other hand, IGBT B power module has an excellent switching performance at the expense of higher conduction losses. It is designed specifically for resonant converters operating at high switching frequencies and it was therefore included in the comparison.

IGBT C power module employs a relatively new Trench-FS IGBT structure. The structure introduces two features which improve the performance of the device. The first feature is a so-called field-stop layer. This layer is designed to level off the electric field. This leads to thinner substrates for the same voltages as used in the conventional devices as well as to low saturation voltages and hence low conduction losses. The field-stop layer offers also the advantage of the switch being able to turn-off much faster with virtually no tail current. This leads to reduced switching losses. The second feature implemented in this power module is a trench gate structure. By adopting this structure, the conducting channel density can be increased and the on-state voltage drop can be reduced even more. This is due to a reduction of the resistance of the JFET part (JFET present in the IGBT body structure) to zero by increasing the cell density. On the other hand, the trench gate and the related high cell density result in a low short-circuit capacity which is especially critical for applications in electric drives [31]. Also, the junction-case thermal resistance of a typical Trench-FS IGBT chip is higher than

that of the conventional planar chips with the same current rating because of higher current densities possible and therefore lower chip area required. In spite of these disadvantages, the trench gate and the field stop layer make the Trench-FS IGBT a very promising device for many applications [32]. The device seems to be also very suitable for ZVS Quasi-ZCS converter topologies [33].

Measurements of Power Losses – Comparison of IGBT Technologies

The considered IGBTs were compared by measurements with respect to their switching behaviour and on-state characteristics in order to select the component with the lowest overall losses. The tested IGBTs were implemented individually in the ZVS Quasi-ZCS converter prototype (Converter Demonstrator I). Voltage and current waveforms were measured by a digital oscilloscope using a high-voltage differential voltage-probe and a high-current current-probe. The switching loss was calculated by multiplying the measured voltage and current waveforms. The on-state power loss was calculated by combining the measured current waveforms with forward characteristics published in datasheets. This method was used as it is difficult to measure the on-state voltage of a few volts accurately because the voltage level is rapidly changing between “0” V and “1” kV due to the switching. As an example, the measured waveforms and the instantaneous power loss for IGBT C (Trench-FS IGBT) operating at 25 kW power output during turn-on, on-state and turn-off are shown in Figure 2-34 a, b and c respectively.

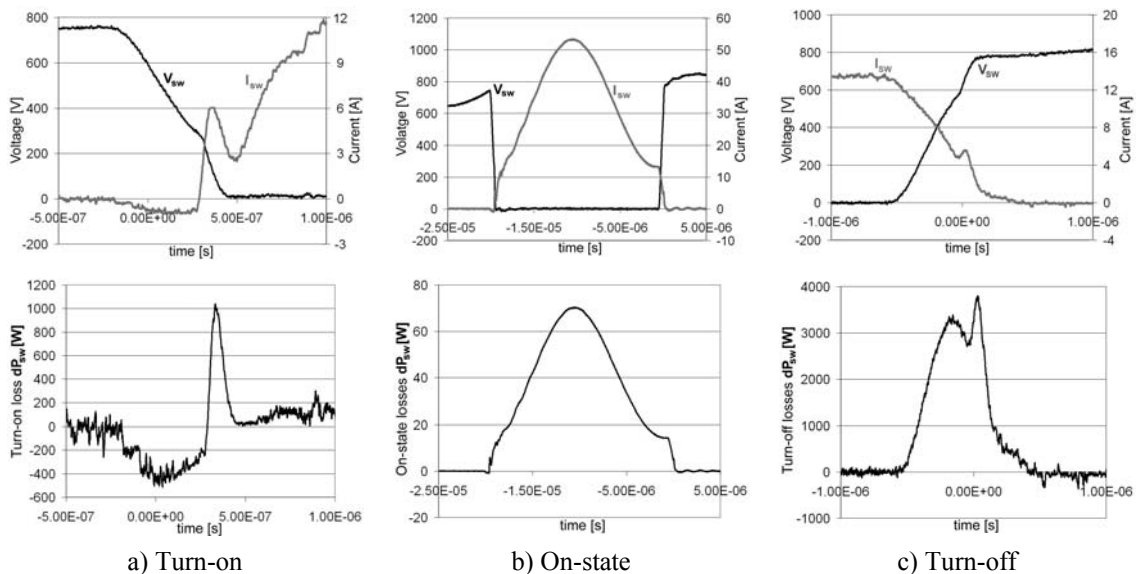


Figure 2-34: Measured voltage, current and instantaneous power loss for IGBT C – 2MBi150U4B120, operation at 25 kW power output; a) turn-on, b) on-state, c) turn-off

As can be seen from Figure 2-34a, the measured turn-on losses are relatively low. This was true for all tested devices even though no pure ZVS was present due to the low turn-off currents. Consequently, the leakage inductance failed to charge respectively discharge the snubber capacitors fully and hence the antiparallel diodes did not turn-on. In spite of this, a small current step and consequently slow current rise after turning-on the switch combined with fairly low voltage values at the instant of turn-on resulted in the low power loss.

Figure 2-34b depicts the main current waveforms and associated instantaneous power loss for IGBT C. The current waveforms were adjusted individually for each tested device by trimming the switching frequency ($\pm 3\%$). The frequency was adjusted so that for a selected load (approximately 60% nominal load) the turn-off current, not necessarily the minimal current, fully charged respectively

discharged the snubber capacitors. The measured conduction losses were as expected; the lowest loss was observed for IGBT A and IGBT C. The best result was obtained with IGBT C because the current waveform has a better shape than in the other two cases. The high on-state voltage of the fast switching IGBT resulted in the highest conduction loss.

The turn-off waveforms of IGBT C are shown in Figure 2-34c. The highest turn-off power loss was measured on IGBT A. This high power loss was caused mainly by a low di/dt during turn-off and a long tail current. The situation was worsened by turning-off at higher current level than the other two devices. The turn-off at the higher current was required by a higher chip capacitance of the device. Both, IGBT B and C have a low turn-off loss. The devices showed short tail current and high di/dt s which minimised the turn-off loss.

The total power loss for all tested devices at different power levels is shown in Figure 2-35 for different loads. The power losses are plotted separately as turn-on, on-state and turn-off loss. As can be seen, IGBT C has the lowest loss. Low on-state voltage drop and fast switching resulted in almost 0.5 % improvement of the overall converter efficiency in comparison with the second best IGBT B. The efficiency increase was obtained although a 150 A device was used, where the other two IGBTs were 100 A devices. Initially it was expected, that high-current devices are slower than low-current devices. As the measurements showed, IGBT C – Trench FS-IGBT is the most suitable for application in ZVS Quasi-ZCS topologies.

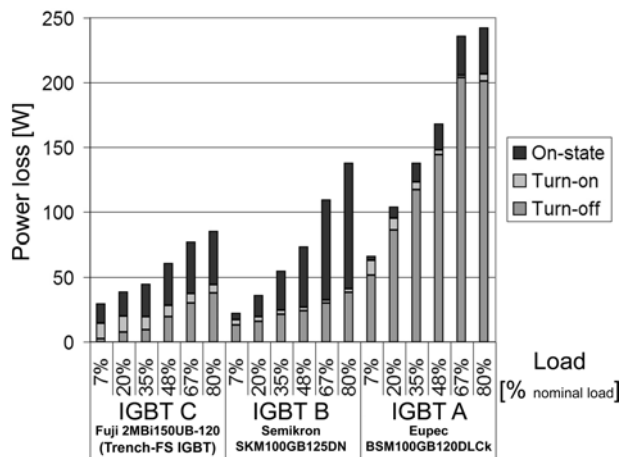


Figure 2-35: Total power loss of tested devices for different load levels, loss per interval representation

2.7.3 Converter Circuits

The circuit diagram of Demonstrator I is shown in Figure 2-36. It consists of two active bridges, a transformer, resonant capacitors and an input and output filter. The leakage inductance and the resonant capacitors were tuned for the operating frequency of 25 kHz. Trench-FS IGBTs were used because they exhibited the lowest power loss (paragraph 2.7.2). The values and the types of the used components are listed in Figure 2-36. The voltage snubbing across the switches was provided only by the internal parasitic capacitances of the selected IGBT devices. External capacitors, which would provide additional voltage snubbing and hence lower turn-off loss, could not be used. The reason for that was that in the selected mode of operation (very low turn-off currents), there was not enough energy stored in the resonant (leakage) inductance to charge any significant external snubber capacitance. The physical layout of Demonstrator I is shown in Figure 2-37.

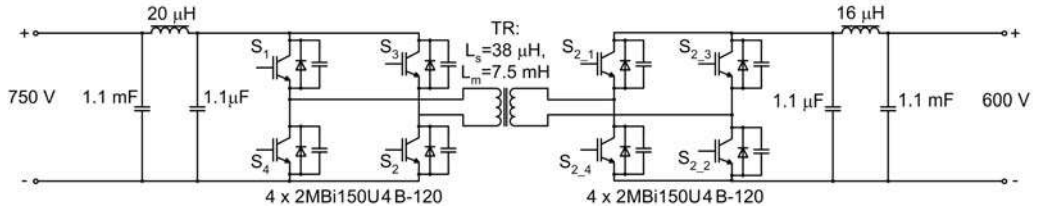


Figure 2-36: Circuit diagram of Converter Demonstrator I.

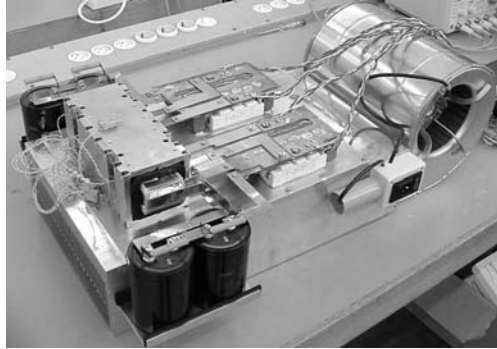


Figure 2-37: Physical layout of Converter Demonstrator I.

The design of Demonstrator II is based on Demonstrator I. The circuit diagram of the second demonstrator is shown in Figure 2-38. The modifications in comparison to Demonstrator I are: different transformer design and different design of the filter inductors. The physical layout of Demonstrator II is shown in Figure 2-39. As can be seen the design is much more compact than that of Demonstrator I. The details of Demonstrator II will be discussed in Chapter 4 with respect to thermal management and in Chapter 5 with respect to spatial organisation of components.

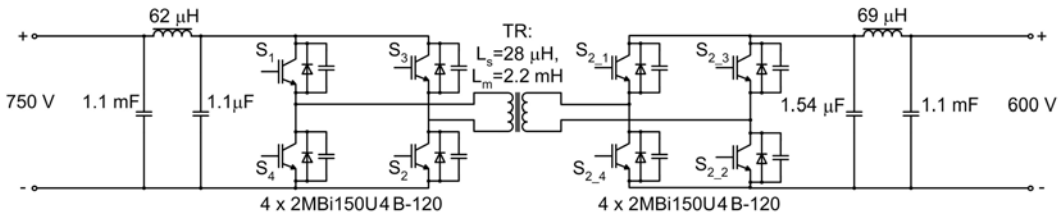


Figure 2-38: Circuit diagram of Converter Demonstrator II.

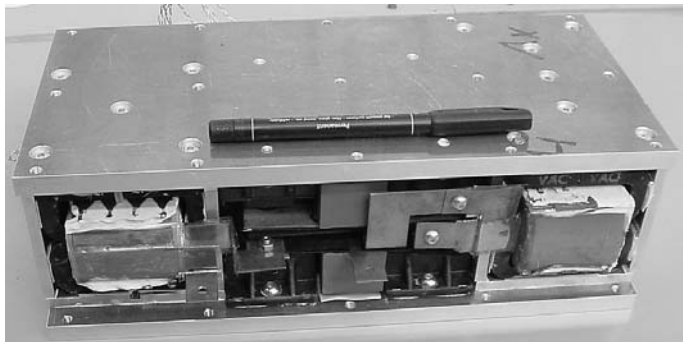


Figure 2-39: Physical layout of Converter Demonstrator II.

2.7.4 Measurements on Converter Prototypes

Three types of measurements were carried out on the converter demonstrators:

- Measurements of general current and voltage waveforms – the goal was validation of converter functions and behaviour
- Detailed measurements of selected current and voltage waveforms – the goal was assessment of power loss in the converter components
- Measurements of converter efficiency – the goal was to compare the converter performance to the state-of-the-art

Demonstrator I was used for all the measurements presented in this chapter because of the good access to all points of measurements.

The block diagram of Demonstrator I basic system set-up is shown in Figure 2-40. As can be seen, the power and the control part of the converter were supplied from independent power supplies. The power part was supplied from 2 x 32 kW, 1 kV, 40 A power supplies capable of parallel operation. Both power supplies were used in current control mode to obtain a better voltage stability of the output. The load of the converter consisted of a bank of 14 water cooled resistors of 100 Ω connected in parallel. Each 100 Ω section could be turned-on and off independently which was used to adjust the converter load as required.

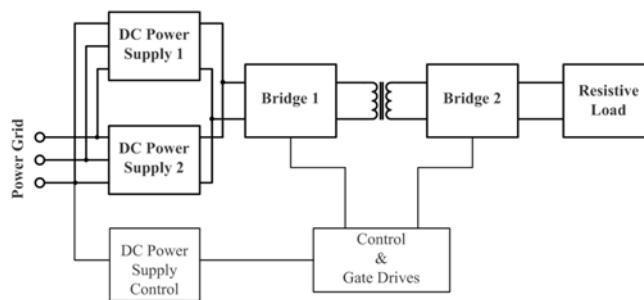


Figure 2-40: Block diagram of the basic set-up of Demonstrator I

The switching frequency and the dead times were kept fixed for all the measurements. They were set at values for which a maximal efficiency was reached in a wide load range. This means that in some load cases, the current and voltage might not had the optimal shape. The maximal performance in such operating point was sacrificed for a better overall converter performance.

The measured waveforms for half-load and full-load and for both directions of operation (750 V \rightarrow 600 V and 600 V \rightarrow 750V) are shown in Figure 2-41 for the semiconductor switches and in Figure 2-42 for the diodes respectively. The switch waveforms (full cycle, turn-on and turn-off) were measured on the switches S_1 and S_{2-1} (see Figure 2-36). As can be seen from the waveforms of Figure 2-41, the amplitude of the resonance varies as the load of the converter varies. Furthermore, it can be observed that the currents at the turn-on and turn-off of the switches vary little with respect to the load. This indicates that the switching loss remains “constant” in the considered upper load range and that the major contribution to the increase of power loss at high-loads is the conduction loss. It can be further observed that there are small spikes present in the current waveforms at the turn-on and turn-off. These were caused by the snubber capacitors (only self capacitances of switches) discharging through the switches. The spikes could be prevented by turning-off the IGBTs at a slightly higher current (turn-off earlier). This option was tested by measurements. As a result, the current spikes were absent but the overall converter efficiency was reduced because of turn-off at a higher current.

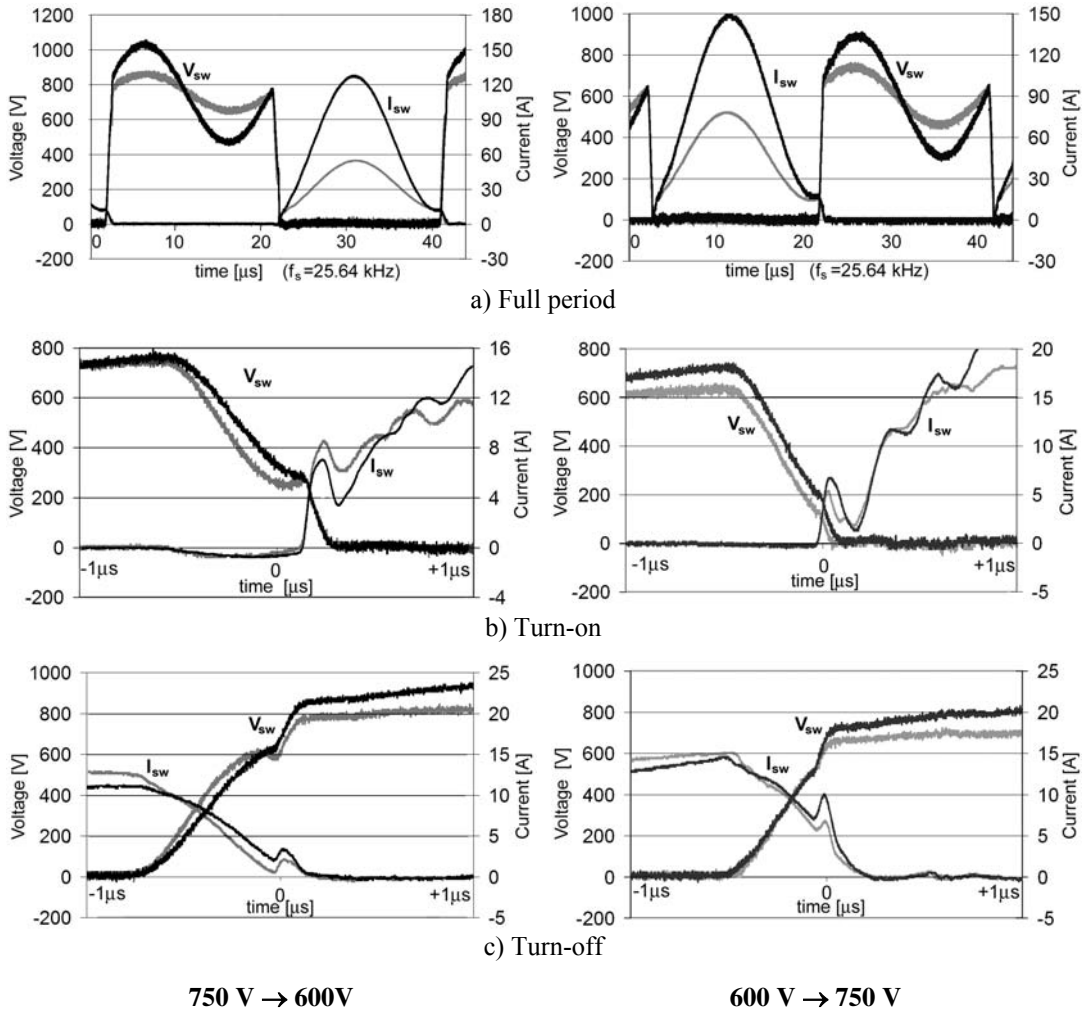


Figure 2-41: Measured voltage V_{sw} and current I_{sw} waveforms of IGBT switches for both power flow directions (750V → 600V left column and 600V → 750V right column); a) full cycle, b) turn-on, c) turn-off; half load (grey) and full load (black)

In Figure 2-42, the waveforms of the diodes are shown for the same operating conditions as for the semiconductor switches. The waveforms were measured on the internal diodes of the IGBT power modules of the rectifier bridge. As can be seen, a similar effect can be observed for the diodes as for the switches; the amplitude of the resonance varies with the load but the currents at turn-on and turn-off remain almost constant. At turn-on, the magnitude of the “current jump” (as discussed in paragraph 2.4.4) is almost independent of the load. The explanation of this phenomenon is that: if the turn-off current and voltage levels remain the same then it takes approximately the same time to charge the self capacitances of the diodes. At the turn-off, the observed reverse recovery behaviour is also similar for both load conditions. This is due to the reverse recovery current and time being dependent on the voltage forcing the current change (see paragraph 2.5.3) and on the current which flowed in the diode in the forward direction prior to its turn-off ([6]). As the turn-off current and the voltage forcing the reverse recovery remained almost constant, the reverse recovery was observed unchanged for both followed loads.

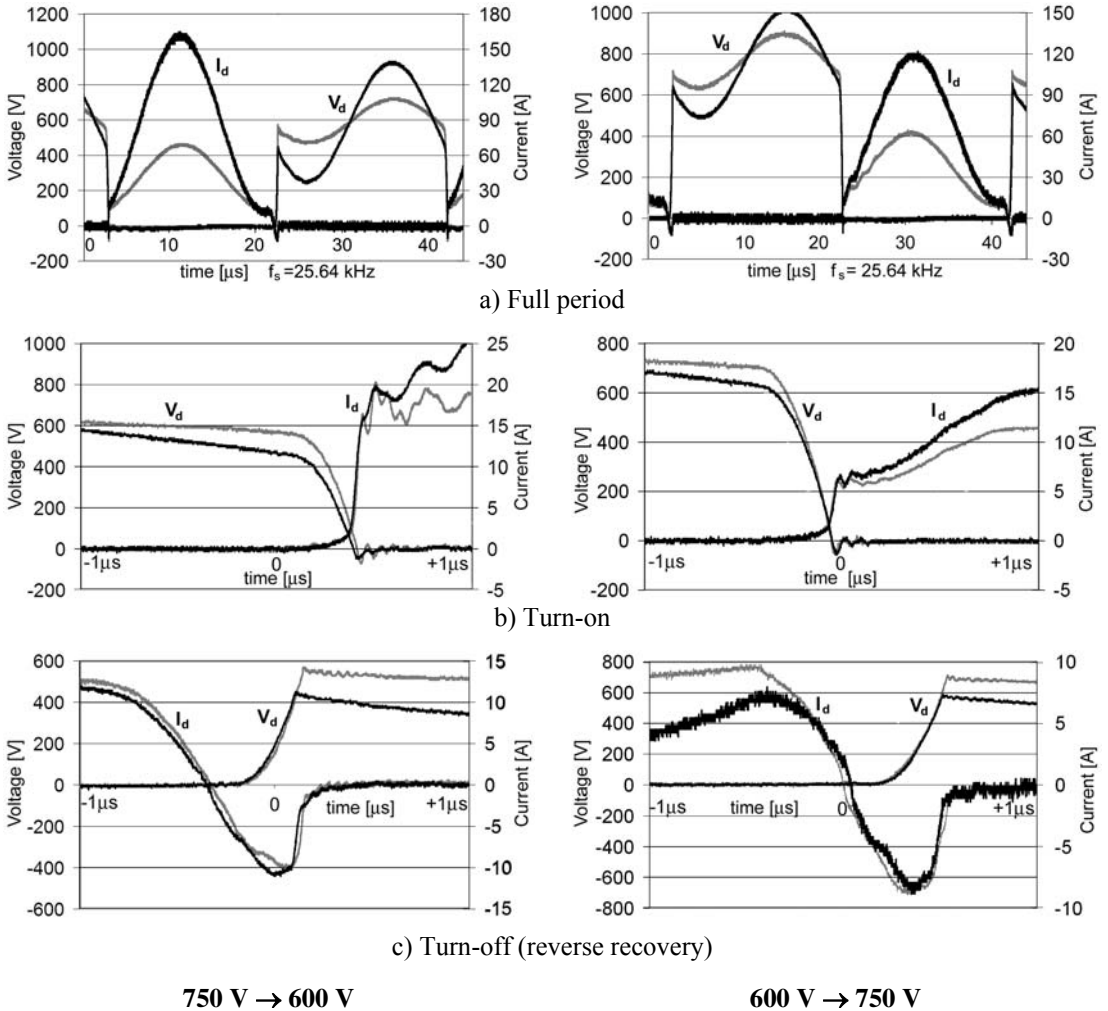


Figure 2-42: Measured voltage V_d and current I_d waveforms of rectifier diodes for both power flow directions ($750\text{V} \rightarrow 600\text{V}$ left column and $600\text{V} \rightarrow 750\text{V}$ right column); a) full cycle, b) turn-on, c) turn-off; half load (grey) and full load (black)

The measured voltage and current waveforms were used to calculate the power loss in the switches as well as in the diodes separately for turn-on, on-state and turn-off intervals. The results for different loads and for both directions of operation are shown in Figure 2-43. As can be seen from the figure, the turn-on loss is much smaller than the other losses for both the diodes and the switches. The turn-off loss gives the main contribution to the power loss of the switch in no-load operation. The turn-off loss increases with the load at low loads (about 100% loss increase from no load to half load) and it remains almost constant for higher loads (half load to full load variation only 20%). This trend is even more noticeable for the diodes where the reverse-recovery loss remains constant or even drops for the direction of operation $600\text{ V} \rightarrow 750\text{ V}$. For the diodes, the conduction power loss is the main contributor to the power loss. For the switches, the conduction loss and the turn-off loss are approximately equal. The conclusion based on this discussion is that to reduce the power loss even further, the attention should be paid to on-state and turn-off losses of the switches and conduction losses of the diodes.

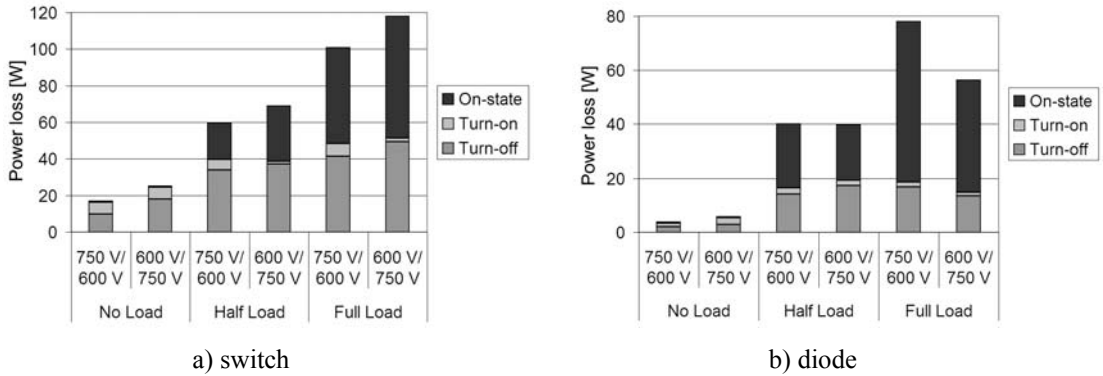


Figure 2-43: Measured power loss in semiconductor switch and diode under ZVS Quasi-ZCS for both directions of operation

The converter efficiency was calculated from the measured dc currents and voltages at the converter input and output. The power consumed by the cooling fan and by the control circuit was not included in this measurement. The measured efficiency curves for both directions of operation are plotted in Figure 2-44. As can be seen, the converter efficiency is “identical” for both directions of operation. It reaches values of almost 97% for power levels above 10 kW. Below 10 kW, the converter efficiency decreases which is a typical behaviour of power converters. This behaviour is caused by contributions of the power loss that are independent from the load such as core losses for example. The minimal power loss at low load is restricted by a minimal circulating current of the converter (current of the main transformer inductance) and the transformer core loss. The efficiency of 82% was measured at the power level of 1.2 kW. The efficiency values and the efficiency curve shape confirm that the Trench-FS IGBT modules and ZVS Quasi-ZCS topology are a good combination and that efficiencies close to 97% can be obtained.

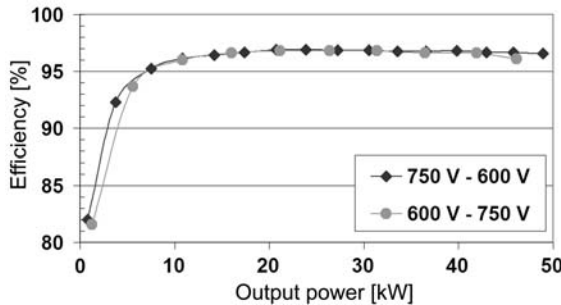


Figure 2-44: Measured efficiency curves for both directions of operation

2.8 Conclusions

An optimal current waveform was proposed in this chapter in order to improve the high frequency operation of power converters. The waveform exhibits ZVS at turn-on and Quasi-ZCS at turn-off. Output Filter Resonant Converter (OFRC) is selected for further application because it seems to be very suitable to high-power applications where the power flow control is not required.

The analysis of OFRC topology showed that the resonant circuit parameters did not have any influence on the conduction loss but they had a great influence on the switching loss. A linear relation was observed between the switching loss and the resonant frequency. In the case of the resonant impedance, the switching loss was shown to decrease non-linearly with increasing the resonant

impedance. On the other hand, the reverse-recovery loss of the rectifier diodes remained constant with varying the resonant impedance. With respect to the resonant frequency, the same linear relation was observed as for the switches. This means that the resonant impedance should be high if low power losses are of main concern.

Controllability of the output voltage and power flow was identified as the limitation of OFRC topology. Conventional voltage control techniques result in a loss of Quasi-ZCS operation and in increased switching losses. A solution to this problem was proposed for applications which require partial voltage control. Several solutions were discussed briefly.

The ability of OFRC topology to attain low power loss and hence high efficiencies was demonstrated by measurements on Converter Demonstrator I. Trench Field-Stop IGBT was selected for ZVS Quasi-ZCS applications. Implementation of this device in the converter demonstrator resulted in the converter efficiency up to 97% in a broad load range. The results of the measurements demonstrate that the ZVS Quasi-ZCS approach is suitable for high-power applications where voltage control is not required. The suitability of OFRC topology for bi-directional operation was demonstrated as well by measurements on the converter demonstrator.

Chapter 3 *High Power Density in Power Magnetics*

3.1 Introduction

A designer of high-frequency power-magnetics faces the challenge of addressing the issues of electromagnetic core and winding design along with the thermal design. At the same time, the final design must meet other special requirements like for example spatial and isolation.

This chapter considers high-power-density design of high-power magnetic components. Firstly core materials and winding technologies are discussed, while bearing in mind their thermal and electromagnetic properties. Next, transformer shape optimisation, new winding technologies and integration of the resonant inductance into the transformer are introduced in order to increase the transformer's power density. Specifics of the filter inductor design are also considered. The chapter is concluded by a presentation of the prototypes and measured results.

3.2 Magnetic Materials

Ferrite cores dominate the market of magnetic cores for power electronic applications. Until a few years ago, these were the only cores that could cope with low power loss requirement at high frequencies. Ferrite materials exhibit high electrical resistivity and thus do not need to be laminated to minimise the eddy current loss [6]. Isotropic properties allow flux to travel in any direction, and the range of core shapes is far greater than that for laminated and tape-wound cores. The limitations of ferrites are: large variations of properties with temperature, low Curie temperature and low saturation flux density.

Cores made of polycrystalline alloys cannot compete with ferrites even at frequencies as low as a few kHz. High-frequency operation results in high eddy current losses due to their low electrical resistivity [6]. For this reason they are almost never used in high-frequency applications. The classic use of these materials is in magnetics for the frequency range from 50 Hz to 400 Hz. In this range they benefit from their high saturation flux densities and high permeabilities.

Good properties of polycrystalline alloys can be exploited in a powder form by mixing them with resin fillers. Such materials offer low losses at high frequencies because the resin isolation between the powder particles prevents eddy currents and creates a "distributed air gap". The distributed air gap and associated low permeability can be very well used in power inductors [34], but for transformers a high permeability is often required.

In the 1980s a group of core materials called amorphous alloys became available on the market. The development of these materials in the last decade led to an improvement of their properties which resulted in wider use in power electronics. The amorphous molecular structure is obtained by rapid cooling of very thin layers of molten material which prevents formation of a crystalline structure. Because of this structure, amorphous alloys have electrical resistivity that is much higher than that of the equivalent polycrystalline alloys. The cores are wound of a strip of material of only several tenths of micrometers thick, which results in laminated cores. The core lamination and the high resistivity

yield eddy current losses which are much lower than in polycrystalline alloys. Because of this, they can be used at considerably higher frequencies. Figure 3-1 shows the losses of Vitroperm amorphous alloy and of 3C91 ferrite material. According to the presented data, the amorphous material exhibits equivalent or lower losses than the ferrite. This makes the amorphous cores usable in the same applications as ferrites. Another fact is that amorphous cores have much better thermal properties than ferrites. They can operate at higher temperatures [35] because of their high Curie temperature. Also, the thermal conductivity of amorphous cores is higher than that of ferrites. Typical thermal conductivity of MnZn ferrite is in the range of 4 W/mK, whereas for amorphous cores this is 9 W/mK in the direction perpendicular to the laminations and even higher in the direction of the laminations.

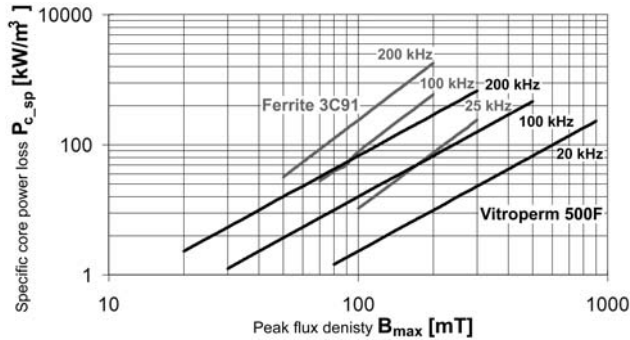


Figure 3-1: Comparison of power loss in Vitroperm 500 F amorphous metal and in ferrite 3C91

High-power-density design of high-power converters requires special properties from the core material. The discussion on materials above shows that excellent thermal properties, high permeability, high saturation flux density and low eddy current losses make amorphous cores very suitable for the considered application. Vitroperm 500F, the amorphous material of Vacuumschmelze, was chosen as the transformer core material for the applications considered in this thesis.

3.3 Winding Technologies

Winding design is a compromise between effective utilisation of available winding space, low eddy current losses, good thermal properties, adequate electrical isolation and easy manufacturability. The characteristics of standard winding technologies are reviewed here shortly. The winding properties are considered with respect to application in high-power-density high-power converters.

The two main technologies of winding construction are barrel and planar windings (Figure 3-2). Barrel windings are based on layers of conductors parallel to the winding axis. With planar winding technology, the winding layers are perpendicular to the winding axis.

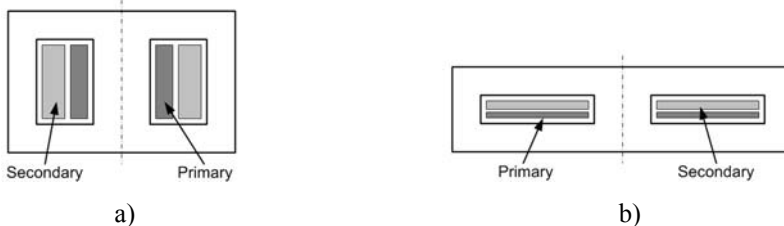


Figure 3-2: Diagram of a) barrel and b) planar winding constructions

Solid Wires (Round and Rectangular) are the most common form of conductors used for magnetic components with barrel windings. A major disadvantage of windings based on solid conductors is that their use is limited to relatively low frequencies because at high frequencies they exhibit high eddy

current and skin-effect losses [36]. Litz wires address the problem of eddy currents in high-frequency transformers by using isolated wire strands. This reduces the high frequency losses but the isolation of each strand and little contact between individual strands yield high thermal resistances and cooling of litz windings might be a problem. Foil windings are made from copper foil wound as a coil where each turn forms an entire winding layer. Isolation must be inserted between turns while the foil is wound. Thin foils are used to reduce the eddy currents, but the winding must be carefully designed so that the current distribution is uniform across the foil cross-section [37]. The thermal conductivity of the winding structure is high except in the direction perpendicular to the foil (because of isolation). Heat removing elements can be attached almost directly to the copper material itself which results in low thermal resistance between the winding's hot spot and a heatsink.

For planar windings, two main winding technologies can be distinguished: PCB windings [38] and Stamped windings (self-supporting planar copper winding). PCB technology uses relatively thin copper layer on a relatively thick board. Due to their properties, PCB-based windings are found almost exclusively in relatively low-power high-frequency applications. An alternative for high power is a planar technology based on stamped windings. Stamped windings can carry relatively high currents. The maximal power is limited by the ability to remove the heat from the windings in inner layers.

High power density requires a winding technology that combines low power loss with a good thermal performance. Choosing from the technologies briefly discussed in the paragraphs above, the foil winding technology seems like a natural choice. It offers relatively low high-frequency loss and good thermal performance. The major problem of this technology is the winding construction especially if more complex winding structures are required such as windings with multiple taps. Considering all advantages and disadvantages of the foil winding, and high power density being the main target of this thesis, the foil winding technology was selected as the most suitable for high-power high-power-density magnetics.

3.4 High-Frequency High-Power Transformer

A power transformer is an indispensable part of any power converter design that requires galvanic isolation or that has a high input to output voltage ratio. Typically, the transformer is also one of the most complex and bulkiest components of a power converter.

There are many publications on the designs of low-power transformers but only a few dealing with high-power transformers above 5 kW. The design process for low-power and high-power high-frequency transformers is similar in only certain respects. The difference results from the fact that the surface to volume ratio of high-power transformers is smaller with respect to the generated power losses. To deal with this, heat generation must be reduced and more effective thermal management must be implemented, as shown for example in [39] on a prototype of a coaxial transformer.

In the following paragraphs, the electromagnetic design of the transformer is considered, whereas the thermal management part of the design is discussed in Chapter 4. The electromagnetic design concerns: transformer function, shape optimisation, winding technology and transformer implementation. The main objective of the electromagnetic design is a transformer construction which is functional and exhibits low power losses and high power density.

3.4.1 Volumetric Optimisation of the Transformer Structure

For years, transformers have been made with more or less standard shapes. The shapes are defined by the manufacturers of transformer cores. These standard cores are available in numerous shapes and sizes, which are typically optimised for minimal overall power loss of the transformer. Designers usually design the core for specific transformer parameters (power, frequency, voltage, current, etc.) and then choose a core from a catalogue of one of the manufacturers.

The question of the core shape arises when the main criterion of the design is not the power loss but the power density. Making the transformer slim and long or thick and short are possibilities which

yield transformer structures of different volumes. With respect to conventional core types used in high power (E, C, U, etc.), it is possible to vary core dimensions in all three axes: x, y and z. Scaling in these three axes would in case of a generic core shown in Figure 3-3 result in changing the width of the central core leg w_c (x axis), depth of the core d_c (y axis) and height of the winding w_w (z axis). The objective is to find dimensions that give the smallest volume for a given power.

Some of the core dimensions are coupled in the transformer design as follows:

- core cross-section A_c of the core legs is fixed by the nominal power of the transformer, $w_c d_c = \text{const}$
- cross-section of upper part of the core and of the side legs is equal to half of the centre core leg cross-section, which implies $H_{ct} = w_w + w_c$,

In the core volume study, core leg width w_c , the core height H_{ct} and the core depth d_c are changed simultaneously. The core height H_{ct} follows from the winding width w_w : $H_{ct} = w_w + w_c$.

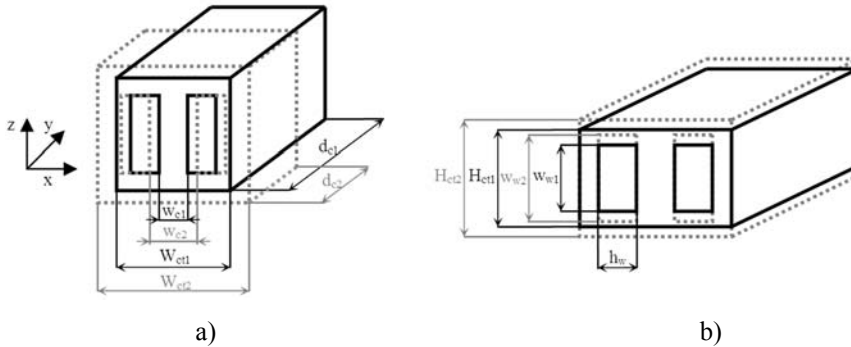


Figure 3-3: Transformer scaling options; a) varying the core leg width and core depth, as a consequence also the core height varies; b) varying the winding height

The transformer volume and losses are calculated as a function of geometrical parameters. The volume is approximated by assuming a box-like shape of the transformer:

$$V_{Tr} = 2(w_c + h_w)(w_w + w_c)(d_c + 2h_w), \quad (3-1)$$

The winding losses are calculated according to the methods described in paragraph 3.4.3. The specific core losses P_{c_sp} are calculated by using standard Steinmetz equation (3-2).

$$P_{c_sp} = k(f_s)^\alpha (B_m)^\beta, \quad (3-2)$$

where k , α , β are material constants, f_s is the operating frequency and B_m is the peak flux density. The material constants were estimated for Vitroperm 500F material from its datasheets as: $k=2.7 \cdot 10^{-7}$, $\alpha=\beta=2.1$. Multiplying the specific losses by the volume of the core results in the total core losses.

The results of the analysis are plotted in Figure 3-4. The figure depicts the variation of volume ΔV_{Tr} and power loss ΔP_{Tr} with respect to the core leg width w_c . The core area A_c and the winding hot-spot temperature T_{w_max} are kept constant for all investigated configurations. The winding width w_w changes with the core leg width w_c to maintain the winding hot-spot temperature T_{w_max} constant. The temperature T_{w_max} was calculated by assuming the heat-removal concept as discussed in Chapter 4.

As can be seen, the standard core (OK48b from Vacuumschmelze) is positioned in the area where the overall transformer loss is the lowest. This confirms the core shape optimisation for the low power loss by the core manufacturer. The transformer loss increases for the core leg width w_c decreasing primarily because of longer windings and hence higher winding losses. For the higher core leg width w_c , the core loss remains almost constant because the reduction of the winding loss due to shorter windings is compensated by the higher core loss due to a larger core volume. The figure also shows

that the transformer volume exhibits a minimum for a certain core leg width w_c . The volume increases on the left of the optimum primarily because the heat-removal area of the windings must increase in order to keep the hot-spot temperature constant. On the right of the optimum, the volume increases because of ratios between the core dimensions. In order to obtain the highest power density, slim and elongated transformer shape is selected for the design considered in this thesis. This shape results in approximately 25% reduction of the transformer volume V_{Tr} and only 3% increase of the power loss P_{Tr} in comparison with a transformer based on the standard core.

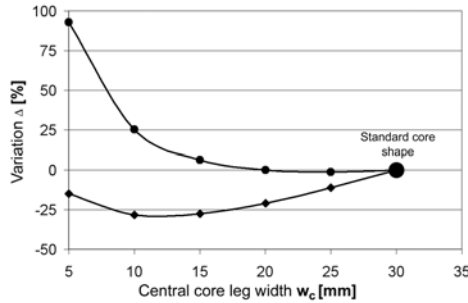


Figure 3-4: Variation of transformer volume ΔV_{Tr} and transformer power loss ΔP_{Tr} with respect to core leg width w_c ; core cross-section A_c and winding hot-spot temperature T_{w_max} assumed constant

3.4.2 Foil Winding Technology for Transformer Windings

Conventional Foil Winding without Interleaving

Foil winding technology is proposed in this thesis for high-power transformers because it offers the possibility of low winding loss and at the same time also good heat-removal properties. Skin effect and proximity effect are the main contributors to the power loss of the foil-based transformer windings. The thickness of the foil can be adjusted to cope with the skin effect [6], but it is harder to deal with the proximity effect. The proximity effect is related to the magnetic field strength in the winding window, which has a maximum on the boundary between the primary and secondary. This is illustrated in Figure 3-5, which depicts the magnetic field intensity and current density simulated by FEM.

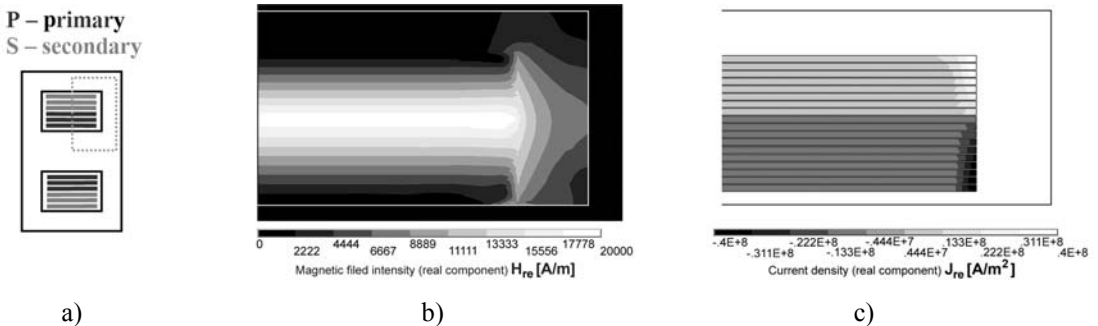


Figure 3-5: Magnetic field intensity and current distribution in conventional foil windings; a) transformer cross-section, dotted line indicates the winding sections displayed in figures b and c, b) real component of magnetic field intensity H_{re} , c) real component of current density J_{re}

As can be seen (Figure 3-5b), the field is very strong on the boundary between the primary and secondary. This is reflected in the current density distribution (Figure 3-5c), where the current density is increased in several foils next to the boundary (not visible in the figure due to strong edge effect). The edge effect, current density increase at the edges of the foils, is strong due to a high magnetic field component perpendicular to the foils.

Conventional Interleaving

Conventional interleaving reduces the magnetic field in the windings and hence also the power loss. The interleaving is based on “sandwiching” layers of primary and secondary. Figure 3-6 illustrates H field distribution for several cases of interleaving. Case a) represents a winding not interleaved at all and case c) a winding with two primary and three secondary sections. The disadvantage of the interleaving is that the foil winding construction becomes complicated with increased interleaving because of the many taps that are required. Also, the field strength for a high level of interleaving might not be enough to realise high leakage inductance values that may be required in certain converter topologies. It must be also stated that the primary to secondary capacitance increases with the interleaving, which might result in EMC problems.

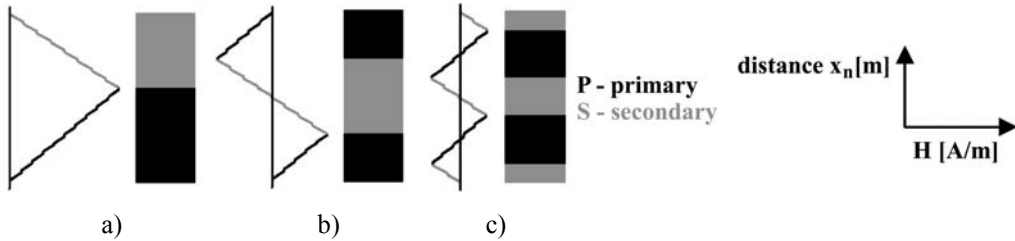


Figure 3-6: Examples of interleaved windings and related H field distributions

Partial Interleaving

An alternative to conventional interleaving is the so-called partial interleaving that was introduced by the author in [40]. This new method of interleaving foil windings offers the following features:

- reduced power loss due to field strength reduction
- simple windings without taps
- the possibility of tuning the field to reach higher values of the leakage inductance

The limitation of this method is that it is suitable only for transformers with a turn ratio close to one. The effect of the partial interleaving on the magnetic field strength decreases with the transformer ratio increasing or decreasing. Another disadvantage is that the increase of interleaving increases also the interwinding capacitance. The high interwinding capacitance might be harmful for EMC.

The principle of the partial interleaving is demonstrated in Figure 3-7. The idea of partial interleaving is similar to bifilar windings, where the wires of primary and secondary are wound together simultaneously. In partial interleaving, the foils are wound simultaneously in the interleaved winding section. The degree of interleaving can be adjusted by interleaving only several turns, like for example in Figure 3-7a, where the interleaving starts with the fourth turn. To define the interleaved winding portion, the so-called interleaving factor is defined as:

$$i_f = \frac{N_{\text{interleaved}}}{N}, \quad (3-3)$$

where $N_{\text{interleaved}}$ is the number of interleaved turns and N is the total number of turns. The arrangement of Figure 3-7 represents a winding with the interleaving factor of 0.6. Figure 3-8 shows the field strength and the current density plot for this configuration. As can be seen, both are reduced in

comparison with Figure 3-5 (without interleaving). According to FEM calculations, the power loss is reduced by as much as 65% in comparison to the windings without interleaving made of the same foil.

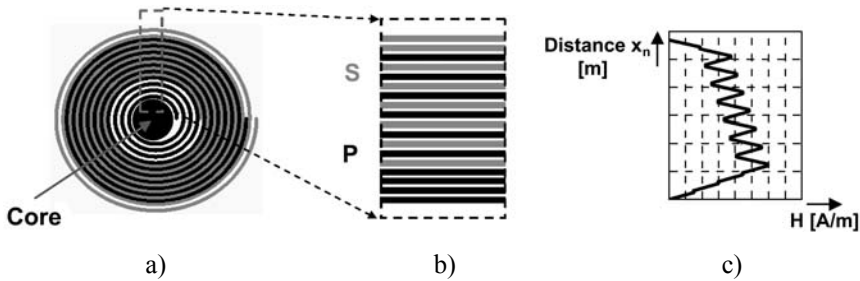


Figure 3-7: Partial interleaving with $i_f=0.6$; a) circular representation of the winding (in reality, the core cross-section is rectangular), b) cross-section of the winding, c) magnetic field distribution for $i_f=0.6$

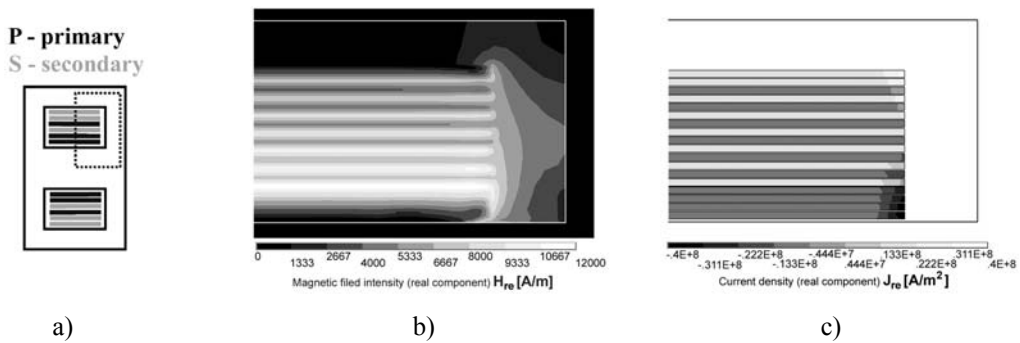


Figure 3-8: Magnetic field intensity and current distribution in windings with partial interleaving, $i_f=0.6$; a) a transformer cross-section, dotted line indicates the winding sections displayed in figures b and c, b) real component of magnetic field intensity H_{re} , c) real component of current density J_{re}

3.4.3 Losses in Transformer Foil Windings

Power loss calculation in windings of power magnetics is complex. One-dimensional analytical models are used as the first-order approach. The accuracy of these models is limited due to the 3D character of the magnetic fields in 3D magnetic components. In recent years, FEM simulations became widely used for the loss calculation in power magnetics. In spite of the ability of FEM to calculate the power loss in 3D components, this ability is seldom used and most of the implemented models are 2D models. The main difficulty with the 3D FEM models is their complexity and their demand for extensive computer resources. In order to have a fast tool for calculation of the losses in partially interleaved windings, the one-dimensional analytical approach is used in the following paragraphs.

The basis for the one-dimensional high-frequency loss calculations was established in 1966 by the study of Dowell [41]. The study was further expanded with respect to variety of winding configurations by several authors. The most recent addition is by Sullivan and Nun [42], which modifies the original method by adding two coefficients (calculated by FEM and tabulated in [42]) to Dowell’s function to better fit 2D FEM simulation results.

The mentioned methods deal with high-frequency power losses in windings excited by sinusoidal currents. It is assumed that the resonant current of zero-voltage-switching quasi-zero-current-switching topology is close to sinusoid and therefore the Dowell method can be used in its basic form. In the following paragraph, the Dowell method is applied to the partially interleaved windings. Analytical equations for the ac resistance with respect to the interleaving factor i_f are derived. The power losses of partially interleaved and non-interleaved windings are compared and conclusions are drawn.

Dowell Method for Partially Interleaved Windings

The method uses a one-dimensional approach to calculate the current density and flux linkage in each winding layer. These two parameters are used to calculate a resistive voltage drop and an induced voltage for each layer. The winding impedance and ac resistance are consequently derived from the voltage equations.

The partially interleaved winding essentially consists of three sections:

- non-interleaved primary winding section
- interleaved section
- non-interleaved secondary winding section

The sectioning is partly shown in Figure 3-7. The detail of the winding layers, field distribution and magnetic fluxes linked to the winding layers are shown in Figure 3-9.

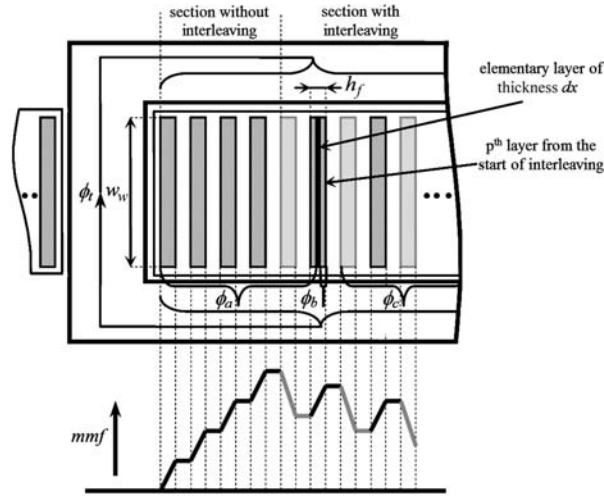


Figure 3-9: Part of the winding, indication of magnetic fluxes and associated mmf diagram

Consider the flux within the elementary layer of thickness dx in the p^{th} winding layer. The flux which influences this layer is the winding flux to the right of the layer. It can be seen from Figure 3-9 that this flux consists of the flux ϕ_c caused by the winding layers on the right of the p^{th} layer and of the flux ϕ_b caused by the remaining section of the p^{th} layer.

$$\text{elementary layer flux} = \phi_b + \phi_c, \quad (3-4)$$

The change of the elementary layer position by dx results in a change of the elementary flux by $d\phi$.

$$\frac{d(\phi_b + \phi_c)}{dx} = -\frac{d\phi}{dx}, \quad (3-5)$$

The flux of the elementary layer at position x is then calculated from:

$$|d\phi| = dxBl_t, \quad (3-6)$$

where l_t is the mean length of the elementary layer. The flux density B can be calculated from the field intensity as $B = \mu H$ where H is defined as:

$$\oint_c Hdl = \sum_n i_n, \quad (3-7)$$

The equations describing H for each section are derived based on the field distribution plot. The H field of the section without interleaving is described as in [41].

$$H(x) = \frac{1}{w_w} \left(I(p-1) + \int_0^x w_w J dx \right), \quad (3-8)$$

where per layer increase of the H field is represented by $I(p-1)$ and the increase of the H field within the layer itself ($0 < x < h_p$) by the integral of J . The H field of the interleaved section is given by:

$$H(x) = \frac{I}{w_w} \left(N(1-i_f) - 1 + p \left(1 - \frac{1}{n} \right) \right) + \int_0^x J dx, \quad (3-9)$$

where $IN(1-i_f)-1$ represents the H field at the beginning of the interleaved section, $Ip(1-1/n)$ represents the per-layer increase of the H field (n – transformer ratio, p – layer for which the increase is calculated) and the integral of J represents again the increase of H within the p -th layer itself.

By using equations (3-5), (3-6), (3-8) and (3-9), the current density and the magnetic flux of each layer are calculated. The current density is further used to calculate the voltage drop, whereas the magnetic flux is used to calculate the induced voltage in each layer. The resulting total voltage yields the winding impedance from $Z=V/I$. The winding ac resistance is finally obtained as the real impedance component. The complete derivation for non-interleaved sections is given in [41] and for the interleaved section in Appendix A. The final results are given below.

Non-interleaved sections are the same as used in [41], which means that the same equations are valid here. The ac resistance of such sections follows from:

$$R_{w_ac} = R_{w0} \left(M' + \frac{(m^2 - 1)D'}{3} \right), \quad (3-10)$$

where R_{w0} is the dc winding resistance calculated as:

$$R_{w0} = \frac{m \rho l_t}{w_w h_f}, \quad (3-11)$$

m is the number of layers in the non-interleaved section, l_t is the mean turn length, w_w and h_f are the width and thickness of the foil and M' and D' are calculated as:

$$M = \alpha h_f \coth(\alpha h_f), \quad (3-12)$$

$$D = 2\alpha h_f \tanh\left(\frac{\alpha h_f}{2}\right), \quad (3-13)$$

$M' = Re(M)$, $D' = Re(D)$ and $\alpha = \sqrt{\frac{j\omega\mu_0}{\rho}} = \sqrt{2j} \frac{h_f}{\delta}$ where δ is the skin depth of the winding.

The interleaved section contains only fully interleaved primary and secondary layers. From the equation for the ac resistance derived in Appendix A, two separate equations to calculate the winding resistances of the interleaved sections of the primary and secondary are derived:

$$R_{p_ac} = \frac{\rho_l}{w_w h_f} \left\{ m_p \left[M' + \frac{D'}{2} \left(m_p N_1 (1-i_f) - \frac{(m_p + 1)}{2} \left(1 - \frac{(4m_p - 1)}{3} \left(1 - \frac{1}{n} \right) \right) \right) \right] \right\}, \quad (3-14)$$

$$R_{s_ac} = \frac{\rho_l}{w_w h_f} \left\{ m_s \left[M + \frac{D}{2} \left(m_s N_1 (n - i_f) - \frac{(m_s + 1)}{2} \left(1 - \frac{(4m_s - 1)}{3} (1 - n) \right) \right) \right] \right\}, \quad (3-15)$$

where $m_p = m_s = N_1 i_f$.

Figure 3-10 depicts the normalised losses of partially interleaved windings calculated analytically and by FEM simulation with respect to the interleaving factor i_f for a model transformer with turn ratio $N_1/N_2=1.25$. As can be seen, there is a clear trend of loss reduction when the interleaving is increased. The winding loss is reduced by more than 60% when 60% of the primary winding is interleaved. The winding loss calculated analytically is slightly different from that calculated by FEM, and this is probably caused by simplifications made in the 1D field calculations. The differences between the results of the analytical method and the FEM simulation are within 10% of the normalisation base.

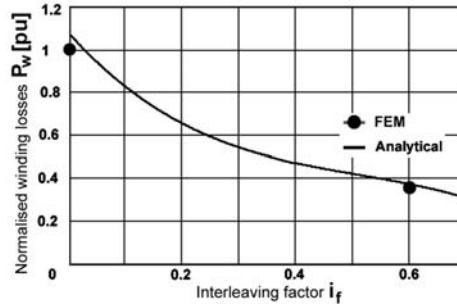


Figure 3-10: Normalised winding loss of partially interleaved winding versus interleaving factor i_f , comparison of analytical calculation and FEM, power loss calculated by FEM for non-interleaved winding is used as the base of normalisation

3.4.4 Leakage Inductance

In conventional converters, the transformer leakage inductance can cause voltage drops and overvoltages during circuit transients. Therefore, one of the goals of a typical transformer design is to minimise this inductance. On the other hand, many resonant converters use the leakage inductance as the resonant inductance and therefore it must have a specific value [43], [44]. The integration of the resonant inductance in the transformer is used because it improves the power density. The required leakage inductances are mostly in the range 10 – 100 μH depending on the implemented topology and design parameters. As mentioned in the previous paragraphs, weakening the magnetic field inside the winding window by interleaving the windings is one of the main methods for reducing the winding losses. The field-weakening counteracts realisation of high leakage inductance values because the leakage inductance is linked to the energy of the magnetic field, as described by (3-16).

$$\frac{1}{2} L_{leak} I_p^2 = \frac{1}{2} \int_{V_w} \mu H^2 dV, \quad (3-16)$$

Special measures will be considered to increase the leakage inductance by increasing the field energy.

Three basic methods of increasing the leakage inductance are:

- loops between the primary and the secondary winding [44], [45] (Figure 3-11 a)
- auxiliary core between the primary and secondary [44] (Figure 3-11 b)
- magnetic material in the winding area [46], [47] (Figure 3-11 c)

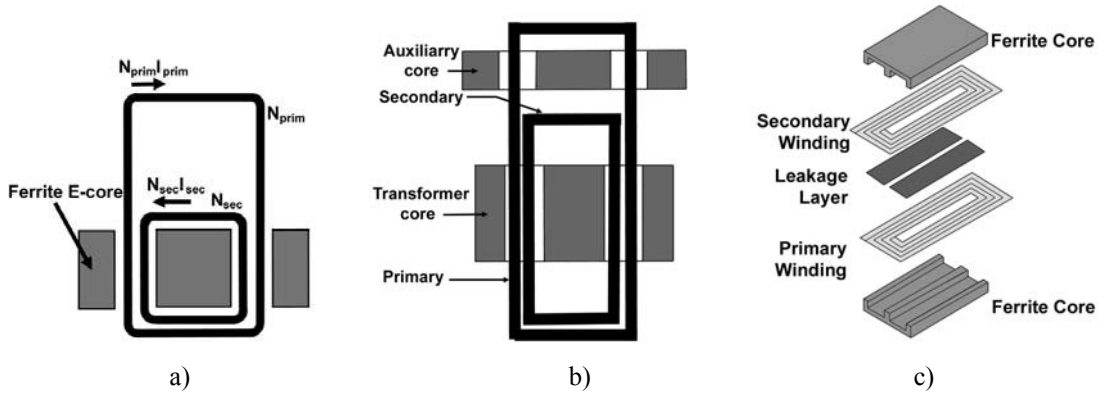


Figure 3-11: Methods to increase transformer leakage inductance; a) adding loops between the primary and secondary windings, b) placing an auxiliary core between the primary and secondary windings, c) placing a magnetic material in the window area between the primary and secondary windings [47]

The method of adding loops between the primary and secondary windings is based on the creation of an empty space between the windings outside of the transformer core. This loop reduces the coupling between the two windings which increases the leakage. The method of using the auxiliary core relies on creating an easier path for the flux in the leakage loop and hence increasing the leakage. The leakage inductance of this solution can be adjusted by an air-gap of the auxiliary core. With the third method, a layer of “high” permeability material is inserted between the primary and secondary windings. This so-called leakage layer forms a path with low reluctance for the magnetic flux and increases the field energy as follows from (3-16). The leakage inductance can be adjusted by modifying the thickness of the layer respectively by using a material of different permeability μ if possible. This method was applied up till now only in low-power planar-transformers.

The first two methods increase the overall transformer size substantially, while this is almost negligible with the third method. For this reason, using the leakage layer inside of the winding window seems to be the most suitable to obtain high power densities. Another aspect is that this method is fully compatible with the chosen foil-winding technology and the interleaving approaches.

Implementation of Leakage Layers in Foil Windings

The most effective location for the leakage layer is in spaces with a high magnetic field. The layer placement in the high field ensures the smallest possible volume of the layer and hence the highest power density for the particular winding configuration. Peaks of the magnetic fields are on the boundaries between primary and secondary windings. The leakage layer position on the boundary (Figure 3-12.) simplifies the winding assembly as well because the layer can be placed after finishing a particular winding section. Other aspects which must be considered for the placement of the leakage layer are:

- leakage layer material must not saturate under the peak field conditions
- leakage layer losses increase due to the high field intensity
- heat removal from the layer is a potential problem due to:
 - layer enclosed between the windings
 - relatively low thermal conductivities of available materials

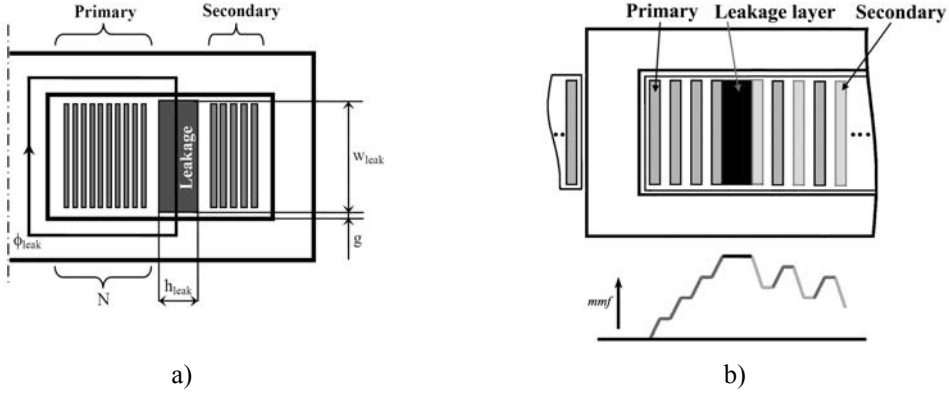


Figure 3-12: Implementation of leakage layer in a) conventional and b) partially interleaved windings

The relation between the dimensions of the leakage layer and the increase of the leakage inductance due to the leakage layer can be derived from (3-16). The equation can be rewritten as follows:

$$\frac{1}{2}(L_{leak_w} + L_{leak_layer})I_p^2 = E_{leak_w} + E_{leak_layer} \quad (3-17)$$

where L_w and L_{leak} are leakage inductances related to foils and leakage layer respectively and E_w and E_{leak} are associated energies. From (3-17) it can be determined that the leakage inductance gain due to the leakage layer is equal to:

$$L_{leak}I_p^2 = \mu H_{leak}^2 V_{leak} \quad (3-18)$$

where V_{leak} is the volume of the leakage layer. The field intensity in the leakage layer depends on the winding configuration. To calculate the field in the leakage layer location, geometry as shown in Figure 3-12a is used. It is assumed that the same leakage flux passes through the leakage layer and also through the air-gaps between the leakage layer and the core. Due to the presence of the air-gaps, the magnetic field intensity in the leakage layer is lowered and can be calculated as:

$$H_{leak} = \frac{H_g}{\mu_r} \quad (3-19)$$

where μ_r is the permeability of the leakage layer material. By solving the magnetic circuit formed by the air-gaps, the leakage layer and the core, the field intensity in the leakage layer can be derived as:

$$H_{leak} = \frac{NI}{w_{leak}(k_{leak}\mu_r + 1)} \quad (3-20)$$

where w_{leak} is the width of the leakage layer, μ_r is the relative permeability of the leakage layer material, N and I are the number of turns and the current flowing through the winding section generating the leakage flux ϕ_{leak} and k_{leak} is the ratio calculated as: $k_{leak} = 2g/w_{leak}$, where g is the air-gap length. The core field intensity was assumed to be equal to zero for this derivation. Substituting (3-20) and $V_{leak} = w_{leak}h_{leak}l_{leak}$ to (3-18) yields the leakage inductance per meter length:

$$L_{leak_sp} = \frac{\mu_0\mu_r N^2 h_{leak}}{w_{leak}(k_{leak}\mu_r + 1)^2} \quad (3-21)$$

This equation can be used as the first approximation in the leakage layer designs of windings without interleaving. Equation (3-21) is not valid for the windings where the leakage layer is placed at places other than the boundary between the primary and secondary windings. For such cases, a new equation must be derived. On the other hand, the same equation could be used also for the partially interleaved windings as shown in Figure 3-12b. The number of turns N would in that case be the number of turns of the primary section without interleaving and equation (3-21) transforms into:

$$L_{leak_sp} = \frac{\mu_0 \mu_r N^2 (1 - i_f)^2 h_{leak}}{w_{leak} (k_{leak} \mu_r + 1)^2}. \quad (3-22)$$

The relation between the leakage layer thickness h_{leak} and the interleaving factor i_f is shown in Figure 3-13. As can be seen, the plotted curve is non-linear which is due to the fact that the leakage inductance L_{leak} is proportional to $(1 - i_f)^2$.

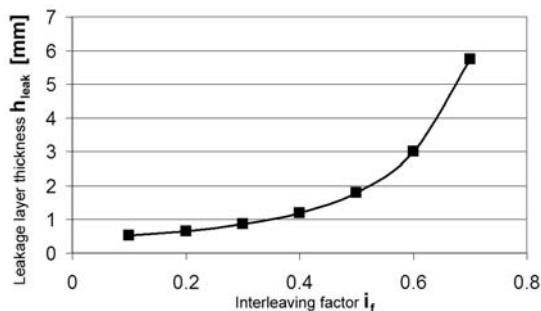


Figure 3-13: Leakage layer thickness as a function of interleaving factor i_f for leakage inductance of $3.4 \mu\text{H}$

From the above discussions, several requirements on the leakage layer can be concluded:

- low power loss \Rightarrow layer placed in the low field \Rightarrow thick layer (see Figure 3-13, influence of the field weakening by interleaving in the partially interleaved windings on the leakage layer thickness)
- high power density \Rightarrow thin layer
- good heat removal from the layer \Rightarrow thin layer
- leakage inductance should have a specific value

As can be seen there is a conflict between the requirement of the low power loss and the other requirements. In the final design, the leakage layer must be optimised to satisfy all four requirements.

Materials Suitable for Leakage Layer

The main requirements on the leakage layer material are:

- flexibility or mould-ability – to wind the material on top of the windings or to mould it in prepared cavities
- high saturation flux density – to place the material in high fields and hence reduce the thickness of the layer
- low losses – to minimise the loss generated inside of the winding structure
- high thermal conductivity – to remove the heat from the layer effectively

Only a few manufacturers of the materials suitable for the use as the leakage layer were identified. In the selection of materials, primarily flexibility and mould-ability of the material were the main criteria. The identified materials are listed in Table 3-1. Most of these materials are not commercially available but only as experimental samples. The only commercially available material is FPC of Epcos which is

primary intended for application in EMI and EMC. Due to the experimental character of the materials and different primary applications, there is limited information available regarding the use of these materials in power magnetics.

Table 3-1: Materials suitable for leakage layer

	FPC	SFC	KPF30	VITROPERM flakes
Permeability	9	~10	~30	20-40
Thickness [mm]	0.2 / mould-able	1.15	1	mould-able
B_s [T]	0.255	---	---	0.6-0.9
T_{max} [°C]	120	---	---	150
Supplier	Epcos	Kaschke	Kaschke	Vacumschmelze
Comment	Flexible / mould-able	Flexible	Substrate	Powder

Winding Losses and Leakage Layer

A leakage layer placed inside the winding window enhances the leakage inductance by increasing the leakage flux in a specific area. On the other hand, the leakage layer affects the H -field in the areas where it can be detrimental to the winding losses as well.

To assess the influence of the leakage layer on the winding losses, several FEM models (Table 3-2) were constructed. The FEM approach was chosen because it would be difficult to calculate the detailed field distributions and related winding power loss by using analytical methods. Winding configuration and design specifications of real transformer prototype were used to build the models. The only differences between the models are concerning the properties and shape of the leakage layer. The same models are used also to assess the power loss in heat pipes which are implemented in the transformer for heat removal from the windings (see Chapter 4).

The models for different configurations of the leakage layer, and the calculated H field distributions and losses are shown in Table 3-2. For better comparison of different field plots, configurations b) to d) are displayed with the same range of field intensity H . The consequence is that the values which are out of scale are displayed as grey (see Table 3-2b field plot).

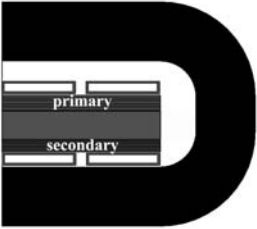
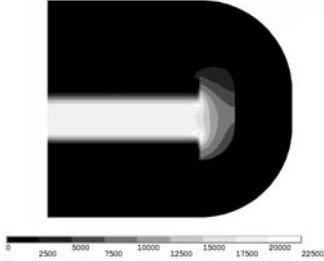
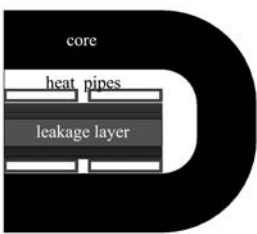
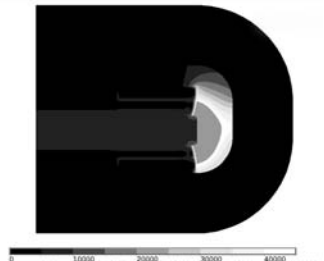
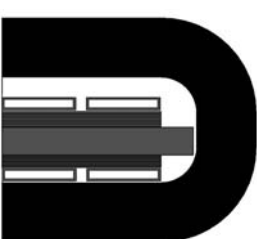
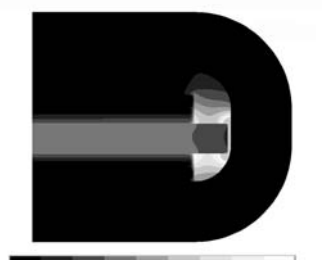
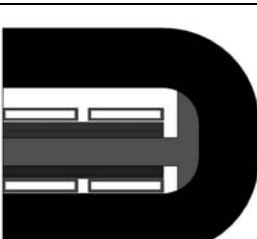
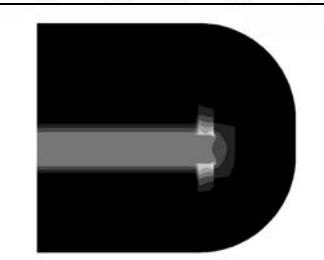
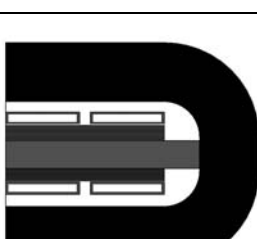
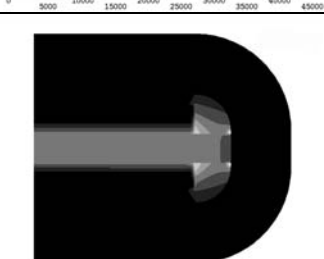
Configurations shown in Table 3-2a and b represent the insertion of the leakage layer into the winding window and its contribution to the winding losses. As can be seen, the insertion of the layer increases the field intensity especially in the edge winding region. The consequence is more than six fold increase of the winding losses and an even larger increase of the losses in the heat pipes.

Possible counteractions to the increase of the power loss were investigated in the cases c, d, and e. It is shown that even a simple extension of the leakage layer beyond the edges of the foils has large effect on the winding losses. By doing so, the area of strong magnetic field is moved away from the foil edges (Table 3-2c) and the winding power loss drops. Case d) gives the best results from the loss point of view but on the other hand, the structure of the leakage layer is much more complex than in the other cases. Therefore a simpler structure that would give a similar result is needed.

The simpler and more practical solution is shown in Table 3-2e. In this case, a simple bar like leakage layer extended all the way to the core resulted in very small air-gaps between the leakage layer and the core. The power loss is only approximately 6% higher than for the configuration d) while the layer is much simpler.

The investigation showed that terminating the leakage layer directly in the core (Table 3-2e) yields a large reduction of the winding loss. The reduction in comparison with the case of the identical foil and leakage layer width (Table 3-2b.) is as high as 80%. The presented results are for the windings without interleaving but similar results were observed for the partially interleaved windings.

Table 3-2: Leakage layer and its influence on field distribution and winding losses, winding without interleaving

Description	Geometry	H_{re} – field [A/m]	Results
<p>a)</p> <ul style="list-style-type: none"> - $\mu_{leakage}=1$, effectively without leakage layer 			<p>P_w: 160.4 W/m \Rightarrow 105.9 W P_{HP}: 9.6 W/m \Rightarrow 3.84 W L_{leak}: 26.7 μH/m \Rightarrow 5.3 μH</p>
<p>b)</p> <ul style="list-style-type: none"> - leakage layer aligned with windings 			<p>P_w: 1028.16 W/m \Rightarrow 678.6 W P_{HP}: 185.6 W/m \Rightarrow 74.2 W L_{leak}: 143.4 μH/m \Rightarrow 28.7 μH</p>
<p>c)</p> <ul style="list-style-type: none"> - extended leakage layer - air-gap 0.5 mm 			<p>P_w: 248.8 W/m \Rightarrow 164.2 W P_{HP}: 69.3 W/m \Rightarrow 27.7 W L_{leak}: 256.4 μH/m \Rightarrow 51.3 μH</p>
<p>d)</p> <ul style="list-style-type: none"> - leakage layer filling the end winding space 			<p>P_w: 184.15 W/m \Rightarrow 121.5 W P_{HP}: 12.3 W/m \Rightarrow 4.9 W L_{leak}: 294 μH/m \Rightarrow 58.8 μH</p>
<p>e)</p> <ul style="list-style-type: none"> - extended leakage layer - gap 0.05 mm 			<p>P_w: 195.1 W/m \Rightarrow 128.8 W P_{HP}: 32.3 W/m \Rightarrow 12.9 W L_{leak}: 279.6 μH/m \Rightarrow 55.9 μH</p>

3.5 Filter inductors

In switching circuits, a filter is needed in order to prevent high-frequencies from penetrating into the outer world. The filter as shown in Figure 3-14 is used. It consists of an inductor L_f to filter high-frequency currents and a capacitor C_f to stabilise the voltage. The capacitor C_f is not considered to be a part of the converter presented in this thesis because it is a filter capacitor typically required by a rectifier or an inverter connected to the dc-dc converter.

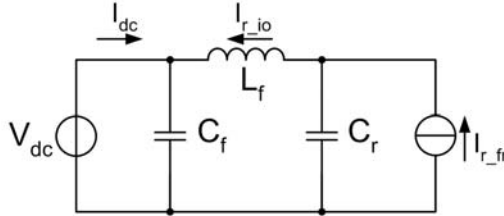


Figure 3-14: Configuration of the C-L-C filter in ZVS Quasi-ZCS converter topology

Requirements of the filter inductors on the cores and windings are in principle the same as in the transformer design. For the same reasons as for the transformer, amorphous core material and foil winding technology were chosen for the filter inductors.

Easy spatial integration of the filter inductors with the transformer and the rest of the converter is another requirement. The consequence of this requirement is that the inductors must have a similar profile as the transformer or have a profile which is easy to integrate in the proposed converter concept. In the prototypes presented in this thesis, the same core size and shape was chosen for the filter inductors as for the transformer. As will be shown later, integration of such design together with the transformer is easy.

Due to the spatial integration requirement, the optimisation of the inductors regarding the power loss is restricted by the selected core shape and size. The winding is designed such, that it occupies a maximal available space in the winding window and the cores operate with a maximal possible flux density. These constraints allow only the variation of the foil thickness and of the number of turns. The core air-gap must be adjusted for each winding configuration in order to prevent saturation. The change of the foil thickness in a restricted winding space results in an inductance variation and hence also in variation of the filter ratio $k_f = I_{r_fs} / I_{r_io}$, where I_{r_fs} is the ripple of the resonant current (ripple source) and I_{r_io} is the current ripple penetrating through the filter inductor. By considering the capacitance C_f large enough that its high-frequency effects can be neglected and by making high-frequency voltage drops across the filter inductor L_f and resonant capacitor C_r equal, following equation can be written:

$$I_{r_fs} \frac{1}{\omega C_r} = I_{r_io} \omega L_f \quad (3-23)$$

This equation is used to derive a description of the relation between the filter ratio k_f and the foil thickness h_f .

The inductance L_f can be calculated as:

$$L_f = \frac{N k_c A_c B_m}{I_{\max}}, \quad (3-24)$$

where N is the number of turns, k_c is the core factor, A_c is the core cross-section, B_m is the peak flux density in the core and I_{\max} is the peak current in the windings. Substituting $N = k_{fill} A_w / w_w (h_f + h_i)$ for the number of turns results in:

$$L_f = \frac{k_{fill} k_c A_w A_c B_m}{w_w (h_f + h_i) I_{max}}, \quad (3-25)$$

where A_w is the winding window area, k_{fill} is the copper fill factor with considering also the cross-section reduction due to the placement of a heat removal element (see Chapter 4) w_w is the winding width, h_f and h_i is the foil respectively isolation thickness. Substituting (3-25) into (3-23) yields:

$$k_I = \frac{I_{r_fs}}{I_{dc}} \left(\frac{\omega_r^2 C_r k_{fill} k_c A_w A_c B_m}{I_{r_fs} w_w (h + h_i) I_{max}} - 1 \right). \quad (3-26)$$

where ω_r is the resonant frequency. Considering that I_{r_fs}/I_{dc} ratio for the ZVS Quasi-ZCS current waveform equals to approximately 2 results in the following equation:

$$k_I = \frac{\omega_r^2 C_r k_{fill} k_c A_w A_c B_m}{w_w (h_f + h_i) I_{dc}} - 2, \quad (3-27)$$

As can be seen from (3-27), the relation between the current ratio k_I and the foil thickness h_f is an indirect proportion. The relation is plotted in Figure 3-15. The curves for the input and output inductors are obtained by considering appropriate dc currents I_{dc} and resonant capacitor values C_r .

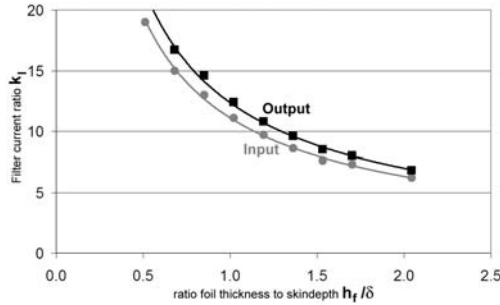


Figure 3-15: Current ratio $k_I = I_{r_fs}/I_{r_io}$ versus foil thickness for filter inductor windings; $\delta =$ skin depth

Winding losses in the filter inductors are also linked to the foil thickness h_f . The winding loss can be split to dc and ac loss as follows:

$$P_{w_lf} = R_{dc} I_{dc} + R_{ac} \frac{I_{r_fs}}{k_I}, \quad (3-28)$$

As mentioned above, the ratio I_{r_fs}/I_{dc} for the ZVS Quasi-ZCS current waveform equals to approximately 2. By substituting this into equation 3-28, it can be derived that the winding losses in relation to the foil thickness h_f follow from:

$$P_{w_lf} = R_{dc} I_{dc} \left(1 + \frac{2 R_{ac}}{k_I R_{dc}} \right), \quad (3-29)$$

where the resistance ratio R_{ac}/R_{dc} as well as the current ratio k_I are functions of the foil thickness h_f . Figure 3-16 shows the relation between the winding loss of the input and output inductor with respect to the foil thickness. The high frequency winding loss was approximated by using the R_{ac}/R_{dc} relation published in [6]. The effects of the air-gap field fringing were neglected.

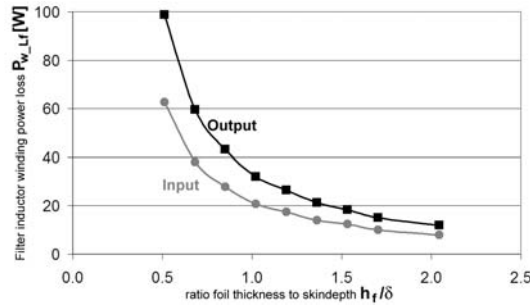


Figure 3-16: Winding loss of filter inductors versus relative foil thickness; δ = skin depth

As can be seen from Figure 3-15, the current ratio increases with the decreasing thickness h_f . On the other hand, Figure 3-16 shows that the power loss increases as the foil thickness decreases and for the foil thickness smaller than the skin depth, the loss curve becomes rather steep due to a high dc resistance. Therefore, the filter specifications must be reviewed with respect to these facts. The filter specifications considered in this case are input and output current ripples less than 10% of the resonant current. The foil thickness equal to the skin depth δ (0.3 mm) was chosen as it offers acceptable power loss and complies with the current ripple specifications.

3.5.1 Filter Inductor Design – Power Loss Calculation

As discussed in paragraph 3.4.3, 2D FEM models are typically used for final power loss calculations of complex 3D magnetic components. A 2D approach to a 3D problem is usually based on modelling a single or multiple 2D cross-sectional cuts of a 3D object. A basic 2D model uses a cross-section through the winding window. Such model suits especially to components with rotational symmetry or with long cores but in many cases it is also used for rotationally asymmetric and short components. In such cases, it is assumed that the losses in the end winding sections are either negligible or similar to the losses in the winding sections placed inside of the winding window. The approach with the single cut can not be used in the case of the filter inductor design presented in this thesis. The reason for this is that the conditions inside the winding window and in the end winding sections are different due to the air-gaps. The air-gap fringing is illustrated in Figure 3-17 which shows a horizontal cut of the inductor structure through the air-gaps. As can be seen, the winding sections placed inside the winding window are exposed to the fringing field of two air-gaps (centre and outer core leg) whereas the end winding sections intersect the field of only one air-gap (centre core leg). For this reason, separate models were constructed for both sections.

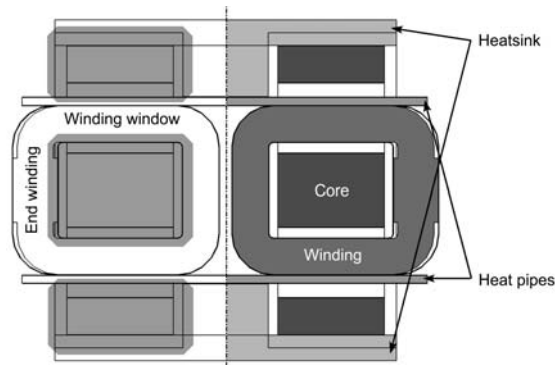


Figure 3-17: Horizontal cut through the inductor structure; left inductor – illustration of air-gap fringing (grey areas), right inductor – definition of structural parts

To model the winding window cross-section, a standard model as shown in Figure 3-18 was used. The model included heat pipes and a heatsink section in order to calculate the losses in these parts as well. The calculation of losses in these components is important because they are made of highly conductive materials and they are also exposed to the fringing field of the air-gaps.

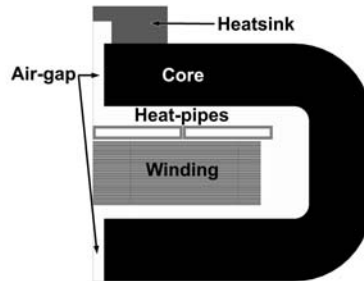


Figure 3-18: FEM model of inductor structure; cross-section of winding window

The model of the end winding section uses a new approach to the end winding simulation. The model is shown in Figure 3-19. As can be seen, the model consists of two windings, the core and the air-gap. This model should in principle contain only the inductor winding, a core slab next to it and the air-gap. Using such model would result in proper simulation of the field generated by the end winding section but the air-gap fringing would be neglected because the core would not be properly excited by only the end winding section. In order to provide a proper air-gap excitation, which is in real inductor provided by the winding section placed in the winding window (not visible in the model) the excitation winding was included in the model. The function of this winding is to properly excite the air-gap fields and by doing this, to include the air-gap fringing effect in the field and loss calculations. Both models shown in Figure 3-19 are simplified by using the symmetry of the inductor structure. Only one quarter of the structure is modelled.

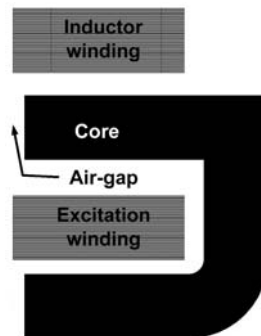


Figure 3-19: FEM model of inductor structure; cross-section of end winding

The results of FEM simulations for the input filter inductor are shown in Figure 3-20 and Figure 3-21. As can be seen, the fringing of the magnetic field in the air-gap area is substantial. The plots of current density show clearly the effect of air-gap fringing on the winding, heat pipes and the heatsink section. The result is an increase of the winding losses and the eddy current losses in the heat pipes and the heatsink. From the calculated losses, it can be concluded that the power loss generated in the elements of thermal management is approximately 9% of the total inductor power loss. This power loss is relatively small and it can be easily removed from these parts. Comparing the total power losses in the winding window and in the end windings reveals that the first generates approximately 70% higher power loss per meter.

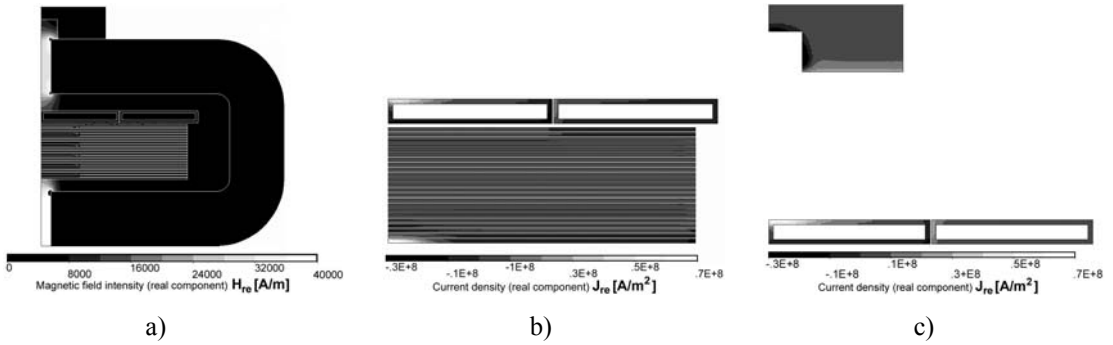


Figure 3-20: FEM results of winding window of input filter inductor; a) H field distribution, b) Current density distribution in winding and heat pipes, c) eddy currents in heat pipes and heatsink section

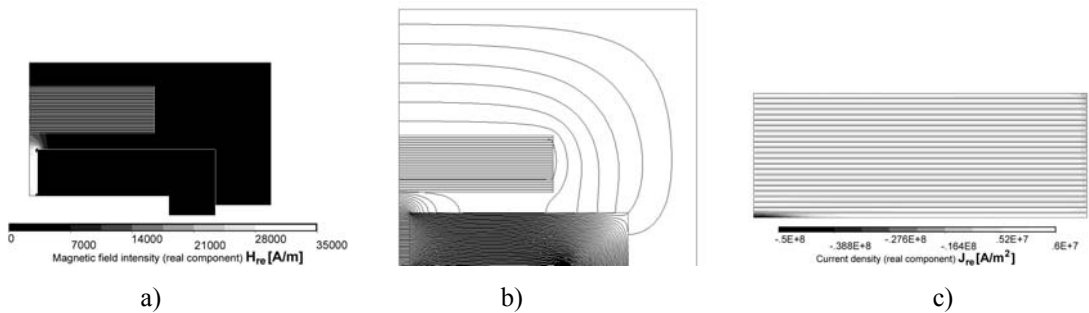


Figure 3-21: FEM results of end winding section of input filter inductor; a) H field distribution, b) 2D field lines, c) Current density distribution in windings

3.6 Results of Practical Experiments

3.6.1 Practical Implementation and Measurements on Transformer Prototypes

To verify and confirm the design assumptions and conclusions discussed in paragraph 3.4, four transformer prototypes were built. Each design is an improvement of its predecessor. Firstly, the prototypes are briefly introduced with main stress on their construction. Further, the results of the measurements and the experience with the construction of the prototypes are discussed. Special attention is given to successes and problems related particularly to the leakage layer and winding losses.

Core Design

The core design is based mainly on the datasheet information, primarily for the core loss estimation. The core consists of 8 custom made oval cores made of Vitroperm 500F amorphous material of Vacuumschmelze core manufacturer. The size and the shape of the single core were selected after discussions with the manufacturer. The drawing of the core is shown in Figure 3-22a. The full core arrangement for Converter Demonstrator I is shown in Figure 3-22b. The slim and elongated shape and the specific dimensions of the complete core are the results of the study discussed in paragraph 3.4.1. The core shape is optimised for the minimal transformer volume. Different arrangement of the cores is used for Prototype II of the transformer and further which is due to the implementation of a different thermal concept. Only the core arrangement is changed while the shape and the dimensions of the cores remain unchanged for all prototypes.

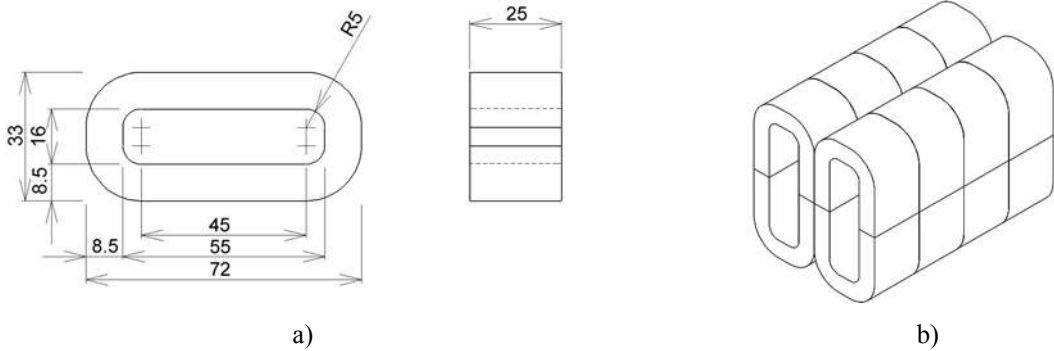


Figure 3-22: Transformer core; a) single core dimensions, b) assembly of 8 cores

Prototype I.

The partially interleaved winding structure and the leakage layer were used in Prototype I in order to reduce the winding losses and to reach the required value of the leakage inductance. The inductance value of $3.4 \mu\text{H}$ was chosen for the initial design. A relatively low leakage inductance value and a high resonant capacitance were chosen in Converter Demonstrator I in order to reduce the fluctuation of the voltage across the resonant capacitors and hence to reduce the size of the filter inductors. The leakage layer width is identical to the foil width. The identical widths were used because the effect of the leakage layer on the winding losses (paragraph 3.4.4) was not known at the moment of designing and construction of Prototype I. The FPC material of EPCOS was used as the leakage layer material. Further design details are listed in Table 3-3.

Table 3-3: Design parameters of Prototype I

Core material	VITROPERM 500F
Core cross-section	1700 mm^2
Operating frequency f_s	50 kHz
Peak flux density B_{max}	0.31 T
Primary turns (voltage)	10 (750 V)
Secondary turns (voltage)	8 (600 V)
Interleaving factor i_r	0.6
Foil thickness	0.25 mm
Foil width	45 mm
Leakage layer material	FPC
Leakage layer thickness	3.2 mm
Leakage layer width	45 mm
Leakage inductance	$3.4 \mu\text{H}$

Figure 3-23 shows the final design of Prototype I. Figure 3-23a depicts the detail of the central part of the leakage layer with description of the specific winding segments. The complete winding structure is shown in Figure 3-23b. As can be seen, the transformer and filter inductors were integrated in a single structure. This was done in order to increase the power density by integrating mechanical and thermal elements of the three components into a single structure.

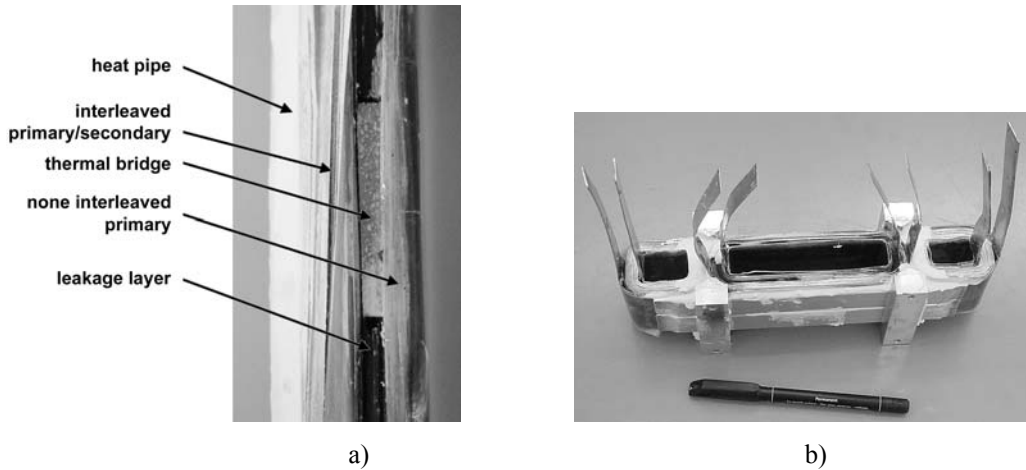


Figure 3-23: Transformer winding of Prototype I; a) detail of the central winding section with thermal bridge, b) view of the complete winding structure with integrated transformer and inductor windings

Prototype II.

Prototype II was constructed to resolve the problems of Prototype I observed during power measurements. The design parameters of Prototype II are listed in Table 3-4. The main change with respect to Prototype I is that Prototype II was designed for the operating frequency of 25 kHz (see section on power measurements) and for high leakage inductance. Optimisation of the foil thickness for the minimal power loss resulted in a foil thinner than in Prototype I in spite of the lower operating frequency. The thinner foil was required because the windings were implemented without interleaving which yielded a stronger magnetic field. The winding without interleaving in combination with a new leakage layer material were employed to reach the required high value of the leakage inductance. The new leakage layer material was a mixture of Vitroperm 500F powder and epoxy resin which was moulded under vacuum for removal of air bubbles. The advantages of this material in comparison with FPC used in Prototype I are: higher saturation flux density, higher permeability and possibly lower high-frequency losses. These properties should allow obtaining high leakage inductances in a dimensionally almost unchanged transformer structure.

Table 3-4: Design parameters of Prototype II.

Core material	VITROPERM 500F
Core cross-section	1700 mm ²
Switching frequency f_s	25 kHz
Peak flux density B_{max}	0.63 T
Primary turns (voltage)	10 (750 V)
Secondary turns (voltage)	8 (600 V)
Interleaving factor i_f	0
Foil thickness	0.15 mm
Foil width	45 mm
Leakage layer material	VITROPERM flakes + Epoxy
Leakage layer thickness	4 mm
Leakage layer width	45 mm
Leakage inductance	28 μ H

The required volume of the leakage layer was at first calculated using an estimated average permeability of the moulded Vitroperm material given by the material manufacturer. It is difficult to predict the exact permeability of the moulded material and therefore sample-bars were made prior to

moulding the complete leakage layer. The pre-assembled winding structure and the sample-bars were used to assess an approximate gain of the leakage inductance per centimetre length. Based on this experiment, it was found that the used combination of Vitroperm flakes and epoxy must completely fill the leakage layer space in order to reach the required leakage inductance of $28 \mu\text{H}$. The estimated permeability of the leakage layer material is 18.

The central part of the winding structure with integrated heat removal elements is shown in Figure 3-24a. The structure consists of secondary turns on the inside, primary turns on the outside and the leakage layer in between. The configuration with the secondary on the inside and the primary on the outside was employed in order to balance the power loss between the primary and secondary windings. The inner and outer winding surfaces were attached to heat pipes for better heat removal (inner heat pipes not visible in Figure 3-24a). For the same reason, ceramic plates were inserted in the central part of the leakage layer. Figure 3-24b shows the complete winding structure which was placed and tested in Converter Demonstrator II. Note that the transformer is not integrated with the filter inductors. This was done because the separate transformer and inductor structures fit the spatial organisation of Converter Demonstrator II better.

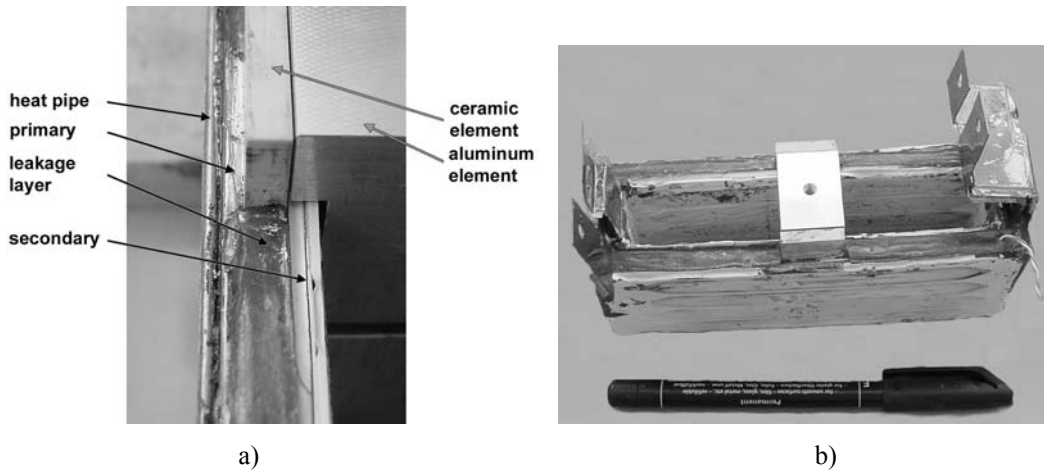


Figure 3-24: Transformer Prototype II; a) detail of central winding section, b) complete windings

Prototype III.

Prototype III was constructed without the leakage layer in order to better assess the overheating experienced with the windings of Prototype I and II (see section on power measurements). The design parameters are otherwise identical to Prototype II. The winding structure of Prototype III is shown in Figure 3-25. The heat removal structure was slightly modified to accommodate the new thinner windings. The external dimensions and shape of the transformer were kept the same so that the existing Converter Demonstrator II could be used for testing.

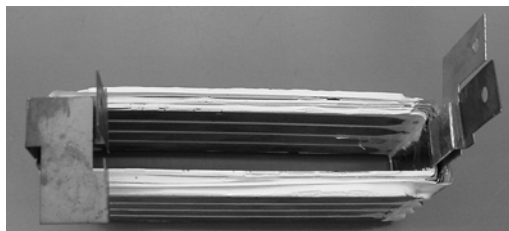


Figure 3-25: Winding structure of Prototype III – without leakage layer

Prototype IV.

Seeping of the leakage layer material into the transformer windings during the construction resulted in an isolation failure in Prototype II during the power tests (section on power measurements). A different leakage layer moulding technique was tested in Prototype IV to avoid the penetration of the material into the windings. The leakage layer was moulded separately from the windings in prepared moulds. The moulded leakage layer plates were then inserted in the windings during the winding construction. The moulded leakage layer plates together with the ceramic plates are shown in Figure 3-26a, whereas Figure 3-26b shows the complete winding structure. Prototype IV is the only prototype which implements the leakage layer extended beyond the edges of the foils. The leakage layer of Prototype IV spans the whole width of the winding gap which should ensure a tight fit of the leakage layer and the cores.

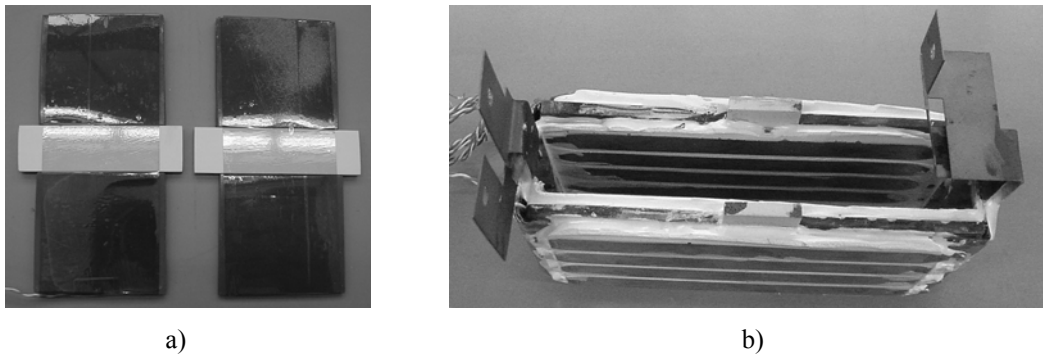


Figure 3-26: a) separately moulded leakage layer plates connected to ceramic elements, b) complete winding structure with inserted leakage layer and heat pipes attached

Small Signal Measurements of Parameters of Transformer Prototypes

The basic measured properties of the transformer prototypes are listed in Table 3-5. The measured leakage inductance of Prototype I is 8.5% smaller than calculated by FEM and 6.7% smaller than calculated by the analytical method. Prototype II and Prototype IV also reached leakage inductances close to the target value. In the case of the leakage layer made of Vitroperm material, the problem is to master the mixing and moulding process of the magnetic powder and epoxy in order to maintain stable permeability of the material. The results confirm that if a stable permeability is maintained, then the leakage inductance can be accurately predicted. The stable material also allows repeatability, which is important for industrial implementation.

Table 3-5: Measured parameters of transformer prototypes

	Prototype I.	Prototype II.	Prototype III.	Prototype IV.
Leakage inductance	3.2 μH	27.3 μH	1.48 μH	26 μH
Magnetising inductance	7 mH	2.2 mH	886 μH	226 μH
Capacitance primary-secondary	7.34 nF	1.48 nF	2.9 nF	560 pF

The values of the main inductance, which are also listed in the table, vary over a broad range. The reason for this is that the cores did not fit equally well with the different types of construction. Unnoticed impurities or inaccurate critical dimensions might have prevented the core from fitting. For example, in Prototype IV the lowest main inductance is obtained due to a skew leakage layer which prevented a proper closure of the cores.

As can be observed from Table 3-5, Prototype I has a large primary to secondary capacitance. This capacitance was caused by the interleaving strategy implemented in the windings. The consequence of a large primary to secondary capacitance is stress on the switching of IGBTs because the capacitance

must be discharged and charged prior to the voltage reversal across the driven winding. Another aspect is that the large capacitance creates an easy path for the circulation of common mode currents through the transformer, power supplies and loads, as was observed for Prototype I during power measurements. The capacitance of Prototype II was reduced almost 5 times in comparison to Prototype I by employing windings without interleaving. The capacitance increased again for Prototype III where the windings were positioned closely together because the design did not use the leakage layer. Ultimately, the lowest capacitance was observed on Prototype IV.

Power Measurements on Transformer Prototypes

Initial experiments performed on Converter Demonstrator I at 50 kHz were unsuccessful due to the problems with the reverse recovery of the rectifier diodes. The reduction of the operating frequency to 25 kHz, which increased the value of the resonant inductance to approximately 30 μH by an external inductance and used Trench Field-Stop IGBT devices, resulted in successful converter operation throughout the complete load range up to 50 kW.

The tests on transformer Prototype I showed proper operation from the functional point of view but they reveal that the transformer windings overheated at power levels above 30 kW. Detailed measurements of power losses were performed on the prototype to identify the problem. The measurements were performed by a digital oscilloscope on a short circuited transformer for the winding losses and on an open circuit transformer for the core losses. The voltage and current probes were calibrated, degaussed and deskewed prior to the measurement in order to get the best possible results. The current probe degaussing was also performed regularly during the measurements. In spite of this effort, the accuracy of the obtained results is doubtful. Variation of the current probe offset with time and opening and closing the probe after degaussing is the source of the doubts. The situation is even worse due to the necessity of using high-voltage differential probes with long cables. The problem with this type of probes is that even on a tuned and calibrated probe, a movement of the negative and positive cables with respect to each other causes a slight variation of the measured waveforms. The mentioned effects might cause a slight phase-shift between the voltage and the current to which the power loss measurements of the transformer are very sensitive. Calculations showed that a phase-shift error as small as 0.5° (27 ns on time scale) results in a power loss error as large as 25%. For these reasons the measured losses shown in Figure 3-27a are used here only as an indication of the increase of the core and winding losses with the processed power.

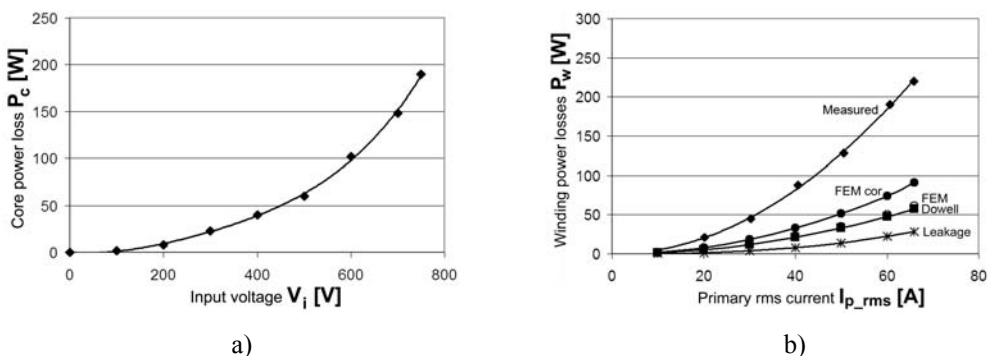


Figure 3-27: a) measured core loss of transformer Prototype I, b) measured and calculated winding losses of transformer Prototype I; Leakage – losses estimated in the leakage layer, FEM – losses in the windings calculated by FEM without the influence of the leakage layer, FEMcor – losses in the windings calculated by FEM with the influence of the leakage layer, Dowell – losses in the windings calculated by Dowell method without the influence of the leakage layer

The measured core loss, even though inaccurate, is much higher than expected. The increase of the core loss with respect to calculations could be caused by the fact that the datasheet loss information for Vitroperm material was provided for uncut ring cores, whereas the used cores were cut oval cores. Cutting the cores could modify the core properties in the vicinity of the cuts and result in an increase of the Steinmetz coefficients α and β from the assumed value of 2.1 (datasheets). Even though the core loss is much higher than expected, this cannot cause the hot-spot temperature to rise to unacceptable values. Direct attachment of the cores to the heatsinks and hence very efficient heat removal from the cores prevents the high temperature rise.

The measurement of the winding loss indicates that the winding loss is much higher than expected as well and, as a result, the winding structure overheated. Figure 3-27b shows the calculated and the measured winding loss with respect to the primary rms current. The curves marked as “Dowell” and “FEM” represent the calculated winding losses that were obtained in the design phase. The knowledge gained about the losses in the foils caused by the presence of the leakage layer (paragraph 3.4.4) and the losses in the leakage layer itself was not available during the design of Prototype I. The curve marked as “FEM cor” (corrected) represents the winding loss with the effect of the leakage layer included. As can be seen, the corrected values are about 50% higher than the initially estimated power loss. In order to calculate the total winding loss, the loss in the leakage layer material must be added to the loss in the foils. The loss of the leakage layer was calculated from the limited information provided by the manufacturer of the material (Epcos). The calculation resulted in another approximately 50% (in the design estimated as 35% guess value) increase of the power loss on top of the initially estimated winding loss. After including these effects, the total winding loss is approximately 100% higher than the value used in the initial design, but it is still much lower than the measured power loss. The difference can be explained by extra losses in the leakage layer material and by the error of the measurements.

The power tests on Prototype II were conducted with unsuccessful results. Voltage discharges were observed on the surface of the leakage layer at voltage levels higher than 500 V. A possible explanation of this problem is that during the moulding process and especially during the vacuuming of the leakage layer, the leakage layer material leaked and made contact with one or several winding foils. The leakage layer material is filled with tiny metal particles partially isolated by the epoxy resin. The higher electric field could possibly break the isolation of epoxy and consequently sparks might have occurred between the closest point of the leakage layer and the core, which was connected to the heatsink and hence grounded. For this reason, special attention must be paid to prevention of seeping of the leakage layer material into the windings during the moulding process. This is addressed in Prototype IV.

The short power tests on Prototype II that were performed below 500 V indicated that the transformer winding was still overheating. At that point, the leakage layer was considered as the main source of the power loss and therefore Prototype III was constructed without the leakage layer in order to identify the reason for the overheating.

The loss curves for the core and winding loss of Prototype III are shown in Figure 3-28. The curves were in this case measured by using a dedicated digital power meter capable of measuring power in high-frequency power-electronic circuits. The measurements revealed that even using this instrument involves a large measurement error due to measuring real power in circuits while $\cos\phi$ is close to zero; errors up to 30% can occur in such cases. Comparison of the measured and calculated winding loss of Figure 3-28b (solid line – measured, dotted line – estimated) shows that the measured loss is almost 30% larger than calculated even after including the measurement error. The only possible explanation is that the real error of measurement is even higher than estimated.

The main objective of Prototype IV was to integrate the large leakage inductance in the transformer and to investigate the influence of the leakage layer on the winding losses (paragraph 3.4.4). The first attempt with Prototype II failed due to the leaks of the leakage layer material into the windings. Prototype IV failed the power tests as well, which confirmed that the manufacturing of this type of

winding structure in laboratory conditions is difficult. The complications with the construction of Prototype IV were related to a precise centring and alignment of the leakage layer for a proper fit of the leakage layer and the core. The winding construction was done in the laboratory of EPP without using any special tools and consequently the transformer cores failed to close due to a misaligned and skewed leakage layer. The leakage layer was trimmed in an attempt to correct the problem. The trimming process involved grinding the layer, which resulted in contamination of the windings by the metal particles of the leakage layer. As a consequence of this, the winding isolation failed after a short operation at nominal voltage of 750 V.

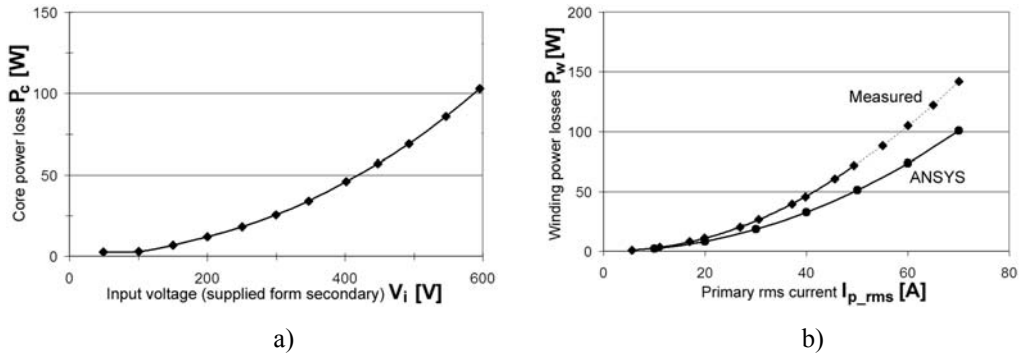


Figure 3-28: a) measured core losses of transformer Prototype III, measured on secondary side, b) measured and calculated winding losses of transformer Prototype III; dashed line – estimated values

The most successful power tests were performed on the prototype without the leakage layer. Prototype III performed well during long-term power tests. The contribution of Prototype III is that it improved on Prototype I with respect to the windings overheating. The measured temperatures were higher than calculated (see Chapter 4) but the winding sustained long-term operation without overheating and thermal runaway. The downside of Prototype III is that the leakage inductance of the windings is very low and an external inductance was used as the resonant inductance. The contributions of each of the prototypes are listed in Table 3-6.

Table 3-6: Overview of contributions of the transformer prototypes

	Prototype I.	Prototype II.	Prototype III.	Prototype IV.
Loss reduction by partially interleaved windings	■	—	—	—
Leakage layer to increase the leakage inductance	■	■	—	■
50 kW full power operation	—	—	■	—

3.6.2 Measurements on Filter Inductors

Measurements on the filter inductors are presented here to support the analyses of paragraph 3.5. The function of the filter inductors is demonstrated on the measured waveforms and their properties. The power loss of the filter inductors was not measured after unsuccessful attempts with the transformer power loss measurements.

The design parameters of the filter inductors of Converter Demonstrator II are listed in Table 3-7, while Table 3-8 lists the calculated and measured values of the inductances. The observed errors between the measured and the calculated inductances are in the order of 10%. The differences were probably caused by core properties different from those specified. The core fill factor of amorphous cores (functional magnetic material cross-section versus total core cross-section), in particular, might be different from the 70% used for the design of inductors.

Table 3-7: Design parameters of filter inductors

Core		Amorphous metal, 4 U cores, dimensions as shown in Figure 3-22a, core fill factor 0.7
Air-gap	Input	6 mm
	Output	7 mm
Number of turns		23
Foil thickness		0.3 mm
Isolation		Kapton® foil 0.07 mm
Foil width		45 mm
Distance winding-core on the inside	Winding window	2.5 mm (winding window)
	End winding	3 mm (end winding)
Calculated inductance	Input	79.6 μH
	Output	68.3 μH
Dc current	Input	66.6 A
	Output	83.3 A
Ac current	Input	9.1 A _{peak}
	Output	10.5 A _{peak}

Table 3-8: Calculated and measured inductance values for filter inductors of Prototype II.

	Input Inductor	Output Inductor
Calculated Inductance [μH]	79.6	68.3
Measured Inductance [μH]	69.7	62
Error [%]	12.4	9.2

The waveforms measured on the filter inductors of Demonstrator II at full power operation (50 kW) are shown in Figure 3-29. Figure 3-29a shows the ac currents flowing through the filter inductors in comparison with the primary current of the transformer. As can be seen, both inductors limit the current ripple very effectively. The amplitude of the current ripple is in the order of 10 A, whereas the amplitude of the resonant current on the primary side is in the order of 120 A. Table 3-9 lists the dc current values and the ac rms currents calculated from the measured waveforms. The current ratio k_I for the measured waveforms is lower than the ratio used in the design. The difference was probably caused by the lower values of the filter inductances. The effectiveness of the complete filters is also demonstrated in Figure 3-29b by comparing the ac voltage ripple on the resonant capacitors C_r and on the filter capacitors C_f . As can be seen, the voltage ripples on the filter capacitors are almost negligible

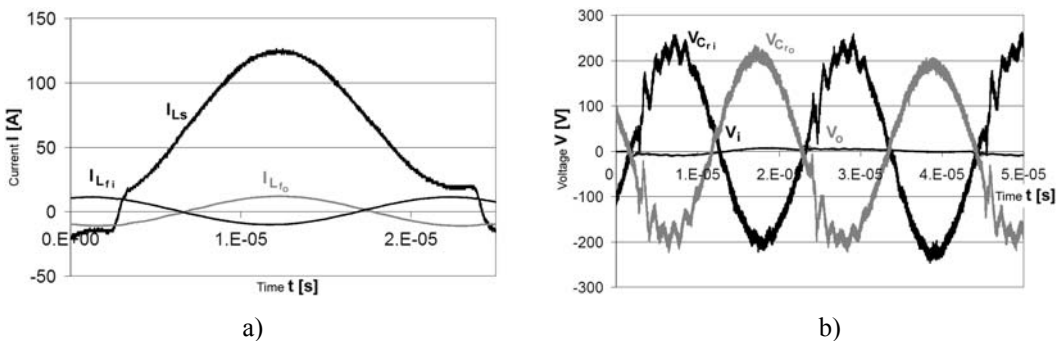


Figure 3-29: Waveforms measured on the filter inductors; a) current waveforms, b) voltage waveforms

Table 3-9: Dc and ac current values for filter inductor currents

	I_{dc} [A]	$I_{ac\ rms}$ [A]	$k_I = I_{dc}/I_{ac\ rms}$
Input	68.1	7.92	8.6
Output	85.1	7.9	10.77

3.7 Conclusions

Amorphous cores and foil winding technology were selected as the most suitable for high-power-density, high-power transformer designs due to their superior magnetic and thermal properties. They were used as the basis for all investigations in this chapter.

The optimisation of the transformer shape showed that the conventional shapes, which are optimised for the power loss, are not optimal from the power density point of view. A slim and elongated shape was proposed as an alternative to conventional shapes. This transformer design yielded a volume reduction of approximately 25%, while the overall transformer power loss increased by approximately 3%. The proposed transformer shape also seems to be easy to integrate with other converter components.

The high-frequency losses in foil windings were also addressed in this chapter. A new type of foil windings was proposed for transformers with a turn ratio close to 1. The proposed partial interleaving reduces the high-frequency losses and at the same time the winding remains simple.

Integration of resonant inductors inside high-power transformers by implementation of a so-called leakage layer was also considered in this chapter. The leakage layer contribution to the transformer leakage inductance was derived. It was shown that the leakage layer aligned with the foils results in tremendous winding loss. Extending the leakage layer beyond the foil edges was proposed to keep the winding loss low. It was shown that doing so results in the power loss approaching the value obtained for the windings without the leakage layer.

The proposed concepts, and their implementation and advantages, were demonstrated on four transformer prototypes. The small signal measurements confirmed successful implementation of the leakage layer in the transformer from the required leakage inductance value point of view. A leakage inductance as high as 28 μH was reached in the transformer prototypes. The power tests were not as successful because of overheating of the windings in initial prototypes. Also, the construction of prototypes with a leakage layer proved difficult in laboratory conditions. Both prototypes with the moulded leakage layer failed the power tests due to winding isolation failures. It is suspected that the isolation failed due to metal particles of the leakage layer penetrating into the windings during the manufacturing process. Improving the process of leakage-layer construction will solve this problem. The final tests on the transformer without the leakage layer were successful and the transformer sustained continuous operation at full power without excessive overheating.

An easy integration of filter inductors with the transformer and other components was defined as one of the main constraints in the design of the filter inductors. The effectiveness and power loss of filters were investigated for such constrained design. A foil thickness optimisation was discussed in order to establish a balance between the filter effectiveness and the power loss. A new model for the simulation of the end winding section of filter inductors was also introduced. The new model involves excitation of the core magnetic field by an auxiliary winding. This resulted in a proper air-gap excitation and therefore in an improved calculation of the winding loss.

Chapter 4 *Thermal Management*

4.1 Introduction

The state-of-the-art thermal management of high-power converters is based primarily on forced-air cooling combined locally with conduction (Figure 1-16). Such a thermal management system occupies a large volume inside converter structures because it requires space between the components for an efficient air-flow. The methods of heat removal must be adapted so that the empty spaces can be reduced and the components can be placed closer together. The new methods must also be able to handle the additional losses that are associated with the increased operating frequency required to attain small passives.

The state-of-the-art heat-removal methods are briefly discussed in Appendix B. The methods differ in cooling performance as well as in the complexity of the resulting thermal management system. Figure 4-1 compares the heat-removal methods in relation to the following aspects: complexity, weight, cost, reliability and cooling capacity. In the figure, the methods are rated on a relative scale from 1 to 10. The ratings were given by ordering the methods according to their performance with respect to the rated parameter. The performance was evaluated by using information about the heat-removal methods published in [48], [14], [13] and elsewhere. The applications considered in this thesis were also comprehended in the rating process.

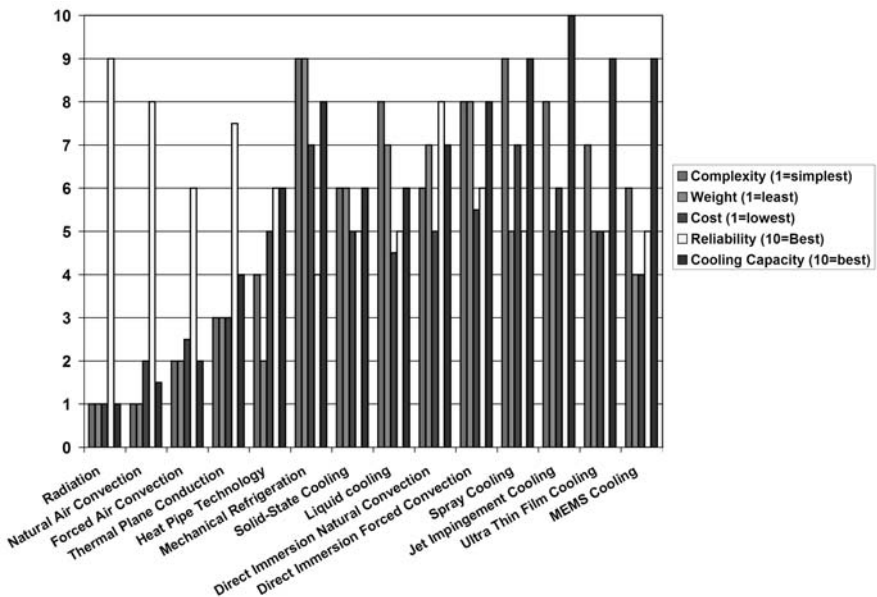


Figure 4-1: Comparison of heat-removal methods

In this chapter, thermal management is considered on the following levels:

- component level
- converter level
- system level

The heat-removal methods are evaluated for each level with the main goals being: effective heat removal, high power density and simplicity of the complete thermal management system. The methods selected in the evaluation process are concluded in a converter thermal-management concept. Based on the proposed concept a number of solutions are generated. These solutions are assumed to be able to remove the generated heat within constraints but they are all different with respect to power density. The solution with the highest power density is selected and further evaluated in detail. Finally, the proposed solution is implemented in a converter demonstrator and the performance of the demonstrator is evaluated by measurements.

4.2 Thermal Management on Component Level

The main power losses are generated in active as well as in passive components. In active components, high power loss is generated in the volume of a silicon chip. As a consequence, heat removal methods are required that can realise high heat fluxes typically in the range of 1...500 W/cm². On the other hand, the power losses in passive components are also high but they are generated in large volumes. Heat fluxes in the range of 0.1...1 W/cm² are typical. The obstacle in realising these small fluxes is the presence of materials with low thermal conductivities – like, for example, isolation materials. In addition to that, the heat must be transported over relatively long distances, as the passive components can be large. Therefore, passives require the addition of effective heat-transfer elements.

The main heat sources are components that are directly involved in the power processing or the so-called power components. The losses in these components are accompanied by power losses generated in control and signal processing circuits which are typically much smaller. Therefore, in this thesis, the power losses of the control circuits are disregarded and only the power losses in the power components are considered further.

4.2.1 Thermal Management of Active Components

The state-of-the-art method for heat removal from active components is conduction. A typical power module assembly is shown in Figure 4-2. As can be seen, silicon chips are attached to a DBC (Direct Bonded Copper) substrate and the substrate to a base-plate. In a converter assembly, the base-plate is mounted on a heatsink, cold plate or a heat-transfer element. The thermal resistance is determined by the materials used for the DBC layers and the base-plate, by the quality of the heat transfer between the layers and by the amount of heat spreading which occurs as the heat flows between the layers.

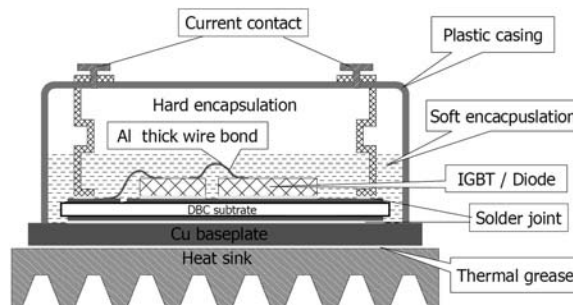


Figure 4-2: State-of-the-art power module assembly diagram (Curamik)

A typical junction-heatsink thermal resistance for a state-of-the-art power module is in the range below 0.2 W/mK for the considered power levels. At a maximal junction temperature of 150 °C and a heatsink temperature of 70 °C, such a thermal resistance allows power dissipation up to 400 W per device. This value exceeds the expected power dissipation in the active components of the converter considered in this thesis and therefore state-of-the-art thermal management will be used.

As will be discussed in Chapter 5, the power loss in active components is expected to increase progressively with the power rating. The power loss increase is compensated for only partially by the reduction of the thermal resistance. Therefore, with scaling-up, the application of advanced heat-removal methods in active components might be needed. The advanced methods discussed in literature are micro-channel cooled base-plates [49], spray [50], jet impinged [51] and cooling methods based on boiling [52]. All these methods offer remarkable heat-transfer improvements expressed by high heat fluxes and lower temperature rises. The common disadvantage of these methods in comparison with the state-of-the-art is the complex supporting infrastructure that is required.

4.2.2 Thermal Management of Magnetic Components

Low-frequency and hence bulky magnetics are prevalent in high-power applications. The problem of high-power magnetics is the high power loss and the relatively long heat-removal paths. The state-of-the-art heat-removal method is forced-air cooling. Low-frequency designs have large surfaces which makes the heat removal easier. Often, the surface area is increased even more by employing air channels as shown in Figure 4-3. Another heat removal method often used at high power is heat removal by oil. In such systems, the components are completely submerged in oil which extracts the heat from the windings as well as from the cores. The risk of oil leaks and in some cases the necessity of using a pump makes this solution problematic and limits its use to high-voltage applications where the isolating properties of oil are advantageous.



Figure 4-3: Open winding structure with air channels to enhance convective cooling

A high operating frequency is a prerequisite when a high power density is required. Apart of a smaller volume, the operation at high frequencies has two side-effects on high-power magnetics: higher specific losses and a lower surface to volume ratio. As a consequence of both effects, the heat removal from the components is more difficult and therefore an advanced thermal management must be implemented.

In the following paragraphs, a two-step approach is used to analyse the heat removal from the power magnetics. In the first step, the heat transfer from a component core to a component surface is considered. On this level, the heat-removal performance is mostly related to the internal structure of the components. The second step considers the heat removal from the component surfaces and the transportation of heat to the point of heat exchange. In this step, the most suitable methods for heat transportation from component surfaces are proposed. Application of heat transfer elements is also considered.

Heat Removal from Hot-Spot to Component Surface

Irrespective of the heat-removal method, the heat must be brought to the component surface in order for it to be removed from the component. In the elementary parts of the magnetic components, the windings and the cores, the heat is usually internally transported by conduction. The internal structure of the elementary parts and their dimensions predispose certain surfaces for heat exchange. These surfaces must be identified in order to introduce the most effective heat-removal concept.

The suitability of the surfaces of amorphous cores for heat removal is related to the orientation of laminations and to the core shape. Figure 4-4a shows the core surfaces that are available for the heat exchange in the transformer proposed in Chapter 3. Two heat-removal concepts are identified as:

- heat removal through the front and rear core surfaces (dark surfaces in Figure 4-4a)
- heat removal through the surfaces of the core envelope (light surfaces in Figure 4-4a)

In the first concept, the heat is transported horizontally from the hot-spot (in the centre of the structure, point 1 in Figure 4-4b) along the lamination planes. In the second concept, the heat is transported initially along the laminations, but in the last part it must cross the laminations to reach the core surface. The two heat-removal concepts are represented in the simplified thermal network diagram of Figure 4-4b by the thermal resistances R_{th_ch} (concept 1) and R_{th_cv} (concept 2). The thermal network diagram is simplified, it shows only the main thermal resistances of the heat-removal paths for the heat removal from the hot-spot of the core.

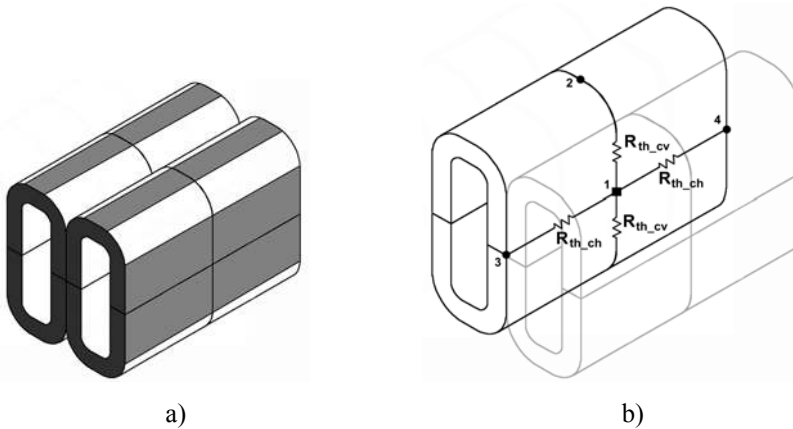


Figure 4-4: Transformer core; a) surfaces available for heat exchange, b) thermal network model applied to half a core, the model for the second half is exactly the same; point 1 – heat source and expected hot-spot, points 2, 3, 4 – heat-exchange points

The effectiveness of the two heat-removal concepts was evaluated for different core shapes by comparison of the associated thermal resistances. Considering only their most relevant component, the thermal resistances R_{th_cv} and R_{th_ch} can be described as:

$$R_{th_cv} = \frac{1}{k_{c_a}} \frac{2x}{A_c}, \quad (4-1)$$

$$R_{th_ch} = \frac{1}{k_{c_a}} \frac{2d_c^2}{A_c x}, \quad (4-2)$$

where k_{c_a} is the thermal conductivity of the core along the core laminations, x is the length of the path between points 1 and 2 in Figure 4-4b, A_c is the core cross-section and d_c is the core depth. The ratio between the thermal resistances associated with the two heat-removal concepts follows from:

$$\frac{R_{th2}}{R_{th1}} = 1.27 \frac{4x^2}{d_c^2}, \quad (4-3)$$

where R_{th1} and R_{th2} are the thermal resistances of the first respectively second concept. As can be seen from this equation, the thermal resistance R_{th1} is higher than R_{th2} if the core depth d_c is more than approximately 2.25x. This means that the extraction of heat through the core envelope is better if the core depth d_c is more than approximately 1.2 times the core height H_c . Therefore, for the transformer design optimised for high power density presented in Chapter 3, the heat removal through the core envelope is more suitable than through the front and rear surfaces.

The presence of the isolation in transformer windings results in anisotropic conduction properties. The thermal conductivity of a foil winding in the direction along the layers can be calculated as:

$$k_{w-a} = \frac{k_f h_f + k_i h_i}{h_f + h_i}, \quad (4-4)$$

where h_f , h_i are the thicknesses of the copper foil and isolation respectively and k_f , k_i are the associated thermal conductivities. In a similar manner, the thermal conductivity perpendicular to the winding layers follows from:

$$k_{w-p} = \frac{(h_f + h_i)k_f k_i}{k_f h_i + k_i h_f}. \quad (4-5)$$

For a typical transformer design, the thermal conductivity in the direction along the winding layers can be as much as a thousand times larger than in the perpendicular direction. For this reason, the heat removal from the windings in the direction of the winding layers should be easier.

Heat removal in the direction of winding layers is implemented in [53] where the heat is removed from the edges of an inductor winding. This proved to be very effective, but the application of this technique to higher voltages is limited. The limitation originates from the requirement of reliable high-voltage isolation. Maintaining this high-voltage isolation might be difficult in this case because the winding edges must be processed for bonding to heat-removal elements. For this reason, the heat removal from winding edges is rejected and not considered further.

Other surfaces available for the heat exchange are shown in Figure 4-5a. In relation to these surfaces, three heat-removal concepts are defined as:

- heat removal through the end winding sections (dark surfaces in Figure 4-5a; hot-spot in point 1, heat exchange at points 4 and 5 in Figure 4-5b)
- heat removal through the outer and inner surfaces of the side winding sections (light grey surfaces in Figure 4-5a, hot-spot in point 1, heat exchange at points 2, 3 in Figure 4-5b)
- heat removal only through the outer surfaces of the side winding sections (outer light grey surfaces in Figure 4-5a, hot-spot in point 2, heat exchange at point 3 in Figure 4-5b)

The thermal resistances associated with the heat paths of all three concepts are indicated in Figure 4-5b for a quarter of the transformer winding (top view, corner winding section).

In the first concept, the heat is transported along the winding layers to the end-winding-sections at first and then perpendicular to the winding layers to the heat-exchange points 4 and 5. In the first part of the heat path, the heat flows along the winding layers exploiting the high thermal conductivity k_{w-a} . In the second part, the heat must cross through the isolation layers, which yields a low thermal conductivity k_{w-p} . The disadvantage of this last concept is that the end winding sections often have a small surface area. In addition to this, terminals are typically placed in these sections, and this might complicate the implementation of heat-transfer elements if required.

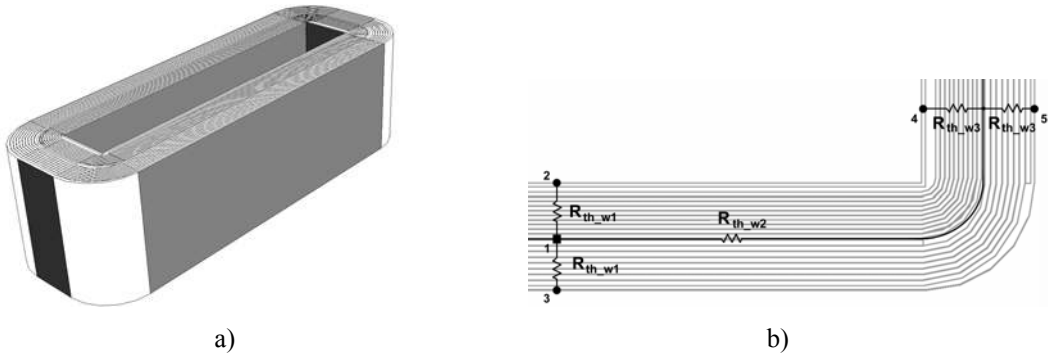


Figure 4-5: Transformer windings; a) indication of surfaces available for heat exchange, b) thermal network model applied to quarter of the winding

The second concept uses the winding surfaces of the side winding sections positioned inside the winding window. The heat is transported from the hot-spot 1 in the shortest possible way to the heat exchange points 2 and 3. The disadvantage of this concept is that the heat is conducted all the way in the direction perpendicular to the winding layers and hence with a low thermal conductivity $k_{w,p}$. The performance of this concept is closely related to the surface area of the heat-exchange surfaces. Additional space must be provided inside of the winding window for elements that remove the heat from the surfaces.

The third concept is similar to the second but the heat transfer is realised only through the outer winding surfaces. This results in the hot-spot moving to point 2. In this case, the heat must be transferred over a longer distance and therefore the thermal resistance of the heat path is higher than in the second concept.

The thermal resistances utilised in the three concepts are directly related to the transformer geometry. The thermal resistances of the heat-removal paths are compared in order to select the concept that is the most suitable for the proposed transformer. It is assumed in the comparison that the primary and secondary windings are made of foils of the same thickness, the leakage layer is not present and the thermal contact between the winding layers is ideal (without additional thermal resistance for the thermal contacts between the winding layers). Including these aspects in the comparison would yield a complex solution which is beyond the scope of this thesis.

Based on the presented assumptions, it can be shown that the thermal resistances of the first and the second concept are equal for the following core depth $d_{c,e}$:

$$d_{c,e} = \sqrt{\frac{1 - \frac{k_{w,p}}{4k_{w,a}} \frac{A_c}{N^2(h_f + h_i)^2}}{\frac{k_{w,p}}{4k_{w,a}} \frac{1}{N^2(h_f + h_i)^2} + \frac{1}{8A_c}}}, \quad (4-6)$$

where A_c is the core cross-section and N is the total number of turns. Evaluation of this equation for the transformer concept proposed in Chapter 3 showed that the second concept is more effective if the core depth d_c is more than approximately 48 mm. This is also illustrated in Figure 4-6, which shows the thermal resistances as a function of the core depth d_c . The figure also shows that for the core depth d_c of 120 mm, as used in Transformer Prototypes II and further, the thermal resistance for the heat removal from the side sections is almost five times lower than for the heat removal from the end sections.

Comparison of the thermal resistances of the first and the third heat-removal concept shows that the thermal resistances are equal if $d_{c,e}$ is equal to:

$$d_{c_e} = \sqrt{\frac{1 - \frac{2k_{w_p}}{k_{w_a}} \frac{A_c}{N^2(h_f + h_i)^2}}{\frac{2k_{w_p}}{k_{w_a}} \frac{1}{N^2(h_f + h_i)^2} + \frac{1}{2A_c}}} \quad (4-7)$$

Evaluation of this equation for Transformer Prototype II resulted in a core depth d_{c_e} equal to approximately 104 mm. This means that for the winding design of Prototype II, even the heat removal from only the outer surfaces is better than the heat removal from the end winding sections.

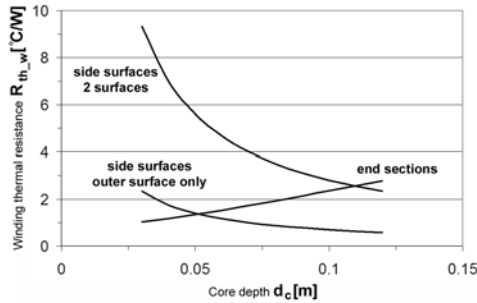


Figure 4-6: Thermal resistance of winding hot-spot to surface R_{th_w} for three heat removal concepts in relation to core depth d_c

Note that the presence of leakage layer and the bad quality of the thermal contact between the winding layers might increase the thermal resistances in all three heat-removal concepts. The effect of the leakage layer will be included later in the FEM simulations. Given these disadvantages, the heat removal from the side sections was selected as the preferred heat-removal concept.

Heat Removal from Core and Winding Surfaces

Once the heat is conducted from the inside of a component to its surface, it can be removed from the component. In general, this function can be performed by several heat-removal methods which will be discussed here.

The first heat-removal method discussed is forced-air cooling for heat-removal from the cores and windings. The method is considered in relation to the transformer design as proposed in Chapter 3. The component cross-section considered is shown in Figure 4-7. As indicated in the figure, the space between the windings and the core creates air ducts. Air can be blown through these air ducts in order to remove the heat from the windings as well as from the cores.

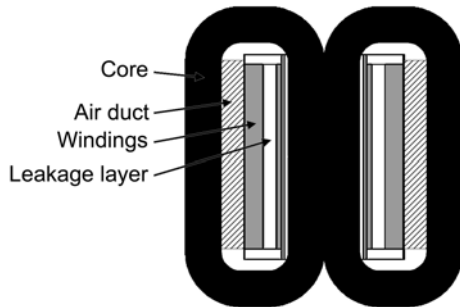


Figure 4-7: Transformer cross-section used for modelling heat removal by forced convection

A simple model was made to investigate the feasibility of forced-air cooling in high-power high power density magnetics. The model estimates the temperature rise of the transformer windings. The surface area available for the heat removal from the windings is smaller than the area available for the cores and therefore the winding structure was selected for this investigation.

The temperature rise due to the thermal resistance across the convection film from the cooling air to the winding surface is calculated from [54]:

$$\Delta T = \frac{Q}{h_c A}, \quad (4-8)$$

where Q is the removed heat, A is the area available for the heat transfer and h_c is the convection coefficient. The coefficient h_c is determined by the air duct geometry and follows from:

$$h_c = J c_p \rho_f v_f \left(\frac{c_p \mu}{k} \right)^{-2/3}, \quad (4-9)$$

where J is the Colburn factor calculated from the Reynolds number N_r , c_p is the specific heat of the cooling fluid, ρ_f is the fluid density, v_f is the fluid speed, μ is the viscosity of the fluid and k is the thermal conductivity of the fluid. The Colburn factor J can be determined from the Reynolds number. For a laminar flow $J=6/N_r^{0.98}$ and for a turbulent flow $J=0.023/N_r^{0.2}$. The Reynolds number is defined as: $N_r = \rho_f v_f D_h / \mu$, where D_h is the hydraulic diameter of the duct.

By limiting the maximal air-to-winding surface temperature rise to 50 °C (assumed 40 °C cooling air, 120 °C hot-spot), the relation between the total winding power-loss and the required air velocity was calculated and the result is shown in Figure 4-8. As can be seen, a high air speed is required to remove any substantial amounts of heat through the air ducts. In a practical realisation, the high air speeds would require the addition of a powerful fan and of a specialised aerodynamic structure to funnel the air through the ducts. Another practical option could be an increase of the winding area available for cooling which would improve the heat removal from the windings. Both solutions would result in a substantial increase of the total transformer volume and hence in a reduced power density. For these reasons, this type of heat removal was rejected.

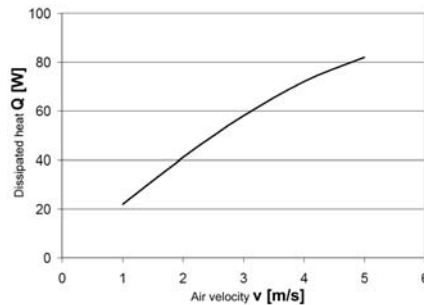


Figure 4-8: Heat removal capability of air-ducts versus air velocity

Apart from the forced-air cooling, other more advanced methods are available for heat removal from the component surfaces. Figure 4-9 illustrates the possibilities of liquid-cooled magnetics for two examples. Figure 4-9a shows a coaxial transformer where a hollow inner wire is used for circulation of cooling liquid. The heat from the cores is removed by liquid-cooled clamps attached to the top and bottom of the cores. Another solution shown in Figure 4-9b uses tubes placed inside the winding windows for the removal of heat from the windings as well as from the cores. Another possibility is application of so-called liquid-cooling elements, similar to those proposed for cooling the base-plates of active components (Figure 4-10). These elements rely on micro channels for effective heat removal.

The flat and thin elements could be attached directly to the winding and core surfaces. To the best of the author's knowledge, this possibility has not yet been explored in practical application in passive components.

In spite of the high cooling capacity of liquid cooling, the use of it is not considered in this thesis for direct heat removal from converter components. Because of its complexity, liquid cooling on the component level typically requires a pump and elaborate tubing, and there is the threat of leaks. This leads to an increase in system volume and also to reduced reliability.

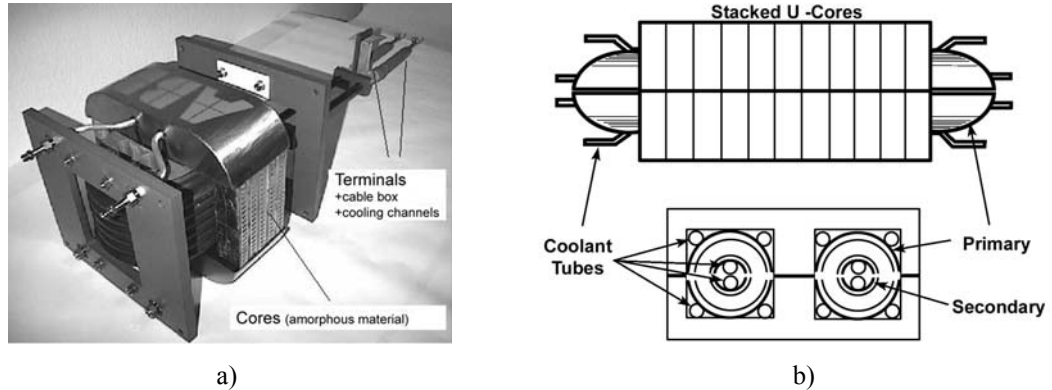


Figure 4-9: Water cooled high-power high-frequency transformers; a) [55], b) [56]

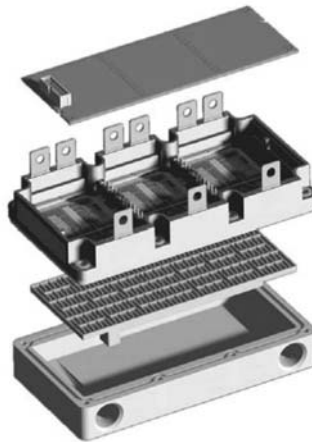


Figure 4-10: Shower Power cooling system of Danfoss [57]

Heat pipes are another type of advanced heat transfer elements that can be applied for heat removal from surfaces of magnetic components. They have a small volume and they can transport relatively large amounts of heat over long distances with a low temperature rise. Flat heat pipes (Figure B-4) can be applied in confined spaces and as heat spreaders in heatsink bases. The flat heat pipes could be attached to surfaces of magnetic components to remove and transport the heat to a common heatsink.

Conduction is another heat-removal method that can be used for the transfer of heat from the surfaces of power magnetics. Low heat fluxes allow the use of conduction over relatively long heat paths. Aluminium is a fairly cheap and generally available material that can be used for the housing of components which effectively extracts the heat. This concept is discussed in [58] and its application to a power inductor is illustrated in Figure 4-11. As demonstrated in [58], very good thermal performance and high power densities can be realised by using this concept.

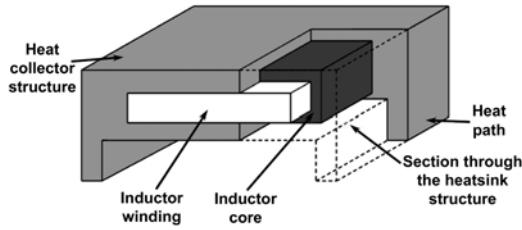


Figure 4-11: Power inductor cooled by conduction [58]

Based on the preceding discussions, conduction was selected as the main heat-removal method for power magnetics. The main reasons for selecting conduction are: good performance, reliability and simplicity. In applications where a higher thermal performance is required, the conduction could be aided by heat pipes.

4.2.3 Thermal Management of Capacitors

The state-of-the-art solution for the removal of heat from capacitors is a combination of convection and conduction (Figure 4-12). The heat is partially conducted through connecting leads into the bus-bar where it is exchanged with the environment by convection. The remaining heat is removed directly by convection through the package.

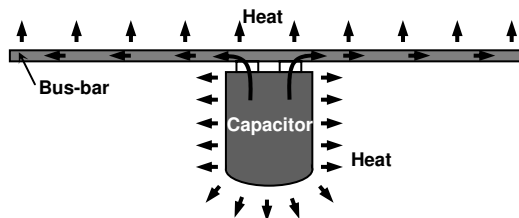


Figure 4-12: Diagram displaying state-of-the-art heat removal from capacitors

Resonant capacitors are in many topologies subjected to high currents and high voltage swings. These two parameters in combination with a high operating frequency are the main contributors to power losses in capacitors. To reduce the power loss of a single capacitor, a series-parallel connection of multiple capacitors is typically used. At the same time, the series-parallel connection is used to tune the capacitance value.

In Converter Demonstrator I, multiple capacitors are connected in parallel in order to split the current and to obtain the required resonant capacitance. The capacitors are packed closely together and with other components in order to eliminate empty spaces and to realise high power densities. The convection of heat from the capacitors is disabled by the close component packing and therefore conduction is proposed as the main heat-removal method. As indicated in Figure 4-13, the heat can be conducted from the capacitor bodies by two paths: through the leads into the bus-bar and through the bottom capacitor surface into the heatsink.

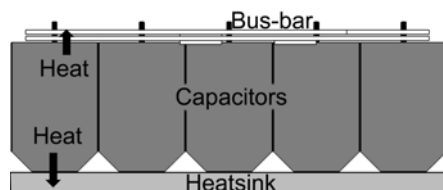


Figure 4-13: Proposed resonant capacitor assembly with indicated heat removal paths

To assess the thermal behaviour of the proposed resonant capacitor assembly, a set of calorimetric measurements of power losses and thermal resistances was performed. Two cases were investigated: a single capacitor placed in the air (state of the art) and the same capacitor placed in a set-up as shown in Figure 4-13. During the measurements, the core and the surface temperature of the capacitor were measured by thermocouples. The measurements on the single capacitor confirmed the datasheet thermal-resistance value of 28 W/mK. It was also observed that the heat removal by conduction in the set-up as shown in Figure 4-13 results in a hot-spot to heatsink thermal resistance of approximately 20 W/mK. The reduction of the thermal resistance by the use of conduction only is therefore almost 30%.

In some cases, the 30% improvement of the thermal performance might not be enough and more advanced heat-removal concepts have to be implemented. In comparison with the arrangement of Figure 4-13, heat removal can be improved by implementing a structure as shown in Figure 4-14. In this structure, two extra heat-removal elements are attached to the front and rear walls of the capacitors. This heat-removal concept is based on a higher thermal conductivity of the capacitor structure along the capacitor axis due to the heat flow along the electrodes. The effectiveness of this concept can be improved further by stripping the capacitors of their plastic outer-shells and using a thinner Kapton® isolation or thermal clad material to isolate the terminals from the heat-removal elements. Encapsulation of the stripped capacitors in an aluminium tub by using a thermally conductive compound could result in an even lower thermal resistance between the capacitor surfaces and the heatsink and hence a better thermal performance. However, stripping the capacitors might be rather time-consuming and labour-intensive. Obtaining bare capacitor rolls from the manufacturer might be an option.

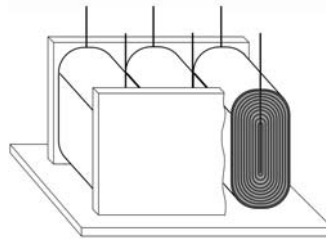


Figure 4-14: Illustration of capacitor structure with advanced heat removal

The proposed concepts are expected to have the same volume and the only difference is their thermal performance. However, none of the advanced concepts was studied in detail and therefore their exact performance is not known. On the other hand, the thermal performance should not influence the function of the resonant capacitors but it would improve their lifespan. Therefore, the first and the simplest proposed concept as shown in Figure 4-13 has been implemented in Converter Demonstrator II. The temperatures of the capacitors will be observed during the operation and, based on the results, an update to a more advanced concept will be suggested for industrial application.

4.3 Thermal Management on Converter Level and System Level

The division of the thermal management into different levels is illustrated in Figure 4-15a. On the component level, the heat is transferred from the hot-spots to the component surfaces. Further, on the converter level, the heat must be transported from the component surfaces to the place where the heat exchange with the system environment occurs. The design of the thermal management typically concerns component structures on the component level, heat-removal elements on the converter level and heat removal with respect to the system requirements on the system level. The thermal management on the converter level serves typically as an interconnection between the component and system level. Therefore, the thermal management on the system level must be specified prior to the design of the thermal management on the converter level.

Conversion systems often consist of several conversion units (Figure 4-15b). These units contribute with their heat dissipation to a common system environment. From the point of view of thermal management on the system level, this often means sharing cooling media with other system components. Therefore, the thermal management on the converter level must also perform optimally in such an environment and it should not detrimentally affect the performance of other units in the system.

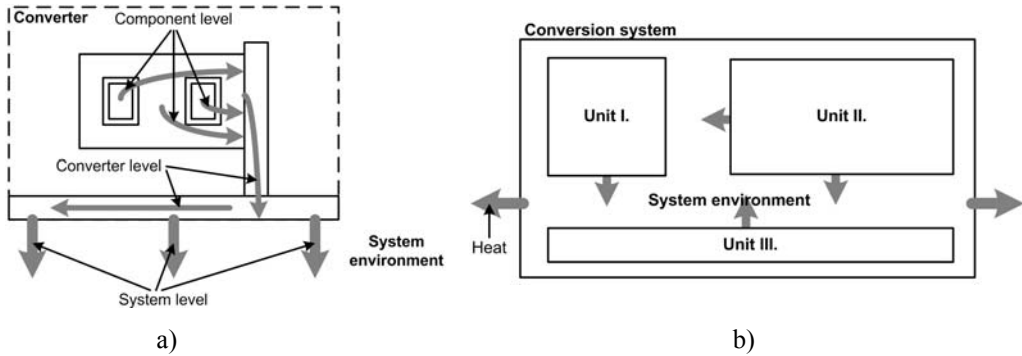


Figure 4-15: Illustration of a) thermal management levels, b) conversion system that consists of several conversion units

It is also often required that a power converter be flexible with respect to the thermal management on the system level. In practice, this means that the converter must be able to operate in an air-cooled or liquid-cooled system environment. This concept requires a power-module-like approach (as discussed in [59]) in which a system designer can choose which of the cooling methods will be used for the heat removal from the converter package.

In order to address the system requirements, heat collection on dedicated thermal surfaces is proposed for the thermal management on the converter level. This approach offers the ability to integrate the power converter into a wide range of conversion systems irrespective of the cooling method used on the system level. In principle, the universal thermal surfaces can be coupled with any type of cooler that can maintain a required temperature on the thermal surfaces. This approach is illustrated in Figure 4-16.

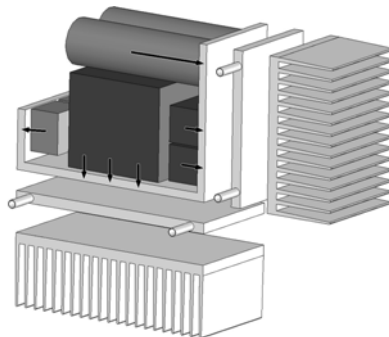


Figure 4-16: 3D model of converter thermal management based on thermal surfaces; arrows indicate heat fluxes realised inside the converter structure

The number of thermal surfaces and their complexity depends only on the system where the power converter will be used. For cost, simplicity and easy system integration, the number of thermal surfaces should be as small as possible and they should be of simple shapes, preferably plane. In some cases,

this requirement might oppose the requirement of the highest power density. This will be demonstrated in paragraph 4.5.1, which discusses several solutions with single and double thermal surfaces.

4.4 Proposed Converter Thermal Management Concept

The discussions presented in paragraphs 4.2 and 4.3 lead to a thermal management concept based on the following fundamentals:

- primarily conduction used for the heat transfer inside the converter
- addition of passive heat-transfer devices (without moving parts) to support the heat removal by conduction if required
- heat collection on thermal surfaces – outer surfaces of the converter package

These concept fundamentals translate into the following design guidelines:

- use of materials and technologies with high electromagnetic and thermal performance – for example, amorphous core material
- integration of electrical, thermal and mechanical functions [60]
- component geometry and placement that enables an optimal utilisation of heat paths
- optimal heat spreading on the thermal surfaces
- small number of simple thermal surfaces
- simplicity of final assembly

These design guidelines were already considered in the proposed thermal management of conventional active components and of resonant capacitors in preceding paragraphs. In the following paragraph, the guidelines will be applied to the heat-removal concept for power magnetics.

Proposed Heat Removal Concept for High Power Density High-Power Magnetics

In high-power converters, power magnetics and particularly transformers are often the most complex components from a thermal management point of view. Therefore, the proposed heat removal concept is discussed below with respect to power transformers but the same principles can be applied to all power magnetics.

Amorphous material was selected for the core assembly because it offers a high electromagnetic and thermal performance. The main properties of the amorphous material are: high saturation flux density (up to 1.5 T), high relative permeability (> 10000), power loss comparable to ferrites for frequencies up to 100 kHz, high operating temperature ($> 150\text{ }^{\circ}\text{C}$) and high thermal conductivity ($> 9\text{ W/mK}$).

Heat removal from the core is realised by a direct attachment of the outer core legs to the thermal surfaces as shown in Figure 4-17.

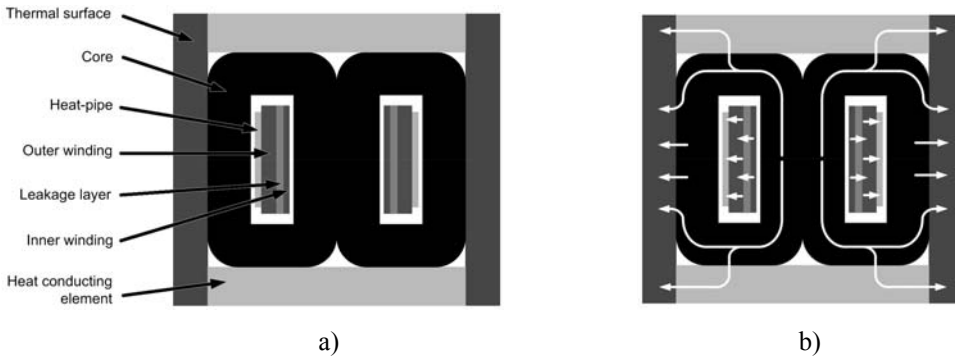


Figure 4-17: Heat removal concept proposed for magnetics; a) description of structural parts, b) indication of heat paths

This configuration removes the heat from the outer legs very effectively because the heat paths are short. To improve the heat removal from the centre core leg, heat conducting elements are attached to the top and bottom core surfaces as well. With respect to the second guideline point, aluminium with its high thermal conductivity is used for all thermally conductive paths.

The analysis of the heat conduction in foil windings showed that the surfaces of the winding sections placed inside the winding windows are favourable for the transformer geometry proposed in Chapter 3. The position of the surfaces inside the winding windows requires employment of heat-removal elements which are able to transport large amounts of heat and occupy little space. In order to follow the design fundamentals, only the heat transport by conduction and by advanced passive devices are allowed. Temperature rises for using heat conduction in copper and aluminium, and for using heat pipes were estimated. The resulting temperature rises for copper and aluminium are 21 °C and 35.5 °C respectively. Based on these values, the pure conduction in solid materials is rejected and the heat pipes with the indicated temperature rise of only 1.25 °C will be considered further.

The heat pipes can be placed on the outside as well as on the inside of the windings. Placement on both sides requires that there is enough space available in the winding window. Using flat heat pipes reduces the space requirements. In some cases, where the generated heat is lower, the heat pipes can be placed only on the outside of the windings. Such a configuration was implemented for heat removal from the filter inductors, for example.

Placement of the electrically-conductive heat pipes (typically made of copper) directly on the winding surfaces results in eddy currents in the heat pipes, which yields higher total transformer losses. The generated heat varies depending on the winding configuration (as indicated in Table 3-2). The FEM analysis of winding configuration of Table 3-2e (used in Transformer Prototype IV) shows that the heat generated in the heat pipes reaches approximately 10% of the winding power loss. It is assumed that the related heating is negligible as it is directly removed by the heat pipes.

Another aspect which plays an important role in the heat removal from the proposed transformer windings is the presence of the leakage layer. The low thermal conductivities of the available materials (see Table 3-1) result in more difficult heat removal from the windings. If the heat pipes are used only on the outside of the windings, a heat path with lower thermal resistance must be provided for the removal of heat from the inner winding layers. This was implemented in Transformer Prototype I by using a thermal clad material (see Figure 3-23a) to bridge the thermal resistance of the leakage layer. The problem is less pronounced if the heat pipes are used on the outside as well as on the inside of the transformer windings (Transformer Prototypes II and IV). Another option is an addition of heat-transfer elements to remove the heat directly from the leakage layer. Electrically non-conductive elements, for example ceramic elements, must be used due to strong magnetic fields. This was used in Transformer Prototypes II and IV, where ceramic bars were inserted inside the leakage layer.

4.5 Design Process of Thermal Management

The process of designing and evaluating the proposed heat-removal concepts is based on three methods: thermal network modelling (TNM), finite element modelling (FEM) and measurements on converter demonstrators. The block diagram of the process is shown in Figure 4-18. Three main design loops can be identified as:

- loop I. (dark grey) – first order thermal model based on TNM
- loop II. (light grey) – FEM model
- loop III. (black) – construction and measurements on real prototype

The design process will be discussed here in relation to the transformer thermal design because it is typically the most complex. The process could be discussed also for the complete converter but such discussion would be too complex and therefore not suitable for the intended purpose.

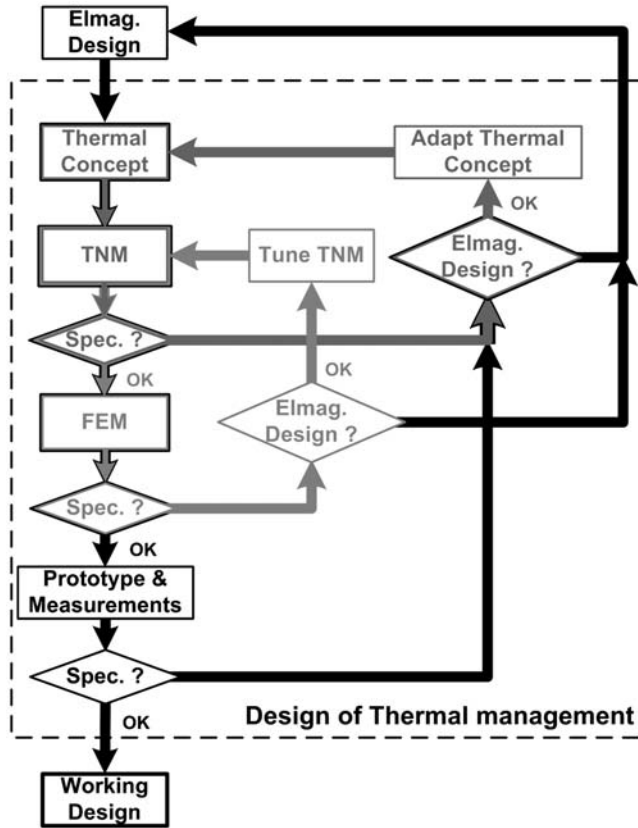


Figure 4-18: Block diagram of design and evaluation process used for power magnetics

Loop I employs a first-order 3D thermal network model. This model is utilised to get a fast first-order estimate of hot-spot temperatures for the cores and windings. The model is mostly used in the initial design stages. If the results do not comply with the specifications, changes are made in the thermal concepts or in the electromagnetic design. The first-order model of Transformer Prototype I is shown in Figure 4-19 superimposed on the vertical and horizontal cross-sections of the transformer structure. This model is more detailed than the previously discussed core and winding models (paragraph 4.2.2) because a higher accuracy is required. As can be seen, the core and windings are modelled separately. This is allowed by the presence of air gaps, which “thermally decouple” the two structures and therefore the heat exchange between them can be disregarded. The power loss of the central core leg is lumped to one heat source that is positioned in the centre of the model. The same spot is also assumed to be the core hot-spot. The power dissipation in the outer core legs is disregarded because hot-spots are not expected in these parts of the cores due to their short distance from the thermal surfaces. The winding model is built in several sections, with power dissipation placed in the central point of each section. There are four sections situated inside of the cores plus two end sections outside the cores. Furthermore, each winding section consists of inner and outer winding layers with their own power dissipations. The heat conduction inside the leakage layer is assumed only in a direction perpendicular to the layer. The heat transfer along the layer can be disregarded due to the low thermal conductivity of the leakage layer material. The heat pipes are modelled by using their effective thermal resistances. The thermal surfaces and short heat-conducting elements are assumed to be ideal without a temperature drop. Models for Transformer Prototypes II to IV were constructed in a similar way.

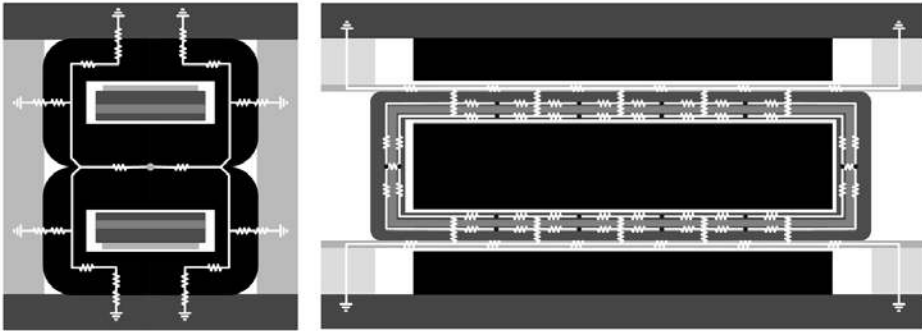


Figure 4-19: Thermal network model of Transformer Prototype I; a) front view - core model, b) top view - winding model; ●, ● - assumed points of power dissipation, possible hot spots.

Loop II (light grey in Figure 4-18) is based on finite element modelling. An example of FEM model is shown in Figure 4-20 for Transformer Prototype I. The FEM models are utilised to obtain more detailed and more accurate results and to tune the first-order models. The symmetry of the transformer structure was used to simplify the model by modelling only one-eighth of the structure. The model shown in Figure 4-20 includes also the filter inductor. The reason for this is that in Transformer Prototype I, the filter inductors and the transformer were integrated into a single structure (see paragraph 3.6.1). The cores and thermal paths were modelled as homogeneous materials with the same thermal conductivity in all directions. The core material is in reality not homogeneous due to core laminations. The curvature of the core and FEM program restrictions for assignment of the thermal conductivities resulted in thermal conductivity perpendicular to the laminations being used for all directions. The windings were assumed with different thermal conductivity along the layers and perpendicular to the layers. For both directions, effective thermal conductivities calculated by equations (4-4) and (4-5) were used. The corner elements were assumed with homogeneous thermal conductivity equal to conductivity of copper for good coupling of horizontal and vertical winding layers. A comparison of the results calculated by the first-order and FEM model showed a deviation of the results within 10% of the hot-spot temperature calculated by FEM. FEM was assumed to be more accurate than the first-order model because it uses a finer mesh.

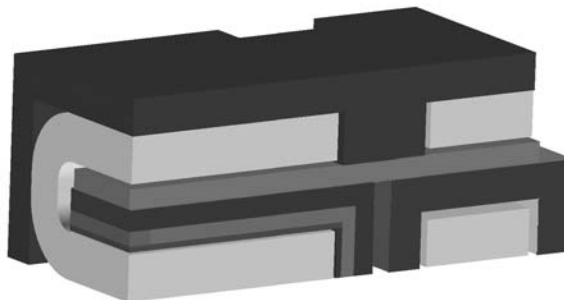


Figure 4-20: 3D model of transformer / inductor structure used in FEM analyses (Prototype I)

The last loop of the design and evaluation process (black in Figure 4-19) concerns the construction and measurements on the prototypes. This loop verifies the assumptions and results of the models. In the event that the results measured on the prototypes are not satisfactory, the whole design process would have to be repeated with a new set of design inputs. The details about the results of this loop are discussed in paragraph 4.7 as the results of the thermal measurements on Converter Demonstrator II.

4.5.1 Conceivable Thermal Management Solutions

The main aspects addressed in a power converter design are:

- Functional – electrical converter function
- Thermal – temperature distribution, preventing hot-spots and accumulation of heat
- Spatial – power density
- Electromagnetic – EMI, EMC mitigation

To attain a good design, all these aspects must be addressed in a way that the optimal converter performance is reached in all of them. EMC and EMI were not addressed because they are beyond the scope of this thesis. In the following paragraphs, four conceivable design solutions will be presented. The main purpose of these discussions is to evaluate the proposed solutions and select the one with the highest power density. It is assumed in the discussions that functional aspects are inherently fulfilled and therefore the main attention is paid to thermal and spatial aspects of the proposed designs.

As discussed in paragraph 4.3, on the system level, the proposed heat-removal concept offers the freedom of choice of heat-removal methods. For this reason the evaluation of the solutions was made for two methods most likely to be used on the system level: forced-air and liquid cooling. The best solution was selected based on the total achievable power densities including the thermal management. The selected configuration was further evaluated for the thermal performance by means of detailed finite element modelling and by measurements on Converter Demonstrator II.

Heatsink Design and Optimisation

Heatsinks are typically included in the total power-density figures of conversion system with the air cooling. Therefore, the heatsinks were designed for each of the solutions prior to a comparison of the solutions.

The optimisation of the forced-air-cooled heatsink was based on [61]. The presented procedure optimises the number of fins and their thickness for a certain heatsink area and a specific fan. The optimisation utilises the thermal network model of a cooling channel as shown in Figure 4-21. More details about the calculation of the appropriate thermal resistances can be found in [61].

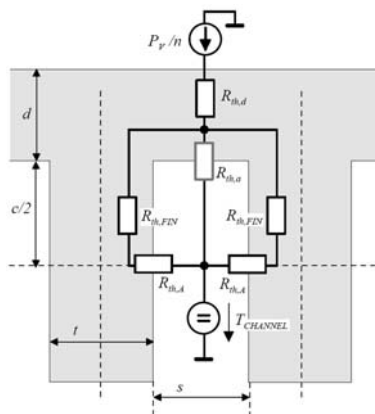


Figure 4-21: Thermal network model used for heatsink optimisation [61], R_{th} – appropriate thermal resistances, P_v – heat dissipated in the heatsink, n – total number of channels, $T_{channel}$ – air temperature in the channel

To remove the heat from the converter demonstrator, several fans are needed. Therefore, a heatsink section was optimised for a single fan and the performance was multiplied by the number of fan-heatsink structures that would fit onto available thermal surfaces. The main optimisation constraints were the power dissipation of the converter module and the maximal allowable temperature rise. A

power dissipation value of 1500 W, which was derived from measurements on Converter Demonstrator I (paragraph 2.7.4), and a specified heatsink temperature rise of 30 °C were used.

The heatsink performance varies with fan type. Therefore three types of fans of standard dimensions were considered: 40 mm, 60 mm and 80 mm. A fan heatsink configuration with the highest cooling performance was selected for each solution. The selected heatsinks are included in the solutions presented below.

An example of the resulting optimisation space for the heatsink thermal resistance is shown in Figure 4-22 for a model heatsink.

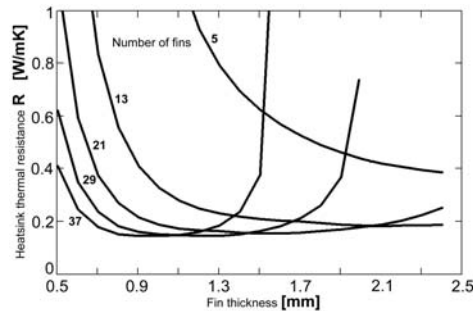


Figure 4-22: Example of an optimisation space for the heatsink thermal-resistance, heatsink thermal-resistance in relation to the fin thickness and number of fins (Solution IV. 110 mm length + fan 40 mm)

As can be seen, the calculated optimisation surface has minima which decrease slightly when the number of fins increases and the fin thickness decreases. A local minimum with a lower number of thicker fins is preferred because it is easier to manufacture such a heatsink. Therefore for the heatsink design of a particular converter solution, one of the local minima, which is a compromise between the low number of fins and low thermal resistance, was selected.

Solution I.

Solution I (Figure 4-23) represents an approach where all converter components are placed on a single thermal surface. The advantage of the resulting structure is that there is only one planar heat-exchange surface, which makes the integration of the converter into a larger conversion system simple. The simplification originates from the necessity of providing the cooling media (air, liquid) for only one heatsink and therefore the required tubing and ducting is minimised.

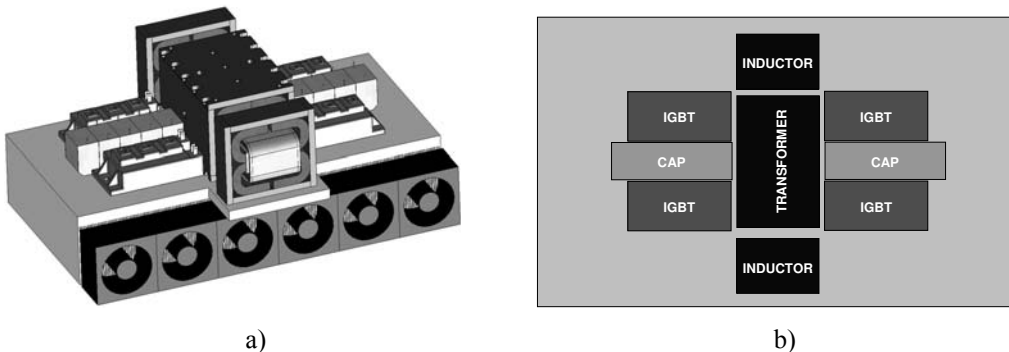


Figure 4-23: Solution I; a) 3D model, b) 2D layout of components on thermal surface

Solution II.

Figure 4-24 shows the layout of Solution II. The structure can be considered a hybrid between a single and double thermal surface structure. The reason for this is that, for the liquid cooling, the whole structure can be cooled with only one cooling plate inserted between the IGBT modules and the magnetics, as shown in Figure 4-24b. In the case of the air cooling, where a larger surface area is needed, two thermal surfaces would be used as shown in Figure 4-24a. The complexity of the total structure increases slightly for the two-surface solution because the cooling media must be provided for two heatsinks. The placement of the IGBT power modules “directly” on the surfaces of the power magnetics could lead to a heat flux crowding in the thermal element placed between these components. This has to be investigated in more detail in the event that this structure is selected for further application.

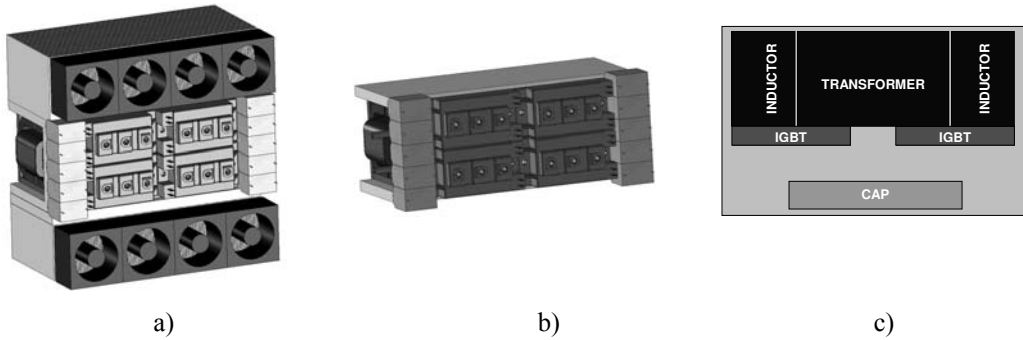


Figure 4-24: Solution II; a) 3D model forced-air cooling, b) 3D model liquid cooling, c) 2D layout of components on thermal surface

Solution III.

The third structure presented utilises two thermal surfaces where the components are organised in such a way that the risk of heat flux crowding is prevented. The differences in the arrangement of the components in comparison with Solution II are: separation of the transformer and inductors into two independent structures and placement of the IGBT modules directly on the thermal surfaces. The transformer and filter inductors are separated because two smaller separate structures suit the two-surface arrangement better. The heat generated in converter components is divided equally between the two thermal surfaces by: placement of the primary and secondary bridges each on a separate thermal surface, and by attachment of passives to both thermal surfaces. The magnetic component structures also serve as “heat-exchange bridges” in the event of inequality in the heat generation on the two surfaces.

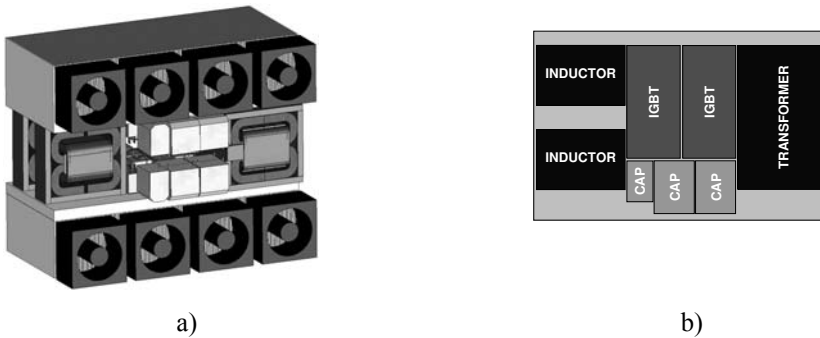


Figure 4-25: Solution III; a) 3D model, b) 2D layout of components on thermal surface

Solution IV.

Solution IV uses the same principles as Solution III. The only difference is that in structure IV the resonant capacitors are placed between the IGBT power modules, as shown in Figure 4-26. The main reason for this is that the separation of power modules allows for better heat spreading and hence a better and more equal distribution of heat dissipation on the thermal surfaces. Another consequence of doing this is an elongated converter structure. The elongated structure offers a larger area of thermal surfaces and therefore allows the use of smaller fans and smaller heatsinks than in the previous cases. A disadvantage of the capacitor placement is that the capacitors might be subjected to higher temperatures because of the proximity of all IGBT modules.

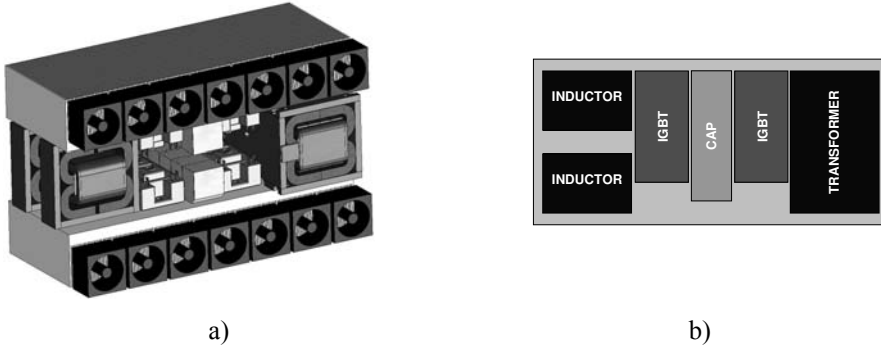


Figure 4-26: Solution IV; a) 3D model, b) 2D layout of components on thermal surface

Evaluation of Power Densities of Solutions

Table 4-1 lists the parameters of the optimised heatsinks and the estimated power densities for each solution. Power densities for the liquid as well as for the forced-air cooling were calculated from estimated structural dimensions. The dimensions were estimated by assuming an imaginary box in which the converter would fit entirely, including the heatsinks and fans.

Table 4-1: Parameters of thermal surfaces, custom designed heatsinks and resulting power densities

Solution	Dimensions of single thermal surface [mm]	Fan diameter [mm]	Number of fans per surface	Fin thickness [mm]	Number of fins per surface	$R_{th,t}$ [W/mK]	Power loss [W]	Volume Forced air cooling [litres]	Power density [kW/l]	
									Forced air cooling	Liquid cooling
I.	175 x 360	60	6	1.6	138	0.0193	1550	13	3.85	11.1
II.	105 x 240	60	4	1.7	76	0.0195	1538	9.1	5.5	14.1
III.	115 x 270	60	4	1.8	77	0.0193	1560	9.5	5.27	11.6
IV.	110 x 300	40	7	1.5	95	0.0197	1521	6.6	6.6	11.9

As can be seen, for both cooling methods considered, the worst results are obtained with Solution I. This is a consequence of placing all the components onto a single thermal surface, which results in large empty spaces throughout the structure. For the liquid cooling, the best results are obtained with Solution II, because only one small cold plate is required for the cooling. In the case of forced-air cooling, Solution IV is the best because of the elongated shape and the possibility of using smaller fans. It can be also noticed that the employment of two thermal surfaces in the case of the air cooling reduced the number of empty spaces inside the converter structures greatly, and this resulted in an increased power density. Solution IV was selected for the application in Converter Demonstrator II because of its high power density and versatility of choice between the two cooling methods considered.

4.6 Thermal Management of Proposed Solution

4.6.1 Practical Implementation of Proposed Solution

3D models of the proposed structures are shown in Figure 4-27 for the transformer, Figure 4-28 for the filter inductors and Figure 4-29 for the complete converter assembly. Figure 4-27 shows an exploded view of the transformer structure with all its subcomponents and heat-removal elements.

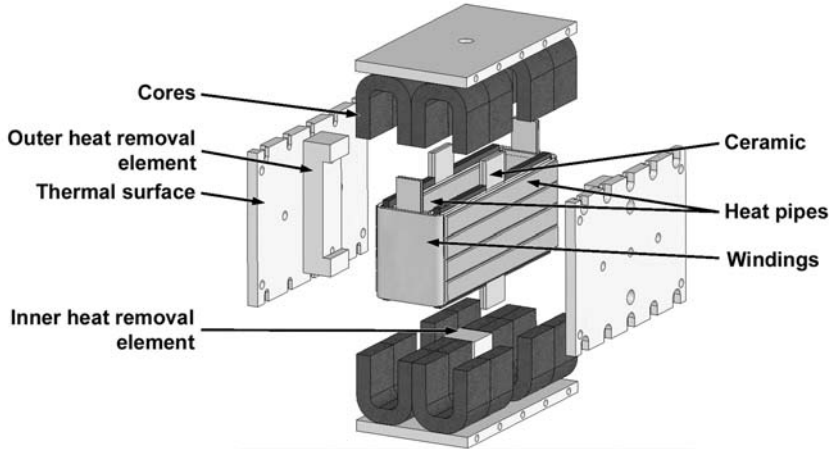


Figure 4-27: 3D exploded view of transformer structure of Prototype II and further

As can be seen, the cores are in a direct contact with the thermal surfaces and top and bottom heat-removal elements. A plastic, thermally conductive sheet is inserted between the cores and the aluminium heat-removal structure to allow for tolerances of the cores and to improve the thermal contact between the touching surfaces. The heat pipes are attached to the winding surfaces by thermally conductive epoxy. The use of epoxy results in a rigid winding structure and a strong bond between the heat pipes and the windings. As shown, the heat pipes are placed on the outside as well as on the inside of the windings. The heat from the heat pipes is conducted to the thermal surfaces through the inner and outer heat-conducting elements. Placing the heat pipes and the heat-conducting elements in the magnetic field of the windings results in additional eddy-current losses generated in these parts. These losses increase the total component loss but it is assumed that the good thermal contact of these elements to the heatsink would prevent excessive heating. In the event of large loss-generation, the aluminium heat-transfer elements must be replaced by elements made of thermally conductive ceramic. Simple ceramic elements are already in use in the presented structure. Their function is to aid the heat removal from the centre of the windings and the leakage layer. Ceramic is used at this place because the space between the primary and the secondary has very high magnetic field strength.

The structure of the filter inductors (Figure 4-28) is of the same design as the transformer structure. The only difference is that the heat pipes are attached to the outside of the windings only. They thermally connect the two inductor windings to the outer surfaces. The collected heat is removed to the thermal surfaces by the outer heat-removal elements. Small trenches are made on the inner side of the thermal surfaces in the locations of the core air-gaps. Their purpose is to reduce the losses in the aluminium structure due to the fringing effect of the air-gaps. The influence of the air-gap fringing on the winding foils and the heat pipes is reduced by not filling the winding window completely with the windings but leaving an empty space on the inside and the outside of the windings.

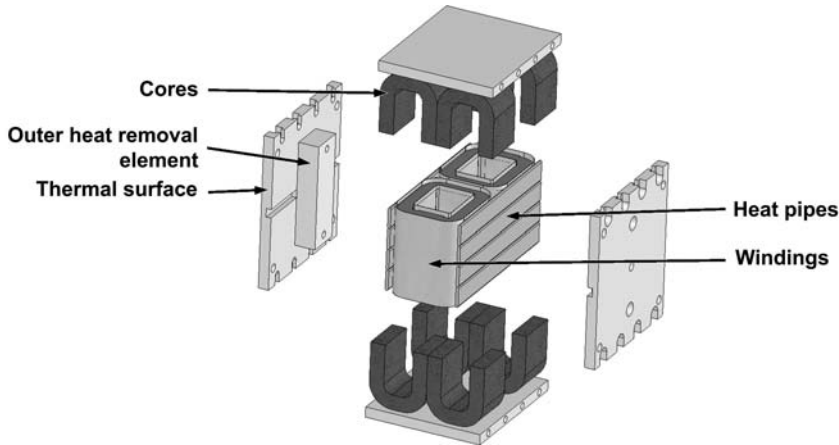


Figure 4-28: 3D exploded view of inductor structure

Figure 4-29 shows the complete converter structure. Each IGBT bridge is placed on one of the thermal surfaces. The resonant capacitors are placed between the IGBT modules. They are pressed on the heatsink by the bus-bar structure, which joins together the capacitors and the power modules. The thermal connection between the capacitors and the heatsink is improved by the use of a thermal clad material as the interface material. The transformer and the inductor structures are placed on the right respectively on the left of the IGBT bridges. The converter input and output are situated on the two opposite sides of the structure.

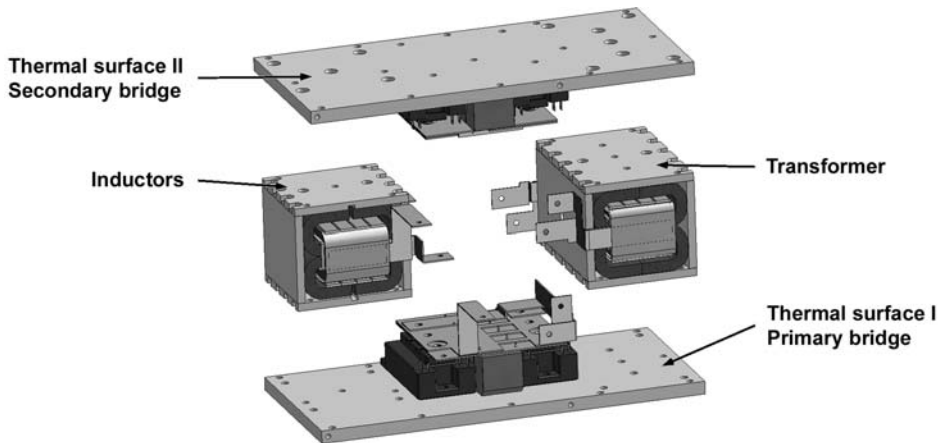


Figure 4-29: 3D exploded view of converter structure

4.6.2 FEM Thermal Analysis of Proposed Structure

The proposed structure was thermally analysed by finite element modelling. The FEM approach was chosen because it offers detailed temperature information throughout the converter volume. The limitation of the FEM approach is the model size. The size and the complexity of the model increase dramatically with the dimensions of a simulated structure, something that is especially true for 3D models. The proposed converter structure is relatively large which makes the 3D FEM simulation of it difficult. The situation is exacerbated by the fact that the FEM simulation software available has a licence that limits applications to the use of 128 000 nodes or elements. Exceeding this number was not possible and therefore other solutions were used to obtain more detailed results.

Splitting the model into several parts, using symmetry and simplifying the models were methods used to reduce the size of the FEM model. Splitting the model into several parts is based on constructing separate models for components that can be modelled independently. The linearity of the conductive heat-transfer permits summation of the particular results and their superposition on the converter structure. The block diagram of the implemented modelling process is shown in Figure 4-30. The detailed component models, their descriptions and the results are attached to this thesis as Appendix C.

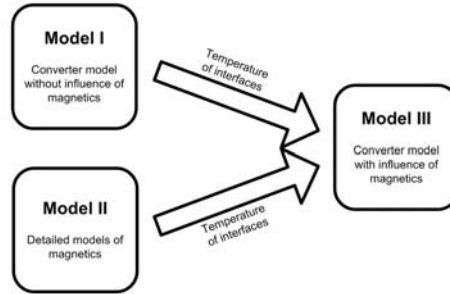


Figure 4-30: Block diagram of split thermal analyses

The hot-spot temperatures calculated by the FEM models are: 95 °C for the IGBTs, 90 °C for the diodes, 132 °C for the transformer and 110 °C for the inductors. The highest temperature rise for the magnetics was observed across the winding isolation, which was also expected. The heating of the magnetic components due to the heat generated by IGBTs and diodes was within 1 °C, which was considered negligible. The results of the modelling confirmed that the proposed heat-removal concept performed as expected. Only the hot-spot temperature of the transformer windings exceeded the maximal temperature defined at 120 °C. The calculated temperature was lower than the limiting temperature of the used materials (150 °C) and therefore this design was used in Converter Demonstrator II.

4.7 Practical Evaluation of Thermal Management

Numerous thermocouples were implemented throughout the structure of Converter Demonstrator II to assess the performance of the converter's thermal management. The measuring system consisted of thermocouples connected to a data logger and a computer. The thermocouples were placed on the surfaces of the components as close to the expected hot-spots as possible. The results presented in this paragraph were measured on the combination of Converter Demonstrator II and Transformer Prototype III. Transformer Prototype III (transformer without the leakage layer) was used because it offered the best and the most stable performance throughout the working load range. The transformers with the leakage layer failed during the power tests due to the isolation failures (see paragraph 3.6.1).

During all thermal measurements, the converter's thermal surfaces were cooled by a water-cooling circuit of load resistors. The cooling system consisted of a pump, tubing and a 1 m³ water storage tank. The cooling water was pumped in a loop through the load and in the same time through the coolers of the converter. The operation of this system was limited in time by the maximal temperature of the cooling water. This temperature was limited to 60 °C in order to prevent the load resistors from overheating. Full-power operation of the converter and load could be sustained for approximately 40 minutes.

A typical thermal response can be described by an asymptotic waveform as illustrated in Figure 4-31. The temperature per unit represents the steady-state temperature reached in per-unit time. Due to the time limitation, for each measurement on the converter demonstrator, what is here called a

“fundamental steady-state” was reached, temperatures were recorded and the sequence was followed by the next measurement. The fundamental steady-state was determined by following the thermal response of the system and subjectively judging the moment when the temperatures started to level off to the real steady-state. As illustrated in Figure 4-31, by doing this, the time required for the measurements can be shortened by as much as 50%, whereas the measurement accuracy is reduced by approximately only 8%. The measurements were performed in a progressive manner with respect to the output power. This means that at low power, where the time available for the measurements was longer, the temperatures were measured closer to the real steady-state than at high power.

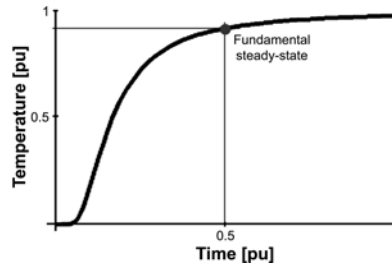


Figure 4-31: Asymptotic waveform represents a typical thermal response

Figure 4-32, Figure 4-33 and Figure 4-34 show the temperature rise for various components with respect to the water temperature at the heatsink inlet. The measurements were taken for the converter operating in the direction 750 V – 600 V. The power load of the converter in the presented figures varies over a wide range from close to zero to almost the nominal load of 50 kW. The load range was defined by the available resistances of the resistive load.

The temperature rise measured on the heatsinks and on the surface of one of the resonant capacitors is shown in Figure 4-32. For the measurements of the heatsink surface temperatures, the thermocouples were placed next to the bases of the power modules. As can be seen, higher temperatures are measured on the heatsink of the active bridge. The difference in the temperature rise between the two heatsinks for the converter operating at full power was about 8 °C, which is rather substantial. These temperature rises are much higher than calculated, which indicates that the thermal conductivity of the base-plate material used is possibly lower than expected.

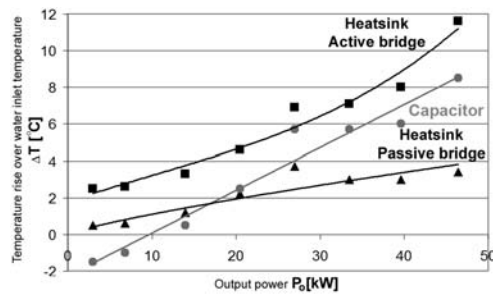


Figure 4-32: Measured temperature rises versus output power for heatsinks and resonant capacitor

The temperature rise of the resonant capacitors was measured on the surface of a capacitor placed in the middle of the capacitor assembly of the passive bridge. As can be seen, at low power levels, the measured temperature rise is negative. This indicates the capacitor being cooled below the temperature of the coolant (around 40 °C at that point) by the bus-bar and the thick output cables connected to the bus-bar. At full-power operation, the temperature of the capacitor surface is about 4.5 °C above the temperature of the base plate. This means that at a base-plate temperature of 70 °C, the capacitor would operate with a hot-spot temperature of 85 °C, which is also its maximal operating temperature.

For the capacitors placed in the active bridge, the same surface temperature is about 86.5 °C, which results in a hot-spot temperature of approximately 100 °C, which is higher than the maximal operating temperature. This means that other more advanced heat-removal concepts presented in paragraph 4.2.3 should be used for the removal of heat from the resonant capacitors.

Figure 4-33 depicts the temperature rise measured on the power transformer. The measured values are higher than calculated by approximately 10 °C and the hot-spot temperature exceeds the specified maximum of 120 °C. A possible explanation for this is that the thermal contact between the power-dissipating volumes and the heatsinks was worse than expected. In the case of the windings, it was probably the thermal contact between the winding layers. The thermal contact between the winding layers was not included in the thermal models due to the related complexity of the model. In the case of magnetic cores, the contact between the cores and the thermal elements could be worsened by high manufacturing tolerances of the amorphous cores but also by thermal conductivities different from those used for the calculations. Another explanation for the high core temperature is that its measurement was influenced by the high winding temperature due to the tight spaces inside the transformer structure. An indication of this is also the rather steep core temperature rise with increasing power. The temperature rise was expected to be lower because of the constant core power-loss related to the fixed excitation voltage. In spite of the measured temperatures being higher than calculated, they were within the operating ranges of the used materials (amorphous cores and Kapton® > 150 °C).

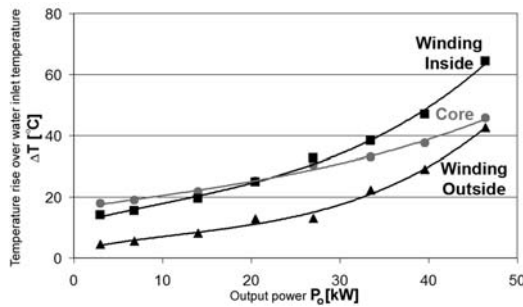


Figure 4-33: Measured temperature rises versus output power for power transformer

The core and winding temperature rises for both filter inductors are depicted in Figure 4-34. The data shows that the winding temperatures are much higher than the core temperatures and that the temperatures measured on both inductors are higher than calculated. The heat removal from the windings was obstructed also in this case by the layering of the windings. The temperature rise of the output inductor winding is higher than that of the input inductor winding because of the higher operating currents. For all measurements, the measured temperatures were below the specified maximal temperature of 120 °C.

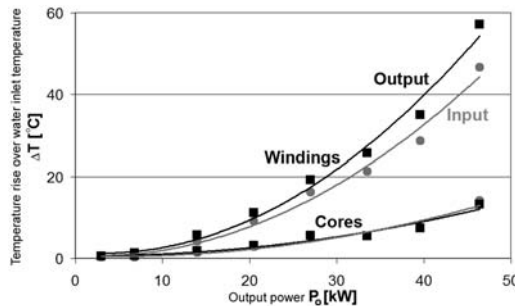


Figure 4-34: Measured temperature rises versus output power for filter inductors

4.8 Conclusions

The goals of the thermal management design process presented in this chapter are good thermal performance, high power density and simplicity. To obtain functionally and constructionally simple design with high performance, the use of primary conduction was proposed as the main heat-transfer method. It was also proposed that heat pipes be used at places where higher heat fluxes were required and the conduction in solid materials was not sufficient. The collection of heat at dedicated thermal surfaces was also included in the thermal management concept because it makes integration of the converter into larger conversion systems easier.

The heat removal from the power passives was analysed thoroughly. The suitability of different component surfaces for heat removal was analysed with respect to component geometries by using simplified thermal network models. It was shown that the best results can be obtained by the removal of heat from the outer core surfaces (core envelope) and from the surfaces of the winding sections placed inside the winding windows.

Several solutions were presented based on the proposed thermal management concept. The best of the solutions with respect to power density was selected for application in the converter demonstrator. The selected solution was analysed further in detail by FEM, and was eventually tested by measurements on the converter demonstrator.

Measurements on the converter prototype revealed higher temperatures than calculated. The main reasons for the observed difference were possibly worse material performance than expected, high core tolerances and additional thermal resistance of the contacts between the winding layers. In the case of the resonant capacitors, it was suggested the tested configuration of the capacitors be replaced with a more advanced solution in order to prevent overheating of the capacitors.

Although the temperatures were higher than expected, they were still within the operating range of materials and components. Converter Demonstrator II could sustain long-term operation at full power. It was shown that the proposed thermal management results in a converter with a full load efficiency of 97% and a high power density of 12 kW/l for the liquid cooling and 6.6 kW/l for the forced-air cooling.

Chapter 5 *Integration of the Three Cornerstones*

5.1 Introduction

In the introduction, three cornerstones of high power density design for high power converters were identified. These cornerstones were addressed separately in the previous chapters. The final converter structure is a result of the design in the three cornerstones but also of the spatial component integration. Because the spatial integration was not included in the previous discussions, the first part of this chapter is dedicated to this aspect.

The second part, called scaling up, considers the application of the proposed concepts to higher power levels. The scaling up influences all three cornerstones by affecting the performance of components. The evolution of the performance is estimated in this chapter with respect to increasing the current and voltage rating. In addition, the component volume is assessed for double voltage and current ratings by a simplified component design. Based on the results, the evolution of the power density is addressed with respect to scaling up.

5.2 Spatial Integration of Components

Spatial integration of converter components is important to obtain a high power density. The key to the successful integration of components is to make design choices which result in components of compatible dimensions and shapes. In such a design, universal rules that can be followed in order to gain the successful component integration do not exist. Therefore, basic guidelines that should serve as an aid in the design of high power density high-power converters are offered in the following paragraphs. The discussions are based on the structure of Converter Demonstrator II.

5.2.1 Restrictions of Spatial Integration of Components

Design tasks preceding the spatial component integration pose restrictions on the component placement. The components must be placed inside a converter structure in such a way that the converter circuit performance is not detrimentally affected by extra parasitic elements. One of the approaches that can avoid the problems related to parasitics is to group components into functional blocks within which the circuit parasitics can be controlled effectively. In this thesis, this approach resulted in the following functional blocks:

- input inductor
- IGBT bridge I (primary, includes IGBTs and resonant capacitors)
- transformer
- IGBT bridge II (secondary, includes IGBTs and resonant capacitors)
- output inductor

These functional blocks are illustrated on the converter structure shown in Figure 5-1a. This subdivision of the converter circuit was chosen because the parasitic inductances between the functional blocks do not harm the converter function. The converter “immunity” to these parasitics

inductances relies on the fact that they are connected in series with the functional inductances – like, for example, transformer leakage inductance and filter inductances. The power flow inside the structure of Converter Demonstrator II is organised as indicated in Figure 5-1b. As can be seen, the power flow creates a continuous 3D loop throughout the converter structure. This means that abrupt transfer of power between different locations inside of the converter is avoided, which reduces the effects of parasitics.

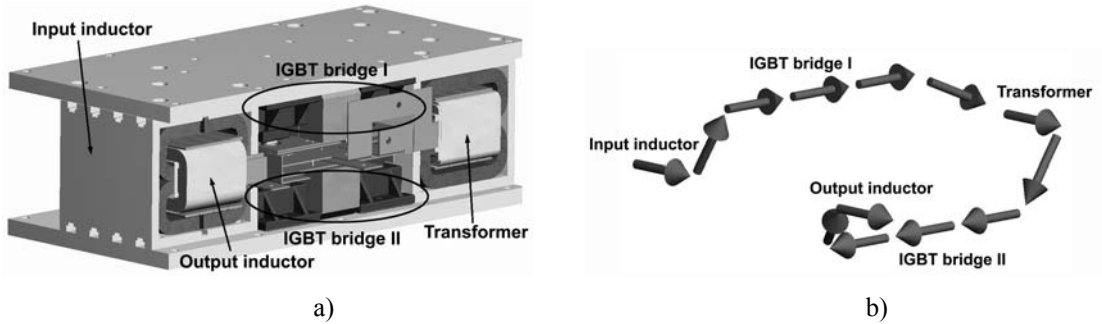


Figure 5-1: a) Spatial organisation of Converter Demonstrator II with indicated functional sub-blocks, b) 3D indication of power flow throughout the structure of Converter Demonstrator II

Other limitations of the component placement often originate from the thermal design. In most thermal design concepts it is required that the components with high heat fluxes such as active components are placed directly on the thermal surfaces to limit their temperature rise. It might also be required that the active components be placed in the centre of the thermal surfaces or further apart for better heat spreading. These aspects were considered in the design of the converter demonstrator and they are included in all the designs presented in Chapter 4.

5.2.2 Integrated Converter Structure

It is difficult to give universal guidelines to the spatial converter design because of the complexity of the converter design process. The spatial component integration is often one of the last tasks of the design process, with many design decisions being made prior to this task. The following guidelines provide some hints on how to make the spatial component integration a part of other design tasks. This will be discussed by using the structure of Converter Demonstrator II and converter design process as discussed in paragraph 1.2.4.

The spatial integration of components relies primarily on component shapes and dimensions. These are typically a result of the component and thermal management design and are related to component functions and processed power. With respect to the design process, the individual design of high-power passives in particular offers some flexibility. For example, in the transformer design, the core cross-section is restricted by the processed power but the dimensions and hence the shape can vary. This was used in paragraph 3.4.1, where the transformer shape and dimensions were studied in relation to the transformer volume and power losses, while the nominal power, currents and voltages were kept constant. This study resulted in a reduced transformer volume in comparison with the conventional power transformers and in the same time in a shape which was easy to integrate into the proposed converter concept.

The shape of the transformer can be seen in Figure 5-2. Figure 5-2a depicts the core winding assembly with the heat-removal elements placed in the centre of the structure. Figure 5-2b shows the complete transformer structure. The structure was designed for the nominal power of 50 kW and operating frequency of 25 kHz.

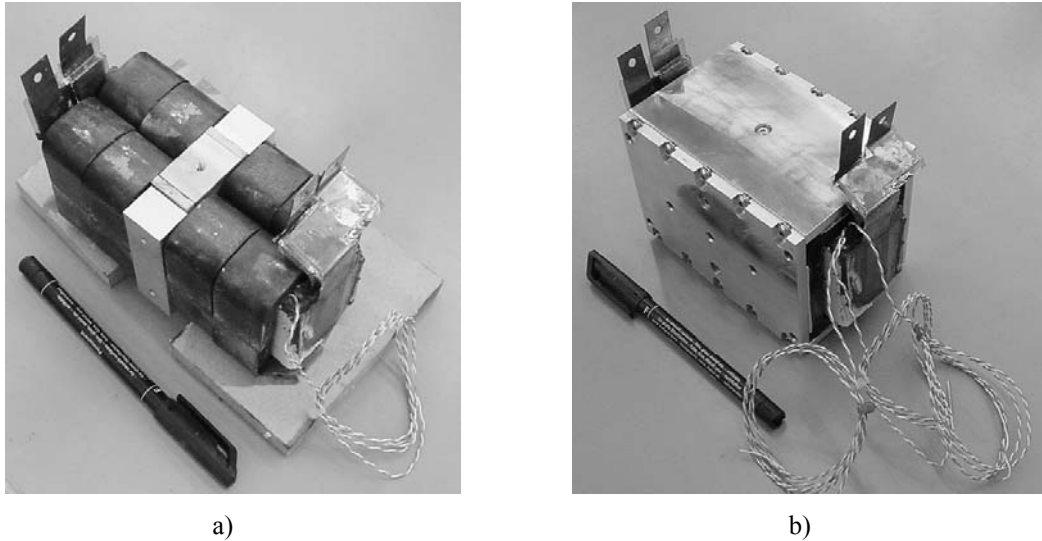


Figure 5-2: Transformer Prototype II.; a) core – winding assembly b) complete structure

The easy spatial integration of components also requires the compatibility of component dimensions. The converter designer must be aware that in some cases an attempt to improve the power density of a single component might result in an unchanged or even reduced power density of the complete converter. This occurs in cases where the resulting component shape is difficult to integrate. In Converter Demonstrator II, the compatibility of the dimensions inside the bridge modules was reached by selecting capacitors of the same height as the IGBT power modules. This is visible in Figure 5-3, which shows a single IGBT bridge placed on a thermal surface.

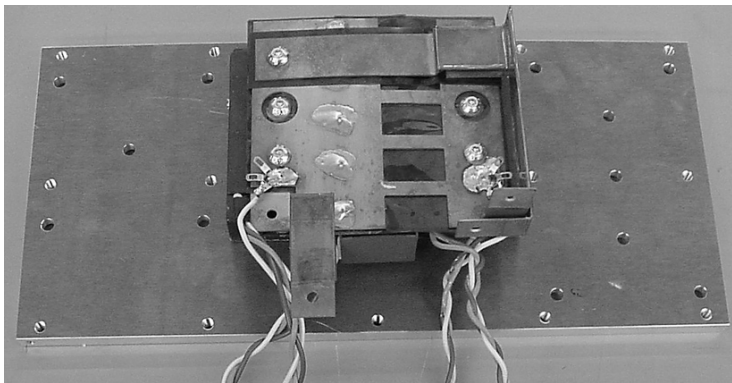


Figure 5-3: Single IGBT bridge functional block

The power magnetics were also designed with respect to the criteria of compatible dimensions. The filter inductors were designed with the same cross-section as the transformer. At the same time, the height of the magnetics was set at approximately twice the height of the bridge modules. The consequence of this is that the magnetics and bridge modules could be seamlessly integrated without much empty space between them (as shown in Figure 5-4).



Figure 5-4: Integration of converter components, view on bridge modules with filter inductor on the left and transformer on the right side

The level of component integration can be increased by the integration of several components into a single structure. This was implemented in the structure of the filter inductors as shown in Figure 5-5. In this structure, thermal management and mechanical parts were integrated for the two filter inductors. This resulted in a reduction in the number of parts used and also in an improved power density.

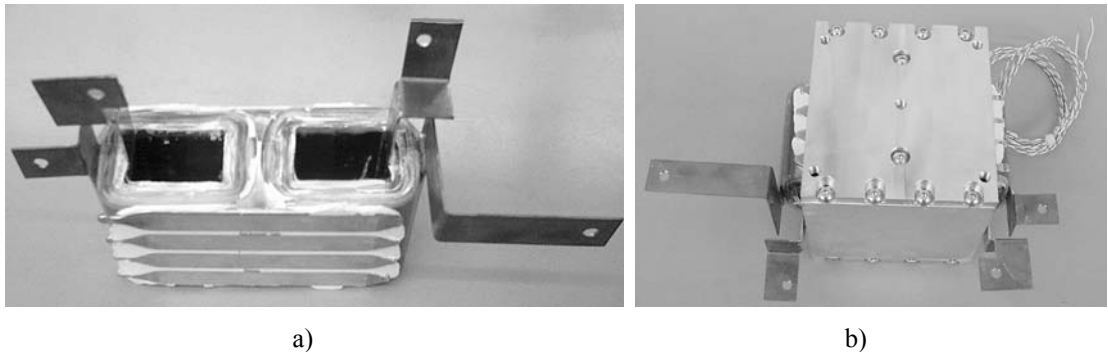


Figure 5-5: Integrated structure of filter inductors used in Converter Demonstrator II.; a) winding structure, b) complete structure

The disadvantages of this configuration in the case of the inductors are: a requirement for increased isolation thickness, and an increased magnetic coupling between the two inductors. The requirement of increased isolation thickness originates from the fact that the two inductors are placed on different sides of the galvanic isolation. This requires special attention to their isolation from the thermal management system (heat pipes). The isolation failure would mean in this case bridging the galvanic isolation that would result in a hard short-circuit between the input and the output of the converter. The increased magnetic coupling between the two inductors is the result of their close proximity. The consequence of this can be worse rejection of common mode noise.

An alternative to conventional 2D converter layout that can improve the utilisation of space is a construction in 3D [59]. In such a construction, the placement of components is not restricted to an available planar surface: the third dimension is exploited as well. The advantages of the 3D approach are demonstrated by four conceivable solutions presented in paragraph 4.5.1. In this paragraph, Solution 1 was proposed as a 2D spatial concept, whereas the other solutions were based on 3D concepts. It was shown that the 3D component placement results in a higher power density. The disadvantage of the 3D approach is that the 3D structures are often more complex than 2D.

Implementation of the 3D component placement in Converter Demonstrator II can be seen in the model shown in Figure 4-29. The practical placement of the components on a single thermal surface is shown in Figure 5-6, while Figure 5-7 shows the complete converter structure from the front and rear

view. As can be seen, the 3D integration of the components resulted in very little empty space between the components. Notice that the only empty space in the presented structure is in the front part of the converter structure, in front of the bridge modules and the inductor structure. In the final converter structure this space could be used for placement of IGBT drivers and control circuits as shown in the 3D model of Figure 5-8. The complete converter would then be a rectangular volume of dimensions 300 x 140 x 107 mm. The only parts reaching beyond the specified volume would be the input and output power terminals. The power density of this complete structure was calculated as 11.13 kW/l. This high power density clearly demonstrates the possibilities and the potential of the concepts and design approaches proposed in this thesis.

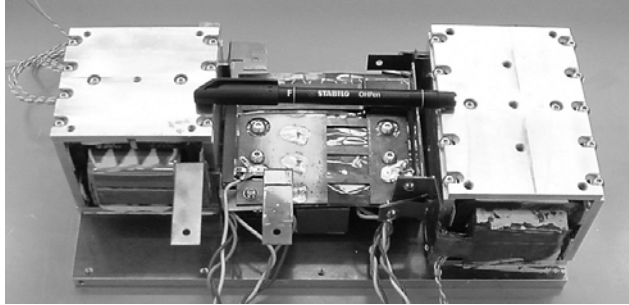
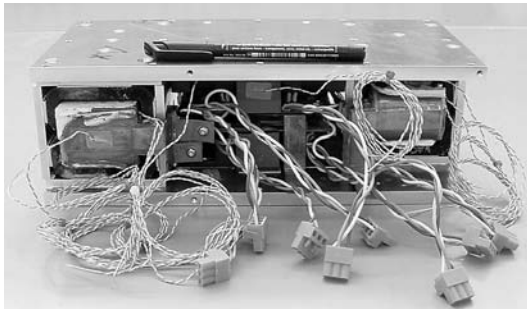
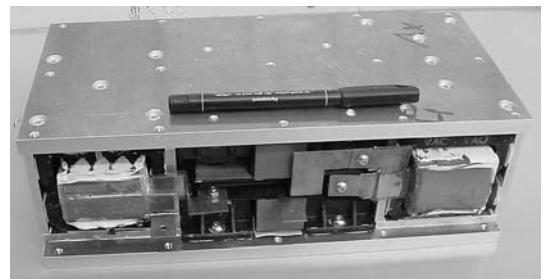


Figure 5-6: Single IGBT bridge, filter inductors (left) and transformer (right) mounted on single thermal surface



a)



b)

Figure 5-7: Complete integrated structure of Demonstrator II; a) front and b) rear view

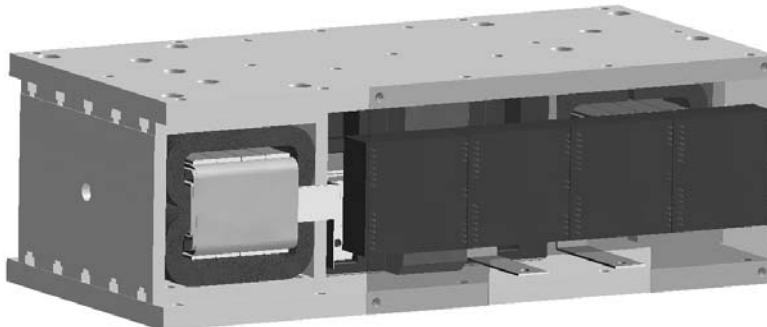


Figure 5-8: 3D model of the complete converter structure with driver and control circuits integrated in single volume, front view

5.3 Scaling-up

The main objective of this section is to discuss the applicability of the proposed technologies and concepts at high power levels. In principle, a system for increased power level could be obtained in two ways:

- by using multiple converter modules
- by designing a single unit for higher power

These two approaches are equivalent from the functional point of view but different with respect to power density and complexity, for example.

The first approach uses multiple identical converter modules where each unit processes a portion of the total power. The input and output voltage levels of the units determine the input and output voltage of the complete system. These voltages can be modified by series and parallel connection of inputs and outputs of the units. In principle, the power density of such a multi-module system could be equal to the power density of a single unit used in the system. In real constructions, the total power density depends also on the level of the spatial integration of the units and on the volume of the required supporting infrastructure. To prevent overloading, special attention must be paid to power-sharing between the converter modules. Also, the heat removal from each converter module must be considered to prevent overheating. In principle, the number of units in a system is unlimited. In practical applications, the limitation is posed by the complexity of the resulting system. The converter concept presented in this thesis should be able to work in a multi-unit configuration. Power-sharing control is possible by controlling the IGBT turn-off in close proximity to the optimal turn-off point. Such control of the turn-off time results in only a slight increase of the power loss. The multi-unit operation was not tested and will have to be the subject of future research.

The second approach uses a single high-power unit designed for a particular application. The advantage of this approach is the simplicity from the system point of view, because the whole system contains only one conversion and control unit. The main disadvantage is that for each application a new converter must be designed. The increase of the power of a single unit can be obtained by increasing the nominal voltage rating, the nominal current rating or both at the same time. In the following paragraphs, the effects of increasing the rating on the component performance and on the power density are discussed.

5.3.1 Component Performance and Scaling up; Single Unit approach

Active Components

The power loss of active components is directly related to the processed voltages and currents and to the properties of the semiconductor devices used. An increase of the voltage and current levels of the power converter usually means that semiconductor devices with higher ratings must be used. The combination of higher power and of the use of larger devices yields an augmented power loss increase.

In general, it can be stated that scaling up influences the conduction as well as the switching losses. The total power loss P_T can be described in a simplified form as:

$$P_T = P_{con} + P_{sw} = V_{ON} I_{av} + f_s E_{sw}, \quad (5-1)$$

where P_{con} is the conduction loss, P_{sw} is the switching loss, V_{ON} is the average voltage drop over the switch, I_{av} is the average current flowing through the switch, f_s is the switching frequency and E_{sw} is the energy lost in the switch in one switching cycle. The maximal power loss P_{max} per switch is limited by the maximal junction temperature T_{max} and the thermal resistance R_{th} of the package as defined by equation 5-2.

$$\Delta T = P_T R_{th_IGBT}, \quad (5-2)$$

If the sum of the conduction and switching loss exceeds the maximal allowable power loss then the switching frequency must be reduced.

The relation between the allowable switching frequency and the power rating is estimated based on the datasheet parameters of semiconductor devices related to the generation and removal of heat. The data of Trench-FS IGBTs is used for the calculations. Unfortunately, the component power loss in a particular topology cannot be predicted directly from the datasheet parameters. The main problem is that these parameters are usually measured at conditions different from those in specific applications. Therefore, the calculated frequencies are used here solely to get the trend, and no relevance is ascribed to the exact numerical values. The trend lines are calibrated by using data obtained from measurements on the converter prototypes discussed in this thesis. The relevant datasheet parameters are identified as:

- E_{sw} – switching energy loss of IGBT switches – related to switching loss
- Q_{rr} – reverse recovery charge for diodes – related to reverse recovery loss
- V_{ON} – on-state voltage for IGBTs and diodes – related to conduction loss
- $R_{th_igbt}, R_{th_diode}$ – thermal resistances junction to heatsink for IGBTs and diodes – related to heat removal

The variation of the switching frequency with scaling up is calculated according to equations 5-1 and 5-2. The power losses measured on the converter prototypes are correlated to the switching energy E_{sw} and the on-state voltage V_{ON} of the used semiconductor switches by using equation 5-1. Further, it is assumed that at higher power levels, the power loss in the high-power switches follows the trend given by the datasheet parameters E_{sw} and V_{ON} . To calculate the allowable switching frequency from the allowable power loss, the same junction temperature is assumed for all considered devices. By assuming this, equations 5-1 and 5-2 can be combined for the known device (converter demonstrator) and the unknown high-power device (scaled converter), which results in the following equation:

$$(V_{ON_1}I_{av_1} + f_{s_1}E_{sw_1})R_{th_igbt_1} = (V_{ON_2}I_{av_2} + f_{s_2}E_{sw_2})R_{th_igbt_2}, \quad (5-3)$$

where subscript “1” marks the parameters of the IGBT switches used in the converter demonstrator and subscript “2” marks the parameters of the devices used in the scaled converter. By manipulating equation 5-3, the following equation can be derived:

$$\frac{f_{s_2}}{f_{s_1}} = \frac{\frac{R_{th_igbt_1}}{R_{th_igbt_2}} P_{T_1} - \frac{V_{ON_2}}{V_{ON_1}} P_{con_1}}{P_{sw_1}} \frac{E_{sw_1}}{E_{sw_2}}, \quad (5-4)$$

The diode parameters are not directly involved in the estimation of the operating frequency. They are used only to estimate the power loss in the rectifier diodes and consequently to estimate the temperature of the diode chips. It is consequently verified whether the chip temperature is below the maximal operating temperature.

From 5-4, the operating frequencies were estimated for a complete range of 1200 V and 1700 V IGBT devices for a chip temperature rise of 30 and 50 °C. The temperature rise of 30 °C is used in the converter demonstrator, whereas the temperature rise of 50 °C is the maximum allowable temperature rise for the considered heatsink temperature of 70 °C. The results of the calculations are plotted in Figure 5-9.

The results plotted in Figure 5-9 can be represented as frequency bands into which the operating frequency would fall with scaling up. The two areas correspond to 1200 V and 1700 V IGBT devices. The transition from 1200 V to 1700 V area represents the increase of the converter voltage rating. Moving in the same area from left to right represents the increase of the current rating. In general, it can be concluded that low-voltage devices can operate at much higher operating frequencies than high-voltage devices. The operating frequencies for the 1200 V devices are indicated to be more than twice those of the 1700 V devices. Notice also that for a temperature rise of 30 °C and 1700 V IGBT

devices, the converter power is limited to approximately 500 kW in this type of application. With respect to the current rating, the high current devices seem to operate at approximately half the operating frequency of the low current devices.

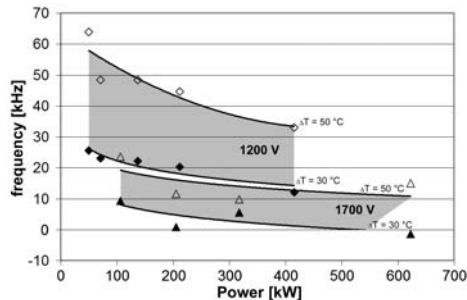


Figure 5-9: Operating frequency versus converter power rating for 1200 V and 1700 V IGBT power modules

The calculated power losses are also used to estimate the total power loss in active devices. This power loss is plotted in Figure 5-10 with respect to the converter power rating as a percentage of the total converter power. The figure indicates that approximately 1 to 2.5% of the processed power is dissipated in the active devices. As can be seen, the power loss of active devices expressed as percentage of the total power decreases as the converter power rating increases. It can also be seen that the power loss generated by the 1200 V and 1700 V devices can be considered identical in the power range where both types can be implemented. Relating the estimated power loss in active devices to the converter efficiency allows one to conclude that the efficiency is expected to increase with the power rating increasing.

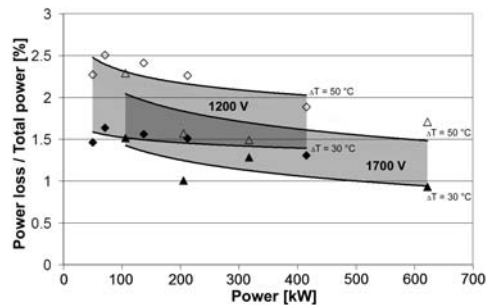


Figure 5-10: Power loss versus converter power rating for 1200 V and 1700 V IGBT power modules

Passive Components

Active devices are typically available as off-the-shelf components. By contrast, passive components and especially magnetics are often custom-designed and every increase of the current and voltage rating requires a new design. Capacitors, inductors and transformers exhibit different sensitivity to scaling up and they will therefore be discussed separately here.

Capacitors that carry large currents must have their electrodes designed specially for this purpose. The current of medium-power metal-film capacitors is limited to approximately 0.04 A/nF. Higher current ratings are typically realised by a series / parallel connection of several capacitors, which lowers the current per capacitor to an acceptable value. With respect to the voltage rating, the dielectric thickness must increase as the voltage increases. This reduces the capacitance and complicates the removal of heat from the capacitor. Typically, series / parallel connection of capacitors must be used here as well.

In the converter topology proposed in this thesis, capacitors are used as the resonant capacitors. These must carry relatively high currents and they must also sustain relatively high voltages. In order to assess the increase of the capacitor volume with the converter power rating, several converter and resonant capacitor configurations were investigated. The following aspects were considered in the investigation:

- voltage derating of the involved capacitors due to high operating frequency
- constant resonant impedance to maintain the same switching conditions for the active devices – capacitance value changes with the current and voltage rating
- issues related to heat removal from particular capacitors were disregarded

The power density of the capacitors was calculated by dividing the apparent power of the complete series / parallel capacitor bank by its volume.

The investigation showed that the power density of the resonant capacitors is independent of the converter voltage and current rating. It also showed that the power density increases with the voltage rating and decreases with the capacitance of a single capacitor used in the series / parallel bank. This is illustrated in Figure 5-11, which shows the relation between the power density and voltage rating. The two curves represent minimal respectively maximal capacitance available for a specific voltage rating.

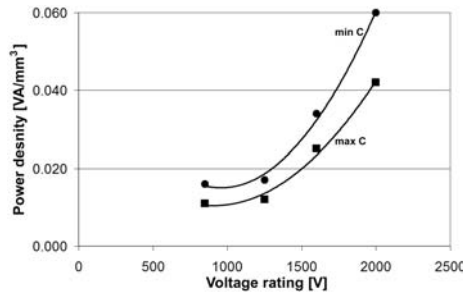


Figure 5-11: Power density of capacitors versus voltage rating of a single capacitor; *min C*, *max C* – minimal respectively maximal capacitance of a single capacitor for a specific voltage rating

Design of power magnetics strives to obtain a balance between the generated heat and the ability to remove it. In scaling up, the component volume must be increased in order to process the increased amount of power. In relation to that, the surface available for the heat exchange should also increase to maintain the balance between the heat dissipation and the heat removal. The balance can be maintained if the so-called surface to volume ratio is kept constant. In the following paragraphs, the scaling up is discussed with respect to the transformer concept proposed in Chapter 3 and to the thermal management concept proposed in Chapter 4. The scaling up was investigated by using the surface to volume ratio calculated for simplified core and winding models as shown in Figure 5-12.

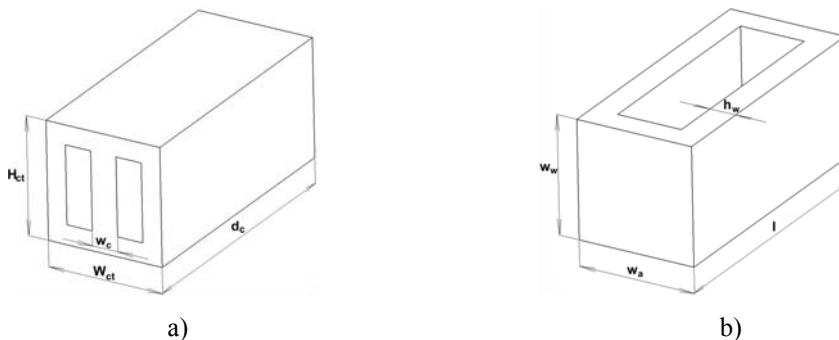


Figure 5-12: Simplified models of transformer parts; a) core, b) winding

The thermal concept presented in Chapter 4 separates the heat removal from the core and from the windings, which allows individual consideration of these two parts. As presented in paragraph 4.2.2, the core envelope is chosen as the preferred surface for the heat removal. The ratio of this surface to the core volume is calculated as:

$$\left(\frac{S}{V}\right)_c = 2\left(\frac{1}{H_{ct}} + \frac{1}{W_{ct}}\right), \tag{5-5}$$

where the dimensions are those defined in Figure 5-12. The volume of the core is considered for the complete transformer including the winding windows. As can be seen, the surface to volume ratio is independent of the transformer depth d_c . The surface to volume ratio for the windings follows from:

$$\left(\frac{S}{V}\right)_w = \frac{2}{h_w}, \tag{5-6}$$

where h_w is the total winding thickness as indicated in Figure 5-12. In order to simplify the derived equation, front and end winding sections were disregarded. The error introduced by this is considered to be small because the end sections of the proposed winding are short in comparison to the depth d_c . As can be seen, the surface to volume ratio is inversely proportional to the winding thickness h_w .

To assess the consequences of scaling up, the relations between the scaling up and the surface to volume ratio S/V , power loss P and temperature T are investigated. Scaling up is assumed to be something that requires an increase in the core and winding dimensions and consequently also changes the surface to volume ratio, power loss and temperature. The core and winding dimensions are varied such that the following parameters are kept constant: peak flux density B , current density J , number of turns N and frequency f_s . Due to the constant flux density B , an increase of the voltage rating results in an increase of the core leg width w_c or the core depth d_c . Similarly, an increase of the current rating results in an increase of the foil width w_w respectively the foil thickness h_f (represented here by the total winding thickness h_w) due to the constant current density. The analysis includes the effects of the winding isolation, which must be increased at higher voltage rating. When the isolation thickness is increased, the current density must be reduced in order to maintain the same operating temperature.

Table 5-1 shows the qualitative results of the analysis. The reading of the table is explained in the following example. Let us say that an increase of the voltage rating is required in order to scale up the converter and it is also preferred that the core width w_c be increased. The consequences for the core would be a reduced surface to volume ratio S/V , an increased core loss P and therefore an increased temperature T . At the same time, the increase of the core width w_c would also influence the windings. In the selected case, the surface to volume ratio S/V , the winding loss P and the temperature T would remain approximately constant. On the other hand, the isolation thickness must also be increased because of the higher operating voltage. The thicker isolation would consequently increase the winding temperature. Because in the presented case the core and the winding temperature would increase, the transformer structure would have to be redesigned to keep the temperatures constant. This would probably result in a further increase of the transformer volume.

Table 5-1: Variation of surface to volume ratio S/V , dissipated power P and temperature T indicated for current and voltage rating increase for power transformer, ↓ – value decreases, ↑ – value increases

Cause	Current rating ↑				Voltage rating ↑					
	Windings		Cores		Windings			Cores		
Structure	w_w ↑	h_w ↑	w_w ↑	h_w ↑	w_c ↑	d_c ↑	h_i ↑	w_c ↑	d_c ↑	
Varying parameter										
Consequences	S/V	const	↓	↓	↓	const	const	const	↓	const
	P	↑	↑	↑	↑	const	↑	const	↑	↑
	T	const	↑	↑	↑	const	↑	↑	↑	const

Table 5-1 shows that the winding width w_w or the foil thickness h_w should be increased with an increase of the current rating. If the winding width w_w is increased, winding temperature remains approximately constant, whereas the core temperature is expected to rise. By contrast, if the foil thickness h_w increases, both temperatures would rise. The table also indicates that the increase of the voltage rating affects the core as well as the windings. It seems that it is better for the core performance to increase the core depth d_c . On the other hand, for the windings it seems to be more suitable to increase the core leg width w_c . However, in both cases, the winding temperature is expected to rise due to the requirement of the thicker isolation and therefore the winding width would have to increase in order to improve the heat removal. The discussion shows that the voltage rating increase appears to yield larger components because of the necessity to increase the core as well as the winding cross-section.

In the case of the filter inductor, the inductance must be increased with increasing voltage rating and it must be decreased with increasing current rating. This originates from the requirement of maintaining the same ripple conditions at the input and output and from the necessity of modifying the resonant capacitance for different ratings in order to maintain the same switching conditions for the active devices. The change of the filter inductance can be performed by modifying the number of turns and keeping the core cross-section constant. This results in increasing the winding width w_w or the winding height h_w with increasing the current rating and in increasing the height of the winding h_w with increasing the voltage rating. In the case of increasing the voltage rating, the isolation thickness h_i must be increased as well, which results in a higher winding window cross-section than for the current rating increase. The relations between the ratings and the inductor surface to volume ratio, power loss and temperature are indicated in Table 5-2.

Table 5-2: Variation of surface to volume ratio S/V , dissipated power P and temperature T indicated for current and voltage rating increase for filter inductors, \downarrow – value decreases, \uparrow – value increases

Cause		Current rating \uparrow , $L_r \downarrow$				Voltage rating \uparrow , $L_r \uparrow$		
Structure		Windings		Cores		Windings		Cores
Varying parameter		$w_w \uparrow$, $h_w \downarrow$	$h_w \uparrow$	$w_w \uparrow$	$h_w \uparrow$	$h_w \uparrow$	$h_i \uparrow$	$h_w \uparrow$
Consequences	S/V	\uparrow	\downarrow	\downarrow	\downarrow	\downarrow	const	\downarrow
	P	\uparrow	\uparrow	\uparrow	const	\uparrow	const	\uparrow
	T	const	\uparrow	\uparrow	\uparrow	\uparrow	\uparrow	\uparrow

As can be seen from the table, the increase of the current rating is easier to accommodate in the inductor design. Increasing the winding width w_w and decreasing the winding height h_w results in an increase of the surface to volume ratio S/V and consequently the winding temperature remains constant. The situation is worse in the case of increasing the voltage rating due to the change of the surface to volume ratio and the increased losses but also due to the necessity of increasing the isolation thickness. The winding width w_w must be increased in addition to the winding height h_w in order to improve the heat removal from the windings. In the case of the cores, an increase of both ratings results in an increase of the core temperature, which must be taken into account in the design.

The discussion of the preceding paragraphs concerning the power magnetics indicates that the core is more influenced by the scaling up than the winding. On the other hand, the winding performance was the limiting factor in the constructed prototypes. For this reason it is difficult to say whether the winding or the core design limits the scaling up. It seems that the main limitation would be related to the internal structure of the windings or the core. Eventually, the limitation will be defined by the attained thermal resistances of the winding and core structures.

5.3.2 Power Density and Scaling up; Single Unit Approach

Active Components

The conventional active components use several standardised types of packages only. The size of the package is related to the voltage and current ratings. Because of the limited number of available packages, the same package type must be used for different voltage and current ratings. This means that a device with higher ratings can have the same volume as a device with lower ratings, which yields a higher power density.

In order to investigate the relation between the power densities of active components with different ratings, component volumes were extracted from component datasheets for a complete range of IGBT power modules. For the selected components, the power rating of ZVS Quasi-ZCS converter was estimated from the component ratings. Finally, the total volume of the active components and the converter power-ratings were used to calculate the power densities of the active components as listed in Table 5-3.

Table 5-3: Power density of active components for devices with different voltage and current ratings

Power density [kW/l]		Voltage [V]			
		600	1200	1700	3300
Current [A]	200	35	95	145	158
	400	65	190	150	155
	600	—	80	125	—
	1200	—	165	250	—

The investigation showed that the power density of active components improves with increasing the voltage and current ratings. Notice that the power density can drop locally for components where the volume increases by a large step due to a larger package (for example IGBT 1200 V / 600 A). In relation to the estimated power densities listed in Table 5-3, the power density of active components of Converter Demonstrator II (using 1200 V / 150 A IGBT power modules) was estimated as 100 kW/l. This value is slightly higher than the value listed in the table, and this is the consequence of using a slightly smaller package from a different manufacturer.

The conclusion that can be drawn on the basis of the results is that the power density of the active components is higher than that of passive components and hence it influences the final power density only a little. Therefore, attention must be paid mainly to the design of passive components. These claims are especially true for the devices with voltage levels of 1200 V and above.

Passive Components

The relation between the power densities of passives and their voltage and current ratings is rather complex due to a complexity of their designs. To assess the power density variation with respect to the component ratings, several simplified component designs were performed for doubling the voltage and current rating with respect to Converter Demonstrator II. The following was assumed for the designs of power magnetics:

- constant peak flux density and operating frequency for all designs
- constant current density for current rating increase
- constant winding temperature for voltage rating increase – reduced current density to cope with heat removal obstructed by a thicker isolation

The winding and core cross-sections were designed with respect to these assumptions. The resulting design was checked for the temperature rise. A series / parallel combination of capacitors of the same type as used in the converter demonstrators was used to double the current and voltage ratings. The total capacitor volume was calculated as the volume of a single capacitor multiplied by the number of

capacitors used in the series / parallel combination. The resulting variations of the component volumes and of the associated power densities are listed in Table 5-4. The given values express the changes with respect to the components of Converter Demonstrator II. The results are listed per component, where the increases of the current or voltage rating are the cause, and the changes of the dimensions, volumes and power densities are the consequences.

Table 5-4: Estimated variation of passive component volumes and of associated power densities with current / voltage rating increasing by factor of 2, compared with components of Demonstrator II

		Transformer			Inductor		Capacitors	
Rating		2 x current	2 x voltage		2 x current	2 x voltage	2 x current	2 x voltage
Varying parameter	Core		d_c	w_c			SER / PAR	SER / PAR
	Windings	w_w	h_i, w_w	h_i, w_w	w_w, h_w	w_w, h_w	connection	connection
Volume		173 %	345 %	300 %	128 %	231 %	200 %	200 %
Power density		115 %	58 %	66.7 %	154 %	86 %	100 %	100 %

As can be seen, the component volumes and power densities vary greatly with respect to the current as well as the voltage rating. It is clear from the results that increasing the voltage rating is worse than increasing the current rating because of much larger gains in volume. Based on the results it can be stated that an increase of the current rating would result in an increase of the power density if the operating frequency was kept constant. The constant operating frequency is not realistic in practical applications. The frequency must often be reduced with scaling up due to the power loss in the active components (paragraph 5.3.1). In general, it can be stated that the size of the passive components is inversely proportional to the operating frequency. This means that the lower frequency introduced by the scaling up would fundamentally result in a much larger increase of the volumes of the passive components than indicated in Table 5-4. The consequence of this would be that the power density would reduce with the scaling up. New advanced components, like for example Silicon Carbide (SiC) devices, could partially mitigate the effect of the frequency reduction. For such components, the operating frequency could be kept constant and it would be limited only by the design of power passives. In such cases, the resulting power density could be kept constant or could even improve with the scaling up. Another solution to the problem of frequency reduction could be the use of the modular approach as discussed in the introduction to this section. The power density in this case would remain “constant” if the volume of the interconnecting accessories is kept small.

5.4 Conclusions

This chapter discusses issues related to all three cornerstones of high-power high power density converter design. In the first section of this chapter, the spatial component integration was discussed as the last remaining task of the integral design process presented in the introduction to this thesis. General guidelines for the spatial integration of components do not exist. Therefore, the spatial integration was described in relation to the structure of the 50 kW dc-dc converter demonstrator. The discussion covered the design decisions made in the converter design process with respect to component shapes. It showed that matching the shapes of the components results in hardly any empty space between the components, which, together with high frequency designs, results in a high power density. The power density of 11.13 kW/l for the liquid cooling and 6.6 kW/l for the forced-air cooling was demonstrated by Converter Demonstrator II. These power densities are a substantial improvement on the state-of-the-art solution with low-frequency 50 Hz passives.

The second section of this chapter dealt with the implications of scaling up the proposed concepts. Analysing the scaling-up problem is very complex and therefore the analyses of this chapter were based on estimations of component performances and volumes by using component datasheets and “fast” approximate designs. The scaling up is made possible by two approaches: the multi-module approach and the single high-power-module approach. The limitation of the scaling up by introducing

series-parallel connection of converter modules seems to be only the complexity of the resulting system. In that case the power density could be kept constant and equal to the power density of a single module if the volumes of the accessories were kept small.

The single high-power-module approach would result in a reduced power density primarily due to the frequency reduction required by the switching operation of active components. It is indicated that if the operating frequency could be kept constant, the power density could be even improved for increasing the current rating. Increasing the power level of a single module while keeping the frequency constant would only be possible if advanced devices like for example SiC devices are used. It was shown that increasing the voltage rating is worse than increasing the current rating. For this reason, the voltage rating of a converter module should be kept low and in the event that a higher voltage is required, the series connection of power modules should preferably be used.

Chapter 6 *Conclusions and Recommendations*

6.1 Summary

The main objective of this thesis was to propose methods that will increase the power density of high-power converters with galvanic isolation. The three cornerstones for attaining the objective were identified as:

- reduction of size of passive components
- reduction of power losses
- implementation of advanced thermal management

Investigating the three cornerstones and the related aspects resulted in several concepts for each cornerstone. The proposed concepts were implemented in the converter demonstrators in order to prove their applicability to high-power converters.

Chapter 2 discussed converter topologies as the means of reducing power loss in active components. A new, Output Filter Resonant Topology was proposed and analysed with respect to power loss in active components. The tests on Converter Demonstrator I revealed functional properties of the topology which led to design modifications implemented in Converter Demonstrator II.

The design of magnetic components was addressed in Chapter 3 with respect to power loss and power density. A combination of material and technology selection, transformer shape optimisation, loss reduction in windings and leakage layer for increasing the leakage inductance led to a large reduction of size. The results obtained were demonstrated in several prototypes.

Chapter 4 addressed thermal management on the component, converter and system level. Conduction locally supported by heat pipes and consequent heat collection on thermal surfaces was proposed as fundamental to the thermal management concept for the considered applications. Four thermal management solutions based on the proposed concept were evaluated. The evaluation resulted in the best solution being implemented in Converter Demonstrator II. The measurements on the converter prototype demonstrated the performance of the proposed thermal management concept.

In Chapter 5, the issues related to all three cornerstones were addressed. In the first section of Chapter 5, the spatial integration of components with respect to the component shapes (designs) and functions was discussed. The results of the spatial integration together with the results obtained with respect to the three cornerstones were presented in the structure of Converter Demonstrator II. In the second part of Chapter 5, further scaling up of the presented concepts was considered. The scaling up was approached from the performance as well as power density point of view.

6.2 Conclusions; Three Cornerstones of the Converter Design

The conclusions are discussed here with respect to the cornerstones of high power density converter design (paragraph 1.2). Figure 6-1 schematically illustrates the three cornerstones with the proposed solutions and achieved results. The conclusions for each cornerstone are discussed individually in the following paragraphs.

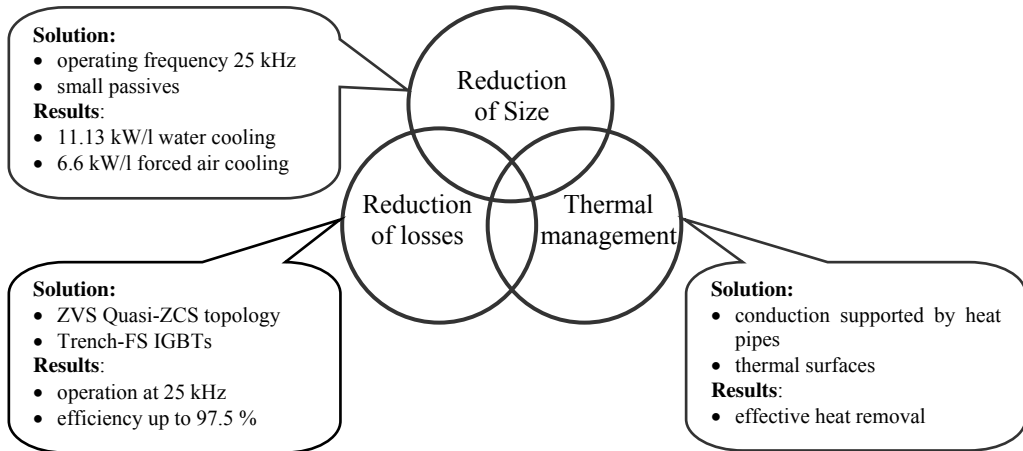


Figure 6-1: Three cornerstones of the converter design, solutions and results

6.2.1 Reduction of Size

The reduction of size was reached primarily by reduction of the size of the passive components through an increase of the operating frequency. The power density of the high-frequency transformer designed for this thesis (25 kHz) is about 47.2 kW/l, whereas the power density of the conventional 50 Hz transformers is about 1.7 kW/l. The power density of the filter inductors used in Converter Demonstrator II is about 110 kW /l.

To enable the high frequency operation of the converter's magnetics, amorphous metal was selected as the core material and foil technology was used for the windings. The advantage of this choice is the combination of good high-frequency and thermal performance. These allowed a compact design of the magnetics through:

- reduction of the component volumes by pushing the operating parameters to their limits
- reduction of the power loss reached by optimisation of components
- improvement of the heat removal from the components

Another aspect implemented to reduce the converter volume is the integration of several discrete components into a single component. A method of integration of resonant inductance into a transformer that is based on a so-called leakage layer was implemented. This was done for the first time in a high-power transformer design. The feasibility of the results obtained from the theoretical studies was confirmed by the practical results. The small signal measurements showed a successful leakage inductance enhancement by the leakage layer. There were problems related to the implementation of the leakage layer because of the methods used in the construction of the layer. All high-power tests resulted in failures of the winding isolation and consequently in the complete component failures. These failures occurred as the result of a possible contamination of the windings during the construction of the leakage layer. In spite of the failures, the results look promising and an improvement of the construction process should yield a successful outcome.

The reduction of the size of passives together with high-density spatial component packaging resulted in a high power density converter prototype. The power density of the converter prototype is

calculated as 11.13 kW/l with liquid cooling, or 6.6 kW/l with forced-air cooling including the heatsinks. These power densities are much higher than what can be reached by the state-of-the-art solutions. In comparison with the power density prediction as shown in Figure 1-3, the attained power densities are following the prediction for the forced air cooling. For the liquid cooling, the power density is much higher than predicted.

6.2.2 Reduction of Losses

Increasing the operating frequency as the main tool for reduction of converter size often results in an increase of the power loss. The power loss was addressed in this thesis on the following levels: converter topology, selection of active devices and design of magnetics.

A new, Output Filter Resonant Converter was proposed, with the main objective being to realise a high switching frequency together with a high efficiency. The topology is based on resonance between the transformer leakage inductance and the filter capacitance. The resonance creates a specific current waveform which results in ZVS at turn-on and Quasi-ZCS at turn-off. The combination of both yields low switching losses.

Three IGBT types were compared in order to optimise the converter performance in relation to the specific resonant current waveform. The trench-FS IGBT technology was selected as the most suitable for high-frequency switching in the proposed topology. The advantage of the trench IGBTs is the combination of low conduction losses and low switching losses. This combination resulted in almost 0.5% improvement of the efficiency in comparison to the second-best IGBT device.

The reduction of the power loss was addressed in the power transformer by optimising its design and investigating new means of reducing the power loss. The partially interleaved winding was proposed to reduce the power loss in the foil windings and at the same time to keep the windings simple. This new way of interleaving is especially suitable for transformers with turn ratios close to one. The reduction of winding loss is obtained by the reduction of the magnetic field intensity. The proposed method of interleaving was successfully implemented in Converter Demonstrator I. The interleaving could not be implemented in Converter Demonstrator II because of the requirement of a high value of the leakage inductance. It was not possible to obtain such a high value in interleaved windings due to a weak magnetic field.

The relation between the shape of the leakage layer and the winding losses was investigated. The investigation showed that adding the leakage layer in the windings might substantially increase the winding losses. A simple extension of the leakage layer beyond the edges of the foils was proposed. This solution reduces the winding loss to almost its original value (without the leakage layer).

Combining the above mentioned concepts resulted in a converter design with a high efficiency together with a high power density. The efficiency measured on the final converter prototype is above 97% over a broad load range and for both directions of operation. The efficiency was measured on Converter Demonstrator II with the transformer without the leakage layer. The transformers with the leakage layer could not be used because the isolation failed in the power tests. In spite of the fact that it was not possible to measure on the transformers with the leakage layer, it is believed that similar performance with slightly lower efficiency could be obtained. The performance of the leakage layer was demonstrated to some extent by measurements on Converter Demonstrator I with partially interleaved windings and the leakage layer aligned with the windings. This non-optimal winding configuration resulted in total converter efficiency of almost 97%.

6.2.3 Thermal Management

The heat-removal concept presented in this thesis is primarily based on the conduction of heat. Conduction was chosen because its implementation is simple and it is also a very effective heat-removal method. Another advantage of using conduction is that a mechanical support structure can be used for the transportation of heat, which increases the integration level of the power converter.

Heat removal by conduction is assisted by using heat pipes. The small size of heat pipes and their good thermal properties were exploited in power magnetics, where heat pipes were used for heat removal from the windings. Inserting flat heat pipes inside the winding window and attaching them to the winding surfaces created very effective heat-removal paths.

Further, implementation of so-called thermal surfaces was proposed. The thermal surfaces collect the heat from the heat-conducting elements and the heat pipes. On these surfaces, the heat is transferred to the environment by various types of heatsinks. Two thermal surfaces were used in the proposed concept as a result of evaluating the power density of several conceivable solutions. The thermal surfaces allow for choosing either forced-air cooling or liquid cooling for heat removal from the converter and hence they keep the converter design flexible with respect to integration into a larger system.

The performance of the thermal management system as the result of the proposed thermal management concept was verified by measurements on the converter demonstrators. The measurements showed higher temperatures of magnetics than expected. This was probably caused by neglecting the core tolerances and the layering of the windings in the thermal models. In spite of higher measured temperatures, the final prototype sustained long-term operation at nominal power without excessively overheating. This confirms the capability of the proposed thermal management concept to remove the heat from the proposed high power density high-power converter.

6.2.4 Conclusions

The concepts presented in this thesis clearly have the potential to improve the power density of high power converters with galvanic isolation. As showed by the converter demonstrators, high power density and high efficiency can be obtained at the same time. In addition to this, the resulting converter concept offers universal heat-exchange surfaces of a simple flat shape which are easy to integrate with other system components. This allows for easy scaling up by means of multiple converter modules. The possibility of scaling up by increasing the power rating of a single module was also demonstrated. It is expected that scaling up will result in a slightly reduced power density. On the other hand, the resulting power density is still expected to be much higher than that attainable using the conventional state-of-the-art solutions.

6.3 Recommendations for Future Research

Recommendations for further research are grouped into six categories, namely: converter topology and components, high frequency transformer design, EMI and EMC, thermal management, reliability and finally voltage and power flow control.

Converter Topology and Components

The investigation of scaling up presented in Chapter 5 indicates that the switching frequency must be reduced with increasing the converter ratings due to the losses in the active components. The currently used IGBT power modules could be replaced by advanced SiC devices which would allow better high-frequency performance. These devices could shift the frequency limitation from active devices to passive devices. The power density would be limited only by the ability to remove the heat from passive devices, which could be addressed individually in the design of passives. This approach could yield a more optimal use of the volume occupied by the passives, which would consequently lead to even higher power densities. Design solutions with advanced active components could also keep the power density constant with respect to scaling up. The advantages but also disadvantages of using the SiC devices in the presented converter concept should be investigated.

High-Frequency Transformer Design

The problems with the transformer observed during the experiments were primarily related to the implementation of the leakage layer. In future uses of the leakage layer in high power, the technology of the construction of the leakage layer must be improved to prevent the isolation failures. In addition to this, leakage layer materials must be investigated – especially with respect to the consistency of the permeability and high frequency losses. The material properties must be reliable if the implementation of the leakage layer technology in industrial applications is going to be successful. The thermal properties of the leakage layer material should also be investigated. Improved thermal properties would lead to better thermal performance of the designs with the leakage layer and therefore possibly simpler transformer designs due to a simpler thermal management.

EMI and EMC

EMI and EMC were not addressed in the work presented in this thesis. Converter designs with high power densities are particularly sensitive to EMI and EMC due to the increased coupling between components. The EMI and EMC must be investigated in order to assure proper converter operation in larger systems (with multiple converters and control circuits) respectively in the industrial environment. The issues related to EMI and EMC must be identified and, if necessary, modifications to the presented design concepts will have to be made.

Thermal Management

It was observed in the models and measurements presented in this thesis that the largest temperature rises occur across the isolation layers of power magnetics. In order to improve the performance of these components other possibilities of removing the heat from the windings should be investigated. Heat removal from the edges of the windings is proposed in [53] for the application in low-power low-voltage inductors. This approach removes the heat from the edges of the winding foils, which is very effective because the heat path is not obstructed by the winding isolation. Implementation of this approach in high-power transformers is difficult because of the high operating voltages. By improving the technology of the winding construction, the heat could be removed from the edges of the foils which would result in a large reduction of the winding thermal resistances; the power density as well as the efficiency could be pushed even further than presented in this thesis.

Another possibility is to improve the thermal properties of the isolation itself. This would require an isolating material which would be thermally conductive and available as an isolation tape or other usable form. Such material would improve the heat removal from the windings which would again yield higher power density than presented in this thesis.

Reliability

The reliability of the presented converter concept is another aspect which was not addressed in this thesis and which must be investigated in the future. High reliability is a prerequisite for implementation in industrial applications. The issues of partial discharges in the windings of power magnetics, lifetime of the capacitors, thermal cycling and thermally induced stresses must be addressed in order to assess the reliability of the proposed converter concept.

Voltage and Power Flow Control

Some industrial applications require voltage control, which is essentially not available with the proposed converter topology. Limited voltage control is also required in the multi-module scaling up approach in order to control the power flow through the individual converter modules. Several concepts of voltage control were briefly discussed in this thesis but a broader investigation must be performed in order to assess the behaviour and the suitability of the proposed concepts.

References

- [1] Mallory, R. R. and Co., *Mallory vibrator data handbook* 1947.
- [2] Severns, R., "History of soft switching," *Switching power magazine*, 2001.
- [3] Royer, G. H., "A switching transistor DC to AC converter having an output frequency proportional to the DC input voltage," *AIEE Transactions on Communication Electronics*, vol. 74 pp. 322-326, 1955.
- [4] Jensen, J. L., "An Improved Square-wave Oscillator Circuit," *IRE Transactions on Circuit Theory*, vol. 4 pp. 276-279, 1957.
- [5] Bates, J. W., "Power Conditioning Systems Design". Wescon. Wescon Session 10 , 1965.
- [6] Mohan, N., Undeland, T. M., and Robbins, W. P., *Power electronics: converters, applications, and design*, 2nd ed. John Wiley & sons, inc., 1995.
- [7] Ohashi, H., "Power electronics innovation with next generation advanced power devices". Telecommunications Energy Conference, 2003.INTELEC '03.The 25th International 9-13, 2003.
- [8] Sayani, M. P. and Wanes, J., "Trends and drivers in isolated board-mounted DC/DC products for communications applications". Applied Power Electronics Conference and Exposition, 2003.APEC '03.Eighteenth Annual IEEE 1 37-41, 2003.
- [9] Bernet, S., "Recent developments of high power converters for industry and traction applications," *Power Electronics, IEEE Transactions on*, vol. 15, no. 6, pp. 1102-1117, 2000.
- [10] Marchesoni, M., Novaro, R., and Savio, S., "AC locomotive conversion systems without heavy transformers: is it a practicable solution?". Industrial Electronics, 2002.ISIE 2002.Proceedings of the 2002 IEEE International Symposium on 4 1172-1177, 2002.
- [11] Steigerwald, R. L., De Doncker, R. W., and Kheraluwala, H., "A comparison of high-power DC-DC soft-switched converter topologies," *Industry Applications, IEEE Transactions on*, vol. 32, no. 5, pp. 1139-1145, 1996.

- [12] Kutkut, N. H., Divan, D. M., Novotny, D. W., and Marion, R. H., "Design considerations and topology selection for a 120-kW IGBT converter for EV fast charging," *Power Electronics, IEEE Transactions on*, vol. 13, no. 1, pp. 169-178, 1998.
- [13] Remsburg, R., *Thermal design of electronic equipment* CRC press LLC, 2001.
- [14] Mudawar, I., "Assessment of high-heat-flux thermal management schemes," *Components and Packaging Technologies, IEEE Transactions on [see also Components, Packaging and Manufacturing Technology, Part A: Packaging Technologies, IEEE Transactions on]*, vol. 24, no. 2, pp. 122-141, 2001.
- [15] Rengang, C., Canales, F., Bo, Y., and van Wyk, J. D., "Volumetric optimal design of passive integrated power electronics module (IPEM) for distributed power system (DPS) front-end DC/DC converter," *Industry Applications, IEEE Transactions on*, vol. 41, no. 1, pp. 9-17, 2005.
- [16] Lavieville, J. P., Baudesson, P., Gilbert, L., and J-M.Bodson., "Industrial 20 kHz/150 kVA insulated soft switching DC-DC converter with no auxiliary circuit". EPE 2001 Graz , 2001.
- [17] Reinold, H. and Steiner, M., "Characterization of semiconductor losses in series resonant DC-DC converters for high power applications using transformers with low leakage inductance". EPE 1999 Lausanne , 1999.
- [18] Lu, B., Dong, W., Zhao, Q., and Lee, F. C., "Performance evaluation of CoolMOS and SiC diode for single-phase power factor correction applications". Applied Power Electronics Conference and Exposition, 2003.APEC '03.Eighteenth Annual IEEE 2 651-657, 2003.
- [19] Claudio, A., Cotorogea, M., and Macedonio, J., "Comparative analysis of SJ-MOSFET and conventional MOSFET by electrical measurements". Power Electronics Congress, 2002.Technical Proceedings.CIEP 2002.VIII IEEE International 96-100, 2002.
- [20] Blaabjerg, F., Pedersen, J. K., and Jaeger, U., "Evaluation of modern IGBT-modules for hard-switched AC/DC/AC converters". Industry Applications Conference, 1995.Thirtieth IAS Annual Meeting, IAS '95., Conference Record of the 1995 IEEE 2 997-1005, 1995.
- [21] Pavlovsky, M., de Haan, S. W. H., and Ferreira, J. A., "Comparison of DC/DC converter topologies with, and without transformer". EPE-PEMC 2002. Proceedings of EPE-PEMC 2002 , 9-12-2002.
- [22] Wanes, J., "A novel integrated packaging technique for high density DC-DC converters providing enhanced efficiency and thermal management". Applied Power Electronics Conference and Exposition, 2004.APEC '04.Nineteenth Annual IEEE 2 1229-1235, 2004.
- [23] Popovic, J. and Ferreira, J. A., "A modular, laminar 42/14 V DC/DC converter concept with integrated thermal busbar". Industry Applications Conference, 2004.39th IAS Annual Meeting.Conference Record of the 2004 IEEE 4 2323-2329, 2004.

- [24] Gerber, M., Ferreira, J. A., Hofsjager, I. W., and Seliger, N., "An improved 3D integrated DC/DC converter for high temperature environments". Power Electronics Specialists Conference, 2004.PESC 04.2004 IEEE 35th Annual 4 2779-2785, 2004.
- [25] Farrington, R., Jovanovic, M. M., and Lee, F. C., "Analysis of reactive power in resonant converters". Power Electronics Specialists Conference, 1992.PESC '92 Record., 23rd Annual IEEE 197-205, 1992.
- [26] Steigerwald, R. L., "A comparison of half-bridge resonant converter topologies," *Power Electronics, IEEE Transactions on*, vol. 3, no. 2, pp. 174-182, 1988.
- [27] Theron, P. C. and Ferreira, J. A., "The zero voltage switching partial series resonant converter," *Industry Applications, IEEE Transactions on*, vol. 31, no. 4, pp. 879-886, 1995.
- [28] Pavlovsky, M., de Haan, S. W. H., and Ferreira, J. A., "The ZVS, Quasi-ZCS Converters, a Family of Topologies with an Optimal Current Waveform for High Frequency Switching.". EPE 2003. Proceedings of EPE 2003 , 9-2-2003.
- [29] "Auxiliary power converters in traction". www.bombardier.com , 2006.
- [30] Azzopardi, S., Vinassa, J. M., Woirgard, E., Zardini, C., and Briat, O., "A systematic hard- and soft-switching performances evaluation of 1200 V punchthrough IGBT structures," *Power Electronics, IEEE Transactions on*, vol. 19, no. 1, pp. 231-241, 2004.
- [31] Otsuki, M., Onozawa, Y., Kanemaru, H., Seki, Y., and Matsumoto, T., "A study on the short-circuit capability of field-stop IGBTs," *Electron Devices, IEEE Transactions on*, vol. 50, no. 6, pp. 1525-1531, 2003.
- [32] Laska, T., "The Field Stop IGBT (FS IGBT), A new power device concept with a great improvement potential". 2000.
- [33] Helsper, M., Fuchs, F. W., and Munzer, M., "Analysis and comparison of planar- and Trench-IGBT-Modules under ZVS and ZCS switching conditions". Power Electronics Specialists Conference, 2002.pesc 02.2002 IEEE 33rd Annual 2 614-619, 2002.
- [34] Cros, J., Perin, A. J., and Viarouge, P., "Soft magnetic composites for electromagnetic components in lighting applications". Industry Applications Conference, 2002.37th IAS Annual Meeting.Conference Record of the 1 342-347, 2002.
- [35] Petzold, J., "Advantages of softmagnetic nanocrystalline materials for modern electronic applications," *Journal of Magnetism and Magnetic Materials*, no. 242-245, pp. 84-89, 2002.
- [36] den Bossche, A. V. and Valchev, V. C., *Inductors and Transformers for Power Electronics* CRC Press, Taylor & Francis Group, 2005.
- [37] Kutkut, N. H., Novotny, D. W., Divan, D. M., and Yeow, E., "Analysis of winding losses in high frequency foil wound inductors". Industry Applications Conference, 1995.Thirtieth IAS Annual Meeting, IAS '95., Conference Record of the 1995 IEEE 1 859-867, 1995.

- [38] Garcia, O., Cobos, J. A., Prieto, R., Uceda, J., and Ollero, S., "A standard design method for high frequency PCB transformers". Telecommunications Energy Conference, 1995. INTELEC '95., 17th International 335-339, 1995.
- [39] Kheraluwala, M. H., Novotny, D. W., and Divan, D. M., "Coaxially wound transformers for high-power high-frequency applications," *Power Electronics, IEEE Transactions on*, vol. 7, no. 1, pp. 54-62, 1992.
- [40] Pavlovsky, M., de Haan, S. W. H., and Ferreira, J. A., "Partial Interleaving: A Method to Reduce High Frequency Losses and to Tune the Leakage Inductance in High Current, High Frequency Transformer Foil Windings". PESC 2005. Proceedings of PESC 2005 , 2005.
- [41] Dowell, P. L., "Effects of eddy currents in transformer windings," *Proceedings of IEE*, vol. 113, no. 8, pp. 1387-1394, 1966.
- [42] Xi, N. and Sullivan, C. R., "An improved calculation of proximity-effect loss in high-frequency windings of round conductors". Power Electronics Specialist Conference, 2003. PESC '03. 2003 IEEE 34th Annual 2 853-860, 2003.
- [43] Gradzki, P. M. and Lee, F. C., "Design of high-frequency hybrid power transformer". Applied Power Electronics Conference and Exposition, 1988. APEC '88. Conference Proceedings 1988., Third Annual IEEE 319-326, 1988.
- [44] Kats, A., Ivensky, G., and Ben-Yaakov, S., "Application of integrated magnetics in resonant converters". Applied Power Electronics Conference and Exposition, 1997. APEC '97 Conference Proceedings 1997., Twelfth Annual 2 925-930, 1997.
- [45] Odendaal, W. G., Ferreira, J. A., and Roos, S. D., "Leakage impedance design as function of frequency scaling in power transformers". Industry Applications Conference, 1996. Thirty-First IAS Annual Meeting, IAS '96., Conference Record of the 1996 IEEE 3 1389-1396, 1996.
- [46] Meinhardt, M., Duffy, M., O'Donnell, T., O'Reilly, S., Flannery, J., and Mathuna, O., "New method for integration of resonant inductor and transformer-design, realisation, measurements". Applied Power Electronics Conference and Exposition, 1999. APEC '99. Fourteenth Annual 2 1168-1174, 1999.
- [47] Zhu, N., van Wyk, J. D., and Wang, F., "Design of integrated parallel resonant transformers". Power Electronics Specialists Conference, 2005. PESC. 2005 IEEE 36th Annual 1787-1992, 2005.
- [48] Ohadi, M. and Jianwei, Q., "Thermal management of harsh-environment electronics". Semiconductor Thermal Measurement and Management Symposium, 2004. Twentieth Annual IEEE 231-240, 2004.
- [49] Schulz-Harder, J., Exel, K., Meyer, A., Licht, T., and Loddenkotter, M., "Micro channel water cooled power modules". PCIM 2000. Proceedings of PCIM , 2000.

- [50] Vanam, K., Junghans, J., Barlow, F., Selvam, R. P., Balda, J. C., and Elshabini, A., "A novel packaging methodology for spray cooling of power semiconductor devices using dielectric liquids". Applied Power Electronics Conference and Exposition, 2005.APEC 2005.Twentieth Annual IEEE 3 2014-2018, 2005.
- [51] Stefanescu, S., Mehregany, M., Leland, J., and Yerkes, K., "Micro jet array heat sink for power electronics". Micro Electro Mechanical Systems, 1999.MEMS '99.Twelfth IEEE International Conference on 165-170, 1999.
- [52] Mudawar, I., "Direct-immersion cooling for high power electronic chips". Thermal Phenomena in Electronic Systems, 1992.I-THERM III, InterSociety Conference on 74-84, 1992.
- [53] Odendaal, W. G., Azevedo, J., Bruning, G. W., and Wolf, R. M., "A high-efficiency magnetic component with superior caloric performance for low-profile high-density power conversion," *Industry Applications, IEEE Transactions on*, vol. 40, no. 5, pp. 1287-1293, 2004.
- [54] Steinberg, D. S., *Cooling techniques for electronic equipment*, 2nd ed. John Wiley & sons, inc., 1991.
- [55] Heinemann, L., "An actively cooled high power, high frequency transformer with high insulation capability". Applied Power Electronics Conference and Exposition, 2002.APEC 2002.Seventeenth Annual IEEE 1 352-357, 2002.
- [56] Klontz, K. W., Divan, D. M., and Novotny, D. W., "An actively cooled 120 kW coaxial winding transformer for fast charging electric vehicles," *Industry Applications, IEEE Transactions on*, vol. 31, no. 6, pp. 1257-1263, 1995.
- [57] Olesen, K., "Liquid cooled power modules for automotive". <http://siliconpower.danfoss.com> , 2005.
- [58] Gerber, M., Ferreira, J. A., Hofsjager, I. W., and Seliger, N., "A high-density heat-sink-mounted inductor for automotive applications," *Industry Applications, IEEE Transactions on*, vol. 40, no. 4, pp. 1031-1038, 2004.
- [59] Gerber, M. B., "The electrical, thermal and spatial integration of a converter in a power electronic module." Delft University of Technology, 2005.
- [60] Popovic, J, "Improving packaging and increasing the level of integration in power electronics." Delft University of Technology, 2005.
- [61] Drofenik, U., Laimer, G., and Kolar, J. W., "Theoretical converter power density limits for forced convection cooling". PCIM Europe 2005. Proceedings of the International PCIM Europe 2005 Conference 608-619, 2005.
- [62] Wei, J., Chan, A., and Copeland, D., "Measurement of vapor chamber performance [heatsink applications]". Semiconductor Thermal Measurement and Management Symposium, 2003.Nineteenth Annual IEEE 191-194, 2003.

- [63] Legierski, J. and Wiecek, B., "Steady state analysis of cooling electronic circuits using heat pipes," *Components and Packaging Technologies, IEEE Transactions on*, vol. 24, no. 4, pp. 549-553, 2001.
- [64] Phelan, P. E., Chiriac, V. A., and Lee, T. Y. T., "Current and future miniature refrigeration cooling technologies for high power microelectronics," *Components and Packaging Technologies, IEEE Transactions on [see also Components, Packaging and Manufacturing Technology, Part A: Packaging Technologies, IEEE Transactions on]*, vol. 25, no. 3, pp. 356-365, 2002.
- [65] Shakouri, A. and Zhang, Y., "On-Chip Solid-State Cooling for Integrated Circuits Using Thin-Film Microrefrigerators," *Components and Packaging Technologies, IEEE Transactions on [see also Components, Packaging and Manufacturing Technology, Part A: Packaging Technologies, IEEE Transactions on]*, vol. 28, no. 1, pp. 65-69, 2005.

Appendix A. *Ac Resistance of Partially Interleaved Windings*

The derivation of the equations for the AC winding resistance is shown below for the interleaved section of the transformer winding. The method is based on [41].

The details of the winding layers, the field distribution (mmf) and the magnetic fluxes (linked to the winding layers) are shown in Figure A-1.

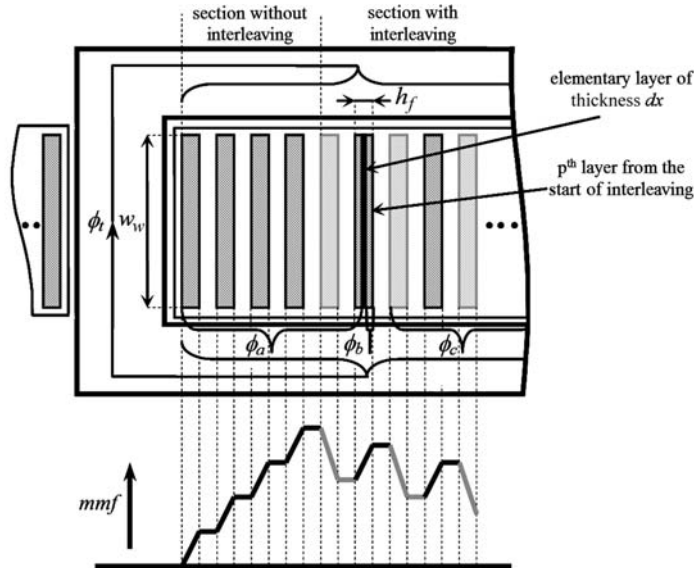


Figure A-1: Part of the winding, indication of magnetic fluxes and associated mmf diagram

The flux influencing the elementary layer is the winding flux to the right of the elementary layer. It can be seen from Figure A-1 that this flux consists of the flux ϕ_c (caused by the winding layers on the right of the p^{th} layer) and of the flux ϕ_b (caused by the remaining section of the p^{th} layer).

$$\text{elementary layer flux} = \phi_b + \phi_c, \tag{A-1}$$

The change of the elementary layer position by dx results in a change of the flux of the elementary layer $d\phi$.

$$\frac{d(\phi_b + \phi_c)}{dx} = -\frac{d\phi}{dx}, \tag{A-2}$$

The flux of the elementary layer at position x is then calculated from:

$$|d\phi| = dxBl_t, \quad (\text{A-3})$$

where l_t is the mean layer length. The flux density B can be calculated from the field intensity as $B = \mu H$ where H is defined as:

$$\oint_c H dl = \sum_n i_n, \quad (\text{A-4})$$

The equations describing H for each section are derived from the field distribution plot. The H field of the interleaved section can be described by (A-5).

$$H(x) = \frac{I}{w_w} \left(N(1-i_f) - 1 + p \left(1 - \frac{1}{n} \right) \right) + \int_0^x J dx, \quad (\text{A-5})$$

where $IN(1-i_f) - 1$ represents the H field at the beginning of the interleaved section, $Ip(1-1/n)$ represents the per layer increase of the H field and the integral of J represents again the increase of the H field within the layer itself. Manipulating equations (A-2) – (A-5) yields

$$\frac{d(\phi_b + \phi_c)}{dx} = \mu l_t \left[\frac{I}{w_w} \left(N(1-i_f) - 1 + p \left(1 - \frac{1}{n} \right) \right) + \int_0^x J dx \right], \quad (\text{A-6})$$

From the equation describing the voltage between the ends of the layer [41] can be derived that

$$\frac{dJ}{dx} = -\frac{j\omega}{\rho l_t} \left[\frac{d(\phi_b + \phi_c)}{dx} \right], \quad (\text{A-7})$$

thus from the equations (A-6) and (A-7) follows:

$$\frac{d^2 J}{dx^2} = \frac{j\omega\mu}{\rho} J = \alpha^2 J. \quad (\text{A-8})$$

Then, the solution of equation (A-8) has a form of

$$J = P \sinh \alpha x + Q \cosh \alpha x, \quad (\text{A-9})$$

where P and Q are constants where Q can be evaluated by substituting (A-9) to (A-7).

$$Q = \frac{\alpha I}{w_w} \left(N(1-i_f) - 1 + p \left(1 - \frac{1}{n} \right) \right), \quad (\text{A-10})$$

To calculate P , the current flowing through the p^{th} layer is given by:

$$I = \int_0^{h_f} J w_w dx, \quad (\text{A-11})$$

By substituting (A-9) to (A-11) constant P is calculated as:

$$P = \frac{\alpha}{w_w} I \frac{1}{\cosh \alpha h_f} - Q \tanh \frac{\alpha h_f}{2}, \quad (\text{A-12})$$

Thus the current density J can be described as:

$$J = \frac{\alpha I}{w_w} \left[\frac{\cosh \alpha x}{\cosh \alpha h_f} - \left(\frac{N(1-i_f)-1}{+p\left(1-\frac{1}{n}\right)} \right) \tanh \frac{\alpha h_f}{2} \cosh \alpha x + \left(N(1-i_f)-1 + p\left(1-\frac{1}{n}\right) \right) \sinh \alpha x \right], \quad (\text{A-13})$$

The current density at the tops of the conductors is then calculated as:

$$J_h = \frac{I}{w_w h_f} \left[M + \frac{D}{2} \left(N(1-i_f)-1 + p\left(1-\frac{1}{n}\right) \right) \right], \quad (\text{A-14})$$

where $M = \alpha h_f \coth \alpha h_f$ and $D = 2\alpha h_f \tanh \frac{\alpha h_f}{2}$ and $\alpha = \sqrt{\frac{j\omega\mu_0}{\rho}} = \sqrt{2j\frac{h_f}{\delta}}$ where δ is the skin depth of the winding foils.

The total voltage at the tops of the conductors is the sum of the resistive voltage drops in each layer defined as:

$$V_{rp} = \rho J_h l_t, \quad (\text{A-15})$$

and of the induced voltage per layer

$$V_{ip} = j\omega\phi_p, \quad (\text{A-16})$$

where ϕ_p is the flux passing through the p^{th} layer defined by integrating equation (A-6) through the layer thickness h :

$$\phi_p = \mu l_t \int_0^h \left[\frac{I}{w_w} \left(N(1-i_f)-1 + p\left(1-\frac{1}{n}\right) \right) + \int_0^x J dx \right] dx, \quad (\text{A-17})$$

thus

$$\phi_p = \frac{\mu l_t}{\alpha^2 w_w} \frac{D}{2} I \left[-1 + 2 \left(N(1-i_f) + p\left(1-\frac{1}{n}\right) \right) \right]. \quad (\text{A-18})$$

The voltage of the winding section can be defined as the sum of the voltages at the tops of the particular layers. The induced voltage in the p^{th} layer is associated with the linking flux of all the preceding $(p-1)$ layers. Hence the total voltage across the interleaved winding section is given by:

$$V = \sum_{p=1}^m V_{rp} + \sum_{p=1}^m (p-1) V_{ip}, \quad (\text{A-19})$$

From the equations (A-14), (A-15), (A-16) and (A-18) can be derived:

$$V = \frac{\rho l_t I}{w_w h_f} m_2 \left[M + \frac{D}{2} \left(m_2 N(1-i_f) - \frac{(m_2+1)}{2} \left(1 - \frac{(4m_2-1)}{3} \left(1 - \frac{1}{n} \right) \right) \right) \right], \quad (\text{A-20})$$

Hence the winding impedance is equal to

$$Z_w = \frac{\rho l_t}{w_w h_f} m_2 \left[M + \frac{D}{2} \left(m_2 N(1-i_f) - \frac{(m_2+1)}{2} \left(1 - \frac{(4m_2-1)}{3} \left(1 - \frac{1}{n} \right) \right) \right) \right], \quad (\text{A-21})$$

of which the real part defines the ac resistance of the interleaved section. The equations for the primary respectively the secondary ac resistance are derived as follows:

$$R_{p_ac} = \frac{\rho'_t}{w_w h_f} \left\{ m_p \left[M' + \frac{D'}{2} \left(m_p N_1 (1 - i_f) - \frac{(m_p + 1)}{2} \left(1 - \frac{(4m_p - 1)}{3} \left(1 - \frac{1}{n} \right) \right) \right) \right] \right\}, \quad (\text{A-22})$$

$$R_{s_ac} = \frac{\rho'_t}{w_w h_f} \left\{ m_s \left[M' + \frac{D'}{2} \left(m_s N_1 (n - i_f) - \frac{(m_s + 1)}{2} \left(1 - \frac{(4m_s - 1)}{3} (1 - n) \right) \right) \right] \right\}, \quad (\text{A-23})$$

where $m_p = m_s = N_1 i_f$, $M' = \text{Re}(M)$, $D' = \text{Re}(D)$.

Appendix B. Overview of Heat Removal Methods

This appendix gives an overview of the heat-removal methods that were identified in the literature research. These methods were also considered in the selection of the thermal management concept discussed in Chapter 4. The overview should provide some basic information about the considered methods..

Convection

Convection is a heat-removal mechanism that occurs in fluids. It is based on the mixing of hot and cold molecules of fluids. The mixing process can be induced either by changes in density of the fluid (natural convection) or by forcing the circulation of the fluid (forced convection). The convective cooling is described by the equation:

$$q = \Delta T A h_c, \quad (\text{B-24})$$

where q is the amount of heat removed through the surface by convection, ΔT is the temperature difference between the surface temperature of the cooled object and the fluid temperature, A is the surface area available for the heat transfer, and h_c is the coefficient of convective heat transfer which is a function of many parameters like temperature rise ΔT , surface area A , orientation of the surface etc.

Conduction

Conduction is the heat-transfer mechanism based on the energy of motion between adjacent molecules, the movement of free electrons and the vibration of the atomic lattice structure. The heat is transferred from a space of high energy to a space of low energy. The conductive heat transfer is in a simplified form characterised as:

$$q = \frac{\Delta T A k}{l}, \quad (\text{B-25})$$

where q is the heat transferred by conduction, ΔT is the temperature difference used for conductive heat transfer, A is the cross-section available for heat transfer, k is the thermal conductivity of the material, and l is the length of the heat transfer.

Radiation

Radiative heat transfer occurs by means of electromagnetic waves and photonic motion. The heat exchange by radiating bodies can be described as:

$$q = \varepsilon \sigma F_{1,2} A (T_1^4 - T_2^4), \quad (\text{B-26})$$

where q is the heat transferred by radiation, ε is the emissivity of the radiating surface, σ is Stefan-Boltzmann constant, $F_{1,2}$ is the shape factor which represents the relative position and shape of

radiating bodies, A is the surface area of radiation and T_1 , T_2 are the surface temperatures of bodies participating in radiation. This mode of heat transfer is usually insignificant in comparison to convection and conduction unless the temperature difference between the radiating bodies is relatively large.

Liquid Cooling

Liquid cooling utilises the property of liquids to absorb heat and to transport it to distant places where a heat exchange with the environment occurs. The heat transfer is based on convection, which uses liquid as the medium of heat transfer instead of air. Two basic cooling concepts are used with liquid cooling. One of them uses conduction to transport the heat from places where it is generated to common surfaces from which the heat is transported by liquid. The second applies liquid coolers directly to the surfaces of components in which the heat is generated. The second concept gives better results than the first one due to the larger surface area available for the heat exchange and due to the direct heat exchange between components and liquid, hence omitting the temperature rise caused by conduction. However, in the second case, rather elaborate tubing is required (Figure B-1).



Figure B-1: Localized water cooling applied to personal computer dissipating approximately 100W

The ability to transport large amounts of heat over long distances is the main advantage of liquid cooling. In many cases, water is used as the cooling liquid due to its high heat capacity (4200 J/kgK). The high capacity allows quite substantial absorption and transportation of heat even at relatively low flow rates. A disadvantage of liquid cooling in general is the presence of a pump, and hence the presence of moving parts, which results in increased maintenance requirements and relatively low reliability. Other disadvantages are: elaborate tubing required and risk of leaks of liquid. In some applications where the liquid comes into contact with the active parts of a converter circuit (parts connected to different electric potentials), non-conductive liquids (demineralised water, fluorinert liquids, ...) must be used.

Advanced Phase-Change Cooling Methods

With respect to reachable heat fluxes, phase-change cooling is far superior to any other form of cooling as is shown in [14]. Its success stems from the phase-change itself, which requires substantial energy to occur.

Heat pipes utilise phase-change of working liquid enclosed in an evacuated tube to absorb heat. A heat pipe consists of an evacuated tube with a so-called wick on the inner surfaces and a small amount of working fluid which is filled in the tube after the evacuation. The working cycle of a heat pipe (Figure B-2) starts in the evaporator. As the heat enters the evaporator, the working liquid evaporates and travels as a vapour to the condenser. The temperature of the condenser is slightly lower than that of the evaporator, which causes the vapour to condense. The liquid is then pumped back to the evaporator by the capillary effect of the wick. In this way, large quantities of heat can be transported with a low thermal gradient.

Heat transfer using heat pipes is becoming more and more popular. This is due to the compactness of the heat pipes, the variety of shapes available (see examples of flat heat pipes in Figure B-3 and Figure B-4) and the decreasing costs. Heat pipes are also quite reliable devices because they do not contain moving parts. In power electronics, heat pipes nowadays realise two main functions: heat spreading in base-plates of large heatsinks (Figure B-3a) and heat conduction to remote heatsinks (Figure B-3b). In both cases, good results are obtained in comparison with conventional solutions [62],[63].

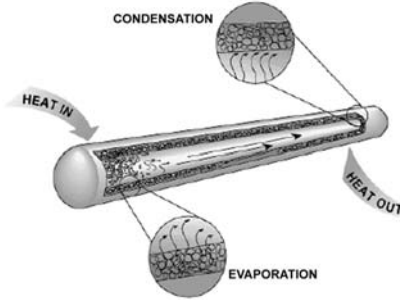


Figure B-2: Heat pipe working principle

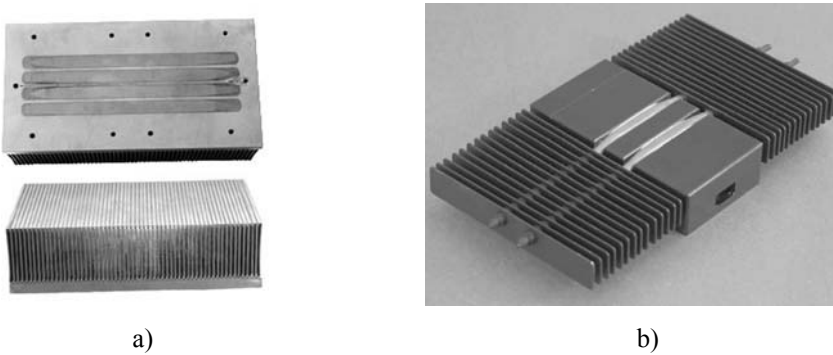


Figure B-3: Thermal management using heat pipes; a) heat pipes used as heat spreaders in heatsink base (Aavid), b) heat pipes used to conduct heat to remote heatsinks (Enertron)



Figure B-4: Examples of flat heat pipes available on the market

Using mini and micro-channels (MEMS cooling) (Figure B-5) is another option for applications where high heat fluxes are needed. A small amount of liquid is in this case forced through micro-channels where the liquid evaporates and travels on to a condenser. The ability to reach very high heat fluxes together with the possibility of preventing the cooling liquid coming into contact with the

surface of the cooled device is the main advantage of micro-channels. The main disadvantage is clogging if the size of micro-channels is smaller than 200 μm .

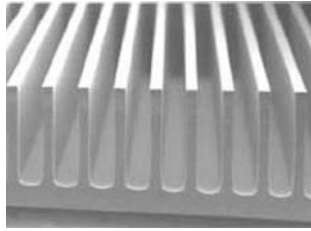


Figure B-5: Micro channel cooler, the width of a channel is in the range of tenths or hundreds of μm

Other phase-change concepts use liquids directly in contact with the surface of the cooled device. The cooling medium used is usually a fluorinert liquid which is electrically not conducting. If the surface temperature exceeds saturation temperature by a few degrees, bubbles begin to form (similar to water boiling) and depart from the device surface. This draws fresh liquid to the surface of the device and the bubble-forming cycle repeats. The bubbles travel on to a condenser, where they condense and return to the system in the form of liquid. This process is shown in Figure B-6a for the phase-change cooling methods called direct-immersion-cooling or pool-boiling. Very high heat fluxes (more than 50 W/cm^2 [14]) can be reached by using pool-boiling.

Another form of phase-change cooling is spray cooling (Figure B-6b). It uses the same principle as mentioned above for the direct immersion cooling but the cooling liquid is sprayed on the surface of a cooled device. In contact with the surface the liquid evaporates and departs in the form of gas. Only a very limited amount of liquid is needed in comparison with pool-boiling. The disadvantage is that very delicate spray nozzles are required, and these are sensitive to clogging.

Jet-impinged cooling (Figure B-6c) is based on a similar principle to spray cooling but the liquid is transported to the surface of the device in form of a jet stream. The nozzles of a jet cooling system are much simpler in comparison with spray nozzles. The disadvantage is the higher impact force on the surface of the device, which might be unacceptable for some delicate components.

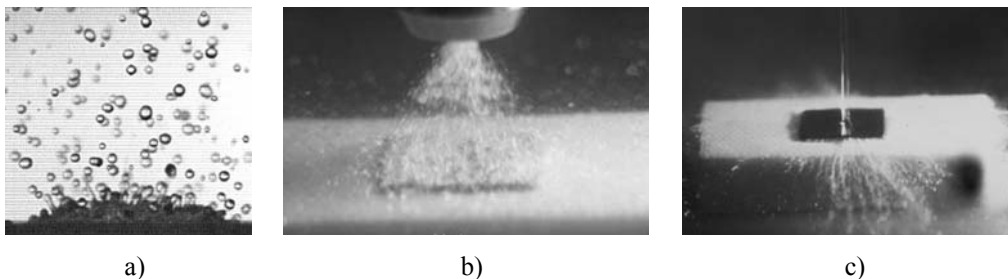


Figure B-6: Advanced high-heat-flux, phase-change cooling methods; a) liquid pool boiling, b) spray cooling, c) jet impingement cooling

Another method which uses phase-change of a liquid for cooling is Ultra-thin-film cooling. The concept of thin-film-cooling (Figure B-7) is based on a sheet of liquid falling from an overhead reservoir along the surface of the cooled devices. The cooling process is in itself passive but a pump is needed to replenish the reservoir. The amount of liquid needed for this type of cooling is highly reduced in comparison with direct immersion cooling. The disadvantage of this method is separation of the fluid from the device surface during intense boiling, which limits the amount of heat that can be removed.

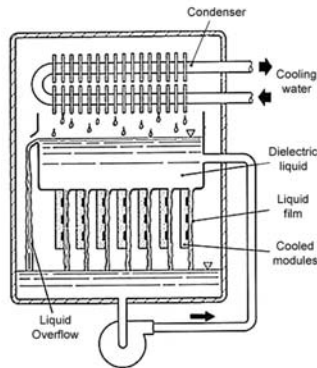


Figure B-7: Ultra-thin-film cooling concept

Refrigeration Cooling

Refrigeration cooling is different from the principles for heat removal mentioned above because it is based on reducing the surface temperature of the cooler below the temperature of the environment. Consequently, the heat is transported from a space of low temperature (cooler) to a space of high temperature (condenser).

Several methods of obtaining refrigeration are known and show great potential for different applications [64]. The most widely used is the concept that relies on the principle of expanding gasses, cooling the environment in which they expand. The cooling itself is rather effective and subzero temperatures can be reached on the surfaces of the cooler. The main problem of the system is that it is rather bulky and miniaturization is difficult. This is illustrated in Figure B-8 on refrigeration applied to a personal computer with power loss of approximately 100 W. Other disadvantages of the refrigeration cooling are: cooling gasses must be refilled occasionally, cooling gasses are potentially harmful to the environment, and the system is rather complex with moving parts present, which results in relatively poor reliability.

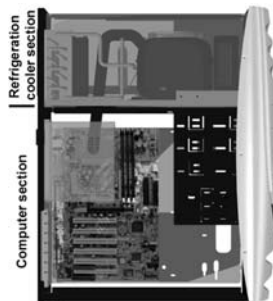


Figure B-8: Refrigeration cooling applied to a personal computer dissipating approximately 100W.

Another type of refrigeration cooling that is increasingly used in electronics is solid-state cooling. This is based on the so-called thermoelectric or Peltier effect. The effect is based on a current passing through a thermoelectric junction. Depending on the current direction, the junction is either heated up or cooled down. This is explained by electrons either “speeding up” or “slowing down” under the influence of thermoelectric contact potential. By speeding up or slowing down, the kinetic energy of electrons varies, which generates heat or absorbs heat. Apart from losses, the Peltier heat can be calculated by:

$$q_p = Pit , \quad (6-27)$$

where P is the Peltier factor that depends on contacting materials and temperature, I is the current applied and t is the time duration of the heat transfer.

A typical application of solid-state coolers is cooling the chips of microprocessors. Such a cooler consists of two layers of thermally and electrically coupled junctions as shown in Figure B-9; the heat is transferred from cold to hot junctions. There are also attempts to use this principle for direct cooling of chip surfaces as discussed in [65]. Heat fluxes up to 600 W/cm^2 can be reached. The limitation of the system is the necessity to supply an external energy for the cooling to take place. The external energy covers the losses caused by the current that flows through the junctions and wiring. Often, the external power is larger than the amount of heat that can be extracted, which makes the system rather inefficient.

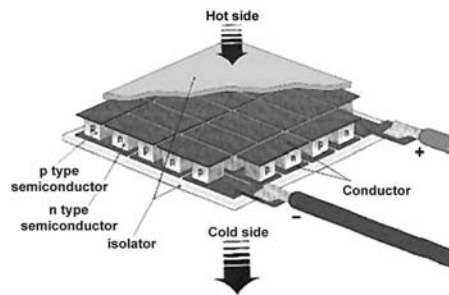


Figure B-9: Peltier element used for solid-state cooling

Appendix C. FEM Thermal Analysis of Proposed Converter Structure

FEM models were used to analyse the proposed converter structure in detail. The FEM approach was chosen because of its ability to model the thermal fields of complex 3D structures in detail. Separate models were realised for the transformer, the inductors and for the converter structures. Each of these structures was modelled separately and the results were added by using the linearity of the conductive heat transfer as discussed in paragraph 4.6.2. This process resulted in temperature distribution over the converter structure with the influence of active as well as passive components.

Models

The implemented 3D model of the converter structure is shown in Figure C-1. Simplifications were made to the structure to reduce the complexity of the model and to be able to simulate the structure with high accuracy. As can be seen, the model contains only half of the power converter structure. This was done to reduce the size of the model and hence to be able to use more detailed mesh. Spatially and thermally, the two halves of the converter structure are assumed to be identical. The only difference is that during the converter operation, the power modules placed on one thermal surface work as IGBT switches, whereas the power modules on the opposite surface work as rectifier diodes. The model presented below is considered for IGBT as well as for diode operation. Both cases are considered because the IGBT chips exhibit a higher power loss than the diodes but, on the other hand, the diode chips have smaller surfaces available for the heat exchange and therefore a higher thermal resistance. The power modules are modelled in full detail, with all layers of the DBC substrate and real dimensions taken from the real modules implemented in Converter Demonstrator II.

The resonant capacitors are not included in the model because their power loss is negligible in comparison to the other components. Another aspect is that the structures of the capacitors are rather complex and difficult to model because of their many layers.

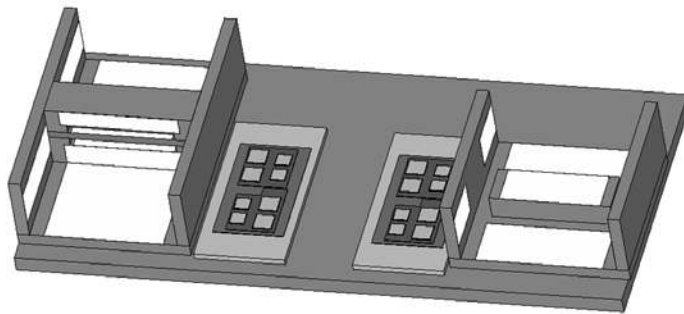


Figure C-1: Spatial model of converter structure used for FEM simulation; half of converter structure, simplification by using reduced transformer and inductor models

The models of the magnetics were realised with a high level of detail. The symmetry of the components was used to simplify the models. This resulted in modelling only one-eighth of the transformer structure (see Figure C-2) and one quarter of the inductor structure (see Figure C-3). The parameters of the materials implemented in the model are listed in Table C-1. Aluminium elements, ceramic elements and thermal sheets are simulated as homogeneous isotropic materials with the same thermal conductivity in all three directions. On the other hand, the cores and the windings are by nature anisotropic due to their layering. As the consequence of this, the winding structure is modelled as a solid homogeneous anisotropic material with different thermal conductivities in the direction along the foils and perpendicular to the foils. These conductivities are calculated on the basis of the share of copper and isolation in the appropriate direction. The resulting values are listed in Table C-1. In the corner elements of the winding model, the properties of the winding materials change because the winding foils change direction. To allow for effective heat transfer between the horizontal and vertical winding elements, the corner elements are defined as isotropic with the thermal conductivity along the foils used for all directions.

The thermal properties of the amorphous cores are not available in the data sheets. The thermal conductivities (obtained upon direct request to the core manufacturer) are: for the direction perpendicular to the laminations approximately 9 W/mK, the value in the direction of laminations is not known but is indicated to be higher than for the perpendicular direction. The anisotropic material models in FEM software allow separate definition of thermal conductivities in x, y and z axis. The complex round shape of the cores results in a change of the orientation of core lamination (with respect to x, y and z axis) which prevents the definition of thermal conductivities in the direction along and perpendicular to the laminations. For this reason, the core material is assumed to be isotropic with the thermal conductivity of 9 W/mK in all directions. This configuration represents the worst-case scenario.

The heat pipes are phase change devices and detailed modelling of these is difficult by FEM software. In the presented thermal models, the heat pipes are replaced by solid blocks with high thermal conductivity. The thermal conductivity used is the effective thermal conductivity given by the heat pipe manufacturer (7000 W/mK).

The leakage layer material is another material in relation to whose thermal properties there is hardly any information available. This material consists of an epoxy with a relatively low thermal conductivity of 0.5 W/mK which is filled with small metal particles of VITROPERM Flakes. The thermal conductivity used in the model is a guess value of 1.5 W/mK. This value includes the increase of the thermal conductivity due to the metal particles. The value of 1.5 W/mK is chosen because it corresponds to the typical thermal conductivity of thermally conductive epoxies. These consist of resins filled with tiny ceramic beads and have conductivity values up to a maximum of 2 W/mK.

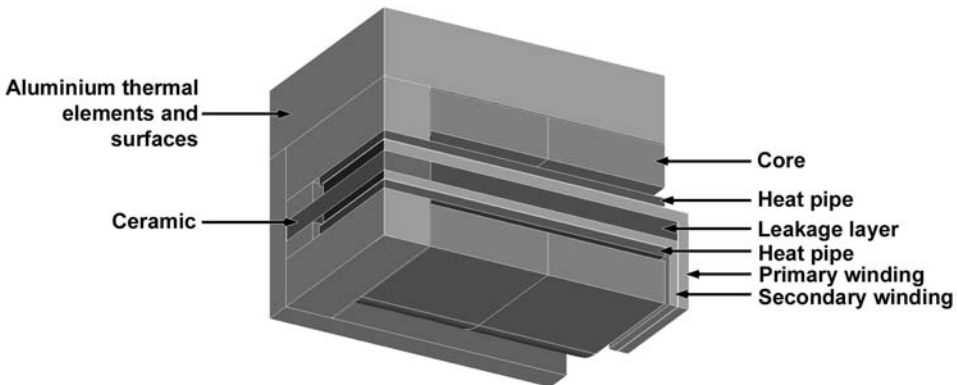


Figure C-2: Spatial model of transformer structure used for FEM simulation, complete detailed model

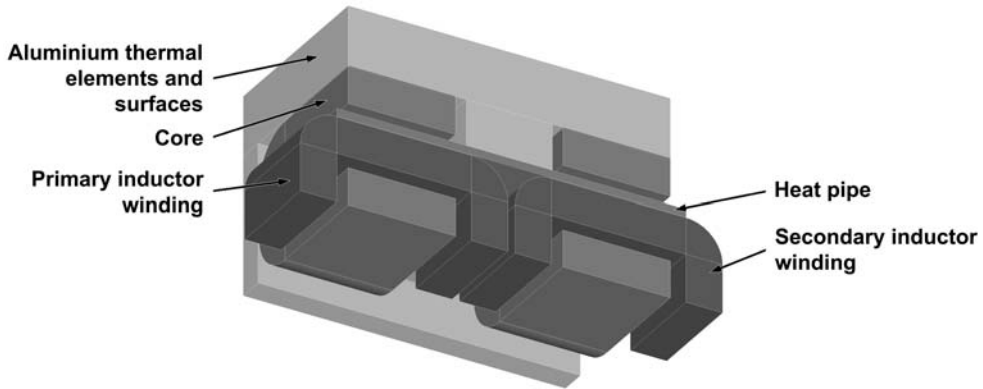


Figure C-3: Spatial model of inductor structure used for FEM simulation, complete detailed model

Table C-1: Thermal properties implemented in FEM model

Material		Thermal Conductivity [W/mK]
Aluminium 51ST6082		120
Ceramic Shapal M®		90
Thermal sheet 0.5 mm		1.5
Transformer Windings 0.25 mm Cu / 0.07 mm isolation	Along	262.5
	Perpendicular	0.314
Inductors windings 0.5 mm Cu / 0.07 mm isolation	Along	312.2
	Perpendicular	0.528
Kapton® isolation 0.07 mm		0.1
Amorphous cores		9
Leakage layer		1.5
Heat pipe		7000

The power dissipation in the models is displaced through the heat dissipating volumes. The values listed in Table C-2 are used in the models presented here. These values were obtained by calculations in the chapters of this thesis and estimated from real measurements.

Table C-2: List of power loss inputs used in FEM models

Object		Power loss [W]
Transformer primary winding	Calculated	67.5
Transformer secondary winding	Calculated	73.5
Transformer core total	Measured	190
Transformer leakage layer	Guess value	60
Inductor input winding	Calculated	22.7
Inductor input core	Calculated	35.4
Inductor output winding	Calculated	34.2
Inductor output core	Calculated	40.9
IGBT	Calculated	120

The constraints for the thermal management are the hot-spot temperatures in different converter components. The temperature of the silicon chips is limited to the maximal junction temperature of 155 °C. Therefore, this temperature is considered as the constraint for the hot-spot temperature of the power semiconductors. The maximal operating temperature of power passives is limited by the materials used in the component assemblies. For the material used in magnetics, the lowest maximal temperature is specified as 150 °C for the epoxy used in the leakage layer. Therefore, for the design

presented in this thesis, the temperature of 120 °C is used as the hot-spot temperature limit. The reason for this is to leave a margin for the local temperature increase within the structure. Local overheating might occur, especially in the windings due to their many layers, and this might result in problems with good thermal contact between these layers.

Results

The results of modelling the converter structure without including the power dissipation of passives are shown in Figure C-4. As can be seen, the maximal operating temperature on the surfaces of the IGBT chips is approximately 95 °C. Another noticeable fact is that the heat produced in the IGBT chips spreads only a little beyond the boundaries of the power modules. This is also illustrated by Figure C-5, which shows the aluminium parts of the transformer and the inductors with the temperature range scaled up. As can be seen, the maximal temperature rise is on the outer side of the aluminium elements of the transformer and inductor structure. This temperature rise is approximately 1 °C, which is very small and can therefore be disregarded. The distribution of heat throughout the converter structure will be discussed once more in the final simulation of the converter structure with the influence of the transformer and inductors included.

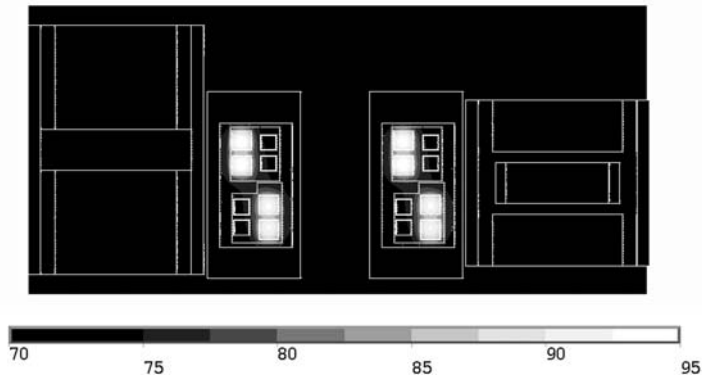


Figure C-4: Temperature distribution through the converter structure with neglecting influence of passives, top view

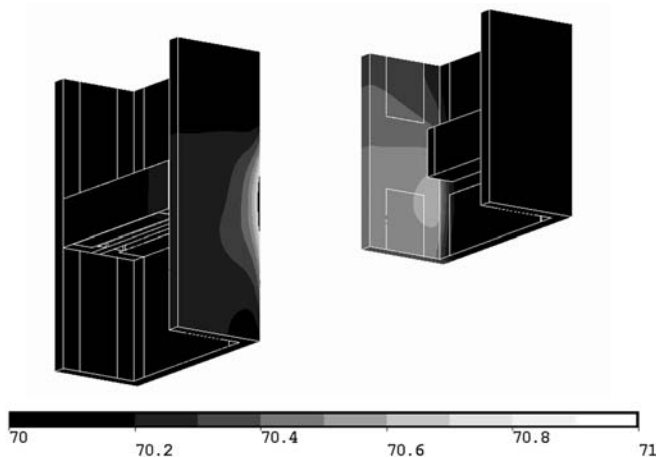


Figure C-5: Temperature rise on the aluminium structures of transformer and inductors without influence of passives

The temperature distribution throughout the transformer structure is depicted in Figure C-6. The maximal temperature of 132 °C is observed in the centre of the winding, inside of the leakage layer. This hot-spot is caused by the relatively low thermal conductivity of the leakage layer and the high thermal resistance between the centre of the winding structure and the heatsink. The high thermal resistance is a result of the isolation layers in the heat-removal path. The maximal temperature observed on the magnetic cores is approximately 100 °C. This temperature is low with respect to the amount of heat dissipated in the cores in comparison to the windings. This temperature is a consequence of the high thermal conductivity of the cores and the large contact area between the cores and the heatsinks. The transformer hot-spot temperature of 132 °C is higher than the maximal specified temperature of 120 °C. The calculated hot-spot is below the maximal operating temperature of the materials considered and therefore this design is used in the converter demonstrator. The real temperature is expected to be even slightly higher due to the layering of the windings.

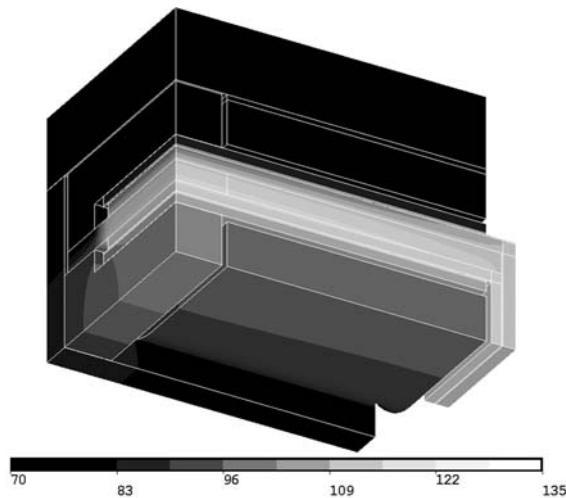


Figure C-6: Temperature distribution throughout the transformer structure

Heat removal from the inductor structure is based on the same concept as the one used in the transformer. The main difference is that in the inductor structure the heat pipes are attached only to the outer surface of the windings. This results in a smaller area available for the heat transfer. Figure C-7 shows the temperature distribution throughout the inductor structure. As can be seen, the highest temperatures are observed on the inductor windings. These high temperatures are the result of the aforementioned smaller surface area available for the heat exchange, which yields a high temperature rise across the isolation present between the winding surface and the heat pipes. A maximal temperature of approximately 110 °C is observed on the winding of the output inductor due to the higher power dissipation in this winding than in the winding of the input inductor. The design with this hot-spot temperature is used in the final converter prototype.

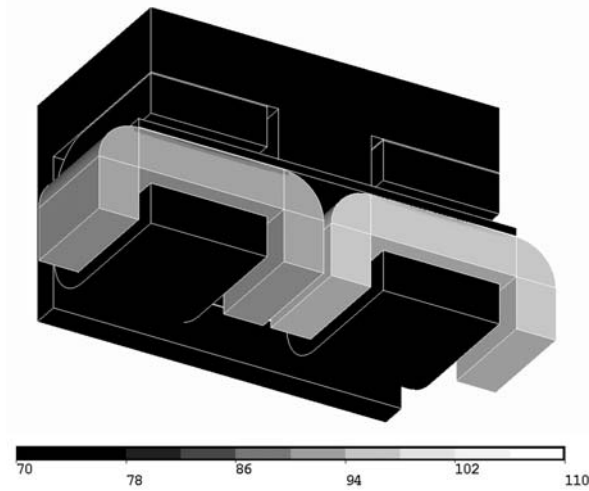


Figure C-7: Temperature distribution throughout the structure of filter inductors

Figure C-8 and Figure C-9 show the temperature distribution throughout the converter structure for the IGBT operation and the diode operation respectively with the influence of the power magnetics included. As can be seen from the comparison of Figure C-8 with Figure C-4, the power loss in the magnetics does not influence the hot-spot temperature of the IGBT chips. The hot-spot temperature of approximately 95 °C is observed in both cases. The same is observed for the diodes with the hot-spot temperature of 90 °C. Figure C-10 and Figure C-11 show the surface temperatures of the power modules' base-plates and the base plates of the magnetic structures. As can be seen, the temperature rise of the base-plates of the power magnetics is within 4 °C of the assumed heatsink temperature. The base-plates of the power modules show the maximal temperature rise of approximately 10 °C for the IGBTs and 7 °C for the diodes.

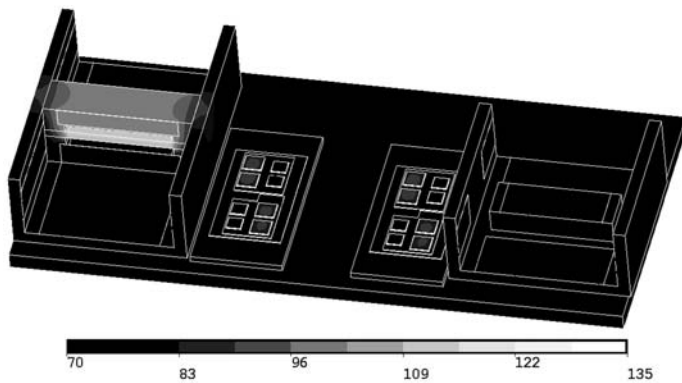


Figure C-8: Temperature distribution throughout the converter structure with “simulated” influence of passives, IGBTs in operation

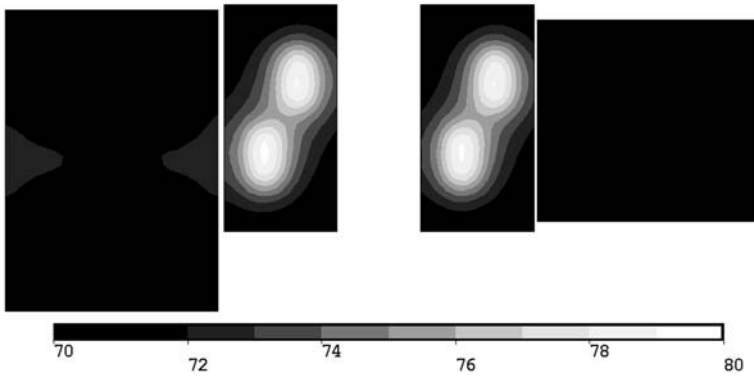


Figure C-9: Surface temperatures of power module base-plates and base-plates of magnetics, simulated influence of passives, IGBTs in operation

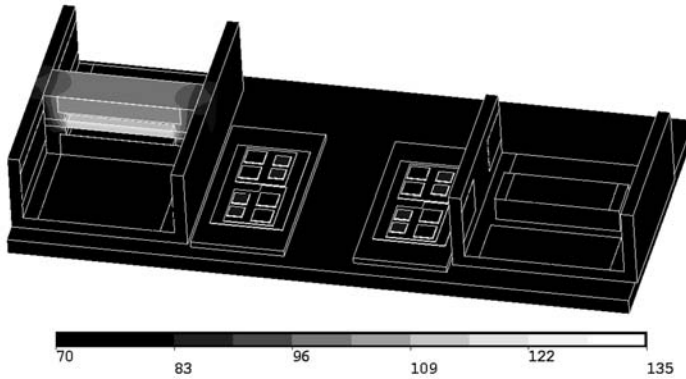


Figure C-10: Temperature distribution through the converter structure with “simulated” influence of passives, Diodes in operation

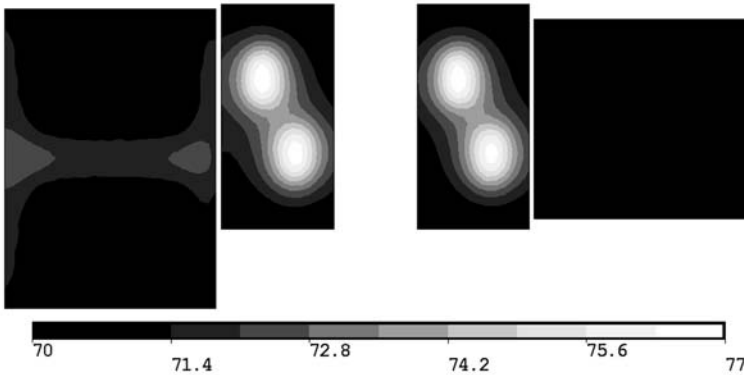


Figure C-11: Surface temperatures of power module base-plates and base-plates of magnetics, simulated influence of passives, Diodes in operation

Summary

In practice, isolated dc-dc converters for high-power are hardly applied although there is a need for them. They are needed for applications which require galvanic isolation for safety or functional reasons and for applications which require a large input to output ratio. Currently, a combination of conventional low frequency transformers and high-frequency converters is applied to realise the required function. Such solutions are often very heavy and bulky.

The possibilities of increasing the power density of high-power dc-dc converters with galvanic isolation are discussed in this thesis. Three cornerstones for reaching high power densities are identified as: size reduction of passive components, reduction of losses particularly in active components and thermal management. These three corner stones are addressed separately in this thesis. In addition to the cornerstones, the spatial integration of converter components is considered as it is also important for high power density.

Size Reduction of Passives

Passive components are usually the bulkiest components of any converter design. This is more pronounced in high-power than in low-power converters because of the lower operating frequencies at high power. The size of passives is directly related to the operating frequency and therefore operation at high frequencies is one of the keys to reaching a high power density.

On the other hand, an increase of operating frequency yields also higher losses in passive components themselves. Therefore, new design approaches and technologies must be used to obtain an optimal performance of the passive components. This is considered in this thesis by investigating power losses in windings of magnetic components with special attention to the transformer windings.

Integration of several passive components into a single component is also considered as the means to increase the power density. In this thesis, a possibility to integrate the resonant inductance into a power transformer is investigated. The main challenge is the integration of components at the considered high power levels.

Converter Topology

A high switching frequency is required to decrease the size of passives and hence increase the power density. Such high switching frequency results in a substantial increase of switching losses in active components. The higher losses yield reduced efficiency and require larger heatsinks which consequently reduce the effect of the higher operating frequency on the overall power density.

The power loss in active components is usually reduced by applying advanced soft switching converter topologies. This is also considered in this thesis where several topologies that have a potential of reducing turn-on as well as turn-off losses are discussed. So called Zero-Voltage-Switching Quasi-Zero-Current-Switching topology is selected and investigated in detail.

Thermal Management

One of the by-products of electrical power conversion is heat. The heat is generated inside converter components and must be removed to prevent them from overheating. Performing this task becomes more difficult as the power density increases because of higher power dissipated in a smaller volume. Often, an advanced thermal management system must be used.

This thesis considers thermal management of a power converter on component, converter and system level. Each of the levels is addressed separately and adequate heat removal methods and concepts are proposed for each of the levels. Based on the selected methods, a thermal management concept for the complete converter is proposed and evaluated in detail. The main objectives of the thermal design are: ability to remove the generated heat with acceptable temperature rise, flexibility with respect to heat exchange with the environment, small size, simplicity and reliability. These objectives are realised in a thermal management based on conduction supported by heat pipes. The heat is consequently collected on so-called thermal surfaces where the heat exchange with the environment occurs.

Spatial Integration of Components

Spatial integration of converter components is important to obtain a high power density as well. The key to the successful integration of components is to make design choices which result in components of compatible dimensions and shapes. In such a design, universal rules that can be followed in order to gain the successful component integration do not exist. Therefore, basic guidelines that should serve as an aid in the design of high power density high-power converters are offered in this thesis. The guidelines are discussed based on the structure of the constructed converter prototypes.

Scaling Up

The operating conditions and requirements vary with the power level processed by a power converter. Therefore, the scalability of the design concepts and approaches is important for their practical implementation in the wide range of considered applications. This thesis briefly discusses scaling up with respect to power density and performance of the converter components.

Conclusions

The main conclusion that can be drawn in this thesis is that by a careful design of passive components, selection of converter topology and by using an advanced thermal management, a high power density can be obtained also in high power converters. This is demonstrated on a 50 kW converter prototype with a power density of 11.13 kW/litre. It is also shown that by designing for high power density, the efficiency might not need to suffer. The measured efficiency of the final converter prototype is as high as 97.5 % in a broad load range.

Samenvatting

Geïsoleerde dc-dc omzeters voor hoge vermogens worden in de praktijk nauwelijks toegepast, hoewel er wel vraag naar is. Ze zijn nodig voor toepassingen die vanuit veiligheidsoogpunt of vanwege functionele redenen galvanische scheiding vereisen en voor toepassingen die een grote overzetverhouding vereisen. Vandaag de dag wordt een combinatie van conventionele laag-frequente transformatoren en hoog-frequente omzeters toegepast om de vereiste functionaliteit te realiseren. Zulke oplossingen zijn vaak erg groot en zwaar.

Dit proefschrift bediscussieert de mogelijkheden om de vermogensdichtheid van hoog-vermogen dc-dc omzeters met galvanische scheiding te vergroten. Drie hoekstenen die een grote vermogensdichtheid mogelijk maken zijn geïdentificeerd: verkleinen van de passieve componenten, reduceren van de verliezen in vooral actieve componenten en de thermische huishouding. Deze drie hoekstenen worden in het proefschrift afzonderlijk behandeld. In aanvulling op de hoekstenen is de ruimtelijke integratie van de omzetter-componenten beschouwd, aangezien deze belangrijk is voor een hoge vermogensdichtheid

Volumeverkleining van passieve componenten

In elk omzetter ontwerp hebben passieve componenten meestal het grootste volume. Vanwege de lagere frequentie bij hoog vermogen is dit duidelijker bij omzeters voor hoog vermogen dan bij omzeters voor laag vermogen. De afmetingen van passieve componenten zijn direct gerelateerd aan de frequentie en daarom is het werken bij hoge frequentie een belangrijke manier om een hogere vermogensdichtheid te bereiken.

Aan de andere kant zorgt een hogere frequentie ook voor hogere verliezen in de passieve componenten zelf. Daarom moeten er nieuwe ontwerpbenaderingen en -technologieën gebruikt worden om een optimale prestatie van de passieve componenten te behalen. Dit is in dit proefschrift gedaan door de verliezen in de windingen van magnetische componenten te onderzoeken, met speciale nadruk op de transformator windingen.

De integratie van verschillende passieve componenten in één component is ook overwogen als een manier om de vermogensdichtheid te verhogen. In dit proefschrift is een mogelijkheid onderzocht om de resonante inductiviteit te integreren in de vermogenstransformator. De belangrijkste uitdaging is de integratie van de componenten bij de beschouwde hoge vermogens

Omzetter-topologie

Om het volume van de passieve componenten te verkleinen, en dus de vermogensdichtheid te vergroten, is een hoge schakelfrequentie vereist. Zo'n hogere schakelfrequentie resulteert in een aanzienlijke toename van de schakelverliezen in de actieve componenten. De grotere verliezen zorgen voor een lager rendement en vereisen grotere heatsinks, met als gevolg dat het effect van de hogere schakelfrequentie op de totale vermogensdichtheid gereduceerd wordt.

De verliezen in actieve componenten worden meestal gereduceerd door het toepassen van ‘soft switching’ topologieën. Dit is ook overwogen in het proefschrift. Verschillende topologieën die de mogelijkheid hebben de inschakel- als wel de uitschakelverliezen te reduceren zijn bediscussieerd. De zogenaamde ‘Zero-Voltage-Switching Quasi-Zero-Current-Switching’ topologie is geselecteerd en tot in detail onderzocht.

Thermische huishouding

Een van de bijproducten van elektrische vermogensconversie is warmte. De warmte ontstaat intern in de componenten en moet worden verwijderd om ervoor te zorgen dat de componenten niet oververhit raken. Dit wordt moeilijker als de vermogensdichtheid toeneemt, omdat een groter vermogen wordt gedissipeerd in een kleiner volume. Vaak moet een geavanceerd systeem voor de warmte behandeling worden gebruikt.

Dit proefschrift overweegt de thermische huishouding voor de omzetter op het niveau van de component, de omzetter en het systeem. Elk niveau is afzonderlijk behandeld en adequate methodes en concepten om de warmte te verwijderen zijn voorgesteld voor elk van de niveaus. Gebaseerd op de geselecteerde methodes is er een concept voor de thermische huishouding voor de hele omzetter voorgesteld en in detail geëvalueerd. De belangrijkste doelstellingen van het thermisch ontwerp zijn: de mogelijkheid om de opgewekte warmte te verwijderen met een acceptabele temperatuurstijging, flexibiliteit met betrekking tot de warmte-uitwisseling met de omgeving, kleine afmeting, eenvoudigheid en betrouwbaarheid. Deze doelstellingen zijn gerealiseerd in een thermisch ontwerp dat is gebaseerd op geleiding ondersteund met ‘heat pipes’. De warmte wordt vervolgens verzameld op zogenaamde thermische oppervlakten waar de warmte-uitwisseling met de omgeving plaatsvindt.

Ruimtelijke integratie van componenten

Ook ruimtelijke integratie van omzetter componenten is belangrijk om een hogere vermogensdichtheid te behalen. De sleutel tot een succesvolle integratie is het maken van ontwerpkeuzes die resulteren in componenten met uitwisselbare afmetingen en vormen. In zo’n ontwerp bestaan geen universele regels die gevolgd kunnen worden om tot een succesvolle integratie te komen. Daarom worden er in dit proefschrift een aantal basisregels aangereikt die kunnen dienen als hulp bij het ontwerp van hoogvermogen omzeters met een hoge vermogensdichtheid. De regels zijn bediscussieerd op basis van de structuur van de geconstrueerde omzetter prototypes.

Opschaling

De bedrijfstoestand en de vereisten variëren met het vermogensniveau dat wordt behandeld door een omzetter. Daarom is de schaalbaarheid van de concepten en benaderingen van belang voor hun praktische toepasbaarheid in een breed bereik van beschouwde toepassingen. In dit proefschrift wordt opschaling kort bediscussieerd, met betrekking tot de vermogensdichtheid en prestatie van de omzetter componenten.

Conclusies

De belangrijkste conclusie die kan worden getrokken uit dit proefschrift is dat door een zorgvuldig ontwerp van passieve componenten, selectie van omzetter-topologie en met behulp van een geavanceerde thermische huishouding ook in hoogvermogen converters een grote vermogensdichtheid kan worden bereikt. Dit is gedemonstreerd met een 50 kW prototype met een vermogensdichtheid van 11.13 kW/liter. Het is ook aangetoond dat het ontwerpen voor een hoge vermogensdichtheid het rendement niet hoeft te schaden. Het gemeten rendement van het laatste prototype is 97.5% in een breed werkingsgebied.

Acknowledgements

The work presented in this thesis was performed in the Electrical Power Processing (EPP) group at the Delft University of Technology, The Netherlands. Interaction with other people was an important part of this work. Therefore, I would like to thank the people that contributed to this work directly by their scientific ideas but also indirectly by their friendship and support.

The first “thank you” goes to my promotor Prof. Ferreira. He was the one who always saw the bigger picture behind the work done on every day basis. Preparing all the future planning and thinking about the contribution of my work was difficult but it made me see what we were aiming for. Also, his direct expertise in constructing power converters was very helpful while building the prototypes.

Sjoerd de Haan was my direct supervisor and the person who I came the most into contact with on the daily basis. I remember all those discussions in his office about new ideas, progress of the work, results and conference papers. I must not forget the effort he put and the time he spent correcting my scientific papers and also this thesis. Sometimes I have the impression that he has done more work in writing this thesis than I did. Thank you.

I also want to mention Paul Bauer who was my contact before starting this work. He also helped me a lot in understanding and making sense of the new world upon my arrival to Holland. Thank you.

Rob Schoevers was the person that I directly worked with in the lab. He offered the expertise in construction of power converters and in troubleshooting of the problems that occurred while building the prototypes. Often, he was the only person who was present in the lab when things went wrong. Thank you for being there when the converter exploded!

Thanks also to all other members of the EPP group that contributed to this work by their comments and questions during the famous presentations at colloquia. It was a pleasure to work with you during the past five years.

This thesis was only possible thanks to IOP (Innovatiegerichte Onderzoeksprogramma’s) of the Dutch government that financed the whole project. My “thank you” goes also to all the members of the BC (begeleidingscommissie) committee that contributed to this work by valuable ideas and comments. In particular I would like to express my gratitude towards Evert Rijen from Exendis, Mart Hurkmans from Imtech and Arno van Zwan from Mastervolt who showed the most interest in the presented research. I am very glad they liked my ideas and that some of them made it to real industrial products.

Thank you also to the Ph.D. defence committee members who took their time and commented on the presented work. These includes: Prof. Rick de Doncker, Doc. Jaroslav Dudrik, Prof. Cees Beenakker, Prof. Michel Antal and Prof. Johan Smit.

Prof. Craig MacKenzie did the English editing on the final version of this thesis, thank you. Johan Moren spent his time translating my summary and propositions into Dutch in the time when he was finishing his own Ph.D. thesis, big thanks for that.

Big big but big thanks goes also to my family; my mum Margita, my dad Jozef, my brother Vlado and my sister Danka. In the past few years each of us children lived in a different country which made it especially difficult for our parents. In spite of this hardship, they supported us during all that time because they knew that that was what we wanted. Much has changed between Danka, Vlado and me during the past five years. By being far apart we became somehow closer together. The only thing that comes to my mind right now is to say that I love you so much and that it is a pity that we were not able to be together and see each other more during these past years.

It is quite easy to say “thank you” but as my girlfriend Joyce says, you shouldn’t say “thank you” to a friend. So instead, I’m going to tell a few stories about the people that meant a lot to me in this past five years living in Holland.

In June 2000, I heard the first time about a Ph.D. position in Delft, The Netherlands. Of course I knew where The Netherlands was but I did not have a slightest clue about Delft. So, what I first did was, on my way home from the university, I went to a book store to check the map of Holland to find out more about my possible future living place. And indeed, after almost a year of organising the required paper work and waiting, I came to Delft.

What a journey! 24 hours on the bus going into a completely new world. The only thing I knew was that at the station in Den Haag, I was supposed to look for a woman wearing a scarf. That was Lenny, at that time the secretary of Prof. Ferreira. That amazing woman offered me “a roof above my head” for a couple of days until I got the keys of my apartment. Later, she became a friend and a person I could talk to at any time. She used to call us, -Mark, Jelena and me- “her kids”. She took us to many nice trips and invited us for super dinner. Then she went to live in France, nevertheless she remained a good friend and a person that I love to see every time I have the opportunity. Thank you Lenny.

Katy, a girl with a smile on her face. She became a great friend and support in the difficult times upon the arrival to Holland. I cannot imagine her not being there, in that case this book probably would not exist. I remember countless talks, standing in the rain under a balcony of a house in Rotterdam and talking for hours, walking the streets and talking and simply just talking talking and talking. She used to call me her best “girl friend”. Thank you for being there and helping me through difficult times.

Jelena & Mark, colleagues, roommates and friends. We did so many things together that I don’t even know where to start. I shall mention one moment when Mark entered my office and said that he wanted to talk to me. I was a bit surprised by the tone of his voice but in seconds I understood it. He came to tell me that he and Jelena have decided to date each other and I was the first person to know it. I also remember Jelena five minutes later. I found her sorting some paperwork... or was she maybe trying to hide from me in the smallest office there was? She wore a white woollen sweater and had a big smile on her face. Just to finish this part of the story, Jelena and Mark will get married six days after my promotion. Congratulations and thank you for all your support and help and willingness to share two years of your life with me as roommates in Buitewatersloot 67. Thank you.

Michiel, one of the few Dutch friends that I have. When we met, he was a master student at EPP department. One weekend he invited me for a ligfiets show close to Lelystad. I did not know what a

ligfiets was, but the proof ride was a success and as well was the friendship with Michiel. Thank you my friend.

Erik, a person with exquisite humour. I enjoy so much talking to him because he always makes a joke in the middle of a serious sentence. The story that comes to my mind is not so funny though. One day in Dallas, we were almost flooded by rain water on our way to the hotel. We were lost in a strange city quarters submerged under the water, trying to get petrol at a petrol station that does not work when it rains and then stucked on the highway with all exits closed because of the flood. But luckily, our exit was opened and we safely reached the hotel. Erik, thank you for all those moments.

Maxime, a colleague with whom I shared the office for two years. He was a great inspiration to me. He came to Holland from Canada to do research in wind energy because he wanted to contribute to a cleaner society. As if the Ph.D. was not enough, he managed to start a company in Canada and to be a father and a husband at the same time. I remember many talks with him in our office about doing a Ph.D. At that time, I did not understand completely what he was talking about but now finishing my Ph.D. I can see and understand what he meant. Thank you Maxime.

Robert, a colleague from next door and a gym buddy. I will probably never forget the sleepless night after the first time that I went to gym with him. Later, I enjoyed so much to share the lunch breaks with him in the gym. There I found the needed relax and distraction from working with the computer the whole day. Thank you and take care with giving a lesson to those weights.

It is a pity that I cannot mention stories that come to my mind when remembering everybody I met in Delft. If I would do that, these acknowledgements would be longer than the thesis itself and that is not the point. I shorten it by saying: Milan was my office mate who I faced at my desk for a year and a half, thank you for many discussions. Jan and Honza, my Czechoslovak friends visiting the EPP group from time to time; it was a pleasure to meet you. Marcel and Petra, I enjoy your company so much every time! when we meet, usually at your place, I do not want to go home and I often end up running for the last train. Peter, Evandro, George, Marnix, Cristian, Frank, Mattia, Yi, Dongsheng, Dongche, Kiljang, Mitchi, Matteo, Mariel, and others; it was great meeting you, your company was often the only thing that made me go to have lunch at our famous canteen.

Groningen and the people there offered a different perspective to my life. A trip from Delft to Groningen is every time like a trip from an engineering world to a world of art. Janja (Lemon), Sonja (Mango), Primoz (Artichoke), Branislava (Orange), Graem (Cherry), Eleonora (Apple), Cristiano (Kiwi) and other fruits, thank you for making me see the world from that different perspective.

I must also not forget my friends in Slovakia. The connection in the past five years was somewhat lost but I have never forgotten you. Martin, Martin, Jozef, Peter, Fero, Aja and others, I am looking forward to meeting all of you again in Slovakia.

Last but not least of the friends, I must mention Peter, my companion to my first trip to Mont Blanc. We went together through crevasse fields, steep slopes, tiredness, coldness, sleepless nights, snow storms and other intense experiences but managed to reach the summit. I will never forget the feeling of having so much trust in someone. The connection by a rope gives more than only a physical connection to stop a fall, it connects the two people mentally as well. The experience of the Mont Blanc trip helped me in many difficult situations during my Ph.D. trip. Peter thank you for having your trust in me and attaching your rope to my harness.

At last, Joyce, Christine, Claudia, Ananas, however I call you, you are the single, most important person in my life. You were also the second person that I attached my ropes to. I would always do so even though sometimes I am afraid that you would jump in the crevasse just to have the experience of

it. One person called you “Muse of engineers”, and that you truly are for me. By not knowing and not having you in my life, I would lose so much. You opened my mind and let me see the world of smiling, talking, enjoying moments. To conclude this book, I only want to say one thing: I so much look forward to spend the future with you. And in this case, by “the future” I do not mean us going to Japan in October or to Slovakia in one week time. I mean the next second, minute, hour, day, the moment I shall hear your voice, the moment I shall see you, the moment I shall think of you. Thank you for coming into my life.

Curriculum Vitae

Martin Pavlovský was born in Prešov, Slovakia, on 23rd of April 1977. In 2000, he received the Ing. degree cum laude from the Faculty of Electrotechnics and Informatics, Department of Electric Drives and Mechatronics, Technical University of Košice, Slovakia.

In April 2001, he started working towards the Ph.D. degree at Delft University of Technology in The Netherlands. The work of this thesis was done in the research group of Electrical Power Processing of the Faculty of Electrical Engineering, Mathematics and Informatics. His Ph.D. research was sponsored by IOP (Innovatiegerichte Onderzoeksprogramma's) of the Dutch government.

His main research interests include packaging, thermal management and high power density of high power converters.